CMS Draft Analysis Note

The content of this note is intended for CMS internal use and distribution only

2010/09/18
Head Id: 15862
Archive Id: 17250
Archive Date: 2010/07/27
Archive Tag: trunk

Measurements of Inclusive W and Z Cross Sections in pp Collisions at $\sqrt{s} = 7$ TeV

N. Adam[36], N. Akchurin[38], J. Alcaraz Maestre[18], N. Amapane[16], P. del Arbol[20], R. Arcidiacono[16], S. Baffioni[3], M. Bachtis[39], D. Bandurin[31], J. Bendavid[32], S. Beri[7], J. Berger[5], J. Berryhill[28], A. Bodek[37], C. Botta[16], S. Bolognesi[21], J. Branson[25], C. Broutin[3], J. Butler[28], A. Calderon[20], R. Castello[16], C. Charlot[3], G. Di Giovanni[27], M. Chen[27], Y. Chung[37], M. Cepeda[18], A. de Cosa[12], J. Damgov[38], B. De La Cruz[18], B. Dahmes[33], G. Daskalakis[6], C. Díez Pardos[18], M. Dittmar[22], T. Dorigo[14], A. Drozdetskiy[27], J. Duarte[20], J. Efron[39], J. Eugster[22], D. Evans[25], P. Everaerts[32], A. Everett[30], F. Fabozzi[13], J. Fernandez[19], L. Freton[3], D. Futyan[23], I. Furic[27], J. Gartner[27], J. Gomez[27], G. Gomez-Ceballos[32], D. Green[28], K. Grogg[39], M. Grothe[39], M. de Gruttola[12], K. Hahn[32], V. Halyo[36], J. Han[37], P. Harris[32], J. Hays[23], N. Heracleous[4], J.M. Hernández[18], O. Hindrichs[4], W. Hintz[22], A. Ivanov[31], M. Jindal[7], M.I. Josa[18], C. Jorda[20], P. Kalavase[26], S. Kesisoglou[6], S. Khalil[31], P. Killewald[35], T.J. Kim[17], P. Klabbers[39], M. Klute[32], A. Korytov[27], I. Kravchenko[34], A. Kubik[29], S. Kwan[28], C. Lazaridis[39], M. LeBourgeois[25], S. Lee[38], D. Lelas[2], P. Lenzi[9], J. Leonard[39], C. Leonidopoulos[21], L. Lista[11], L. Lloret[19], D. Majumder[8], M. Makouski[31], M. Malberti[10], C. Marchica[22], E. Di Marco[15], C. Mariotti[16], M. de Mattia[14], K. Matchev[27], K. Mazumdar[8], P. Meridiani[22], K. Mishra[28], G. Mitselmakher[27], S. Nahn[32], R. Nandi[23], N. Neumeister[30], C. Ochando[3], P. Paganini[3], R. Paramatti[15], C. Paus[32], D. Piparo[5], C. Plager[24], I. Puljak[2], V. Rekovic[33], R. Rodrigues[1], Y. Roh[38], N. Rompotis[23], C. Rovelli[21], D. Sabes[3], A. Saha[8], L. K. Saini[7], R. Salerno[3], A. Sancheiz[22], M. Sani[25], J. Santaolalla[18], A. Savin[39], A. Sharma[7], C. Seez[23], A. Schorlemmer[34], J. Singh[7], M. Soares[18], L. Spiegel[28], S. Stoynev[29], K. Sung[32], A. Svyatkovskiy[30], T. Tabarelli de Fatis[10], P. Tan[28], S. Tkaczyk[28], D. Trocino[16], L. Uplegger[28], A. Vartak[25], I. Vila[20], R. Vilar[20], N. Wardle[23], D. Wardrope[23], J. Werner[36], S. Xie[32], F. Yang[28], E. Yazgan[38], H. Yoo[30], A. Zabi[3], and M. Zeise[5]

[1] Centro Brasileiro de Pesquisas Fsicas, Rio de Janeiro, Brazil
[2] Technical University of Split, Split, Croatia
[3] Laboratoire Leprince-Ringuet, Ecole Polytechnique, IN2P3-CNRS, Palaiseau, France
[4] Rheinisch-Westfaelische Technischen Hochschule, Aachen, Germany
[5] Institut für Experimentelle Kernphysik, Karlsruhe, Germany
[6] Institute of Nuclear Physics "Demokritos", Aghia Paraskevi, Greece
[7] Panjab University, Chandigarh, India
[8] Tata Institute of Fundamental Research - EHEP, Mumbai, India
[9] Istituto Nazionale di Fisica Nucleare (INFN) Sezione di Firenze and Università degli Studi di Firenze

[10] Istituto Nazionale di Fisica Nucleare (INFN) Sezione di Milano-Bicocca and Università degli Studi di Milano-Bicocca, Milano, Italy
[11] Istituto Nazionale di Fisica Nucleare (INFN) Sezione di Napoli , Napoli, Italy
[12] Istituto Nazionale di Fisica Nucleare (INFN) Sezione di Napoli and Università degli Studi di Napoli "Federico II", Napoli, Italy
[13] Istituto Nazionale di Fisica Nucleare (INFN) Sezione di Napoli. Also with Università della Basilicata
[14] Istituto Nazionale di Fisica Nucleare (INFN) Sezione di Padova and Università degli Studi di Padova, Padova, Italy
[15] Istituto Nazionale di Fisica Nucleare (INFN) Sezione di Roma-I and Università degli Studi di Roma "La Sapienza", Roma, Italy
[16] Istituto Nazionale di Fisica Nucleare (INFN) Sezione di Torino and Università degli Studi di Torino, Torino, Italy
[17] Korea University
[18] Centro de Investigaciones Energeticas Medioambientales y Tecnologicas (CIEMAT), Madrid, Spain
[19] Universidad de Oviedo, Oviedo, Spain
[20] Instituto de Fisica de Cantabria (IFCA), CSIC-Universidad de Cantabria, Santander, Spain
[21] CERN, European Organization for Nuclear Research, Geneva, Switzerland
[22] Institute for Particle Physics, ETH Zurich, Zurich, Switzerland
[23] Imperial College, University of London, London, United Kingdom
[24] University of California, Los Angeles, Los Angeles, California, USA
[25] University of California, San Diego, La Jolla, California, USA
[26] University of California, Santa Barbara, Santa Barbara, California, USA
[27] University of Florida, Gainesville, Florida, USA
[28] Fermi National Accelerator Laboratory, Batavia, Illinois, USA
[29] Northwestern University, Evanston, Illinois, USA
[30] Purdue University, West Lafayette, Indiana, USA
[31] Kansas State University, Manhattan, Kansas, USA
[32] Massachusetts Institute of Technology, Cambridge, Massachusetts, USA
[33] University of Minnesota, Minneapolis, Minnesota, USA
[34] University of Nebraska-Lincoln, Lincoln, Nebraska, USA
[35] The Ohio State University, Columbus, Ohio, USA
[36] Princeton University, Princeton, New Jersey, USA
[37] University of Rochester, Rochester, New York, USA
[38] Texas Tech Univeristy, Lubbock, Texas, USA
[39] University of Wisconsin, Madison, Wisconsin, USA

Abstract

We present the first measurements of inclusive W and Z production cross sections in muon and electron decay channels at $\sqrt{s} = 7$ TeV, obtained using 37-53 nb^{-1} of pp collisions in the Compact Muon Solenoid (CMS) detector at the Large Hadron Collider (LHC). We additionally measure the luminosity-independent cross section ratios. The measurements are in agreement with NNLO QCD cross section predictions and current parton distribution functions.

This box is only visible in draft mode. Please make sure the values below make sense.

PDFAuthor:	The CMS Collaboration
PDFTitle:	Measurements of Inclusive W and Z Cross Sections in pp Collisions at sqrt“(s“)=7 TeV
PDFSubject:	CMS
PDFKeywords:	CMS, physics, software, computing

Please also verify that the abstract does not use any user defined symbols

Contents

1 Introduction

This note describes the first measurement in pp collisions of the inclusive cross production of W and Z boson production, observed via their decay to electrons and muons. The production rate of W and Z bosons subsequently decaying to charged leptons is an important process to measure at the LHC: it is simultaneously a benchmark for lepton reconstruction and identification to be used in future analyses, a precision test of perturbative QCD and the parton distribution functions of the proton (PDFs), a possible estimator of integrated luminosity for proton collisions [1–4], and the first electroweak process to be observed at the LHC. At the LHC, QCD predictions, in next-to-next-to leading order (NNLO) in the strong coupling α_s, exist for the matrix elements describing inclusive W and Z production [5–10]. When combined with recent NNLO PDFs [11, 12], the cross section is predicted with theoretical uncertainties of less than 4% [11–14]. The production of the W and the Z in hadron collisions has been measured at several previous experiments over a range of collision energies [15–19], and has been observed to agree well with Standard Model predictions. The inclusive cross section ratio of W and Z, R_{WZ}, and the charge cross section ratio of the W, R_{+-}, are also precisely predicted at the same accuracy, but do not suffer from experimental uncertainties in proton collision luminosity, which cancel, along with other uncertainties. The study uses 37-53 nb^{-1} of proton collisions collected at $\sqrt{s} = 7$ TeV in the 2010 LHC run.

2 Data and Monte Carlo samples

CMS colleceted LHC collision data corresponding to an integrated luminosity $\mathcal{L}_{\mathrm{int}} = \int \mathcal{L} \mathrm{d}t = 37.7\ \mathrm{nb}^{-1}$ for the W analyses, $45\mathrm{nb}^{-1}$for $\mathrm{Z} \rightarrow \mu^+\mu^-$, and $53\mathrm{nb}^{-1}$for $\mathrm{Z} \rightarrow \mathrm{e}^+\mathrm{e}^-$.

Several high statistic Monte Carlo (MC) simulated samples are used to evaluate signal and background efficiencies and to validate the analysis techniques deployed. Samples of electroweak processes with Z and W production, both for signal and background events, are produced with POWHEG [20–22] interfaced with PYTHIA [23] parton-shower generator. QCD events with a muon in the final state and $t\bar{t}$ events are studied with PYTHIA. Generated events are processed through the full GEANT4 [24, 25] detector simulation, trigger emulation and event reconstruction chain of the CMS experiment. The analysed samples are reported in Table 1. In the inclusive muons from QCD sample, decays-in-flight included, but no punch-through, and EM-enriched QCD samples contain no $\mathrm{b/c} \rightarrow \mathrm{e}$ decays, that are simulated in separate samples. Signal samples simulated with PYTHIA are used as cross-check with respect to POWHEG samples. Further details on the MC collections processed for both muon and electron channels are available in Ref. [26].

3 Muon identification

The muon identification is cut based which aims to simplify the efficiency estimations and make the selection procedure as transparent as possible. As explained in details in dedicated notes [27], [28], there are specific handles helping to select high quality muons. For the purpose of this analysis we aim to select prompt high p_T (> 20 GeV/c) muons. We are not to deal yet with ultra-high momentum muons, thus we are not to address the specific issues with them. In addition the triggering muon has to be in the well examined range $|\eta| < 2.1$ of the HLT trigger which, effectively, also suppresses the muon background and serves as a muon ID preselection. The muon ID selection is as follows.

- A muon has to be identified as a tracker (TRK) and a global (GLB) muon. This

Generator	Process	Kinematic cuts (in GeV, $c = 1$)	σ (pb)	Events	PDF set
POWHEG	$W^+ \rightarrow e^+\nu_e$	no cuts	6152	~700k	CTEQ66
POWHEG	$W^- \rightarrow e^-\overline{\nu}_e$	no cuts	4179	~700k	CTEQ66
POWHEG	$W^+ \rightarrow \mu^+\nu_\mu$	no cuts	6152	~700k	CTEQ66
POWHEG	$W^- \rightarrow \mu^-\overline{\nu}_\mu$	no cuts	4179	~700k	CTEQ66
POWHEG	$W^+ \rightarrow \tau^+\nu_\tau$	no cuts	6152	~700k	CTEQ66
POWHEG	$W^- \rightarrow \tau^-\overline{\nu}_\tau$	no cuts	4179	~700k	CTEQ66
POWHEG	$Z \rightarrow e^+e^-$	$m_{e^+e^-} > 20$	1686	> 1M	CTEQ66
POWHEG	$Z \rightarrow \mu^+\mu^-$	$m_{\mu^+\mu^-} > 20$	1686	> 1M	CTEQ66
POWHEG	$Z \rightarrow \tau^+\tau^-$	$m_{\tau^+\tau^-} > 20$	1686	> 1M	CTEQ66
PYTHIA	$t\bar{t}$	no cuts	94.3	500k	CTEQ6L
PYTHIA	Inclusive μ QCD	$\hat{p_T} > 20$, $p_T^\mu > 15$, $\|\eta_\mu\| < 2.5$	109853	6M	CTEQ6L
PYTHIA	EM-enriched QCD	$20 < \hat{p_T} < 30$	1719150	30M	CTEQ6L
PYTHIA	EM-enriched QCD	$30 < \hat{p_T} < 80$	3498700	40M	CTEQ6L
PYTHIA	EM-enriched QCD	$80 < \hat{p_T} < 170$	134088	5M	CTEQ6L
PYTHIA	$b/c \rightarrow e$	$20 < \hat{p_T} < 30$	108330	2M	CTEQ6L
PYTHIA	$b/c \rightarrow e$	$30 < \hat{p_T} < 80$	138762	2M	CTEQ6L
PYTHIA	$b/c \rightarrow e$	$80 < \hat{p_T} < 170$	9422	1M	CTEQ6L
PYTHIA	$W \rightarrow e\nu$	$\|\eta_e\| < 2.7$	6153	2M	CTEQ6L
PYTHIA	$W \rightarrow \mu\nu$	$\|\eta_\mu\| < 2.5$	5861	2M	CTEQ6L
PYTHIA	$W \rightarrow \tau\nu$	no cuts	7899	2M	CTEQ6L
PYTHIA	$Z \rightarrow e^+e^-$	$m_e^+ e^- > 20$	1300	2M	CTEQ6L
PYTHIA	$Z \rightarrow \mu^+\mu^-$	$m_\mu^+ \mu^- > 20$	1300	2M	CTEQ6L
PYTHIA	$Z \rightarrow \tau^+\tau^-$	$m_\tau^+ \tau^- > 20$	1300	2M	CTEQ6L

Table 1: Summary of analyzed Monte Carlo samples for the various signal and background processes.

is effective against decays-in-flight, punch-through and accidental matching (with noisy or background tracks or segments).

- The number of hits in the tracker track part of the muon has to be larger than 10. Generally tracks with small number of hits give bad p_T estimate. In addition decays in flight give rise to lower hit occupancy in the tracks. The chosen value to cut at was shown ([28]) to be close to optimal for selecting good quality muons with high efficiency.
- There should be at least one pixel hit in the tracker track part of the muon. The innermost part of the tracker is an important handle to discard non-prompt muons. By asking just a minimal number of hits there we introduce negligible reconstruction inefficiency (to be measured with Z).
- In addition, the muon track has to have at least two chambers in different stations with "matching" (consistent with the propagated to the muon chambers tracker track) segments. This is also to comply with a similar looser requirement in the trigger.
- Very bad fits are rejected by requiring reasonable GLB muon fit quality: $\chi 2/NDF < 10$ (NDF is the number of degrees of freedom).
- The GLB muon has to contain at least one "valid" muon hit. By this requirement we make sure that the GLB muon is not a "bad" match between the information from the muon system and the tracker. This could happen in particular for non-prompt muons.
- The impact parameter d_{xy} with respect to the beam spot has to be compatible with the IP hypothesis (muon from the interaction point). A loose, yet a powerful against cosmic background, cut is set at $|d_{xy}| < 2$ mm.

Given the selection above, the parametrization of the muon ID efficiencies can be made in the following way:

$$\epsilon_{\text{ID}} = \epsilon_{\text{trk}} \times (\epsilon_{\text{gbl+}} | \epsilon_{\text{trk+}}) \times \prod_i \epsilon_i \,, \tag{1}$$

where ϵ_{trk} is the TRK muon efficiency, $\epsilon_{\text{gbl+}}|\epsilon_{\text{trk+}}$ is the GLB muon efficiency given a TRK muon with its selection cuts exists and ϵ_i is the efficiency of each of the remaining selection criteria (applied on TRK and GLB muons) of the muon identification. Correlations between these variables would change the expression which is to be dealt with separately.

Appendix A describes how the muon identification efficiency is determined from Monte Carlo samples and cross-checked with available data samples recorded in LHC collisions. The TRK and GLB muon reconstruction efficiencies, before applying any identification cut for the TRK muon case, as estimated on the available samples are given in Table 2. The correction factors accounting for divergences in data and MC are evaluated and the results are reported in Table 3.

	Tracker muon efficiency	Global muon efficiency
data	98.0 ± 0.6	99.8 ± 0.1
$\text{pp} \to \mu + X$	97.2 ± 0.2	99.84 ± 0.03
$\text{W}^- \to \mu^- \bar{\nu}_\mu$	99.64 ± 0.02	99.87 ± 0.01
$\text{W}^+ \to \mu^+ \nu_\mu$	99.69 ± 0.02	
$\text{Z} \to \mu^+ \mu^-$	99.72 ± 0.02	

Table 2: TRK and GLB muon efficiencies. The TRK muon efficiency here is measured with "quality" STA muons with $p_T > 12$ GeV/c. The GLB muon efficiency is with respect to the selected TRK muons. These are explained in the appendix.

	$\lvert\eta\rvert < 0.9$	$0.9 < \lvert\eta\rvert < 1.2$	$\lvert\eta\rvert > 1.2$
Correction factors	0.98 ± 0.03	1.00 ± 0.03	0.975 ± 0.025

Table 3: Correction factors for the muon ID efficiency. These are to be applied on MC muons to obtain the "real" efficiencies.

3.1 Summary

For the present analysis, we keep muon identification and reconstruction efficiencies from Monte Carlo estimates, and assign them an overall 5%, uniform on all angular regions, of total systematic uncertainty. For muon reconstruction plus the selection of a good quality track, which is used for the 'loose' leg of the $\text{Z} \to \mu^+\mu^-$ analysis, we conservatively take as systematic uncertainty the largest deviation from MC efficiency of selecting a muon with more than 10 tracker hits (which occurs in the region with $0.9 < |\eta| < 1.2$, see Table 34 in Appendix A), which we can account for a 1.2% of systematic uncertainty.

4 Muon trigger

Collision events in muon channel are selected wih muon High Level Trigger (HLT), `HLT_Mu9` trigger. This trigger requires at least one muon candiate with $p_T > 9$ GeV/c and $|\eta| < 2.5$, which is reconstructed using both tracker and muon detector inforamtion. No isolation is required.

The trigger efficiency on 7 TeV collision data is determined by using the sample triggered by orthogonal trigger path to the muon trigger path. The minimum bias trigger or jet trigger is considered primarily. To calculate the trigger efficiency, we use the matching between Level-1 (L1) muon and offline global muon with particular requirement. This procedure is presented in details in Appendix B. The trigger efficiency is factorized by L1 and HLT, and it is measured separately. The overall trigger efficiency is defined as follows:

$$\varepsilon = \varepsilon_{L1} \times \varepsilon_{HLT}\,, \tag{2}$$

where L1 and HLT will be determined separately by detector geometry: DT, CSC and overlap region.

In addition, data-driven method, called as Tag and Probe (T&P) method, will be used for the estimation independently. Very low statistics of $Z \rightarrow \mu^+\mu^-$ candidate is expected with 100 nb^{-1}, but it is useful for the cross-check.

To determine the trigger efficiency, the offline global muons matched by the L1 muon are collected, which pass through following muon id cut:

- $p_T > 15$GeV, $|\eta| < 2.1$
- Number of pixel hits > 0, Number of hits in the tracker > 10
- Transverse impact parameter of the muon with respect to the beam spot < 2 mm
- Chi2/ndof of the global muon fit < 10
- Number of valid hits in the muon chambers used in the global muon fit > 0
- Number of muon stations > 1
- Relative combined isolation = (sumPt + emEt + hcalEt)/(muon p_T) < 0.15 in a deltaR < 0.3 cone

, where are exactly same requirement for W selection in this analysis. We separate the results with isolation and without isolation because the isolation cut is too tight for current integrated luminosity. Therefore we have very large statistical uncertainty on the results after the isolation cut.

Table 4 shows the results on jet-triggered events for both data and MC. Due to very low statistics, the results of three split η regions are not available with isolation cut currently. They will be updated with more integrated luminosity.

We observe about 10-15% inefficiency in data to compare to MC, and the scale factor to correct the disagreement is calculated in Table 5.

5 W → $\mu\nu$ event selection

W → $\mu\nu$ events are characterized by a high-p_T, isolated muon, together with a significant amount of missing E_T, due to the presence of a neutrino in the final state, that escapes undetected. A full reconstruction of the W system is thus not possible but a mass reconstruction in the transverse plane can be performed from the measured missing E_T and the muon momentum, through the expression $\mathrm{M}_T = \sqrt{2 p_T(\mu) \not{E}_\mathrm{T} (1 + \cos(\xi))}$, where ξ ($\xi = \pi - \Delta\phi_{p_T(\mu),\not{E}_\mathrm{T}}$) is the acoplanarity between muon and MET directions, the resulting distribution exhibiting the characteristic shape of the W Jacobian peak. Muon isolation and a high reconstructed M_T (and high missing E_T) are thus the main handles to discriminate between W signal events and other processes also delivering high-p_T muons in the final state.

In general, $\not{E}_\mathrm{T}$ is calculated as the negative sum of the energy/momentum in the transverse

	dataset	efficiency	$\|\eta\| < 0.8$	$0.8 < \|\eta\| < 1.2$	$\|\eta\| > 1.2$	overall (%)
No Iso.	Data	ε_{L1}	90.2 ± 2.2	69.6 ± 5.9	94.5 ± 2.2	88.6 ± 1.5
		ε_{HLT}	94.6 ± 1.7	83.5 ± 6.1	87.5 ± 3.0	90.9 ± 1.6
		$\varepsilon_{L1\times HLT}$	85.3 ± 2.59	58.1 ± 6.5	82.7 ± 3.4	80.6 ± 2.0
	MC	ε_{L1}	98.3 ± 0.01	92.6 ± 0.04	94.2 ± 0.03	95.2 ± 0.01
		ε_{HLT}	95.3 ± 0.02	90.2 ± 0.04	92.9 ± 0.02	93.5 ± 0.01
		$\varepsilon_{L1\times HLT}$	93.7 ± 0.02	83.5 ± 0.05	87.5 ± 0.003	89.0 ± 0.01
With Iso.	Data	ε_{L1}	$xxx \pm xxx$	$xxx \pm xxx$	$xxx \pm xxx$	83.0 ± 7.4
		ε_{HLT}	$xxx \pm xxx$	$xxx \pm xxx$	$xxx \pm xxx$	93.1 ± 6.8
		$\varepsilon_{L1\times HLT}$	$xxx \pm xxx$	$xxx \pm xxx$	$xxx \pm xxx$	77.3 ± 8.9
	MC	ε_{L1}	98.3 ± 0.10	92.8 ± 0.30	93.4 ± 0.18	95.7 ± 0.03
		ε_{HLT}	98.2 ± 0.04	96.1 ± 0.07	95.8 ± 0.05	96.8 ± 0.03
		$\varepsilon_{L1\times HLT}$	96.5 ± 0.11	89.2 ± 0.30	89.5 ± 0.18	92.7 ± 0.04

Table 4: Trigger Efficiency on jet-triggered sample. Trigger efficiencies are estimated in three split regions: DT only ($|\eta| < 0.8$), overlap ($0.8 < |\eta| < 1.2$), and CSC only ($|\eta| > 1.2$). Trigger efficiency is factorized by L1 and HLT.

	$\|\eta\| < 0.8$	$0.8 < \|\eta\| < 1.2$	$\|\eta\| > 1.2$	overall (%)
No iso.	$xxx \pm xxx$	$xxx \pm xxx$	$xxx \pm xxx$	90.6 ± 2.25
With iso.	$xxx \pm xxx$	$xxx \pm xxx$	$xxx \pm xxx$	83.4 ± 9.60

Table 5: Scale factor of trigger efficiency (Data/MC) using results on Table 4.

plane of all the particles reconstructed in the detector. Two different algorithms are used to compute $\not\!\!E_T$: (tcMET) where E_T from calorimeter deposits associated to charged hadrons are substituted by their corresponding charged-track momentum; and (pfMET) where a full reconstruction of the final state particles is performed with Particle Flow techniques. The $W \to \mu\nu$ analysis is carried out in parallel with the two $\not\!\!E_T$ definitions. Results obtained fully agree between them.

Events relevant for this analysis are triggered by the single muon trigger path, with a High Level Trigger threshold in the muon p_T of 9 GeV/c. The first step in the $W \to \mu\nu$ candidate selection is to reject those events having two global muons satisfying: $p_T(\mu_1) > 20$ GeV/c and $p_T(\mu_2) > 10$ GeV/c, where $p_T(\mu_1)$ is the highest muon p_T and $p_T(\mu_2)$ is the second highest muon p_T in the event, in order to minimize the contribution from Drell-Yan events to the selected sample.

Events with a good quality muon, as described in Section 3, in the fiducial volume $|\eta| < 2.1$, and with a transverse momentum higher than 20 GeV/c are kept. With this p_T cut, background arising from QCD processes is significantly reduced, affecting minimally the signal efficiency. Transverse momentum and pseudorapidity distributions of muons selected by these quality criteria are presented in Figure 1.

To establish whether the muon is isolated, a normalized combined isolation definition is used:

$$I^{\text{rel}}_{\text{comb}} = [\sum p_T + \sum E_T(em) + \sum E_T(had)]/p_T(\mu) \qquad (3)$$

where the sums extend in a $\Delta R = \sqrt{\Delta\eta^2 + \Delta\phi^2} < 0.3$ cone around the muon direction. $\sum p_T$ and $\sum E_T(em)$, $\sum E_T(had)$ are the sums of the p_T of the tracks and of the calorimeter deposits in the electromagnetic and hadronic calorimeter in this cone, excluding the muon track and calorimeter deposits associated to it. The muon is considered to be isolated if $I^{\text{rel}}_{\text{comb}} < 0.15$. Isolation distribution of the experimental data, together with the MC expectations, is shown in

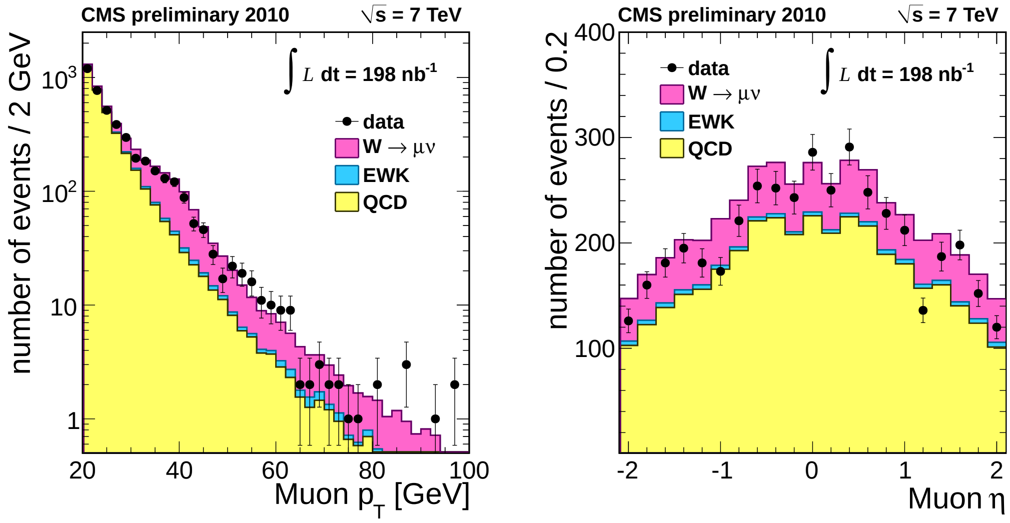

Figure 1: Left: Muon p_T distribution of candidates with a good quality muon in the fiducial volume $|\eta| < 2.1$; Right: Muon η distribution of candidates with a good quality muon and $p_T > 20\,\mathrm{GeV}/c$. The experimental set corresponds to an integrated luminosity of $\mathcal{L}_{\mathrm{int}} = 198\ \mathrm{nb}^{-1}$. Dots represent the data and the solid histograms the contribution from the different SM processes, evaluated by MC and normalized to the theoretical cross sections. MC distributions are corrected by the MC/data difference in muon identification, isolation and trigger efficiencies, as determined in the dedicated studies reported in sections 3, 4 and 8 of this AN. In practice, only a correction factor of 0.98 due to trigger efficiency is needed, all the others being compatible with unity.

Figure 2.

The breakdown of the data reduction at the different stages of the selection is summarized in Table 6 both for the total sample of muon events, and splitted by the muon charge. The acceptance of the selection cuts for W $\rightarrow \mu\nu$ events with muons emitted in the $|\eta| < 2.1$ pseudorapidity region is $(64.1 \pm 0.2)\%$, as estimated from MC simulation.

Event Sample	Events with $\mu^{\pm}$	Events with μ^{+}	Events with μ^{-}
Candidates	44100	22050	22050
Triggered	16567	8607	7960
DY Rejection	16277	8444	7833
Muon ID	13365	6873	6492
$p_T > 20\,\mathrm{GeV}/c$	12856	6602	6254
$\|\eta\| < 2.1$	4294	2275	2019
Comb-Iso: $I^{\mathrm{rel}}_{\mathrm{comb}} < 0.15$	1254	757	497
$M_T > 50$ GeV $^{(*)}$ (tcMET)	731	451	280
$M_T > 50$ GeV $^{(*)}$ (pfMET)	728	450	278

Table 6: Data reduction at every step of the selection process. Experimental data sample analyzed corresponds to an integrated luminosity of $\mathcal{L}_{\mathrm{int}} = 198\,\mathrm{nb}^{-1}$. Number of events are given for the whole muon data sample, as well as separated by the muon charge.
$^{(*)}$ $M_T > 50$ GeV criterium is not part of the selection process but it indicates the number of events in the most W-like region.

The number of W $\rightarrow \mu\nu$ events expected, for a data sample of $\mathcal{L}_{\mathrm{int}} = 100\,\mathrm{nb}^{-1}$, after each of

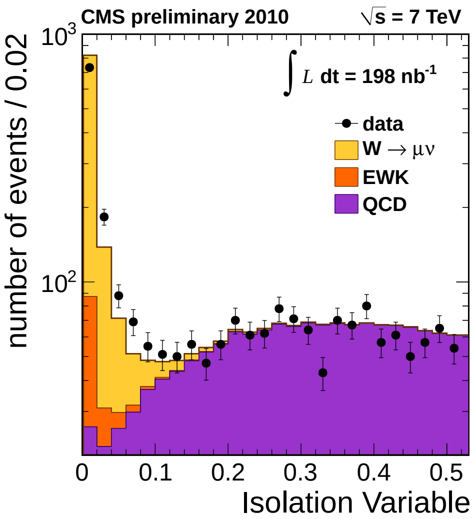

Figure 2: Isolation distribution of candidates with a good quality muon of $p_T > 20$ GeV/c in the fiducial region $|\eta| < 2.1$. The experimental set corresponds to an integrated luminosity of $\mathcal{L}_{\text{int}} = 198$ nb^{-1}. Dots represent the data and the solid histograms the contribution from the different SM processes, evaluated by MC and normalized to the theoretical cross sections. MC distributions are corrected by the MC/data difference in muon identification, isolation and trigger efficiencies, as determined in the dedicated studies reported in sections 3, 4 and 8 of this AN. In practice, only a correction factor of 0.98 due to trigger is needed, all the others being compatible with unity.

the steps of the selection criteria is evaluated by MC, with a high statistic sample, generated with POWHEG and CTEQ66 PDFs and it is given in Table 7. The cumulative efficiency of the selection process for W signal events is also evaluated by MC and it is presented in Table 8.

After the selection process just described, 1254 events are selected, 757 of them with a positive charged muon and 497 with a negative charged muon. The M_T distribution of the final selected sample is shown in Figure 4 for the total muon sample and in Figure 5 for the sample of positive and negative muons separately.

A certain fraction of the events passing the selection criteria will still be due to background processes. Several sources of contamination have been identified. They include events where a high p_T muon results from the semi-leptonic decay of quarks (QCD background). The majority of these muons come from the decay of b quarks with an smaller contribution of light mesons (pion and kaon) decays in flight. Electroweak processes other than the one under study will also contribute: these are mainly $Z \to \mu^+\mu^-$ events where one of the muon lies beyond the detector acceptance ($\eta < 2.5$), thus escaping detection. Muons from $Z \to \tau^+\tau^-$ and $W \to \tau\nu$ events, with the tau decaying into a muon will have in general a lower momentum, and be less isolated, being therefore strongly suppressed by the selection cuts.

Table 7 summarizes the expected number of events, due to the different physics processes, after each of the selection steps. The number of events is normalized to a collected luminosity of 100 nb^{-1}. The acceptance and efficiencies at every step of the selection procedure, for the different physics processes considered, and determined with high statistics MC samples, presented in a previous section are given in Table 8.

Background subtraction is performed by means of a binned-likelihood fit of the observed M_T distribution to a sum of three different contributions, each of them accounting for the different

Sample	$W \to \mu\nu$	QCD	$Z \to \mu^+\mu^-$	$W \to \tau\nu$	$t\bar{t}$	$Z \to \tau^+\tau^-$
Input	1031.2	7968.8	166.7	1031.2	16.2	166.7
Candidates	765.8	7680.0	137.5	152.8	9.4	10.3
Triggered	623.7	6542.4	109.1	56.6	5.0	1.9
DY Rejection	623.0	6491.6	57.2	56.5	4.4	1.9
Muon ID	609.0	6236.0	56.0	54.9	4.1	1.8
$p_T > 20\,\mathrm{GeV}/c$	576.7	6034.9	51.3	52.1	4.0	1.8
$\|\eta\| < 2.1$	484.2	1864.4	22.1	16.8	2.5	0.7
Comb-Iso: $I^{\mathrm{rel}}_{\mathrm{comb}} < 0.15$	477.1	127.1	21.8	16.5	1.8	0.7
$M_T > 50$ GeV $^{(*)}$ (tcMET)	402.8	1.0	12.9	6.3	1.1	0.1
$M_T > 50$ GeV $^{(*)}$ (pfMET)	401.2	0.7	11.9	6.2	1.1	0.1

Table 7: Number of events expected after every step of the selection criteria, for the several physics processes producing a muon in the final state. Projection for an integrated luminosity of $\mathcal{L}_{\mathrm{int}} = 100\,\mathrm{nb}^{-1}$. They are evaluated with high statistics MC samples, generated with POWHEG MC (except QCD and ttbar, generated with PYTHIA MC) and CTEQ66 PDF set. Dilepton predictions ($Z \to \mu^+\mu^-$ and $Z \to \tau^+\tau^-$) refer to the dilepton mass region $M_{\ell\ell} > 20\,\mathrm{GeV}/c^2$.
$^{(*)}$ $M_T > 50$ GeV criterium is not part of the selection process but it indicates the number of events in the most W-like region.

Sample	$W \to \mu\nu$	QCD	$Z \to \mu^+\mu^-$	$W \to \tau\nu$	$t\bar{t}$	$Z \to \tau^+\tau^-$
Candidates	74.3	96.4	82.5	14.8	58.5	6.2
Triggered	60.5	82.1	65.4	5.5	31.0	1.2
DY Rejection	60.4	81.5	34.3	5.5	26.9	1.1
Muon ID	59.1	78.3	33.6	5.3	25.5	1.1
$p_T > 20\,\mathrm{GeV}/c$	55.9	75.7	30.7	5.1	24.9	1.1
$\|\eta\| < 2.1$	47.0	23.4	13.3	1.6	15.6	0.4
Comb-Iso: $I^{\mathrm{rel}}_{\mathrm{comb}} < 0.15$	46.3	1.6	13.1	1.6	11.3	0.4
$M_T > 50$ GeV $^{(*)}$ (tcMET)	39.1	0.1	7.7	0.6	7.0	< 0.1
$M_T > 50$ GeV $^{(*)}$ (pfMET)	38.9	0.1	7.1	0.6	6.9	< 0.1

Table 8: Cumulative efficiencies of the selection criteria, for the several physics processes producing a muon in the final state. They are evaluated with high statistics MC samples, generated with POWHEG MC (except QCD and ttbar, generated with PYTHIA MC) and CTEQ66 PDF set. Efficiencies are referred to the full phase space. Dilepton predictions ($Z \to \mu^+\mu^-$ and $Z \to \tau^+\tau^-$) refer to the dilepton mass region $M_{\ell\ell} > 20\,\mathrm{GeV}/c^2$.
$^{(*)}$ $M_T > 50$ GeV criterium is not part of the selection process but it indicates the number of events in the most W-like region.

origin of the events (W signal, QCD background and EWK background):

$$N(\mathrm{M}_T) = \{\sigma_W \times [\mathcal{A}_W(\mathrm{M}_T) + K \times \mathcal{A}_{EWK}(\mathrm{M}_T)] + \mathcal{F}_{QCD}\mathcal{T}(\mathrm{M}_T)\} \times \mathcal{L}_{\mathrm{int}} \quad (4)$$

The W and EWK terms are expressed in terms of their cross sections and acceptance and selection efficiencies ($\mathcal{A}_W(\mathrm{M}_T)$ and $\mathcal{A}_{EWK}(\mathrm{M}_T)$). $Z \to \mu^+\mu^-$, $Z \to \tau^+\tau^-$ and $W \to \tau\nu$ contributions are normalized to the $W \to \mu\nu$ channel, through their theoretical cross section ratio.

The QCD contribution is described as well in terms of a normalized template on M_T ($\mathcal{T}(\mathrm{M}_T)$) and a constant ($\mathcal{F}_{QCD}$) setting the absolute background level.

In fact, we are interested not only in the total W cross section but also in the W^+ and W^- cross sections independently, or equivalently in the $\sigma(W^+)/\sigma(W^-)$ ratio. Above equation is therefore applied separately for W^+ and W^- spectra. Different signal templates and efficiencies ($\mathcal{A}_W(M_T)$) are evaluated for W^+ and W^-. For the $W \rightarrow \tau\nu$, different templates for positive and negative muons are considered, as this channel is also charge asymmetric. $Z \rightarrow \mu^+\mu^-$ and $Z \rightarrow \tau^+\tau^-$ backgrounds are symmetric in charge. QCD is also assumed to contribute in the same amount and shape to both W^+ and W^- spectra. No significant difference in the low M_T region is observed in experimental distributions.

The signal shape is determined in a realistic way from high statistics MC where the measured lepton efficiencies, as measured from data and reported in sections 3, 4 and 8 of this AN, are taken into account. The electroweak vector boson acceptance for the other EWK vector boson processes, is determined in the same way.

M_T shape for the QCD component is modeled from the same preselected data sample requiring the full set of selection criteria but inverting the isolation cut; in particular events with a non-isolated muon according to $I^{\rm rel}_{\rm comb} > 0.2$ are taken.

The template obtained in this way is shown in Figure 3 and compared with QCD MC expectation, both for the isolated and not isolated regions. A good agreement between the data template and MC for the not isolated region is observed. The template is not able to fully describe the isolated one, at least when compared with the QCD MC expectation. Several possibilities to improve the description of the isolated region were worked out. This initial template can be reweighted according to the relative distribution (as expected from MC) of the azimuthal angle between the muon and $\not\!\!E_{\rm T}$ ($\Delta\phi_{p_T(\mu),\not E_{\rm T}}$) for isolated and not isolated QCD events.

A fully data-driven correction can also be devised. The observed variation of the mean and width of M_T distribution with the isolation variable, in the not-isolated region, can be parameterized (with a simple linear function as a first approach). This parameterization is then extrapolated to the low isolation values and used to correct the M_T distribution in the isolated region.

For this first analysis, a conservative approach was finally chosen. The plain isolation-inverted template from data was used to determine W cross section. The full difference with respect to using a pure MC template from the isolated region was assigned as a systematic uncertainty in the final result.

A global fit to the two M_T spectra (W^+ and W^-) is then performed. The fitting function can be expressed in terms of two different sets of parameters: either 1) the total $W \rightarrow \mu\nu$ cross section ($\sigma(W^+) + \sigma(W^-)$) and the ratio $R = \sigma(W^+)/\sigma(W^-)$, together with the overall normalization of QCD events ($\mathcal{F}_{QCD}$) or 2) the individual $\sigma(W^+)$ and $\sigma(W^-)$, also with a third parameter giving the overall normalization of the background. The fit is performed over the full M_T range $[0, 200]$ GeV/c^2.

The fitted M_T distributions are presented in Figure 4 (full sample) and Figure 5 (samples separated by muon charge). The fitted individual contributions of the W signal, EWK processes and QCD are also shown in the plots.

The fitted W-parameters are summarized in Tables 9 and 10 for the two choices of fit parameters, together with the correlation coefficient among them. The error shown is only statistical.

5.1 Systematic uncertainties

Common effects affecting to all the components in the previous fit are muon identification and reconstruction, isolation and trigger efficiencies and muon momentum scale and resolution.

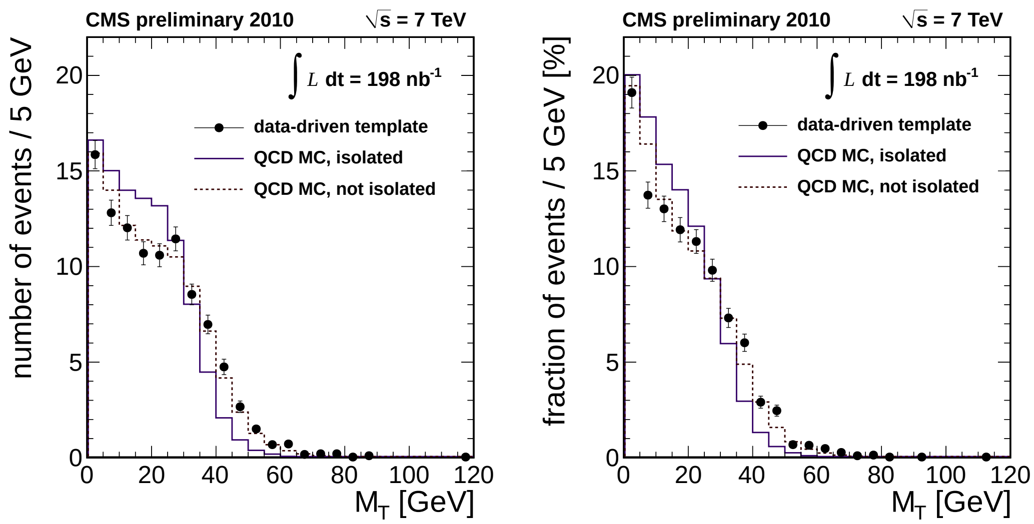

Figure 3: M_T QCD template obtained from the non-isolated events ($I^{rel}_{comb} > 0.2$) of the preselected data sample (black dots). It is compared with the QCD MC expectation both for the isolated region ($I^{rel}_{comb} < 0.15$) (solid black histogram) and for the not isolated region (dashed black histogram). (Left) The $\not{E}_T$ reconstruction algorithm applied is tcMET. (Right) The $\not{E}_T$ reconstruction algorithm applied is pfMET.

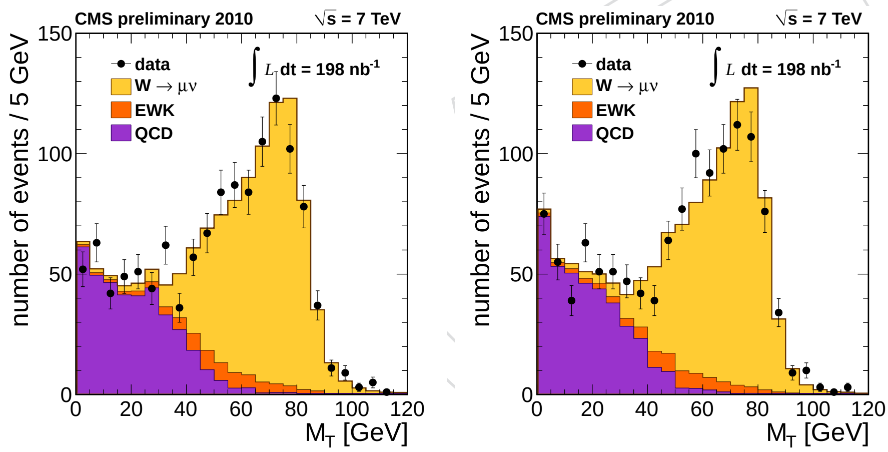

Figure 4: Total M_T spectrum (black dots) and fitted contributions from the different processes shown stacked, W signal (light yellow histogram), other EWK processes (medium orange histogram), and QCD background (dark purple histogram). (Left) The $\not{E}_T$ reconstruction algorithm applied is TcMET. (Right) The $\not{E}_T$ reconstruction algorithm applied is pfMET.

	$\not{E}_T$ algorithm	
	tcMET	pfMET
$\sigma(\mathrm{W})$ (nb)	9.15 ± 0.33	9.14 ± 0.33
$R = \sigma(\mathrm{W}^+)/\sigma(\mathrm{W}^-)$	1.68 ± 0.12	1.69 ± 0.12
$\rho(\sigma(\mathrm{W}), R)$	-0.020	-0.018

Table 9: Total W production cross section (times the Branching fraction of the W decaying into a muon and a neutrino) and ratio between W^+ and W^- cross sections from the analysis of the $\mathcal{L}_{int} = 198\ \mathrm{nb}^{-1}$ data set. Correlation between the total cross section and ratio is also given.

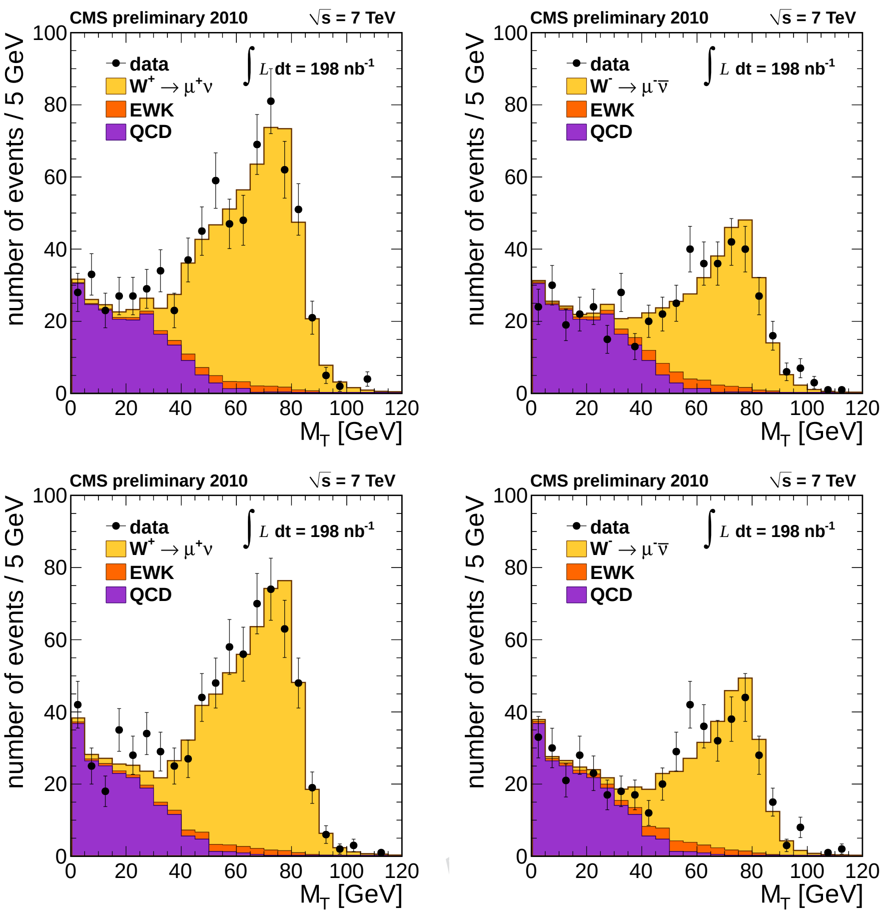

Figure 5: W^+ (left plots) and W^- (right plots) experimental distributions (black dots), together with the fitted contributions from the different processes (shown stacked): W signal (light yellow histogram), other EWK processes (medium orange histogram), and QCD background (dark purple histogram). Top: The $\not{E}_\mathrm{T}$ algorithm applied is tcMET. Bottom: The $\not{E}_\mathrm{T}$ algorithm applied is pfMET

	$\not{E}_\mathrm{T}$ algorithm	
	tcMET	pfMET
$\sigma(\mathrm{W}^+)$ (nb)	5.64 ± 0.25	5.67 ± 0.25
$\sigma(\mathrm{W}^+)$ (nb)	3.42 ± 0.20	3.40 ± 0.20
$\rho(\sigma(\mathrm{W}^+), \sigma(\mathrm{W}^-))$	0.012	0.010

Table 10: W^+ and W^- production cross section (times the Branching fraction of the W decaying into a muon and a neutrino) based on the analysis of the $\mathcal{L}_{\mathrm{int}} = 198\ \mathrm{nb}^{-1}$ data set. Correlation between the two fitted cross sections is also given.

Uncertainties in lepton efficiencies directly translate to the signal yield. Effects due to muon momentum scale and resolution are estimated repeating the fitting process with new signal templates where the muon p_T in MC is modified according to the results from dedicated studies. Impact of muon momentum scale and resolution through the muon contribution in the $\not{E}_\mathrm{T}$ is also considered and treated in the same way. The uncertainty in the signal yield is smaller than 1%. To evaluate the uncertainty associated to the M_T signal template due to E_T scale and resolution effects, the fraction of the event recoiling to the lepton is parameterized in terms of two components: parallel and perpendicular to the lepton, and fitted in high $\not{E}_\mathrm{T}$ W-events [29].

Uncertainty in this fit has a small impact in the $W \to \mu\nu$ cross sections ($< 1\%$). Finally, the full difference between the resulting yield when using the isolation-inverted template for the QCD M_T shape and the prediction from MC ($\sim 3.5\%$) is assigned as the uncertainty due to the background subtraction.

The error due to the EWK cross section ratio with respect to the signal one is estimated varying the scaling factor K according to their systematic errors and trying different theoretical predictions and PDF sets. The effect is found to be negligible.

The main theoretical contribution arises from the computation of the detector geometrical and kinematical acceptance. Uncertainty due to the PDF assumptions and uncertainties in the PDFs themselves are studied using the full PDF eigenvector set and comparing among PDFs provided by different groups CTEQ and MSTW. It is estimated to be of the order of 2%.

6 $Z \to \mu^+\mu^-$ event selection

$Z \to \mu^+\mu^-$ are characterized by the presence of two high-p_T isolated muons. The expected background to this process is very low.

The present analysis, due to the low statistics, is based on a cut-and-count strategy, where the $Z \to \mu^+\mu^-$ candidates are selected using a robust and high purity selection. During preparatory studies [30] developed for high luminosity ($\simeq 10\ \text{pb}^{-1}$), we planned a simultaneous fit of multiple categories, which allows to determine from data the $Z \to \mu^+\mu^-$ production yield and the average muon trigger, reconstruction, and selection efficiencies. We do not apply this strategy in the present note, due to the lack of statistics. From MC studies we expect of the order of few tenths of candidate events containing two global muons (i.e. the category with the highest purity defined in [30]), while the other lower purity categories lack of sufficient statistics to perform precise quantitative estimates.

The amount of background under the signal peak and the relevant efficiencies are estimated from MC, with reasonable systematic errors, and cross-checked as much as possible with the available data.

We select events which satisfy the single non-isolated muon trigger `HLT_Mu9` (Section 4). For each event, we consider all the possible di-muon pairs made by opposite-charge muons and with invariant mass $60 < m_{\mu\mu} < 120\,\text{GeV}/c^2$. The muons in the pair must satisfy, in addition, the following acceptance cuts:

- both muons must have $|p_T| > 20\,\text{GeV}/c$;
- at least one of the muons must be within $|\eta| < 2.1$ for triggering[1], the remaining muon must be within $|\eta| < 2.4$ (fiducial region of the muon system).

Both muons must be identified as *Global Muons* and must have > 10 total (pixel+strips) hits in the Tracker detector (referred in the following as 'loose' muon selection). In addition to the above loose quality cuts, at least one of the muons must pass all the quality cuts described in Section 3. The muon passing all the quality cuts must also match to a Level-3 (L3) trigger object firing the `HLT_Mu9` trigger path (trigger and muon quality selections are referred in the following as 'tight' muon selection). For the trigger matching we require the L3 muon to be within a cone of aperture $\Delta R = \sqrt{\Delta\phi^2 + \Delta\eta^2} = 0.2$ around the offline muon, and their relative p_T difference $\Delta p_T / p_T$ to be < 1, which is a very loose requirement given the L3 muon resolution in this

[1] Actually, the CSC L1 trigger extends till to the region $|\eta| < 2.4$; however, in MC the trigger is correctly emulated till to $|\eta| < 2.1$, so for the moment we stay to this stricter interval

p_T range. The choice of requiring trigger match and muon quality selection is motivated by the correlation of trigger and muon identification selection, which, applied to the same muon, make easier the evaluation of related systematic uncertainties.

Both muon candidates must be isolated, according to the default tracker isolation variable provided by the Muon POG, I_{trk}, defined as the sum of the transverse momenta of all tracks within a cone of radius $\Delta R = 0.3$:

$$I_{\text{trk}} = \sum_{\Delta R < 0.3} p_T^{(i)} . \quad (5)$$

Only tracks with $\Delta z < 0.2$ w.r.t. the muon track are considered for the sum. Tracks within a cone of $\Delta R = 0.01$ are vetoed in order to avoid counting the muon track. We require for each muon $I_{\text{trk}} < 3$ GeV/c.

6.1 Selection results on data and comparison with MC

We have analyzed a data sample of 198 nb^{-1} and 77 events pass the $Z \to \mu^+\mu^-$ event selection. The data sample is composed by runs/lumisections up to run 140182 The di-muon invariant mass, p_T, and rapidity distributions of the selected Z candidates are shown respectively in Figures 6, 7, and 8. More plots are reported in Appendix D [**to be updated**]. They are compared to the expected MC distribution for the nominal luminosity. MC is scaled according to the NLO generator cross-section (POWHEG with CTEQ66 PDF). We have applied a global scaling factor to the expectation from the PYTHIA $t\bar{t}$ sample given by the ratio of NLO MCFM [31] to LO PYTHIA cross sections (162 pb/94.3 pb = 1.718). From MC we expect 78.2 signal events in

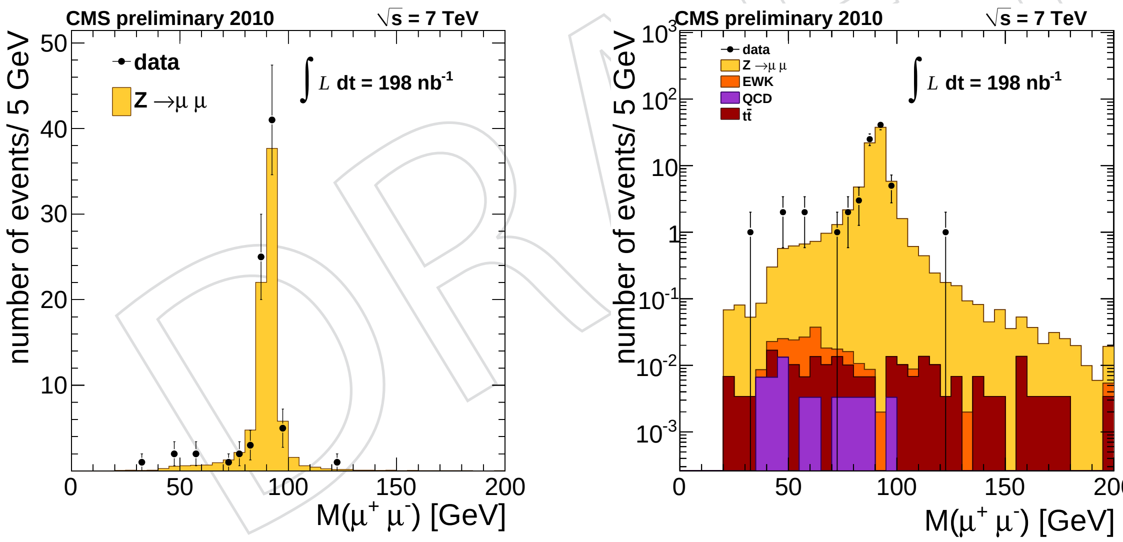

(a) (b)

Figure 6: Invariant mass distribution of the selected $Z \to \mu^+\mu^-$ candidates in data superimposed to the MC expectation. (a): linear scale; (b): log scale.

the $[60, 120]$ GeV/c^2 mass range and very low background: 0.21 expected events, dominated by $t\bar{t}$ and EWK events, 0.10 and 0.10 expected events respectively. In Table 11 we report the performance of the selection evaluated on the signal and background MC samples and the expected yields for the nominal luminosity.

Due to the low statistics of possible control samples from data (for instance no same-sign di-muon events pass the Z selection), we can determine the expected background with the lowest possible uncertainty from Monte Carlo. Considering the small expected background

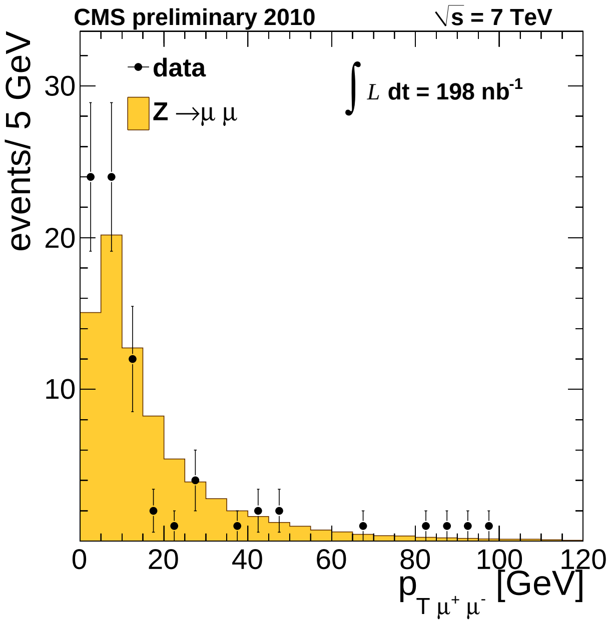

Figure 7: Transverse distribution of the selected $Z \rightarrow \mu^+\mu^-$ candidates in data superimposed to the MC expectation.

Table 11: MC cross sections, cross sections times acceptance and efficiency of the full selection, and expected yields for the nominal luminosity. All the numbers have been evaluated on the reference MC samples (POWHEG). The reported errors are only the statistical uncertainties due to the MC statistics.

	σ (pb)	$\sigma \times A \times \epsilon$ (pb)	Expected yields
$Z \rightarrow \mu^+\mu^-$	1686	395.0 ± 2.0	78.21 ± 0.40
$W \rightarrow \mu\nu$	10331	0.26 ± 0.05	0.051 ± 0.010
QCD	$296.9 \cdot 10^6$	0.10 ± 0.03	0.020 ± 0.006
$t\bar{t}$	162	0.48 ± 0.07	0.095 ± 0.014
$Z \rightarrow \tau^+\tau^-$	1686	0.23 ± 0.05	0.046 ± 0.010

size ($\approx$ 0.3% of the signal), the systematic uncertainty due to MC prediction will not affect the cross section measurement. We also perform several data-driven background estimates as cross-checks. The cross-checks include estimating the backgrounds using the fake rate method, and deriving it from low-purity categories. The studies set limits to the expected amount of background, and confirm, though within the very limited available statistics, that the expected background is very low. Details are reported in Appendix E.

6.2 Muon efficiencies

We use two muon selections: one 'tight' and one 'loose' in $Z \rightarrow \mu^+\mu^-$ selection, and we require that both muon legs must satisfy the 'loose' selection and that at least one of the muon legs satisfies the 'tight' selection. We can write the efficiency to select a 'loose' muon as:

$$\epsilon_{\mathrm{rec}} = \epsilon_{\mathrm{trk}} \times \epsilon_{\mathrm{sta}} \times \epsilon_{\mathrm{Nhits}}, \tag{6}$$

where ϵ_{trk} is the reconstruction efficiency of a muon in the tracker, ϵ_{sta} is the reconstruction efficiency in the muon detector, and $\epsilon_{\mathrm{Nhits}}$ is the probability for a reconstructed muon to pass

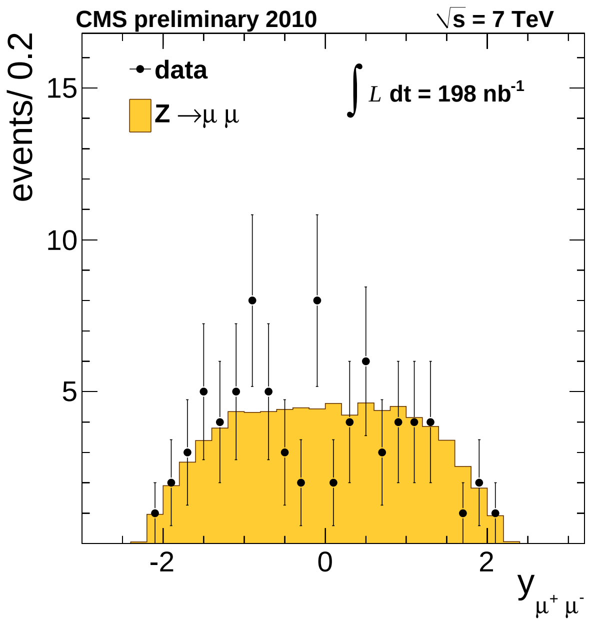

Figure 8: Rapidity distribution of the selected $Z \to \mu^+\mu^-$ candidates in data superimposed to the MC expectation.

the cut on the number of tracker hits. All those efficiencies are taken from MC.

The efficiency to reconstruct a 'tight' muon is:

$$\epsilon_{\text{tight}} = \epsilon_{\text{rec}} \times \epsilon'_{\text{ID}} \times \epsilon'_{\text{trigger}} \,, \tag{7}$$

where ϵ'_{ID} is the probability that a muon passing the 'loose' selection also passes all muon identification cuts[2], and $\epsilon'_{\text{trigger}}$ is the probability that a muon passing the 'loose' selection plus the muon identification cuts is also matched to a trigger muon. The efficiency ϵ'_{ID} for a Z candidate to pass the muon quality requirements is estimated from MC and the observed data/MC discrepancies are considered as source of systematics, as described in Section 3. We find in MC that the difference of $\epsilon'_{\text{trigger}}$ w.r.t. the efficiency $\epsilon_{\text{trigger}}$, measured on all 'loose' muons (not necessarily passing the muon identification cuts) is about 0.6%, due to the (small) correlation of muon trigger performance with muon quality. The trigger efficiency $\epsilon'_{\text{trigger}}$ is estimated from MC after applying the proper data/MC correction factors as reported in Section 4. The MC trigger efficiency estimate is estimated by counting the numbers N_{2HLT} of $Z \to \mu^+\mu^-$ candidates having both legs matched to trigger muons and N_{1HLT} of $Z \to \mu^+\mu^-$ candidates having only one leg trigger-matched:

$$\frac{N_{\text{2HLT}}}{N_{\text{2HLT}} + N_{\text{1HLT}}} = \frac{\epsilon_{\text{trig}}}{2 - \epsilon_{\text{trig}}} \tag{8}$$

We consider for this estimate the $Z \to \mu^+\mu^-$ candidates having both legs which pass the tight muon selection. Thus, the estimate of the trigger efficiency takes correctly into account correlations with the muon selection cuts. We find $N_{\text{2HLT}} = 56$ and $N_{\text{1HLT}} = 10$, which gives, using Clopper-Pearson binomial confidence interval [32]:

$$\epsilon_{\text{trig}} = 0.916^{+0.026}_{-0.034} \,. \tag{9}$$

[2]Note that the cuts on number of tracker hits is already applied in the loose selection.

This number agrees with the MC extimate within the statistical uncertainty.

The isolation efficiency is determined from data by sampling the isolation distribution with the random cone method (Section 8). The measured values is in good agreement with MC predictions, with a systematic discrepancy below the 0.5% level. This value is cross-checked by counting the number of di-muon candidates $N_{1\mathrm{NotIso}}$ which fail the isolation cut on one of the legs (but pass all the other cuts). We find 4 candidates in this category and set: $\epsilon_{\mathrm{iso}} = 0.980^{+0.010}_{-0.018}$. The isolation efficiency can be also cross-checked using a sample of muons from $W \to \mu\nu$ candidates selected by applying tight cuts on their transverse mass.

The tracker efficiency is cross-checked with data by counting the di-muon candidates where one of the legs is a standalone muon but fails the global muon reconstruction. We find no candidate in this category and set $\epsilon_{\mathrm{trk}} = 1.00^{+0.00}_{-0.01}$. The standalone muon efficiency is cross-checked in data by counting the number of di-muon candidates where one of the legs is a tracker track but fails the global muon reconstruction. We find 2 candidates in this category and set: $\epsilon_{\mathrm{sta}} = 0.987^{+0.008}_{-0.016}$

In Table 12 we report the muon efficiencies estimated from MC and the results from cross-checks in data (largely limited by the statistics), where possible.

Table 12: Muon efficiencies for $Z \to \mu^+\mu^-$ analysis. In the first column we report the MC efficiencies estimated from the $Z \to \mu^+\mu^-$ reference MC sample. In the second column we report the results obtained by counting di-muon candidates in different categories.

	MC efficiency	Data estimates (di-muon counting)
ϵ_{trig}	0.927 ± 0.001	–
$\epsilon'_{\mathrm{trig}}$	0.932 ± 0.001	$0.916^{+0.026}_{-0.034}$
ϵ_{trk}	0.9992 ± 0.0001	$1.00^{+0.00}_{-0.01}$
ϵ_{sta}	0.9894 ± 0.0005	$0.987^{+0.008}_{-0.016}$
ϵ'_{ID}	0.9758 ± 0.0006	–
$\epsilon_{\mathrm{Nhits}}$	0.9979 ± 0.0001	–
ϵ_{iso}	0.9837 ± 0.0007	$0.980^{+0.010}_{-0.018}$

6.3 $Z \to \mu^+\mu^-$ cross section determination

The inclusive $Z \to \mu^+\mu^-$ cross section is determined from the $N_{\mu\mu}$ yield in a data sample corresponding to an integrated luminosity $\mathcal{L}_{\mathrm{int}}$, by using:

$$\sigma(\mathrm{pp} \to Z(\gamma^*) + X \to \mu^+\mu^- + X) \times \mathcal{A} = \frac{N_{\mu\mu}}{\epsilon^2_{\mathrm{rec}}\, \epsilon^2_{\mathrm{iso}}\, [1 - (1 - \epsilon'_{\mathrm{ID}}\epsilon'_{\mathrm{trig}})^2]\, \mathcal{L}_{\mathrm{int}}}\,, \qquad (10)$$

where $\mathcal{A}$ is the kinematic cut acceptance, and the efficiency terms have been introduced above. The cross section is determined in a kinematical region defined by the p_T and η cuts on the muons and by the $m_{\mu\mu}$ invariant mass cut.

Using the corrected efficiencies in Table 12 and $\mathcal{L}_{\mathrm{int}} = 198 \pm 22\ \mathrm{nb}^{-1}$ we obtain, quoting only statistical uncertainty:

$$\sigma(\mathrm{pp} \to Z(\gamma^*) + X \to \mu^+\mu^- + X) \times \mathcal{A} = 0.418 \pm 0.048(\mathrm{stat.})\ \mathrm{nb} \qquad (11)$$

Using the acceptance estimated at the generator level from the Powheg $Z \to \mu^+\mu^-$ reference MC sample:

$$\mathcal{A}\,(\mathrm{POWHEG}) = 0.476 \pm 0.002 \qquad (12)$$

we can extrapolate the cross section bejond the kinematical cuts, ad we can determine:

$$\sigma(\mathrm{pp} \to \mathrm{Z}(\gamma^*) + X \to \mu^+\mu^- + X)\ [60 < m_{\mu\mu} < 120\,\mathrm{GeV}/c^2] = 0.88 \pm 0.10(\mathrm{stat.})\ \ \mathrm{nb}\ . \quad (13)$$

Only the statistical error is quoted; systematic errors are described in Section 15.

7 Muon momentum scale and resolution

The muon momentum scale and resolution is measured with four complementary methods:

- Calibration of muon momentum using di-muon resonances
- Analysis of Tracker tracks vs standalone muons residuals
- Cosmics end-point method
- Measurement of momentum scale using muons from W bosons

Each method is described in detail in Appendix C.

The results of all the analyses allow to exclude shifts of the muon momentum scale above 1% at $p_T \sim 40$ GeV. The muon momentum resolution is also measured and the result is found to be in agreement with the MC resolution apart from the region $1.5 < |\eta| < 2$ where the difference can be as big as 10%.

For the derivation of the systematics we choose to be conservative and apply a p_T dependent scale shift to muons from $Z \to \mu\mu$ and $W \to \mu\nu$ of the order of 1% for 40 GeV muons. For the resolution case, a smearing is applied of amplitude equal to the discrepancy between the resolution in data and in MC. The resulting systematic errors on Z and W from muon momentum scale and resolution are of 0.5% and 0.8% respectively. A description of the procedure used to compute these errors and the detailed results are in section 15.2.

8 Muon isolation efficiency calibration from data

In order to measure the isolation cut efficiency for prompt muons from data, two distinct methods can be exploited: Tag and Probe (T&P) [33] and lepton kinematic templates (LKT), which is an extension of the random-cone [34], both relying on using $Z \to \mu\mu$ data sample. T&P has not been adopted for the present analysis due to the small amount of collected $Z \to \mu\mu$ statistics.

The control sample $Z \to \mu\mu$ is selected as follows... (**to be completed**).

The essence of the LKT method consistes of "throwing" pre-defined directions in the event and studying energy deposits and tracks around these directions as if they were associated with the cones. In random cones method the directions are random, while in the LKT method the directions are defined by the direction (η,ϕ) of muons from a MC sample of a given signal, $W \to \mu\nu$ and $Z \to \mu\mu$ in this case. Templates also include p_T information, so, they are suitable to calibrate relative isolation variables too.

Figure 9 shows:

- isolation cut efficiency for prompt muons from W and Z from MC (ϵ_1)
- LKT isolation cut efficiency of W and Z muons using pre-selected $Z \to \mu\mu$ MC events (ϵ_2)
- LKT isolation cut efficiency of W and Z muons using pre-selected $Z \to \mu\mu$ and $W \to \mu\nu$ data events (ϵ_3)

In the W case we used as in the rest of the analysis the combined relative isolation, $Iso = (Iso_{trk} + Iso_{ecal} + Iso_{hcal})/p_{T_{muon}}$, while for the Z case we use $Iso = Iso_{trk}$, the absolute, tracker-only isolation. In both cases we report the isolation efficiency per muon.

Figure 10 shows the final result of this study: a correction factor to be applied to isolation cut efficiency value as calculated for prompt MC-truth-matched-muons from W and Z to match real data prediction using LKT. Here we simply rely on the hypothesis that the bias introduced by the method in the same in data and MC:

$$\epsilon_{true,data}/\epsilon_{LKT,data} = \epsilon_{true,MC}/\epsilon_{LKT,MC}\,, \tag{14}$$

and therefore:

$$\epsilon_{true,data} = \epsilon_{true,MC} \times (\epsilon_{LKT,data}/\epsilon_{LKT,MC})\,, \tag{15}$$

or in our notations:

$$\epsilon_{true,data} = \epsilon_1 \times (\epsilon_3/\epsilon_2)\,. \tag{16}$$

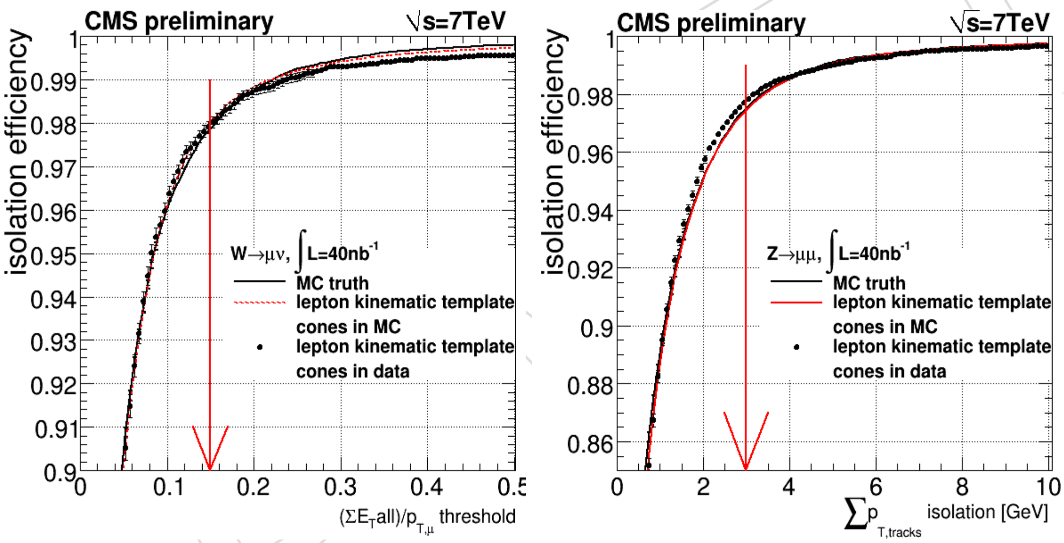

Figure 9: **Isolation cut efficiency for prompt muons (per muon).** Left: $W \to \mu\nu$ case - black curve - isolation cut efficiency for prompt MC-truth matched muons from W (ϵ_1), red - LKT isolation cut efficiency of W using pre-selected $Z \to \mu\mu$ MC events (ϵ_2), symbols - LKT isolation cut efficiency of W and Z muons using pre-selected $Z \to \mu\mu$ and $W \to \mu\nu$ data events (ϵ_3). Right: ditto for Z.

For the particular cuts used in the analysis, we estimate the correction factors to be:

- for W: $correction = \epsilon_3/\epsilon_2 = 1.00$ ($\epsilon_1 = 0.981$, $\epsilon_2 = 0.977$, $\epsilon_3 = 0.98$)
- for Z: $correction = \epsilon_3/\epsilon_2 = 1.00$ ($\epsilon_1 = 0.975$, $\epsilon_2 = 0.973$, $\epsilon_3 = 0.976$)

We also checked efficiencies and correction factors for different p_T, η, ϕ bins and didn't observe any changes of the results beyond the statistical fluctuations (difference is typically in the third significant digit)[3].

[3] (*In progress*):

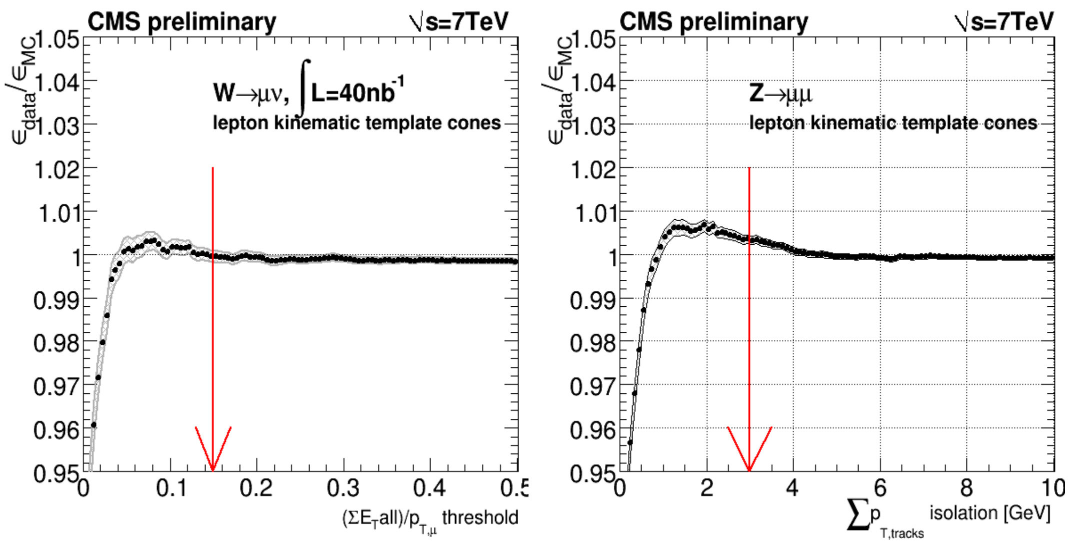

Figure 10: **Isolation cut efficiency correction for prompt muons (per muon).** Left: $W \to \mu\nu$ case, $correction = \epsilon_3/\epsilon_2$. Right: ditto for Z.

9 Electron selection

Isolated high transverse momentum electrons are reconstructed in CMS by first building "superclusters" – a group of one or more associated clusters in the electromagnetic calorimeter (ECAL) – by an algorithm which takes account of their characteristic narrow width in the η coordinate and their characteristic spread in ϕ due to the bending in the magnetic field of electrons radiating in the tracker material . The superclusters are then matched to track seeds (pairs or triplets of hits) in the inner layers of the tracker, and from this track seed a track is built by an algorithm which accounts for the energy loss due to radiation. A second algorithm starts from tracks, and is most effective for low transverse momentum electrons, and electrons inside jets, and also slightly adds to the efficiency for high transverse momentum electrons, particularly in the region of the barrel/endcap transition. More details of electron reconstruction are given in Refs. [35, 36].

The electron reconstruction has been commissioned using both minimum bias events and events selected online by the ECAL L1 triggers. The perfomance of the algorithms used for the electron seeding, electron preselection, and the electron charge and momentum determination have been assessed by comparing data with MC expectation and the results are described in Refs. [37, 38].

For the current analysis only electrons reconstructed by the first ("ECAL driven") method are used. A fiducial region in the ECAL is defined which excludes electrons close to the barrel/endcap transition, and electrons in the first endcap trigger tower which lies in the shadow of cables and services exiting between the barrel and endcap. The fiducial region cut is applied by placing a cut on the position of the ECAL supercluster ($|\eta| < 2.5$ with $1.4442 < |\eta| < 1.566$ excluded).

- There is some noticeable difference for very small cuts in isolation efficiency curves. It's well before cut values we are interested in, but we still are invistigating the reasons for the difference.
- Results are produced with PYTHIA MC samples, they will be updated shortly for most recent ones. Change, if any, is not expected to be significant.
- There are more sophisticated approaches to correct for possible biases and we are considering them. In any case, it is obvious that whatever corrections will be made it would be a second order effect for efficiency at the level 97-98%.

Electron preselection imposes a cut of $E_T > 4$ GeV on the supercluster and $H/E < 0.15$ where H is the energy deposited in the HCAL in a radius of $\Delta R < 0.15$ centred on the supercluster position, and E is the supercluster energy. Additionally, although the supercluster to track seed matching described above is very loose it does impose some weak implicit restriction on the track match to the supercluster in both position and energy, and on the track transverse impact parameter and the radius of the first tracker hit.

A transverse energy cut on the supercluster is applied: $E_T > 20GeV$ for the Z selection and the W selection. The supercluster is matched to the trigger object. In the W selection events are rejected if there is a second electron passing the Z electron selection. (Monte Carlo suggests that this cut rejects only 0.024% of selected W events).

For early analyses an electron selection using simple cuts, rather than a multi-variate approach, provides a useful tool to understand the data and make comparison with Monte Carlo. In the approach used in this analysis different cuts are used for electrons found in the ECAL barrel (EB) and the ECAL endcap (EE). Other than that no categorization is used – in contrast to the category based selection. Fuller details of electron selection methods can be found in Ref. [39]. Simple cuts without use of categories gives simplicity and transparency for early analyses, with little loss of performance when compared to the use of categories. Cut inversion is simple, a full understanding and efficiency measurement can be obtained using a smaller data sample, and it is simple to cleanly separate the e-ID, isolation and conversion rejection pieces.

Electron selection variables may be categorized in 3 groups which will be considered in turn:

- e-ID variables (shower shape, track cluster matching etc)
- isolation variables
- conversion rejection variables

9.1 Electron identification variables

The electron identification variables that have been found to be the most powerful, and are used in the selection, are: the variables measuring spatial matching between track and ECAL supercluster, $\Delta\eta_{in}$and $\Delta\phi_{in}$, the shower RMS width variable $\sigma_{i\eta i\eta}$, and the hadronic leakage variable H/E.

For the spatial matching the inner momentum of the GSF track (i.e. the momentum at the primary vertex) is helix-extrapolated to the ECAL and compared to the supercluster position (whose position reconstruction ideally gives the shower position which would result from an electron which did not radiate in the tracker material).

The shower width in η is to very good approximation unaffected by the spreading by the magnetic field of showering in the tracker material. It is calculated counting distance in crystal widths, and is thus not affected by the intermodule gaps in the barrel or by the varying size (in η, ϕ coordinates) of the crystals in the endcap. After the calculation, which uses a log rather than linear weighting of the energy, the value is multiplied by the barrel crystal size, or by a nominal average endcap crystal size, as appropriate.

The hadronic leakage variable is calculated using the HCAL energy found within $\Delta R < 0.15$ of the ECAL seed cluster, divided by the seed cluster energy.

9.2 Electron isolation variables

The isolation variables used are tranverse energy/momentum sums computed in regions of $\Delta R < 0.3$. Sums of track p_{T} in the tracker, and of individual channel transverse energies in the ECAL and HCAL (details of the cuts placed on the objects before summing can be found in Ref. [??]). For the ECAL and HCAL the region is centred on the supercluster position, and for the tracker the region is centred on the track direction at the vertex. For all 3 sums there is an inner exclusion region which removes the electron "footprint", resulting from showering in the tracker and ECAL, and in the case of the HCAL excludes the region summed for the H/E variable. The sums are divided by the electron E_T and a cut applied on these ratios.

9.3 Conversion rejection variables

Three discriminants have been investigated for rejection of electrons resulting from conversion of photons in the tracker: the absence of track hits in tracker layers between the vertex and the first measured hit of the track, the presence of a conversion partner, and the observation of a significant transverse impact parameter. The electron selection used in this analysis uses a cut on number of allowed missing tracker hits before the first hit in the reconstructed track. For tight selections electron candidates are rejected if they have an accompanying track satisfying both $Dist < 0.02$ and $Dcot\theta < 0.02$ where $Dist$ is the distance of closest approach of the accompanying track in mm. and $Dcot\theta$ measure the difference in dip angle between the accompanying track and the electron track [40].

9.4 Cut tuning

The cut values chosen have been obtained using a methodology described in [41] which shares the rejection power between the selection variables so as to achieve the maximum background rejection for any given selection efficiency. The methodology produces sets of cut values for any chosen tightness of selection.

The methodology was used on Monte Carlo data samples (Spring 10 samples, reconstructed using CMSSW 357). A series of reference selections of graded severity was produced with efficiency for electrons having nominal values of 95%, 90%, 85%, 80%, 70%, and 60%. When $\not\!\!E_{\mathrm{T}}$ or reconstructed tranverse mass, M_T, is plotted, it can be seen that the number of events in the background region (i.e. low $\not\!\!E_{\mathrm{T}}$ or M_T) decreases dramatically as the tightness of the selection is increased, while the number of events in the signal region (high $\not\!\!E_{\mathrm{T}}$ or M_T) decreases by only a small amount. See Figs. 11, 12, 13, where the M_T measurement is obtained using the particle flow algorithm. This provides a first level of validation of the selection, and also of the $\not\!\!E_{\mathrm{T}}$ measurement.

The slightly smaller decrease of the background in Monte Carlo, as compared to data, which can be seen in the figures, is expected. The main background comes from di-jet events where one of the jets provides a fake (charged hadron/π^0 overlap, or early showering charged hadron), or real (heavy flavour decay, or photon conversion) electron signal. The generator preselection that has been applied to enable simulation of a large sample of this background includes cuts (in particular loose isolation requirements) which reduce the number of background events seen before selection.

Two selections have been chosen as "baseline selections" for the Z and W analysis. The chosen selections have nominal efficiencies of 95% and 80% for signal electrons, and are refered to as WP95 and WP80. The 2 selections are detailed in Table 13. WP95 is a loose selection with a rejection factor of about 20 against jet background. WP80 is a selection tight enough to reveal the W signal in an $\not\!\!E_{\mathrm{T}}$ or M_T plot. Until more data is available to understand the detailed behavior of the selection variables for signal electrons it seems inadvisable to cut harder.

After accumulating $55\mathrm{nb}^{-1}$, it was observed that the WP80 cut in $\Delta\eta$ was too tight in the EE even after applying endcap misalignment corrections (see Figs. 18 and 26 below). This is be-

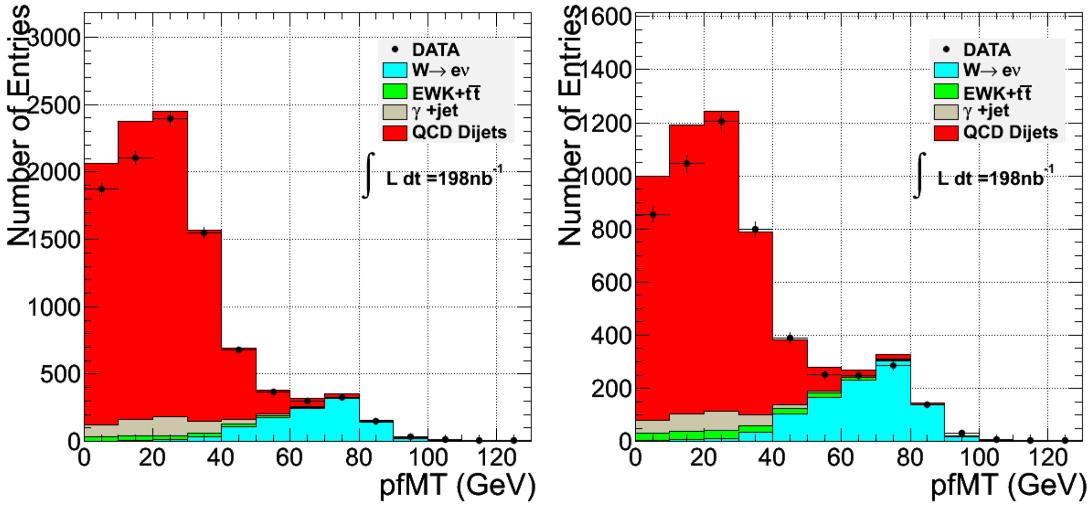

Figure 11: M_T distribution seen in data (points) compared with Monte Carlo (histograms) after WP95 and WP90 selections

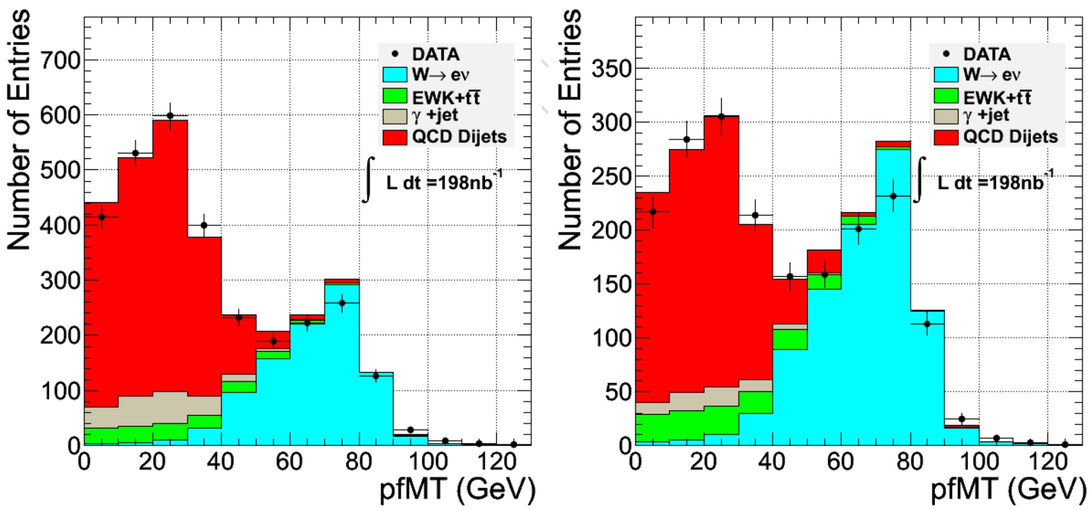

Figure 12: M_T distribution seen in data (points) compared with Monte Carlo (histograms) after WP85 and WP80 selections

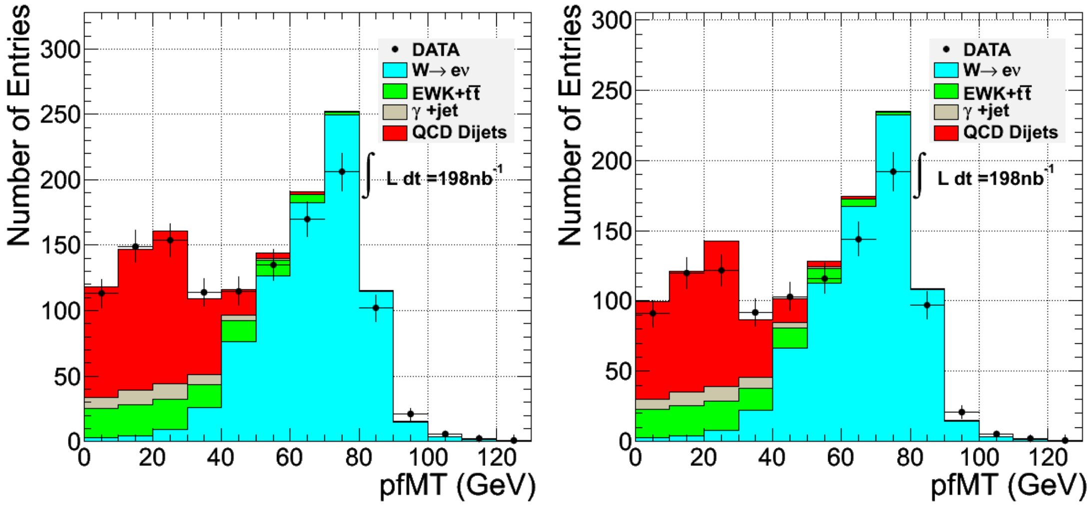

Figure 13: M_T distribution seen in data (points) compared with Monte Carlo (histograms) after WP70 and WP60 selections

lieved to be due to residual EE-tracker misalignment, introducing inefficiencies in data relative to the simulated efficiencies. The $\Delta\eta$ cut was removed from the endcap selection cuts in response to this observation.

Table 13: Selection cuts for electrons derived from Monte Carlo. After investigation of data the $\Delta\eta_{in}$cut* was removed from the endcap selection (see text).

	WP95		WP80	
	Barrel	Endcap	Barrel	Endcap
Track iso	0.15	0.08	0.09	0.04
ECAL iso	2.0	0.06	0.07	0.05
HCAL iso	0.12	0.05	0.10	0.025
Missing hits $\leq$	1	1	0	0
Dcot	n/a	n/a	0.02	0.02
Dist	n/a	n/a	0.02	0.02
$\sigma_{i\eta i\eta}$	0.01	0.03	0.01	0.03
$\Delta\phi_{in}$	n/a	n/a	0.06	0.03
$\Delta\eta_{in}$	0.007	[0.01]*	0.004	[0.007]*
H/E	0.15	0.07	0.04	0.025

9.5 Selection validation with data

The MC description of the variables used in the selection has been checked against data and found to be extremely good. This comparison has been made in a number of different ways. It is most simply done by looking at the distributions of variables after all other selection cuts have been applied – i.e. the "N-1" plots. Examples of such distributions for the track-cluster matching variables are shown in Figs. 14, 15, 16, for endcap and barrel separately, for the 80% selection.

An $\not{E}_T$ cut can be used to reveal either the signal or the background distribution. Figures 17, 18, 19, show the same distributions as the previous figure after requiring $\not{E}_T > 30 GeV$, where $\not{E}_T$

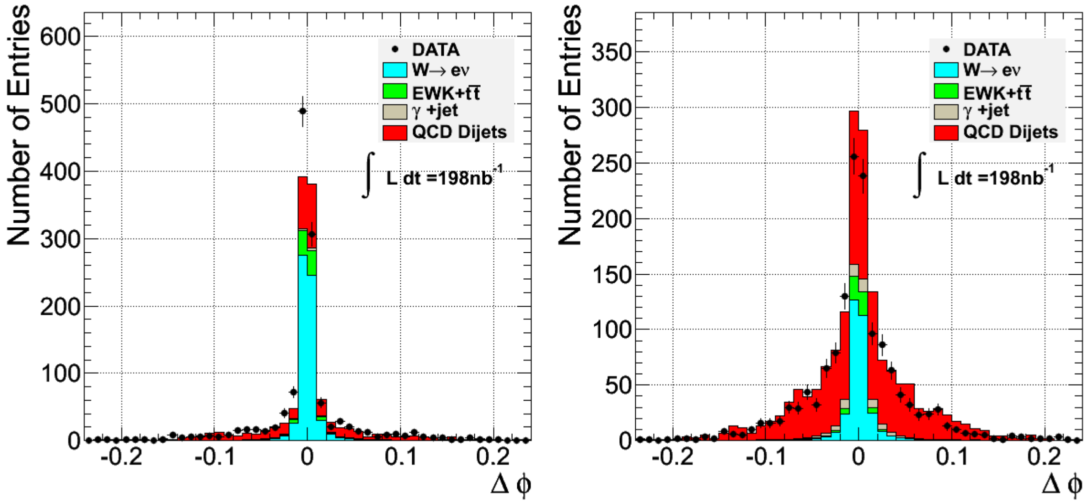

Figure 14: (N-1) distributions of $\Delta\phi_{in}$in barrel (left) and endcap (right)

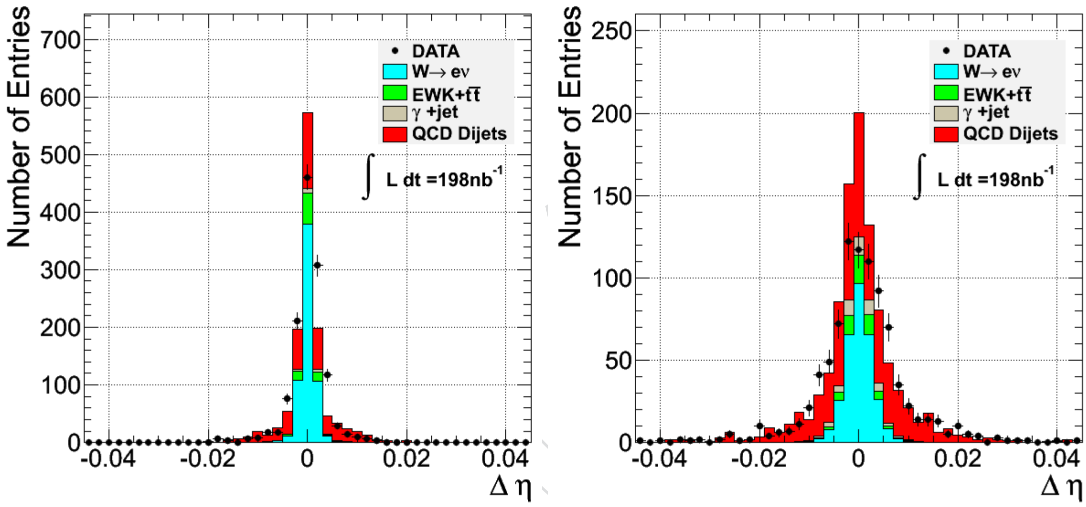

Figure 15: (N-1) distributions of $\Delta\eta_{in}$in barrel (left) and endcap (right)

is calculated using the particle flow algorithm. It can be seen that the distribution for $\Delta\eta_{in}$in the endcap is not well reproduced by the Monte Carlo. This might be due to residual misalignment of the endcaps with respect to the ECAL, even after the correction for the known misalignment has been applied [42]. Generally, as far as can be seen with the available number of events, the variable distributions in the barrel agree very well with Monte Carlo, whereas the situation in the endcaps is less clear.

Figures 20-24, show the distributions of the other selection variables after requiring $\not{E}_{\mathrm{T}} > 30GeV$, again the $\not{E}_{\mathrm{T}}$ has been calculated using the particle flow algorithm.

Another way to display the selection variable distributions for the signal is to use a background subtraction technique (${}_{s}Plots$ [43]). After applying a veto on accompanying jets and a selection on $\not{E}_{\mathrm{T}}/p^{e}_{T} > 0.3$ in the event to reduce the dominant jet background an unbinned maximum likelihood fit is made to the M_T distribution with signal and background functions to produce a function which gives an event by event signal probability. Applying this function results

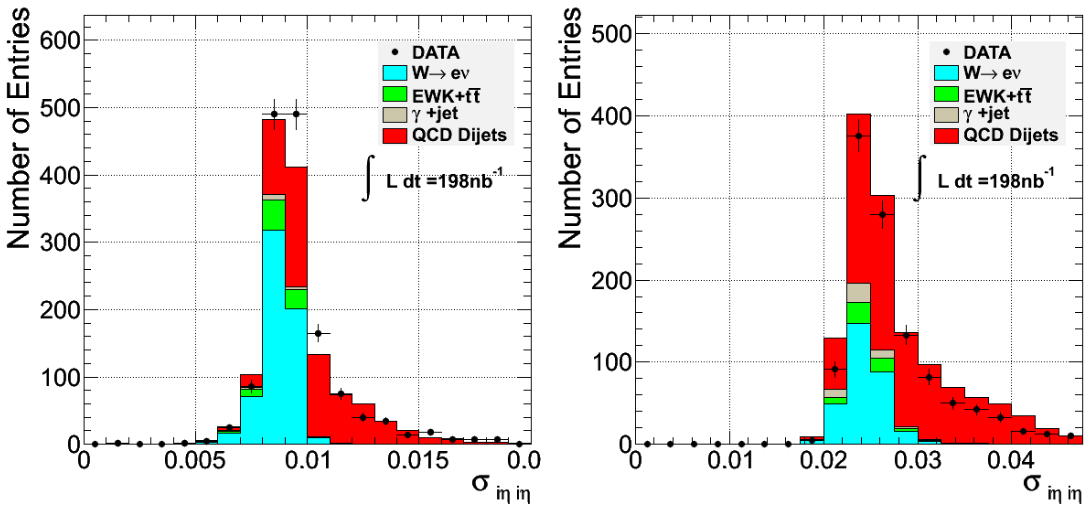

Figure 16: (N-1) distributions of $\sigma_{i\eta i\eta}$ in barrel (left) and endcap (right)

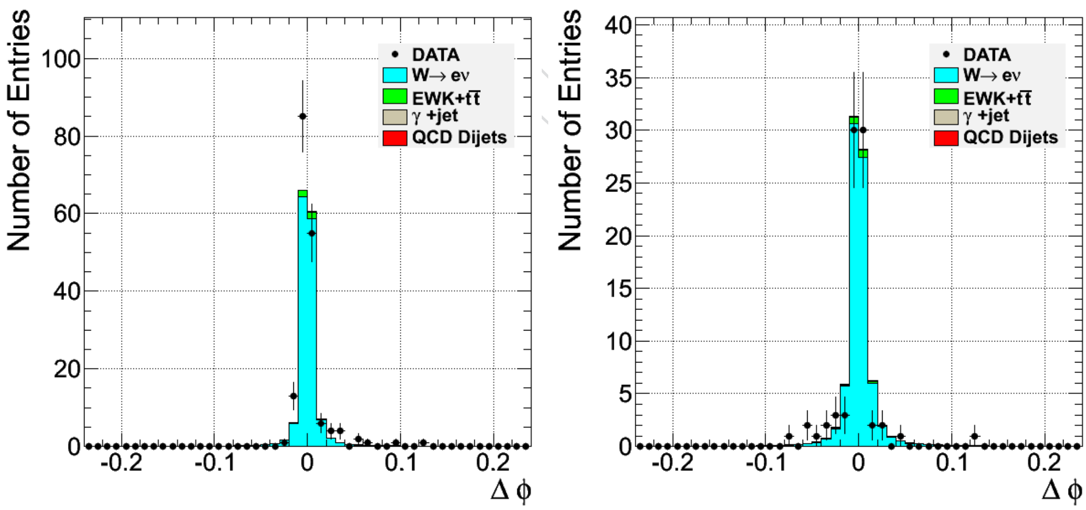

Figure 17: (N-1) distributions of $\Delta\phi_{in}$in barrel (left) and endcap (right) after applying the cut $\not{E}_{\mathrm{T}} > 30 GeV$

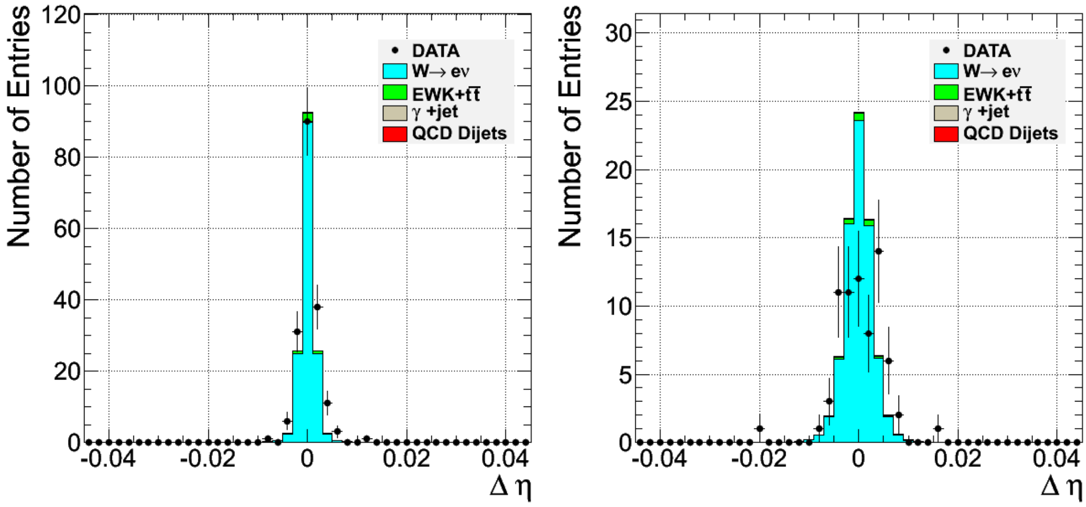

Figure 18: (N-1) distributions of $\Delta\eta_{in}$in barrel (left) and endcap (right) after applying the cut $\not{E}_T > 30 GeV$

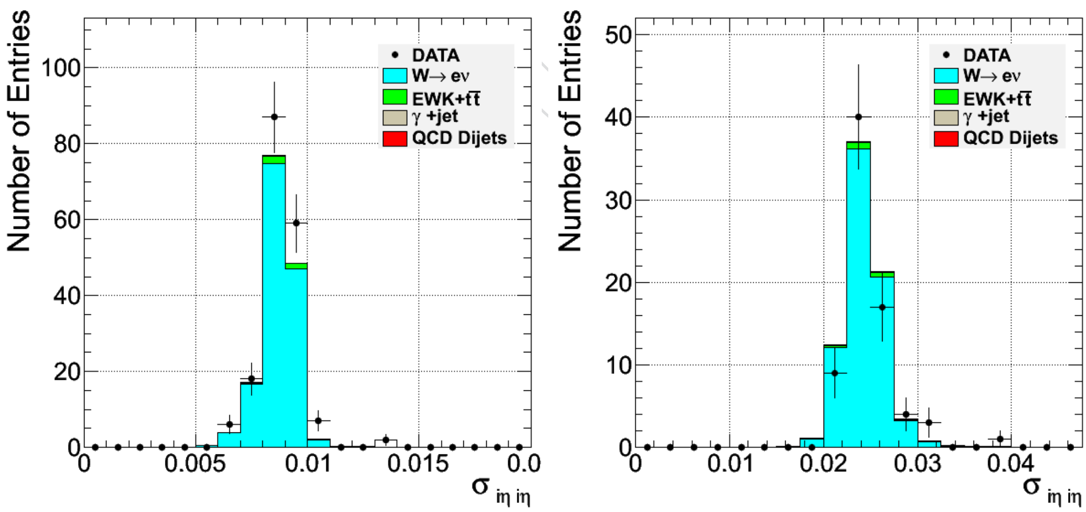

Figure 19: (N-1) distributions of $\sigma_{i\eta i\eta}$ in barrel (left) and endcap (right) after applying the cut $\not{E}_T > 30 GeV$

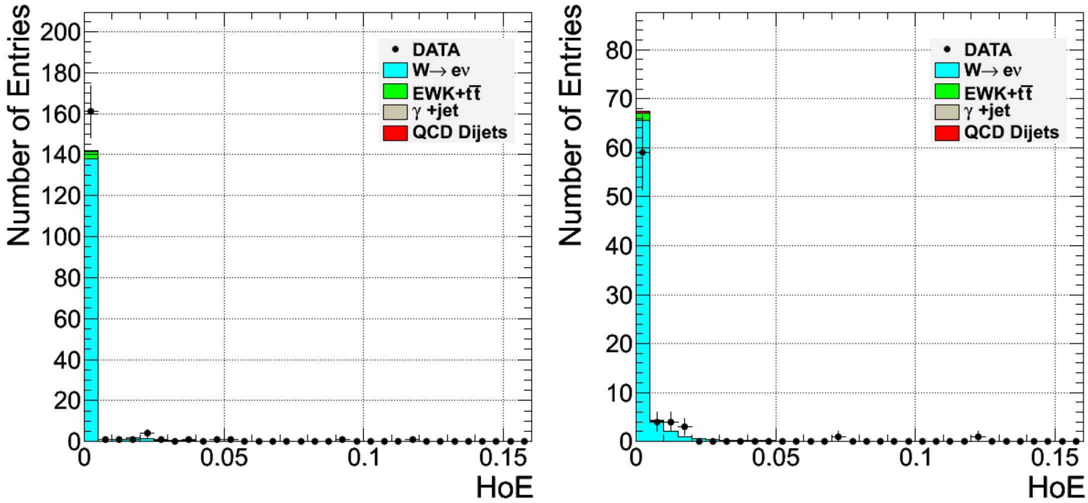

Figure 20: (N-1) distributions of H/E in barrel (left) and endcap (right) after applying the cut $\not{E}_{\mathrm{T}} > 30GeV$

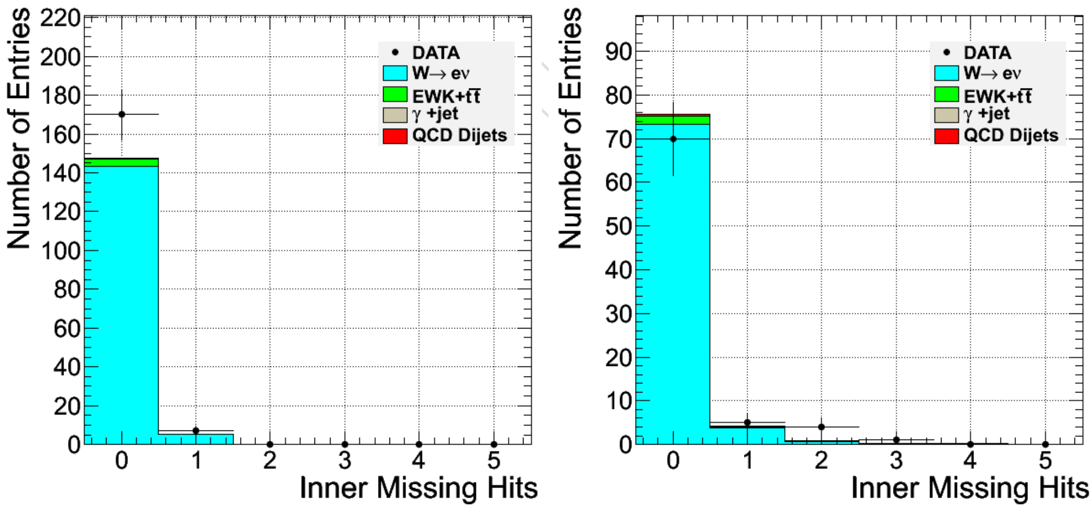

Figure 21: (N-1) distributions of the number of missing hits before the track start, in barrel (left) and endcap (right) after applying the cut $\not{E}_{\mathrm{T}} > 30GeV$

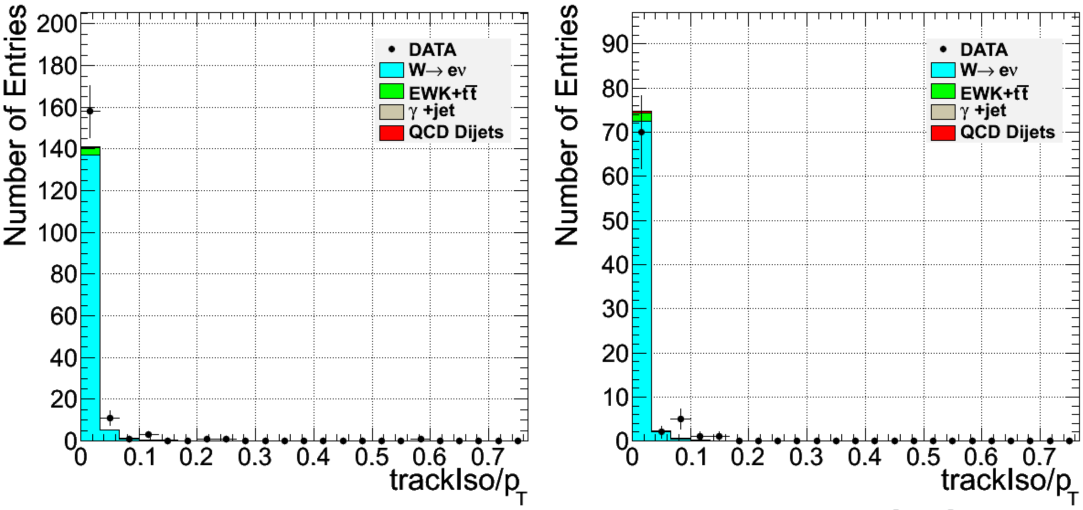

Figure 22: (N-1) distributions of the track isolation variable in barrel (left) and endcap (right) after applying the cut $\not\!\!E_{\mathrm{T}} > 30 GeV$

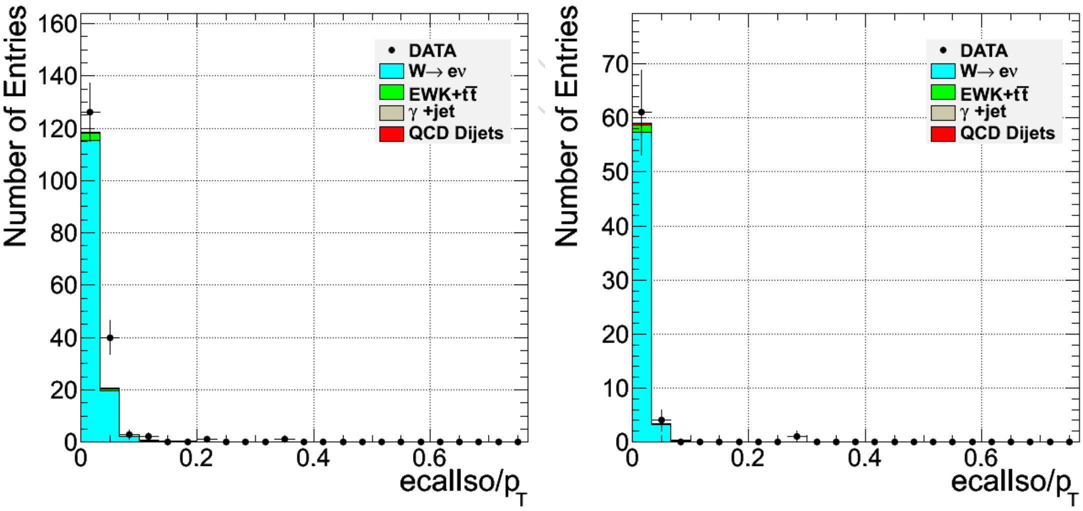

Figure 23: (N-1) distributions of the ECAL isolation variable in barrel (left) and endcap (right) after applying the cut $\not\!\!E_{\mathrm{T}} > 30 GeV$

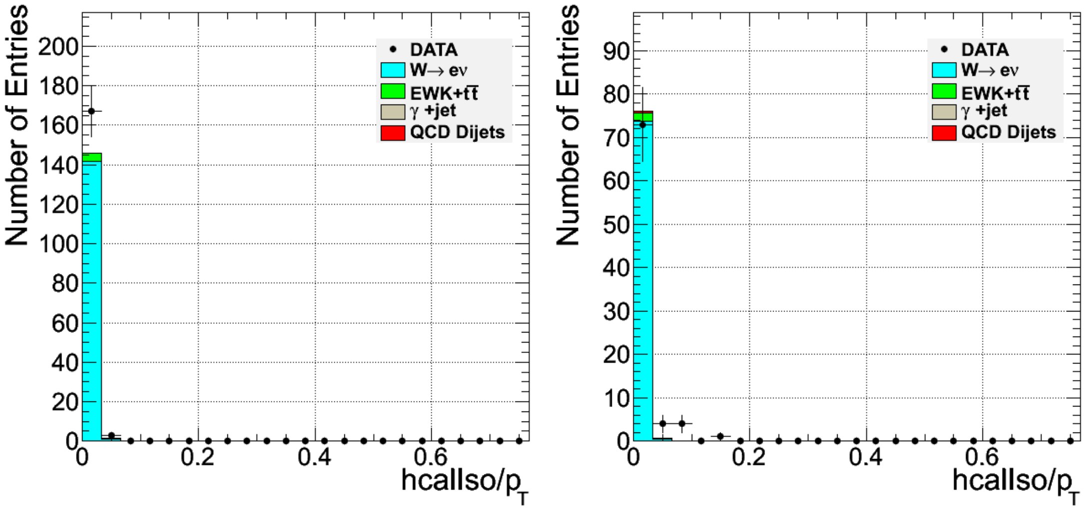

Figure 24: (N-1) distributions of the HCAL isolation variable in barrel (left) and endcap (right) after applying the cut $\not{E}_{\mathrm{T}} > 30 GeV$

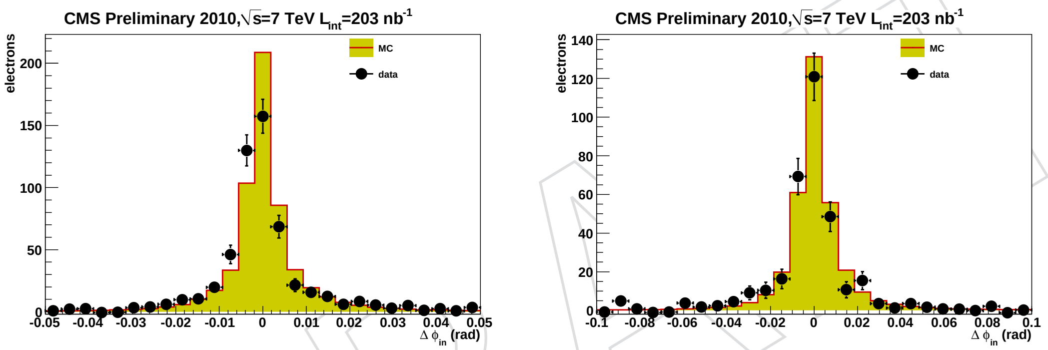

Figure 25: Signal distribution for $\Delta\phi_{in}$in barrel (left) and endcap (right) extracted using splot technique

in a selection variable distribution corresponding to the signal. Figures 25, 26, 27, show the resulting distributions compared to signal Monte Carlo.

9.6 Electron reconstruction and identification efficiency

9.6.1 Reconstruction efficiency

The baseline technique for measuring electron reconstruction and identification efficiency at CMS is "tag and probe" using Z bosons decaying to electrons, in which one of the electrons, the "tag", is required to pass stringent electron identification criteria whilst the other electron, the "probe", is used to measure efficiencies. The invariant mass of the tag and probe pair are required to be within a window around the mass of the Z boson, ensuring a very high purity electron sample.

Since an insufficient number of Z bosons have been produced in the data collected during Spring 2010 to use the above technique, different techniques have been developed for measuring electron reconstruction and identification efficiency using W bosons decaying to electrons. Since the control sample defined in this way is completely correlated with the one under study

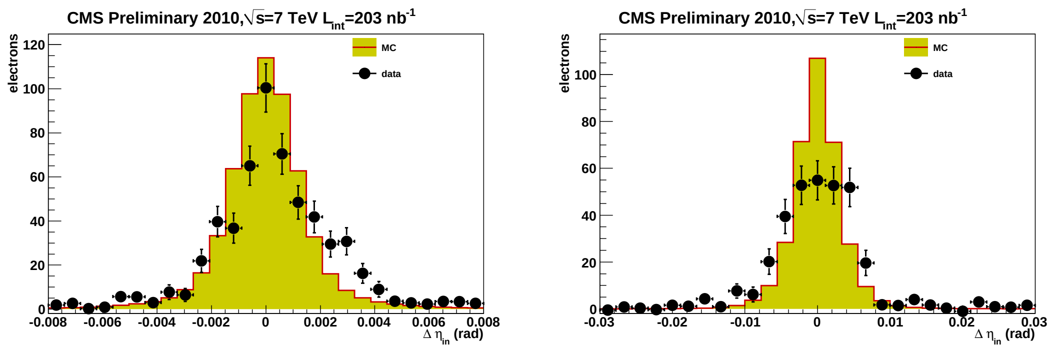

Figure 26: Signal distribution for $\Delta\eta_{in}$in barrel (left) and endcap (right) extracted using splot technique

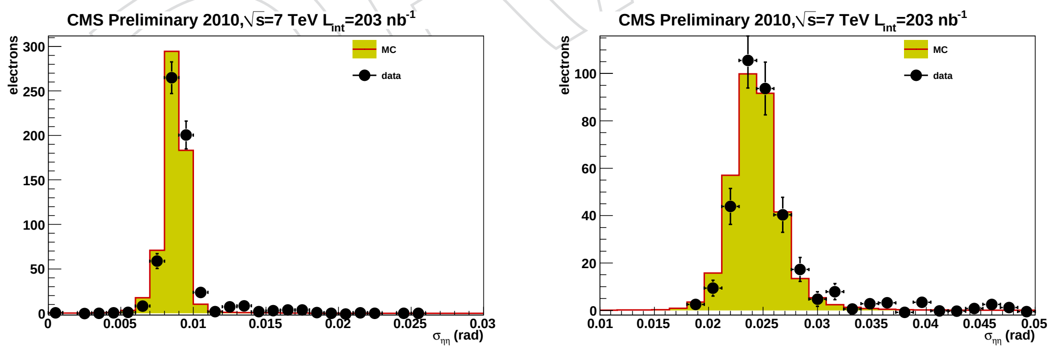

Figure 27: Signal distribution for $\sigma_{i\eta i\eta}$ in barrel (left) and endcap (right) extracted using splot technique

for W $\rightarrow$ eν measurement, the measurments of efficiency with data will not be used for the cross section estimation, but only as a cross check that the value estimated from Monte Carlo is consistent data.

For the reconstruction efficiency, the signature for the W $\rightarrow$ eν control sample is a reconstructed supercluster in the ECAL plus $\not{E}_{\mathrm{T}}$. This assumes the knowledge of the reconstruction efficiency, estimated from Monte Carlo, which is close to 100% for electrons with $p_T > 25$ GeV/c.

The supercluster is selected having $E_T > 20$ GeV in the ECAL region interesting for the electron reconstruction ($|\eta| < 2.5$) and the cleaning of ECAL anomalous signals is applied. In order to reduce the di-jet background, a requirement of H/E, $\sigma_{i\eta i\eta}$ of the seed cluster of the SC are applied, together with the tracker, ECAL and HCAL isolations defined for the 80% working point of the electron ID described before. We check on MC that these requirements induce biases on the reconstruction efficiency of less than 1%. To achieve further rejection, W $\rightarrow$ eν candidates without associated jets are selected vetoing events where a jet with $E_T > 25$ GeV (energy corrected for the calorimetric response) is found in $|\eta|$ <3.0 We also require that $\not{E}_{\mathrm{T}}/E_T^{SC}$ >0.3. This cut has a negligible effect on signal M_T distribution and rejects about 20% of the QCD, slightly biasing the M_T distribution towards higher values, allowing the full determination of the QCD M_T shape in the fit region on data.

An unbinned maximum likelihood (ML) fit is applied to the M_T fixing the W PDF to Monte Carlo and floating all background PDF parameters on data. The fit returns simultaneously the signal, background yields together with their reconstruction efficiency.

We check for possible fit biases in the estimate of the yields and reconstruction efficiency by running many toy experiments for an integrated luminosity of 100 nb^{-1} with the nominal fit strategy (background shape floating, signal one fixed). We estimate the bias on the parameter θ ($\theta = N^{sig}$, ϵ^{sig}, N^{bkg}, ϵ^{bkg}) evaluating the pull on it:

$$pull_\theta = \frac{\theta^{fit} - \theta^{true}}{\sigma_\theta} \tag{17}$$

In case of unbiased estimation of θ and correct estimation of uncertainty σ_{theta} we expect for the pull a Gaussian distribution with mean equal to zero and standard deviation one. The results are shown in Fig. 28, showing unbiased estimation both for signal and for background identification efficiency. The projected uncertaity on the reconstruction efficiency, rescaling the signal and background yields observed in 71 nb^{-1} to 100 nb^{-1} is 2.7%.

We show in Fig.29 the distribution of the W candidates reconstructed with a EE+, EE- and EB electron with the fit superimposed, in a data sample equivalent to 55 nb^{-1}, showing the background contribution (dominated by QCD di-jets and γ+jets).

In Table 14 we report the signal yields and the efficiencies obtained on data in ECAL barrel (EB), and ECAL endcaps (EE- and EE+) and expected values from MC.

	$N_{W\rightarrow e\nu}$	$\epsilon_{W\rightarrow e\nu}$ data	$\epsilon_{W\rightarrow e\nu}$ MC
EB	524 ± 27	$0.969\ ^{+0.022}_{0.022}$ (stat) ± 0.01 (syst)	0.978 ± 0.002
EE	226 ± 10	$0.928\ ^{+0.020}_{-0.020}$ (stat) ± 0.03 (syst)	0.953 ± 0.003

Table 14: Fitted W$\rightarrow$eν yield, electron identification efficiency in ECAL barrela and endcap as fitted on data (L_{int} = 78 nb^{-1}). The estimation of systematic uncertainty is described below in the text.

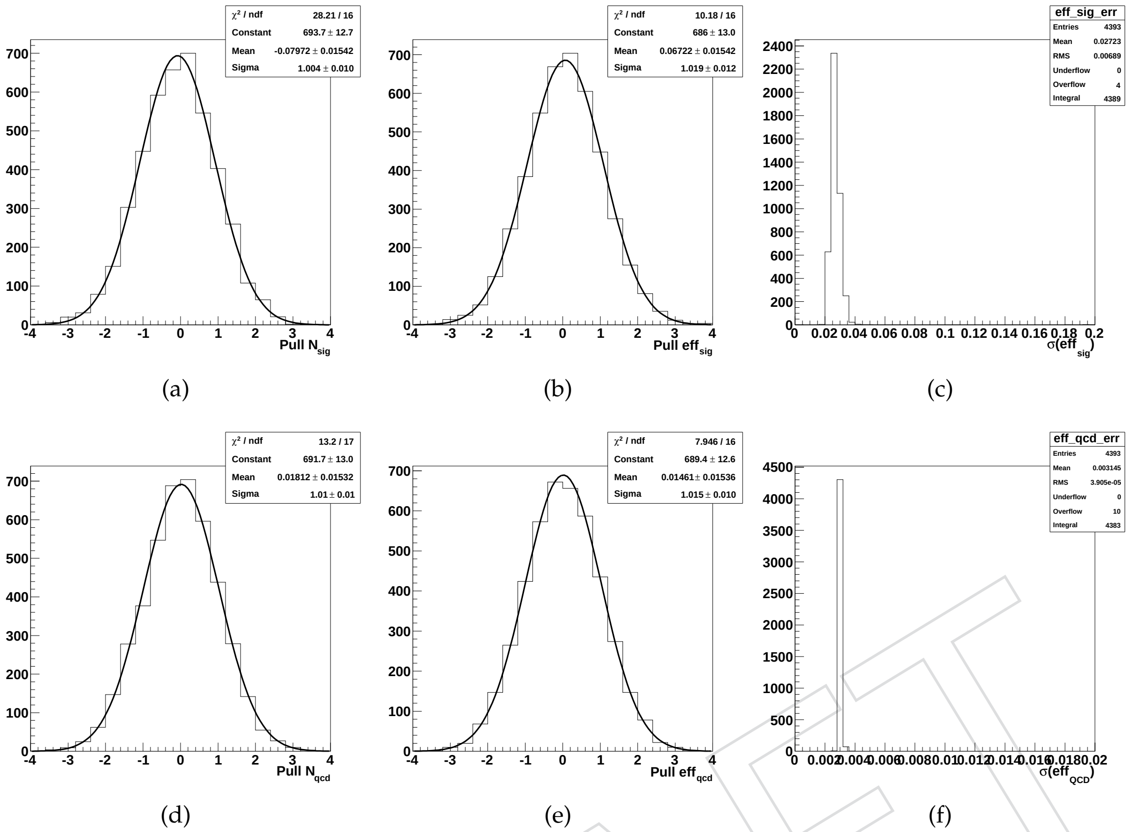

Figure 28: Distributions of the pull on the yield, the pull on the efficiency, the uncertainty on the efficiency for signal (a, b, c respectively) and for QCD background (d, e, f respectively) estimated from 1000 toy Monte Carlo experiments for an equivalent luminosity of 100 nb^{-1}.

We cross-check (on a subsample of dataset used for ML fit) the values obtained from the fit counting the fraction of electrons matching a SC which passes the above selection with $M_T >$ 70 GeV. We get 69 (31) SCs passing the above criteria in EB (EE), and of these we get 60 (21) with an associated reconstructed electron. This corresponds to 87% (68%) efficiency, which is slightly lower, but consistent with what we get from the fit metod (background is assumed negligible in this region for this simple test: this is not quite a good approximation mostly for EE, where the background pollution can be up to 10%. So we expect a bias towards lower efficiency from this method respect the fit).

As a cross check of the validity of the background M_T shape (whose functional form has been decided on simulation, but whose parameters are completely float in the fit to data), we define a background control sample inverting the $\sigma_{i\eta i\eta}$ cut. This reduces the signal contamination to negligible level. We show in Fig. 30 the fit to this sample in ECAL barrel and endcaps. We performed this test on 78 nb^{-1}.

The consistency of the shape is validated performing the fit to the nominal sample fixing the pdf for the QCD background to the one obtained from the anti-electron sample. This is shown in Fig. 31. The change both in the yields and in the efficiencies are negligible with respect the nominal fit. We also show in Fig. 32 the projections of the fit on barrel and endcap candidates for the events passing the supercluster-electron matching (reconstructed electrons) and the ones failing that.

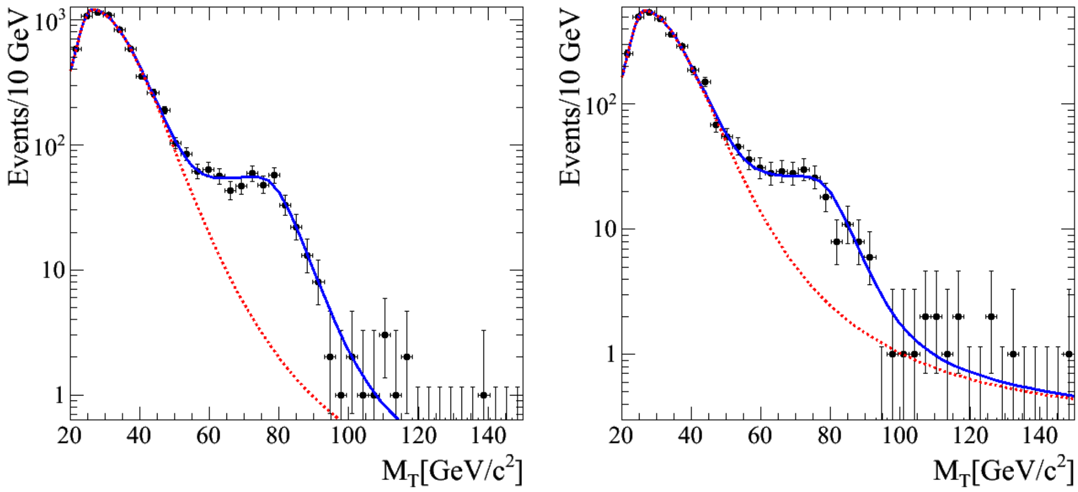

Figure 29: Fit to the M_T distribution obtained with a SC and MET. Blue solid line represents the total likelihood, red dashed curve represents background contribution. Left: EB electrons, Right: EE electrons. Fit is performed on 203 nb^{-1} of integrated luminosity.

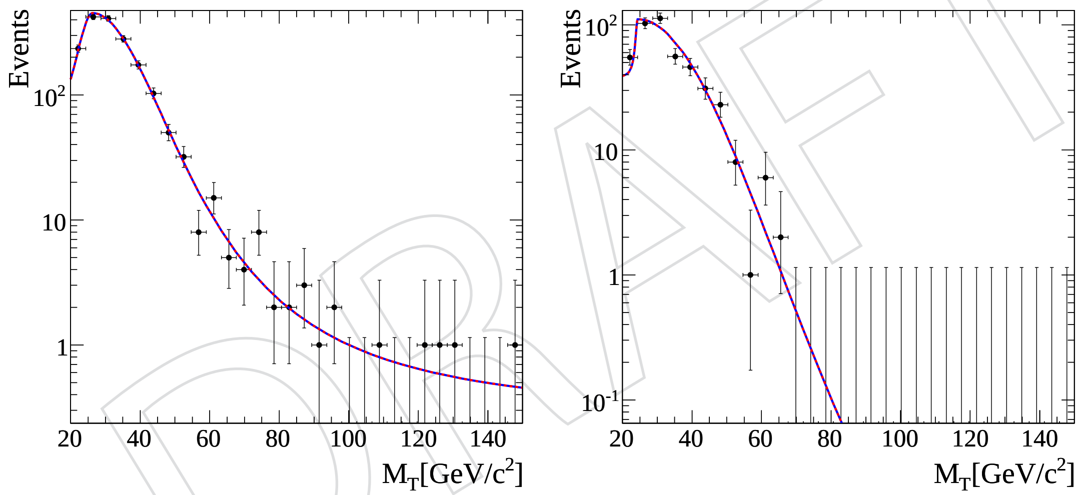

Figure 30: Fit to the M_T distribution for barrel candidates (left) and endcap candidates (right) obtained with a SC and MET on the anti-electron sample obtained inverting the $\sigma_{i\eta i\eta}$ cut. The fitted pdf is superimposed, assuming 0 signal events.

We estimate a systematic uncertainty on the efficiency associated to the fixed shape of the signal varying the scale of the M_T distribution of 1% for the barrel and 3% in the endcaps, generously with respect what expected for the ECAL absolute scale We also vary the other signal M_T PDF between two bounding shapes as described for the W signal extraction systematics in Section 12.3. We fit the data sample, varying the parameters uniformly covering these bounding shapes. The distribution of the difference between the nominal fit and these fits is shown in Fig. 33 for the signal yield and for the reconstruction efficiency. We then estimate the systematic uncertainty as 1% for the barrel and 3% for the endcap.

As a complementary method, the reconstrution efficiency is estimated with a slightly differ-

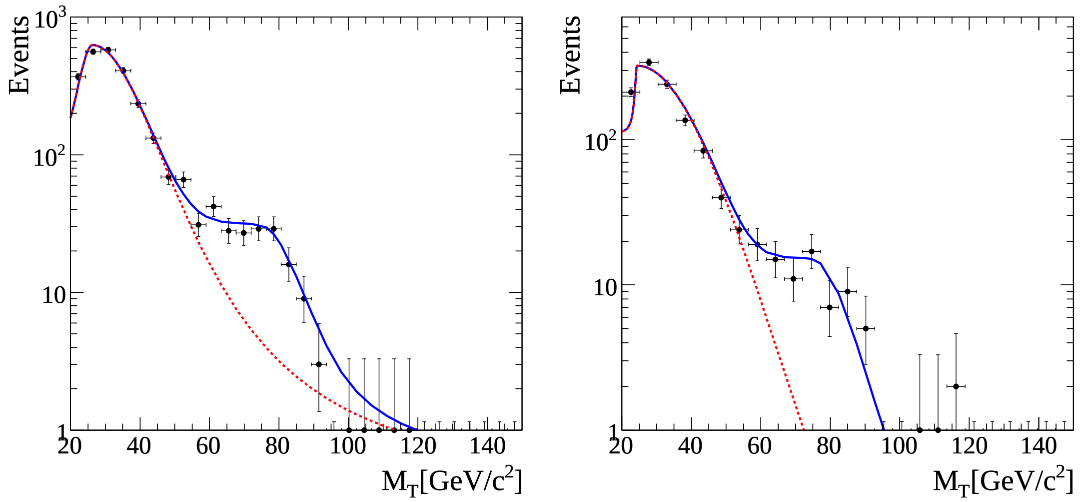

Figure 31: Fit to the M_T distribution for barrel candidates (left) and endcap candidates (right) obtained with a SC and MET on the nominal sample with the QCD pdf fixed to the one obtained inverting the $\sigma_{i\eta i\eta}$ cut.

ent selection and subtracting the QCD background from a large statistics di-jets Monte Carlo simulation. The selection is the following:

- no jet with $p_T > 10$ GeV/c
- MET (track-corrected) $>$ 30 GeV
- Exactly one probe SC with E_T >15 GeV and $|\eta| < 2.5$
- $|\delta\phi(MET, SC)| > \pi/2$
- $60 < m_T(SC, MET) < 100 GeV$

The distribution of the transverse mass after this selection is shown with and without the transverse mass cut for the W signal and for the major backgrounds in Fig. **??**. In order to extract the signal yield, the background yields from Monte Carlo expectations are subracted. The major contribution comes from the QCD di-jets. In order to estimate this background, large samples of di-jets (without e.m. enriching filters) are used, with $\hat{p_T} > 15$ GeV and $\hat{p_T} > 30$, properly combined . After subtracting the background, the estimated signal yield on 13.3 nb^{-1} is 23.18 (*uncertainty to be evaluated!*). We then require the matching of the candidate supercluster with a reconstructed electron and we repeat the background subtraction procedure. In this case we estimate 20.7 signal candidates. The evaluated electron reconstruction efficiency starting from a reconstructed supercluster is about 89%. This results, using a different selection and different signal extraction method, is consistent with the estimation described previously.

9.6.2 Identification efficiency

The efficiency of electron identification can be estimated with the same fit strategy using the same selection described above, but using a reconstructed electron + $\not{E}_T$.

- probe electron with E_T >20 GeV and $|\eta| < 2.5$
- ECAL isolation applied on electron SC ($\sum_{h=ECALhits}^{\Delta R=0.4} E_T^{hit} < 4$ GeV)
- $H/E < 0.15$ (applied in the electron pre-selection)
- no jets with $p_T > 25$ GeV/c

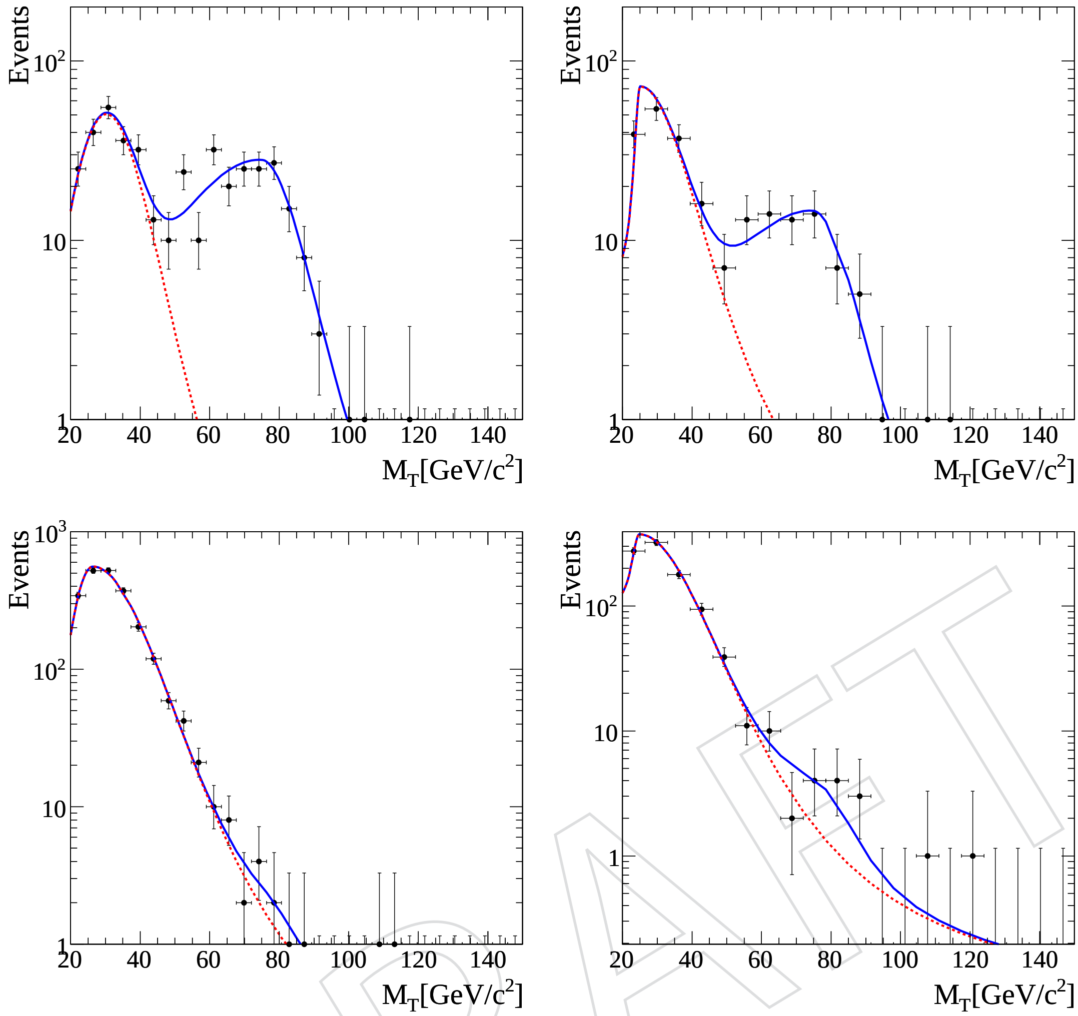

Figure 32: Projections of the fit to the M_T distribution obtained with a SC and MET on the nominal sample for barrel (left) and endcap (right) for the electron-reconstructed candidates (top) and the ones not reconstructed (bottom).

- $M_T > 20$ GeV (fit region definition)
- $MET/E_T^{SC} > 0.3$

Each event is flagged having an electron which would pass a given electron identification working point (we test *WP70, WP80, WP90, WP95*), defined before in this note. We perform the ML fit extracting simultanously the signal, backround yields together with their identification efficiency.

We validate the fit with toy Monte Carlo studies for a luminosity of 100 nb^{-1}. We get negligible biases on both the yields and the efficiencies. From toys we also estimate the statistical error on the signal identification efficiency to be 4.4%.

We show in Fig.36 the distribution of the W candidates in the barrel and endcaps obtained with this selection with the fit superimposed, showing the background contribution. We also run toy Monte Carlo studies for an equivalent luminosity of 78 nb^{-1} and we also get unbiased results of the efficiency and an uncertainty consistent to what we get from the fit to data.

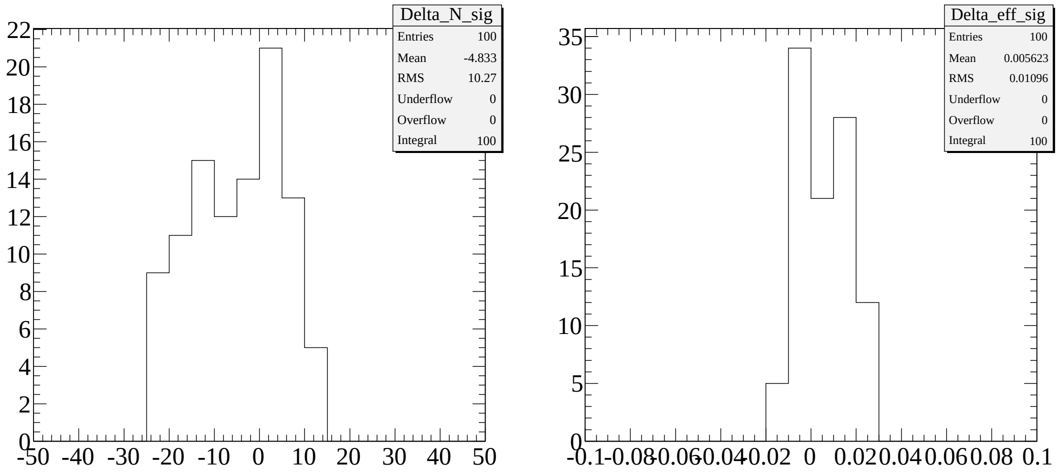

Figure 33: Distribution of the difference between the nominal fit and these fits for the signal yield (left) and for the reconstruction efficiency (right).

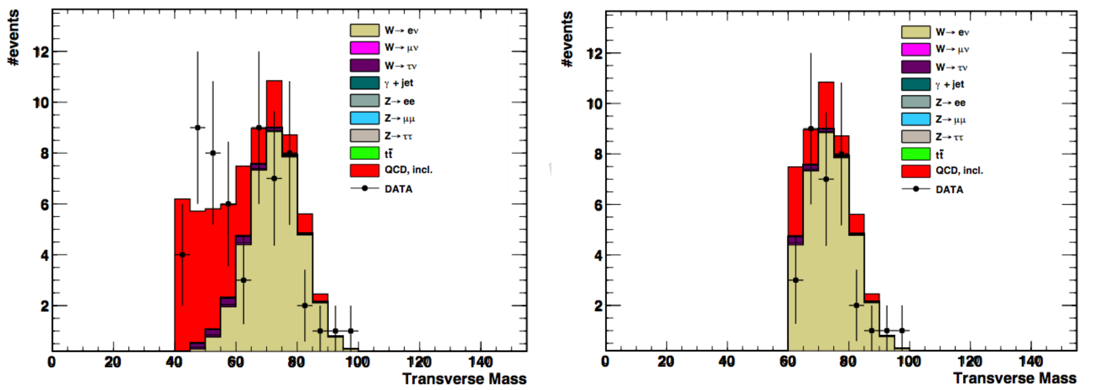

(a) (b)

Figure 34: Distribution of track-corrected missing energy

We estimate the efficiency of the whole electron selection, namely: identification plus isolation plus conversion rejection. We also report the efficiency on the Monte Carlo simulation of sample obtained with the same selection we applied to measure efficiency on data in Table 15.

For the measurement of W charge asymmetry is necessary to know the efficiencies of electrons and positrons separately, in particular at large η (in the endcaps). We provide them, even with large uncertainties, on Table 16, for the two used working points: WP80 and WP95.

Also in this case we do a cross check with a cut and count analysis requesting $M_T > 60$ GeV in addition to the previous cuts definig the fit sample. In this case we select 63 (33) candidates with electron in the EB (EE). Requesting the dientification we get:

- Working Point 70%: 48 (17) for an efficiency of 76% (52%) for EB (EE)
- Working Point 80%: 50 (20) for an efficiency of 79% (61%) for EB (EE)
- Working Point 80% “EE-relaxed”: 50 (29) for an efficiency of 79% (88%) for EB (EE)

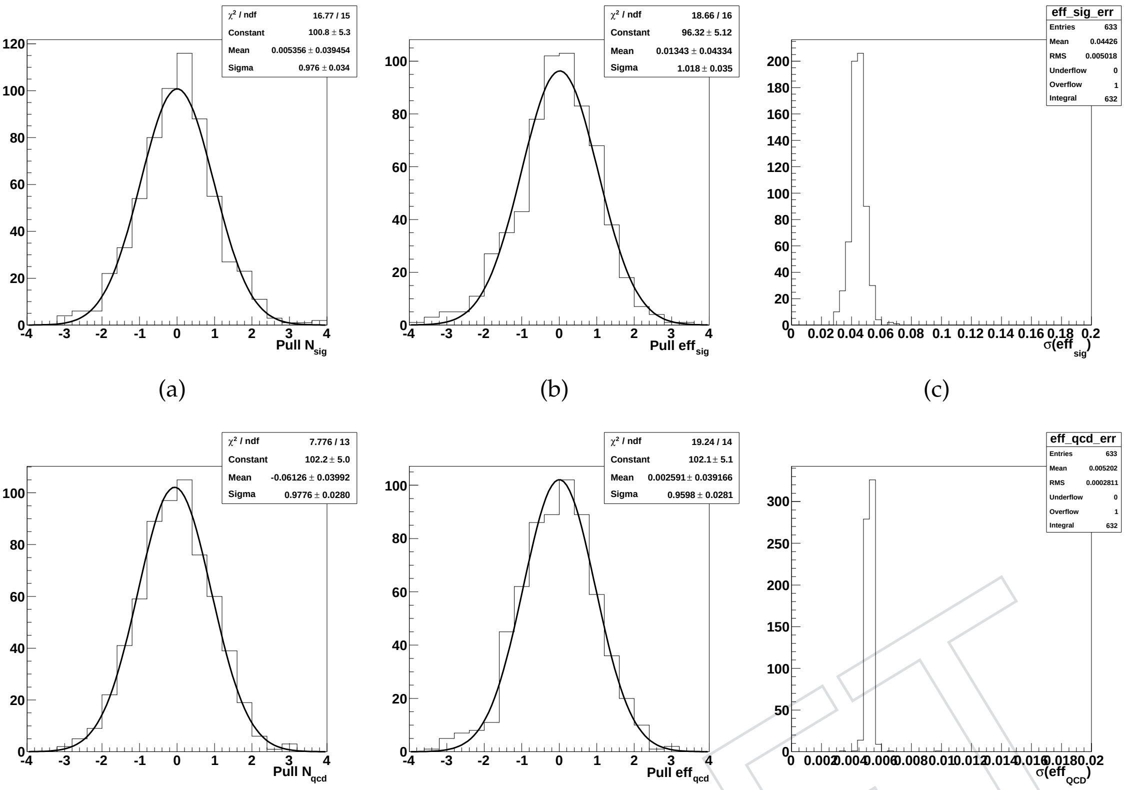

(a) (b) (c)

(d) (e) (f)

Figure 35: Distributions of the pull on the yield, the pull on the efficiency, the uncertainty on the efficiency for signal (a, b, c respectively) and for QCD background (d, e, f respectively) estimated from 1000 toy Monte Carlo experiments for an equivalent luminosity of 100 nb^{-1}.

- Working Point 95%: 53 (31) for an efficiency of 84% (94%) for EB (EE)

As we already described for the reconstruction efficiency, the shape of the QCD (floating in the nominal fit) is validated on a control sample obtained inverting the $\sigma_{i\eta i\eta}$ cut of the *WP80*. The shape is shown in Fig. 37 To show the consistency of this shape with the one obtained with the nominal selection we repeat the fits fixing the shape to the anti-electron samples. This is shown in Fig. 38. Both the signal yield and the identification efficiency do not change. We also estimate more quantitatively the dependency of the results on the background shape performing several fits to the data sample varying the background shape (and keeping it fixed) within the uncertainties. We get variations on the signal efficiencies with a RMS of 5% for EB and 6% for EE. These uncertainties, which would be systematics in the case the nominal fit were done in such a way, added in quadrature with the statistical error gives a larger error of the statistical error of the nominal fit with QCD floating. For this reason we keep this fit only as a sanity check of the results.

Also in this case we estimate the systematic uncertainties associated to the fixed M_T shape and absolute scale in the same way desribed for the reconstruction efficiency in Section 9.6.1. We get negligible uncertainties: $< 0.1\%$ for the barrel and 0.1% for the endcaps.

We show in Fig. 39 the projections of the fits over the sample passing or not-passing the electron identification (not considering isolation and conversion rejection).

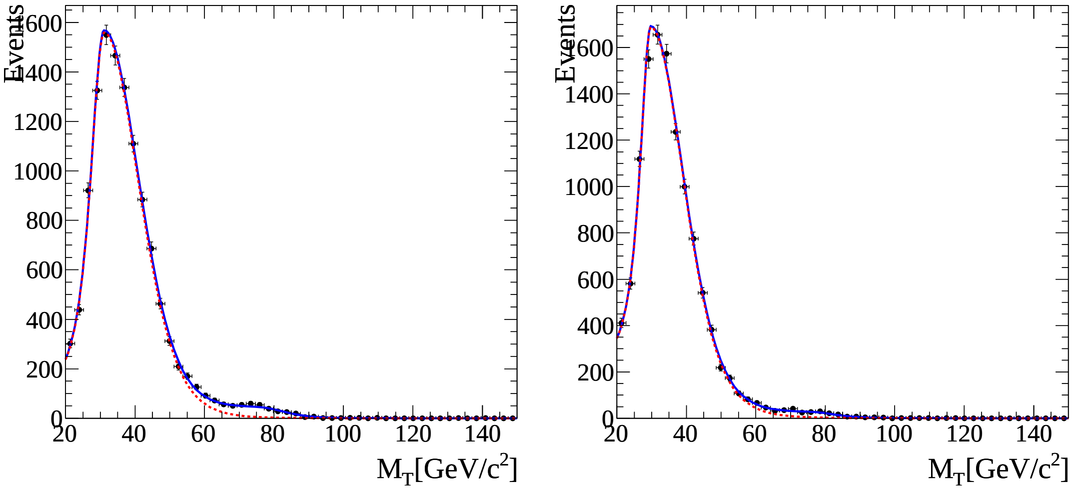

Figure 36: Distribution of M_T for $W \to e\nu$ candidates selected with *W candle selection* with the likelihood function superimposed for barrel (a) and endcap (b) electrons. Continuous curve represents the total likelihood, while the dashed line represents the background contribution. Fit is performed on 203 nb^{-1}.

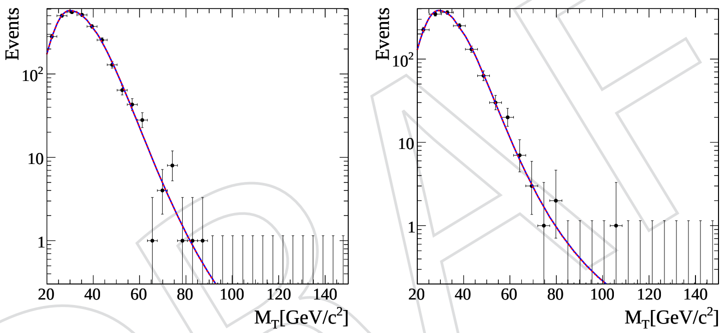

Figure 37: Distribution of M_T for $W \to e\nu$ candidates selected with anti-electron selection with the likelihood function superimposed for barrel (left) and endcap (right) electrons. No signal is assumed in this fit.

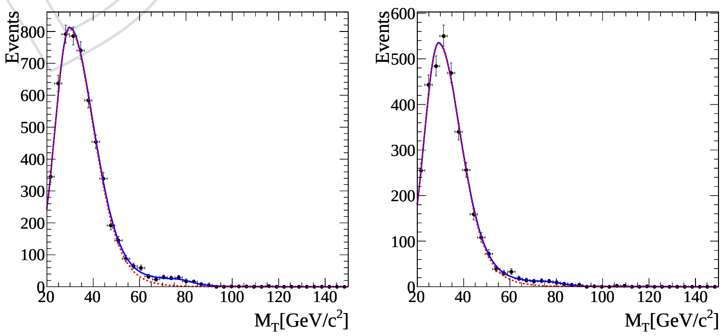

Figure 38: Distribution of M_T for $W \to e\nu$ candidates selected with anti-electron selection with the likelihood function superimposed for barrel (left) and endcap (right) electrons. No signal is assumed in this fit.

	$N_{W\to e\nu}$	$\epsilon_{W\to e\nu}$ (data)	$\epsilon_{W\to e\nu}$ (MC)	N_{QCD}	ϵ_{QCD}
Working Point 70%					
EB	622 ± 42	$0.689\,^{+0.043}_{-0.041}$ (stat) $\pm$ 0.01 (syst)	0.762	11245 ± 111	0.000 ± 0.001
EE	362 ± 35	$0.546\,^{+0.054}_{-0.049}$ (stat) $\pm$ 0.03 (syst)	0.567	11409 ± 110	0.002 ± 0.001
Working Point 80%					
EB	626 ± 42	$0.734\,^{+0.043}_{-0.042}$ (stat) $\pm$ 0.01 (syst)	0.830	11240 ± 111	0.005 ± 0.001
EE	360 ± 33	$0.653\,^{+0.057}_{-0.053}$ (stat) $\pm$ 0.03 (syst)	0.695	11411 ± 110	0.007 ± 0.001
Working Point 90%					
EB	595 ± 39	$0.882\,^{+0.045}_{-0.043}$ (stat) $\pm$ 0.01 (syst)	0.931	11271 ± 110	0.023 ± 0.002
EE	363 ± 33	$0.768\,^{+0.058}_{-0.054}$ (stat) $\pm$ 0.03 (syst)	0.837	11408 ± 110	0.039 ± 0.002
Working Point 95%					
EB	591 ± 39	$0.889\,^{+0.044}_{-0.043}$ (stat) $\pm$ 0.01 (syst)	0.943	11275 ± 110	0.039 ± 0.002
EE	364 ± 32	$0.821\,^{+0.058}_{-0.054}$ (stat) $\pm$ 0.03 (syst)	0.863	11407 ± 110	0.053 ± 0.002

Table 15: Fitted W→eν yield, electron identification, plus isolation plus conversion rejection efficiency in ECAL barrel and endcap as fitted on data (203nb^{-1}) for signal and QCD background. The MC expectations for a sample is also reported.

The fit to the missing transverse energy distribution in events passing the W→eν selection is performed to assign the event by event $_{s}Weight$. The signal weighted distributions in this way are shown in Figures 25, 26 and 27 for some variables used in the simple cut based electron identification.

The estimation of the combined electron identification and isolation can be done with separate fits to numerator and denominator samples, where the denominator is defined with reconstructed electrons with $p_T > 20$ GeV. In each of the fits, the templates for the W→eν signal and EWK backgrounds are constructed from Monte Carlo, and the template for the QCD background is extracted from data by inverting cuts on $\Delta\eta$ and $\Delta\phi$ in order to remove the signal. The electron ID efficiency is obtained as the ratio of the signal yields from the two fits. The shapes of the signal and background templates obtained from Monte Carlo and data respectively are the primary sources of systematic uncertainty for this method. The method has been validated with 5000 toy Monte Carlo experiments for an equivalent luminosity of 100 nb^{-1}. The spread in the extracted efficiency is shown in Figure 40. The RMS of the distribution is 7.2%, which provides a measure of the expected statistical uncertainty from the technique. Applying this technique to available 13.3 nb^{-1} of data we get a value of 0.88 ± 0.33.

9.7 Electron isolation efficiency: random cone studies

The efficiency of the electron isolation requirements has been studied on its own using the random cone technique. The details of this study are described in CMS AN-10-206; the results are summarized below.

In W MC, the electron isolation efficiency is compared with that of random cones drawn from the same events, and their ratio is computed for (successively applied) tracker, ECAL, and HCAL isolation cuts. In our collision data, the W selection is applied, with a transverse mass requirement $M_T > 60$ GeV applied to arrive at a 95% pure W sample. The efficiency of random cone isolation is then estimated from data, and corrected by this ratio. The systematic assigned to this procedure is the full difference of this ratio from unity, i.e. any MC inefficiency from leakage of energy from an electron into its isolation cone is counted as a systematic uncertainty. In all cases this error is dominated by ECAL leakage.

	$N_{W\to e\nu}$	$\epsilon_{W\to e\nu}$ (data)	N_{QCD}	ϵ_{QCD}
Working Point 80%				
EB e^+	368 ± 32	$0.7112\ ^{+0.0541}_{0.0000}$	5622 ± 79	0.0036 ± 0.0015
EB e^-	260 ± 26	$0.7573\ ^{+0.0671}_{-0.0629}$	5614 ± 77	0.0060 ± 0.0016
EE e^+	204 ± 25	$0.6798\ ^{+0.0794}_{-0.0710}$	5919 ± 79	0.0060 ± 0.0014
EE e^-	155 ± 21	$0.6220\ ^{+0.0857}_{-0.0753}$	5492 ± 76	0.0089 ± 0.0015
EE+ e^+	97 ± 16	$0.7755\ ^{+0.1131}_{-0.0986}$	2836 ± 54	0.0071 ± 0.0022
EE+ e^-	73 ± 14	$0.6155\ ^{+0.1254}_{-0.1046}$	2585 ± 52	0.0089 ± 0.0023
EE- e^+	110 ± 19	$0.5727\ ^{+0.1062}_{-0.0859}$	3078 ± 57	0.0049 ± 0.0017
EE- e^-	82 ± 16	$0.6186\ ^{+0.1228}_{-0.1005}$	2905 ± 55	0.0087 ± 0.0021
Working Point 95%				
EB e^+	363 ± 30	$0.8500\ ^{+0.0547}_{0.0000}$	5627 ± 78	0.0358 ± 0.0030
EB e^-	234 ± 26	$0.9287\ ^{+0.0000}_{-0.0719}$	5641 ± 78	0.0427 ± 0.0031
EE e^+	202 ± 24	$0.8562\ ^{+0.0823}_{-0.0754}$	5921 ± 79	0.0519 ± 0.0032
EEe-	160 ± 21	$0.7848\ ^{+0.0846}_{-0.0765}$	5487 ± 76	0.0535 ± 0.0033
EE+ e^+	96 ± 15	$0.9475\ ^{+0.0000}_{-0.0969}$	2836 ± 54	0.0513 ± 0.0046
EE+ e^-	75 ± 14	$0.8187\ ^{+0.1247}_{-0.1082}$	2584 ± 52	0.0596 ± 0.0050
EE- e^+	109 ± 19	$0.7446\ ^{+0.1164}_{-0.0964}$	3079 ± 57	0.0522 ± 0.0044
EE- e^-	86 ± 16	$0.7435\ ^{+0.1223}_{-0.1043}$	2901 ± 55	0.0480 ± 0.0043

Table 16: Fitted W$\to$e$^+\nu$ and W$\to$e$^-\nu$ yield, electron identification, plus isolation plus conversion rejection efficiency in ECAL barrel and endcap as fitted on data (203nb^{-1}) for signal and QCD background. The MC expectations for a sample is also reported.

For our electron selection, this translates into a total isolation efficiency of $96.5 \pm 1.2\%$ in EB and $95.3 \pm 2.2\%$ for EE. The corresponding data/MC ratios are $100.3 \pm 1.2\%$ and $101.1 \pm 2.2\%$, respectively.

10 Trigger Requirements for $W \to e\nu$ and $Z \to ee$

10.1 Level-1 electron trigger

The CMS Level-1 ECAL trigger decision is based on trigger candidates such as electrons/photons which use local energy deposits called trigger primitives as inputs. The trigger primitives each refer to a single trigger tower. They are computed by the front-end electronics as the summed transverse energy deposited in the tower, completed and then synchronized by the Trigger Concentrator Cards (TCC) before being sent to the Regional Calorimeter Trigger (RCT). The RCT implements the algorithm which combines pairs of trigger primitives into Level-1 trigger candidates. The algorithm is based on a 3×3 sliding window around the trigger primitive with maximum energy. At this point, the HCAL trigger primitives are combined. Isolated and non-isolated candidates are produced depending on the amount of energy deposited in the towers around the central one. The Global Calorimeter Trigger (GCT) is then responsible for sorting the candidates from all regions of interest according to their transverse energy. Only the four most energetic are sent to the global trigger (GT) which generates the final decision.

During the CMS 7 TeV collision data taking period, the Level-1 ECAL trigger was fully deployed and operational. ECAL trigger primitive were produced and sent to the RCT. Noisy or absent ECAL channels were masked to the level of 2.5% in the barrel and 5% in the endcaps. Only the simplest trigger object algorithms were enabled at the GT level and the lowest energy

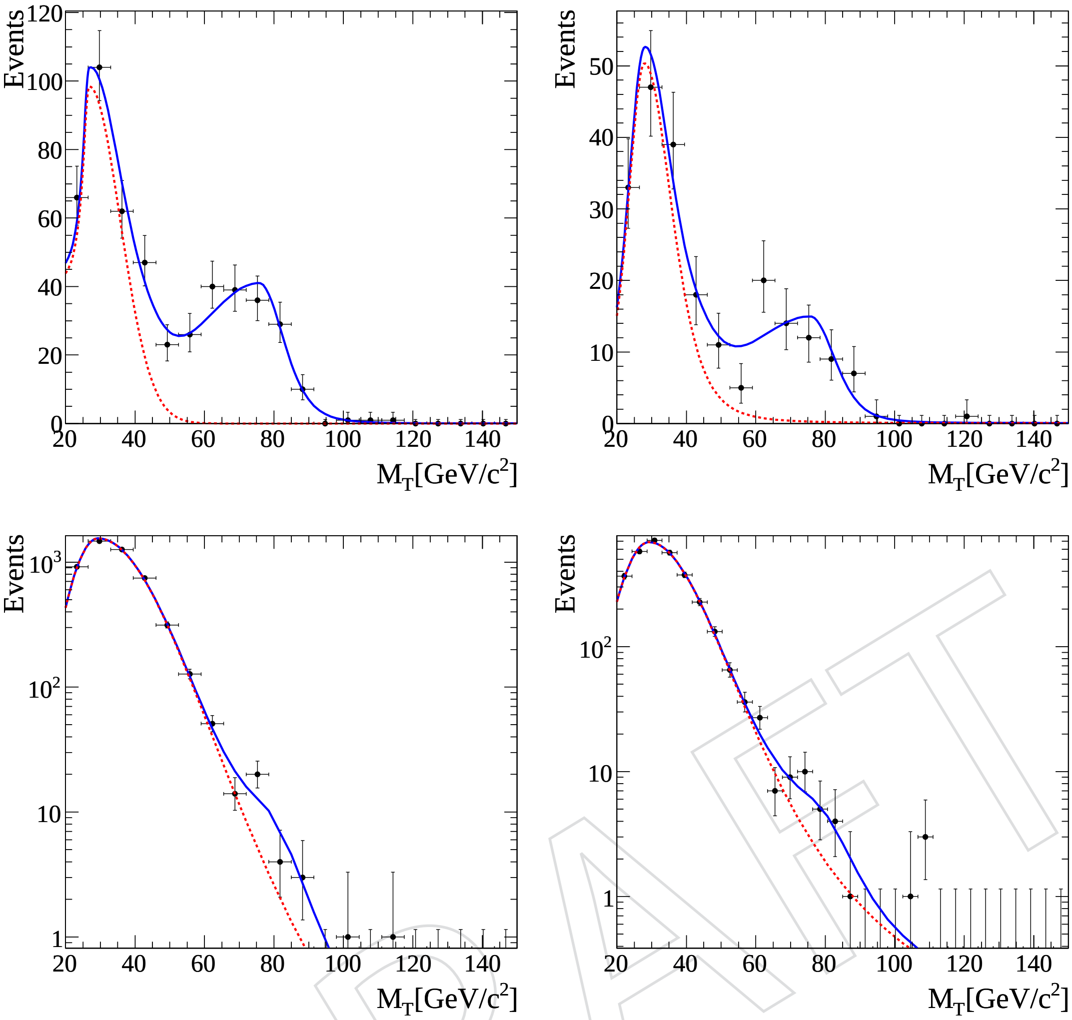

Figure 39: Projections of the fit to the M_T distribution obtained with a reconstructed electron and MET on the nominal sample for barrel (left) and endcap (right) for the identified candidates (top) and the ones not identified (bottom).

threshold allowed by the noise rate for calorimeter objects. The e/γ trigger requires a calorimeter deposit above a configurable cut: L1_SingleEG5 for a candidate with $E_T > 5$ GeV. The single e/γ trigger ran unprescaled for luminosities below 8×10^{28} and remained stable at 1 Hz in absence of collisions.

The performance of the barrel e/γ trigger was evaluated in terms of efficiency by selecting events collected with Ecal "activity" trigger described further. This dataset was unbiased with respect to the trigger understudy. Events containing at least one offline reconstructed electron have been retained for the analysis. It is required that electrons are identified and isolated choosing the WP80 requirements described in table 13. The electron superclusters were used as tags to probe for the production of L1 trigger candidates. Due to the requirement of an energy deposit on ECAL this measurement evaluated the trigger efficiency only in the active part of the detector and was relative to the detector efficiency to detect electromagnetic energy.

The L1 e/γ trigger is considered efficient if a L1 candidate with E_T above the threshold understudy, can be associated with the electron supercluster. The association procedure consists of

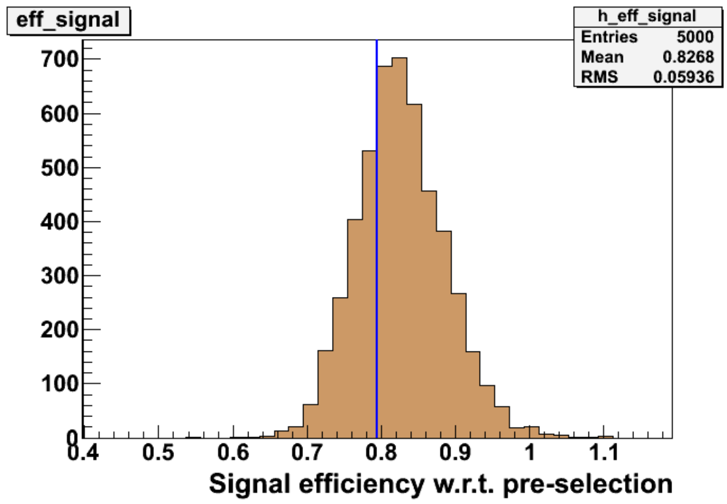

Figure 40: Distribution of the electron identification and isolation effciency from 5000 toy Monte Carlo experiments correspondent to a luminosity of 100 nb^{-1}. The solid line represents the generated value.

looking for a L1 candidate in the region of interest (RCT region) corresponding to the supercluster. This region is identified as the one in which the supercluster's highest energy crystal is located. Fig. 41 shows the trigger efficiencies for the L1Single_EG5 algorithms for the barrel and the endcaps.

An unbinned likelihood fit has been performed on the data point. From this results it can be derived a Level-1 electron trigger efficiency of $1.0^{+0.00}_{-0.01}$ % in the barrel and $0.99^{+0.00}_{-0.01}$ % in the endcaps.

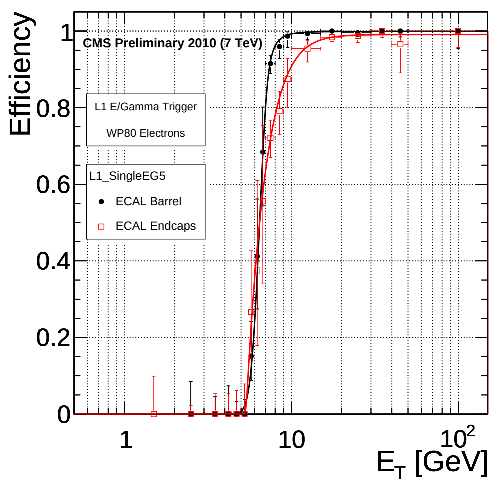

Figure 41: Level-1 trigger efficiency of the L1_SingleEG5 algorithm as a function of the electron's supercluster transverse energy for the barrel ($|\eta| < 1.48$, black dots) and the endcaps (red squares). An unbinned likelihood fit has been performed on the data points and is superimposed.

10.2 e/γ Selection in the High Level Trigger

Events containing a satifactory L1 electromagnetic seed were required to pass additional HLT criteria. ECAL energy deposits in the region defined by the L1 e/γ candidate are combined to form superclusters. The total transverse energy of the supercluster is then used to mark the event for offline storage. No additional requirements were placed on the candidate event.

The HLT selection makes no assumption on the candidate e/γ object beyond requiring a sufficient ECAL transverse energy deposit. For instantaneous luminosities below 10^{30} cm^{-2}sec^{-1} the rate of events that contain a supercluster with $E_T > 15$ GeV does not exceed 30 Hz. Consequently, information from additional detectors (e.g. HCAL and the Tracking detectors) are not necessary to maintain an acceptable trigger rate. This allows a simple, robust trigger to collect W/Z candidate events while the more complicated algorithms (that employ tracking, H/E requirments, etc.) can be studied offline for future use. It is worth noting that the HLT photon triggers were modified to remove ECAL "spikes" after run 138046. This protection was added to the photon triggers to maintain a manageable trigger rate and had no effect on the HLT efficiency results.

Events with an e/γ HLT object with at least 15 GeV of transverse energy were considered in this analysis. For data taking up to Run 138045 data was collected using the HLT_Photon10_L1R trigger path. The 10 GeV threshold on the trigger object was raised to 15 GeV during offline event selection. This trigger was used to select data for luminosities below 4×10^{29} cm^{-2}sec^{-1} as it is seeded by a 5 GeV e/γ L1 bit, L1_SingleEG5. This L1 seed reaches the efficiency plateau sooner than L1_SingleEG8 (shown in Figure 41). From Run 138046 onwards, data was collected using the HLT_Photon15_Cleaned_L1R trigger path, which requires a 15 GeV e/γ object and applies ECAL spike cleaning. The nominal L1 seed for this path (L1_SingleEG8) was lowered to L1_SingleEG5 for consistency with early running.

10.3 Trigger Efficiency and Monte Carlo Corrections

The trigger efficiency for W/Z events is determined relative to the full event selection described in Section 9. The estimation of this efficiency is accomplished using two independent methods. In the first case, the L1 efficiency is determined from an unbiased sample of collision events and the HLT efficiency is estimated using a dedicated sample of events that pass the relevant L1 trigger bit. The trigger efficiency is then determined by multiplying the individual L1 and HLT results. In the second case, the full L1+HLT efficiency is evaluated directly on an unbiased event sample. These two methods are expected to produce identical results within statistical precision.

An unbiased event sample is obtained during the low luminosity period using the technical triggers associated with the beam scintillation counters (BSCs). For higher luminosity running, these triggers were highly prescaled and contained very few e/γ candidate events. For this reason, dedicated ECAL "activity" triggers were employed to collect events with ECAL energy deposits. These activity triggers, seeded by the BSC L1 bits, searched all of ECAL for a supercluster of sufficient energy.

A sample of events passing L1_SingleEG5 was also collected throughout the data-taking period. The HLT efficiency was checked on this dedicated sample and combined with the L1 efficiency measurement to produce an L1+HLT efficiency correction to Monte Carlo events.

Sample HLT and L1+HLT efficiency turn-on curves for events satisfying the WP80 requirements listed in Section 9 appear in Figures 42 and 43. The HLT efficiency results (measured from a sample of events with L1_SingleEG5 set) were obtained from data collected after run 138046 (roughly 64 nb^{-1}) to correspond to the run range used to determine the L1 efficiency. The L1+HLT efficiency was computed from data collected between runs 132440 and 140174, although runs with HCAL problems were not included (the EGMonitor dataset was not reprocessed with the necessary improvements, which limits the luminosity to roughly 71 nb^{-1}). In both cases, the trigger performance is compared between data and W/Z Monte Carlo.

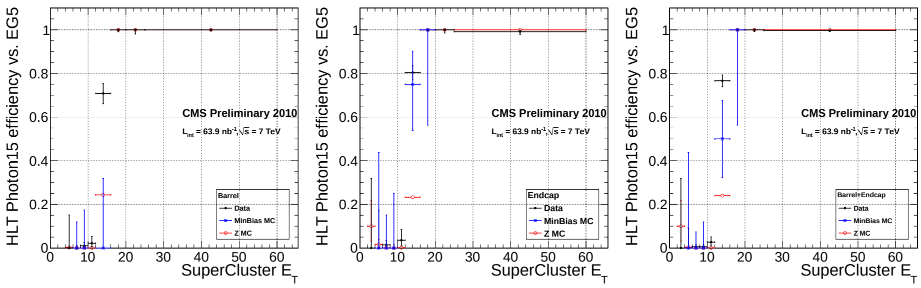

Figure 42: HLT_Photon15_Cleaned_L1R Turn-on curves for electron candidates found in the ECAL barrel (left), endcap (center), and EB+EE (right) for a sample of events that with L1_SingleEG5 set from Runs 138046-139459 (black), Summer10 $Z \to ee$ (red) and minimum bias (blue) Monte Carlo. The electron candidates are required to satisfy the WP80 requirements as defined in Table 13.

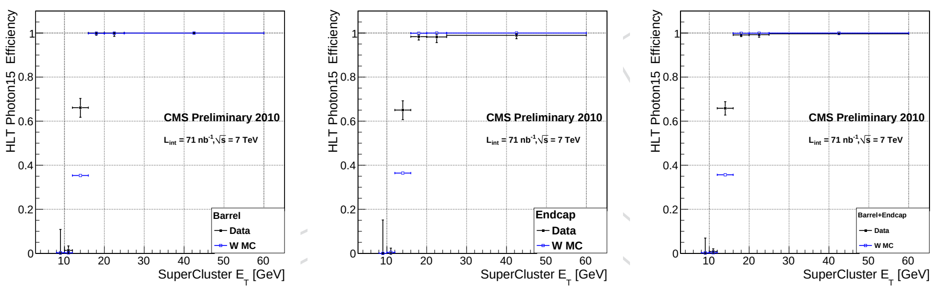

Figure 43: L1+HLT turn-on curves for electron candidates found in the ECAL barrel (left), endcap (center), and EB+EE (right) using events collected with the ECAL activity triggers from Runs 138046-140179 (black) and Summer10 $W \to e\nu$ MC (blue). The electron candidates are required to satisfy the WP80 requirements as defined in Table 13. Events were selected using HLT_Photon15_Cleaned_L1R.

We use the results of Figures 42 and 43 to correct the Monte Carlo based on the observed electron trigger efficiency in data. These results are summarized as a function of the electron supercluster E_T in Table 17. As the EGMonitor dataset was not reprocessed in the final days before ICHEP, the efficiency results were computed with 60-70 nb^{-1}. Results from the two independent methods are consistent within statistical precision.

11 Isolation and final efficiencies

11.1 Electron Trigger Efficiency

The L1 and HLT trigger efficiency for electron candidates satisfying the selection criteria given in Section 9 is calculated using two methods:

- The L1 trigger efficiency is first computed using a sample of unbiased events. The total efficiency is then determined following an HLT efficiency study using a sample of events that satisfy L1 trigger requirements.

Table 17: Data/MC correction factors c_ϵ for L1,HLT and L1+HLT electron trigger efficiency as a function of the transverse energy of the electron supercluster and detector region. The HLT object is required to satisfy $E_T > 15$ GeV. The uncertainties are dominated by the electron statistics in data. The individual HLT correction factors were obtained from a 64 nb^{-}1 subset of the collision data collected between runs 138046 and 139459. The individual L1 and combined L1+HLT corrections are computed using roughly 71 nb^{-1} available between runs 138046 and 140174.

	c_ϵ(L1)	c_ϵ(HLT|L1)	c_ϵ(L1) $\times$ c_ϵ(HLT|L1)	c_ϵ(L1+HLT)
EB, 20-25 GeV	$1.000^{+0.}_{-0.009}$	$1.000^{+0.}_{-0.019}$	$1.000^{+0.}_{-0.021}$	$1.000^{+0.}_{-0.015}$
EB, 25+ GeV	$1.000^{+0.}_{-0.004}$	$1.000^{+0.}_{-0.006}$	$1.000^{+0.}_{-0.007}$	$1.000^{+0.}_{-0.006}$
EE, 20-25 GeV	$0.962^{+0.018}_{-0.026}$	$1.000^{+0.}_{-0.015}$	$0.962^{+0.018}_{-0.030}$	$0.982^{+0.013}_{-0.026}$
EE, 25+ GeV	$0.986^{+0.008}_{-0.013}$	$0.991^{+0.006}_{-0.013}$	$0.977^{+0.010}_{-0.018}$	$0.990^{+0.008}_{-0.015}$
EB+EE, 20-25 GeV	$0.985^{+0.007}_{-0.010}$	$1.000^{+0.}_{-0.008}$	$0.985^{+0.007}_{-0.013}$	$0.992^{+0.006}_{-0.011}$
EB+EE, 25+ GeV	$0.995^{+0.003}_{-0.004}$	$0.997^{+0.002}_{-0.005}$	$0.992^{+0.004}_{-0.006}$	$0.996^{+0.003}_{-0.005}$

- The total L1+HLT trigger efficiency is computed using an unbiased event sample.

These methods will be shown below to yield consistent results.

11.1.1 Trigger Eras

The online selection of electrons evolved over the initial 7 TeV data-taking period. The performance of the L1+HLT trigger during this evolution can be grouped into XX distinct periods of stability. These trigger "eras" are summarized in Table 18 and Figure 44.

At the moment, all data collected is considered as a single trigger era. This assertion will be studied in greater detail.

Run Range	Integrated Luminosity (nb^{-1})	Description

Table 18: Distinct data taking eras marked by changes to the L1+HLT selection of electron candidate events.

.

Figure 44: Performance of L1_SingleEG5 as a function of Run number. Changes in performance mark the eras as defined in Table 18.

11.1.2 L1 Efficiency

11.1.3 HLT Efficiency for events passing L1_SingleEG5

The efficiency of HLT_Photon10_L1R and HLT_Photon15_L1R will be measured relative to a dedicated sample of events passing L1_SingleEG5. An unbiased sample of L1_SingleEG5 events are collected by the HLT using the HLT_L1SingleEG5 path. This trigger path automatically accepts events accepted by L1 with no additional selection. The rate of this path is controlled via a prescale factor.

This study is currently pending completion.

11.1.4 L1+HLT Efficiency using an unbiased input sample

The online selection efficiency of electron candidates can be estimated using an unbiased event sample. During low-luminosity running, nearly all collision events were recorded by requiring the BSC technical triggers to fire. These events were collected in the GOODCOLL skim, which was valid until Run 135735. After this run, minimum bias events were stored with reduced frequency in the MinimumBias dataset.

The efficiency of HLT_Photon10_L1R and HLT_Photon15_L1R measured for minimum bias events are shown in Figures 45 and 46. For each event that contains an electron that satisfies the WP80 requirements (see Section 9), the electron candidate is matched to the HLT photon object and the efficiency for the HLT path to accept the event is determined as a function of the electron supercluster E_T for electrons reconstructed in the ECAL barrel and endcap. Due to the small number of W/Z electrons currently available in the data, the efficiency measurement in data displays a significant statistical uncertainty.

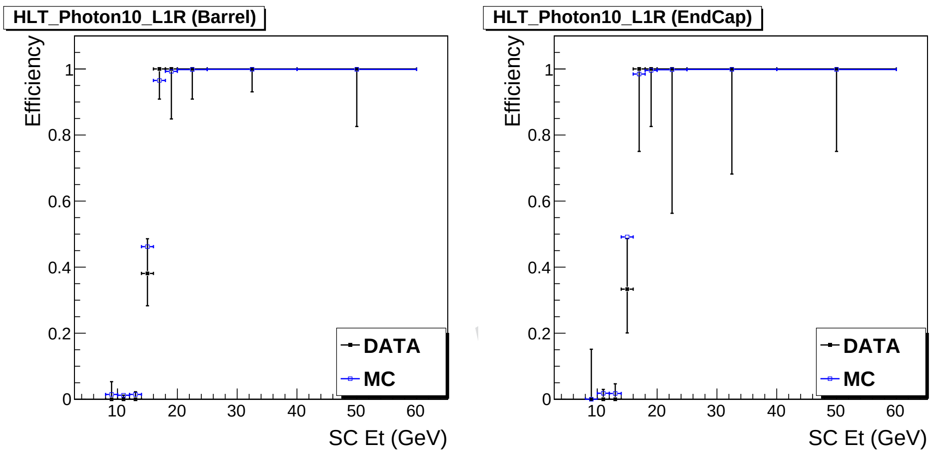

Figure 45: HLT_Photon10_L1R Turn-on curves for electron candidates found in the ECAL barrel (left) and endcap (right) using minimum bias events from Runs 132440-136259 (black) and Spring10 $W \rightarrow e\nu$ MC (blue). Events passing the HLT necessarily satisfy L1_SingleEG5 requirements. The electron candidates are also required to satisfy the WP80 requirements as defined in Table 13.

Figures 45 and 46 compare the trigger efficiency in data to the efficiency expected from W Monte Carlo (the Spring10 sample was used for this comparison). Beyond 20 GeV, the efficiency measured in data is consistent with Monte Carlo expectations. As we continue to accumulate data, it is possible that increased statistics will demonstrate some difference between data and Monte Carlo. For this reason we compute data-based corrections to the Monte Carlo.

The correction factors are computed using a toy Monte Carlo analysis. For a given E_T bin, Monte Carlo and data “distributions” are created using their (assymetric) uncertainties. On an event-by-event basis, the distribution for the data/MC correction is created by dividing data by Monte Carlo. The resulting data/MC distribution is then fit to an bifurcated Gaussian distribution to obtain the correction factor (and uncertainties). This procedure is repeated for each E_T bin for both ECAL barrel and endcap. Toy distributions for the 25-40 GeV bin for HLT_Photon15_L1R in EB are presented in Figure 47, and the data/MC correction factors are given in Table 19.

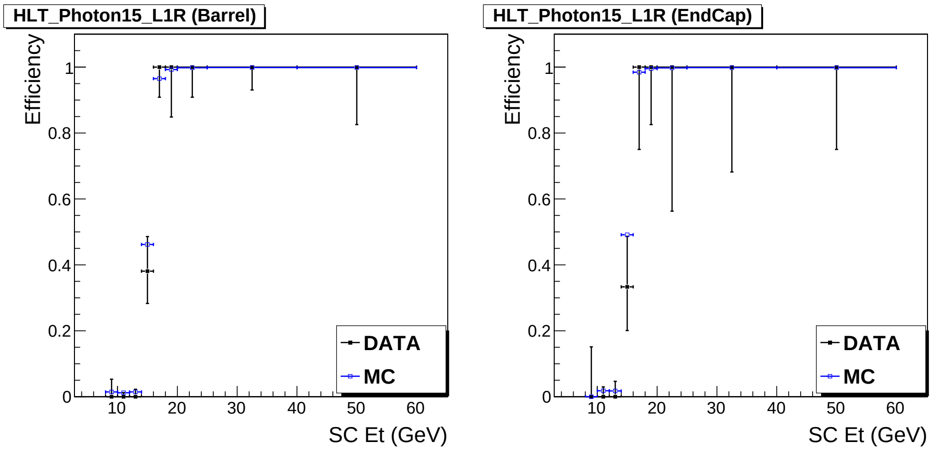

Figure 46: HLT_Photon15_L1R Turn-on curves for electron candidates found in the ECAL barrel (left) and endcap (right) using minimum bias events from Runs 132440-136259 (black) and Spring10 $W \to e\nu$ MC (blue). Events passing the HLT must necessarily meet the L1_SingleEG8 requirements. The electron candidates are also required to satisfy the WP80 requirements as defined in Table 13.

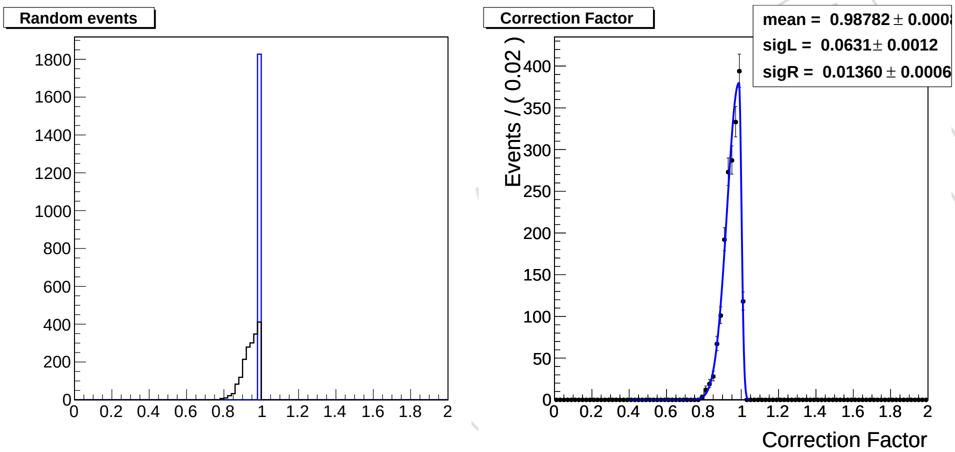

Figure 47: A toy Monte Carlo is used to compute the data/MC correction factors for the HLT_Photon15_L1R efficiency in the ECAL barrel for $25 < E_T < 40$ GeV. (Left) Toy distributions of data (black) and W Monte Carlo (blue), taking the efficiencies and uncertainties as input paramaters for a bifurcated Gaussian distribution. Event-by-event, the data and Monte Carlo distributions are divided to yield the distribution for the correction factor (right). The distribution is fit to a bifurcated Gaussian and the central value and $\pm\sigma$ are used as the correction factor and uncertainty.

11.1.5 Electron L1+HLT efficiency for ICHEP Dataset

In this section, the correction factors determined using the two different methods will be compared. At present only one method is available.

Table 19: Data/MC correction factors for HLT_Photon15_L1R

	20-25 GeV	25-40 GeV	40-60 GeV
Barrel	$0.99^{+0.01}_{-0.09}$	$0.99^{+0.01}_{-0.06}$	$0.99^{+0.01}_{-0.17}$
Endcap	$0.94^{+0.04}_{-0.41}$	$0.99^{+0.01}_{-0.31}$	$1.01^{+0.00}_{-0.26}$

12 $W \to e\nu$ Signal Extraction

The substantial $\not\!\!E_{\mathrm{T}}$ and M_T produced in $W \to e\nu$ events are a natural means of discriminating this signal from background. We perform parametrized fits to these distributions in the electron channel to extract W yields. Alternative methods provide cross-checks on our primary signal yield estimates (Appendix G). Our signal extraction techniques share several sources of systematic uncertainty, which we review in Section 12.3.

We apply a base selection of $\mathrm{E}_{\mathrm{T}}^{\mathrm{SC}} > 20$ GeV, conversion rejection and WP80 electron ID/isolation (Table 13) in each of the methods we describe. Events containing additional, fiducial electrons with $\mathrm{E}_{\mathrm{T}}^{\mathrm{SC}} > 20$ GeV and passing WP95 ID are vetoed. The 78 nb^{-1} sample contains a total of 688 events after full selection, 377 of which include a leading e^+ and 311 a leading e^-, as determined from the charge of the associated GSF tracks. We utilize both $\not\!\!E_{\mathrm{T}}^{PF}$ and $\not\!\!E_{\mathrm{T}}^{TC}$; however, in the interest of space, plots shown in this section are for $\not\!\!E_{\mathrm{T}}^{\mathrm{PF}}$ and $\mathrm{M}_{\mathrm{T}}^{\mathrm{PF}}$ only. Equivalent plots for $\not\!\!E_{\mathrm{T}}^{TC}$ and M_T^{TC} are included in Appendix H.

12.1 Parametrized Fits

A flexible fitting approach models signal and background distributions with parametrized functions. We first attempt fits to the $\not\!\!E_{\mathrm{T}}$ and M_T distributions of the inclusive W sample using fully parametrized forms for both signal and background. The $\not\!\!E_{\mathrm{T}}$ shape of QCD background is described by a modified Rayleigh distribution, where a linear term is added to the denominator of the exponent.[4] We model the signal $\not\!\!E_{\mathrm{T}}$ distribution as a sum of two Gaussians with a common mean :

$$f_{bkg}(x = \not\!\!E_{\mathrm{T}}) = N_{bkg} \cdot x e^{-\frac{x^2}{2\sigma^2(x)}}, \tag{18}$$

$$\sigma(x) = a + bx \tag{19}$$

$$f_{sig}(x = \not\!\!E_{\mathrm{T}}) = N_{sig} \cdot (e^{-\frac{(x-\mu)^2}{2\sigma_1^2}} + e^{-\frac{(x-\mu)^2}{2\sigma_2^2}}) \tag{20}$$

Figure 48 shows the combined $\not\!\!E_{\mathrm{T}}$ model superimposed on the $\not\!\!E_{\mathrm{T}}$ distribution of a large Monte Carlo sample.

We model the M_T shape of QCD background with a "Cruijff" function, where in the equation below $\sigma = \sigma_L(\sigma_R)$ and $\alpha = \alpha_L(\alpha_R)$ for $M_T < m(M_T > m)$. The parameter m refers to the means (m_b, m_{s1} or m_{s2}) of the respective distributions. The signal distribution is described as a combination of two Cruijff functions sharing the same σ_R and α_R parameters :

[4] The Rayleigh distribution describes the magnitude of a vector with Gaussian distributed, uncorrelated components of equal variance. The $\not\!\!E_{\mathrm{T}}^{X}$ and $\not\!\!E_{\mathrm{T}}^{Y}$ distributions of QCD background satisfy these criteria, modulo small ΣE_T-dependent resolution effects.

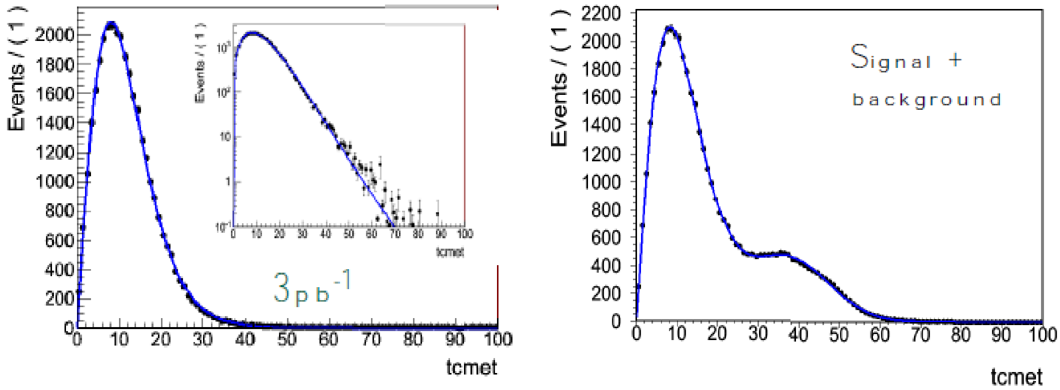

Figure 48: Fully Parametrized $\not\!\!E_{\mathrm{T}}$ Models. The fully parametrized model of signal and background $\not\!\!E_{\mathrm{T}}$ is a good description of the distribution in large-sample pseudo-data.

$$f_{bkg}(x = M_T) \;=\; N_{bkg} \cdot e^{-\frac{(x-m_b)^2}{2\sigma_b^2+\alpha_b(x-m_b)^2}} \tag{21}$$

$$f_{sig}(x = M_T) \;=\; N_{sig} \cdot e^{-\frac{(x-m_{s1})^2}{2\sigma_{s1}^2+\alpha_{s1}(x-m_{s1})^2}} \cdot e^{-\frac{(x-m_{s2})^2}{2\sigma_{s2}^2+\alpha_{s2}(x-m_{s2})^2}} \tag{22}$$

We fix σ_L and α_L to values determined from Monte Carlo and float σ_R, α_R and the means.

The fully parametrized models are good representations of signal and background in large-sample Monte Carlo, however their complexity introduces too much freedom for fits to perform reliably in 0.1 pb^{-1}. Figure 49, for example, shows a 0.1 pb^{-1} signal yield pull distribution from $\not\!\!E_{\mathrm{T}}$-fit pseudo-experiments that is non-Gaussian and asymmetric.

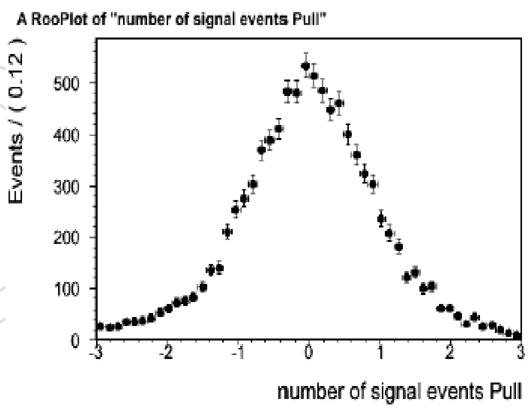

Figure 49: Fully Parametrized $\not\!\!E_{\mathrm{T}}$ Model Pulls. The fully parametrized models are not sufficiently constrained to provide good fit performance in small samples.

In contrast with the $\not\!\!E_{\mathrm{T}}/M_T$ produced by QCD background, that in $W \to \ell\nu$ events results from underlying physics that should be well modeled by the Monte Carlo. With this in mind, we develop "hybrid" models that use the parametrized background shapes described above together with fixed-shape signal templates derived from Monte Carlo. We study these models by generating pseudo-experiments in which we Poisson fluctuate model predictions. We then perform unbinned extended maximum likelihood (EML) fits to the generated $\not\!\!E_{\mathrm{T}}/M_T$ distributions with RooFit.

Hybrid fit results for single 0.1 pb^{-1} pseudo-experiments are shown in Figure 50 [**The 0.1 pb-1 toy MC results for the MT fit were made using the older SC ET $>$ 25 GeV cut. The yield increases to around 400 when moving to 20 GeV and we are re-running toy MC for this selection. All data results are with the new $>$ 20 GeV cut**]. Signal yields and uncertainties from the ensemble of pseudo-experiments are presented in Figures 51 and 52. These plots respectively indicate relative statistical uncertainties of 5.7% and XXX%, on average. Pseudo-experiments performed with $\not\!\!E_T^{TC}$ and M_T^{TC} give 6.0% and XXX%. The mean estimated 0.1 pb^{-1} signal yields are 451.4 ($\not\!\!E_T$ fit) and XXX (M_T fit). Corresponding values from the TC fits are 451.5 and XXX. Both of the pull distributions in Figure 53 have means near zero and widths close to unity, demonstrating that the corresponding fits are essentially unbiased and properly account for the statistical uncertainties on the yields.

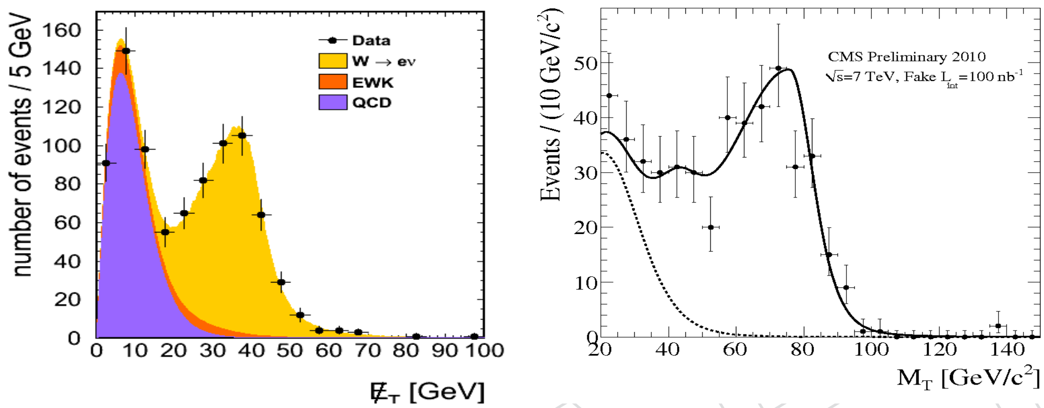

Figure 50: Example Hybrid Model Fits. We perform unbinned EML fits of the hybrid $\not\!\!E_T$ (left) and M_T (right) models to 0.1 pb^{-1} pseudo-data.

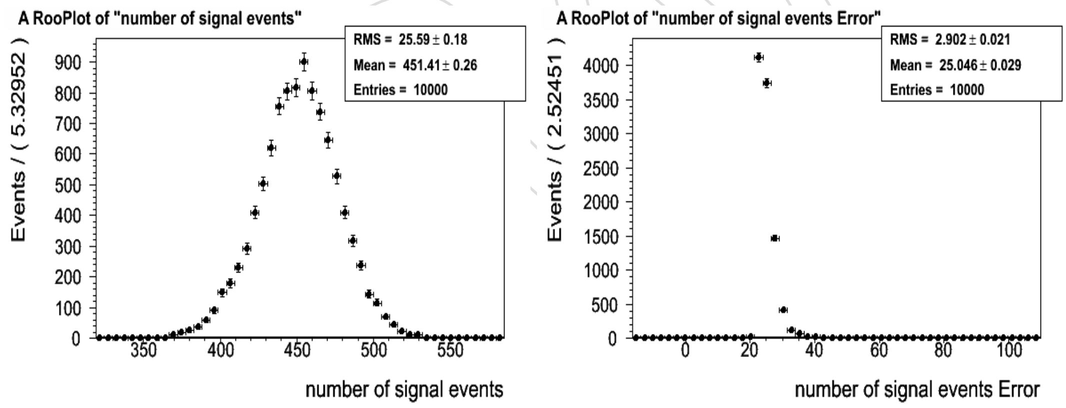

Figure 51: Yields (left) and Uncertainties (right) for the Hybrid $\not\!\!E_T$ Model. The statistical uncertainty on signal yield from the hybrid $\not\!\!E_T$ model is 5.7%, which is 1% larger than $1/\sqrt{N}$.

Figure 54-left presents results from the hybrid $\not\!\!E_T$ fit performed in 78 nb^{-1}. To improve fit performance in this < 0.1 pb^{-1} sample, we fix parameter b in Eqn. 19 to the value determined from a large-sample Monte Carlo study, 0.15. The parameter a is allowed to float. The fit returns $a = 7.64 \pm 0.32$, which is close to the Monte Carlo determined value of $a = 6.91 \pm 0.33$. We find a full acceptance W yield of 300.8 $\pm$ 18.7 (stat) (TC: 305.2 $\pm$ 19.6 (stat)) and a KS probability 63% (TC: 61%).[5] The KS scores indicate that our model describes the data well. We use the fit yield, a POWHEG acceptance and Monte Carlo efficiencies to obtain a rough

[5] We use ROOT's *KolmogorovTest* method with the 'X' option to determine goodness of fit. The p-value returned

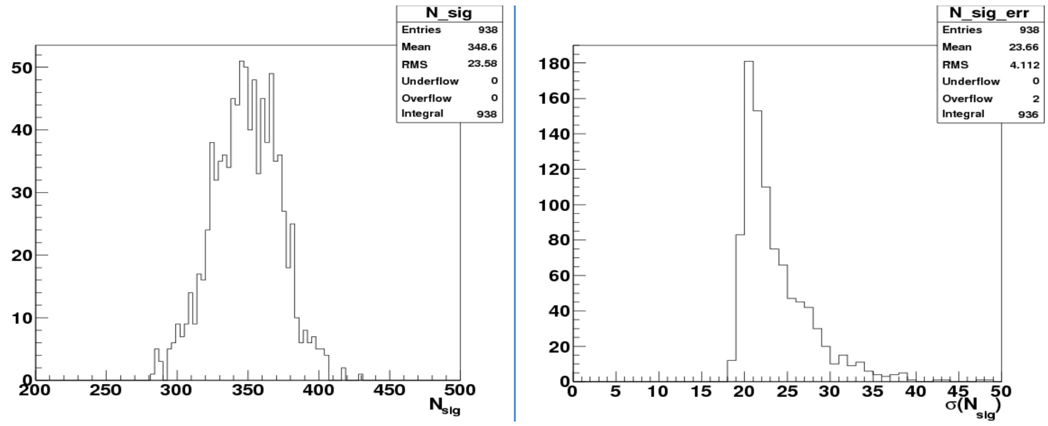

Figure 52: Yields (left) and Uncertainties (right) for the Hybrid M_T Model. The statistical uncertainty on signal yield from the hybrid M_T model is 6.8%, which is slightly larger than $1/\sqrt{N}$.

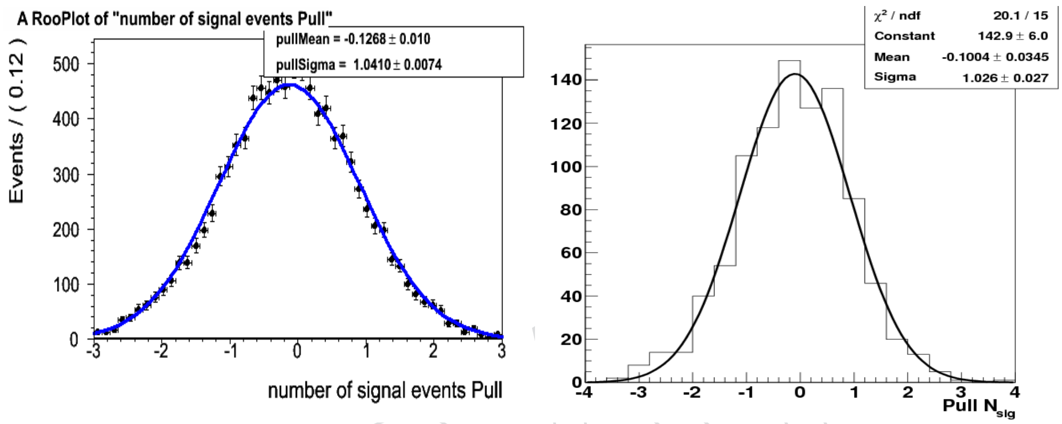

Figure 53: Hybrid $\not{E}_{\mathrm{T}}$ Model (left) and M_T Model (right) Signal Pulls. The hybrid models show low bias in 0.1 pb^{-1} pseudo-experiments. The widths of the pull distributions indicate that statistical uncertainty on the yield is properly modeled.

estimate of the $W \rightarrow e\nu$ cross section times branching ratio. Our result, $\sigma(W) \times BR(e\nu) =$ 8.7 nb $\pm$ 0.5 nb (stat) (TC: 8.9 nb $\pm$ 0.6 nb (stat)), reasonably agrees with the NLO prediction of 10.3 nb.

Figure 54-right shows results of the hybrid $\not{E}_{\mathrm{T}}$ fit when both the a and b parameters in Eqn. 19 are allowed to float. The fit determines $a = 10.7 \pm 1.9$, $b = -0.02 \pm 0.11$ and an inclusive W yield of 312.9 ± 18.9(stat). The difference between the best-fit model parameters found in this case and those expected from cut-inversion studies ($a = 6.85 - 8.92$ and $b = 0.14 - 0.20$) is presently consistent with a statistical fluctuation. The relative difference in yield with respect to that found when b is fixed is 4.0% and is covered by the statistical uncertainties of both measurements. The corresponding fit for $\not{E}_{\mathrm{T}}^{TC}$ returns $a = 8.24 \pm 1.38$ and $b = 0.12 \pm 0.08$, consistent with expectation ($a = 7.83 - 9.37$ and $b = 0.13 - 0.16$). We find a W yield of 310.4 ± 21.9(stat) and a relative difference in yield with respect to that obtained with parameter b fixed of 1.7%. We perform KS tests for each of the fully-floating fits and find acceptable p-values: 84% for $\not{E}_{\mathrm{T}}^{PF}$ and 62% for $\not{E}_{\mathrm{T}}^{TC}$.

Figure 55 shows results from the hybrid M_T fit performed in 37.7 nb^{-1}. The σ_L and α_L param-

from this test is an empirical probability based on pseudo-experiments. This approach avoids the bias that occurs in the usual KS test when model parameters are determined from the same data the model is tested against.

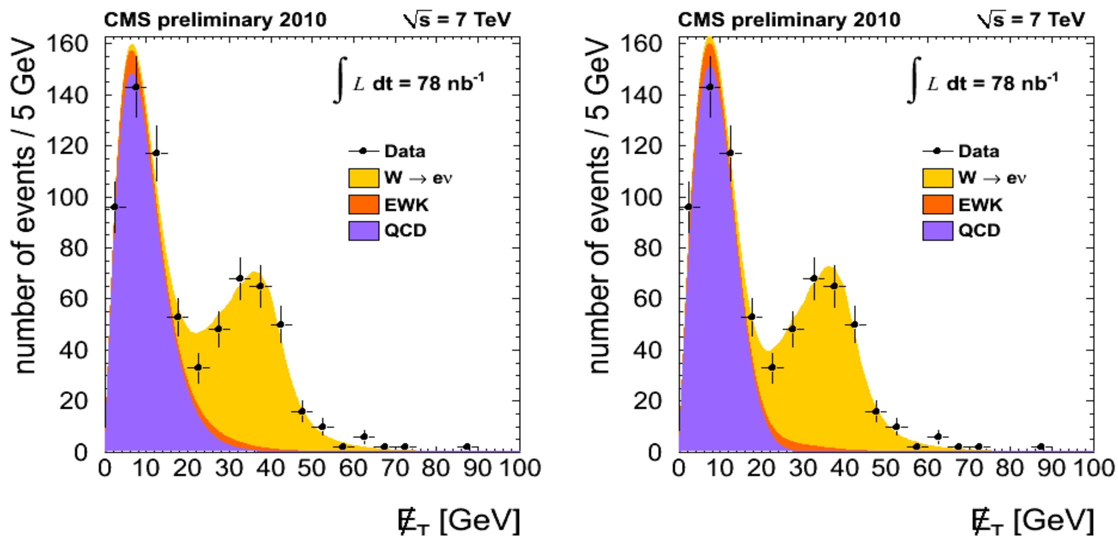

Figure 54: Hybrid $\not{E}_T$ Fit for 78 nb^{-1}. We fit the hybrid $\not{E}_T$ model to 78 nb^{-1} with parameter b fixed to its expected value (left) and with parameters a and b floating (right). The fit results are consistent within present statistical uncertainties.

eters are fixed to values determined from Monte Carlo, as described earlier in this section. We improve fit performance in 37.7 nb^{-1} by additionally fixing m_b to the Monte Carlo determined value of 29. The full acceptance W yield is 111.9 $\pm$ 11.7 (stat) and we determine a χ^2/dof of **[GOF value]** and p-value of **[p value]**.

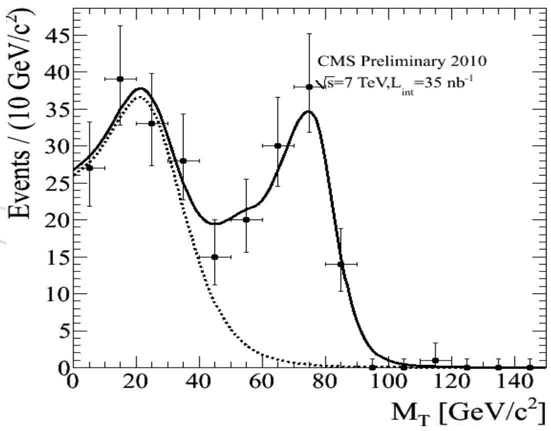

Figure 55: Hybrid M_T Fit for 37.7nb^{-1}. We apply the hybrid M_T model to 37.7 nb^{-1} and find good performance from the fit.

Systematic uncertainty on our model predictions follows from uncertainties on the shapes of the signal and background $\not{E}_T$ and M_T distributions. We discuss methods for estimating these uncertainties in Section 12.3.

12.2 W^+ and W^-

We use the models described in Section 12.1 to additionally fit for individual W^+ and W^- yields. Signal templates are again derived from Monte Carlo, however we can not freely float separate background shape parameters due to the small size of the W^+ and W^- samples. Instead, we perform a simultaneous fit to both samples of events using background $\not{E}_T$ (M_T) models that share a common a (XXX) parameter. The values of b (m_b) are again fixed to 0.15

(29). Figure 56 shows results of the simultaneous fit performed with $\not\!\!E_{\rm T}$ in 78 nb^{-1}. The extracted W^+ (W^-) yields are 163.4 $\pm$ 14.1(stat) (141.4 $\pm$ 13.1(stat)). Corresponding yields for the $\not\!\!E_{\rm T}^{TC}$ fit are 159.8 $\pm$ 13.6(stat) and 140.5 $\pm$ 12.7(stat).

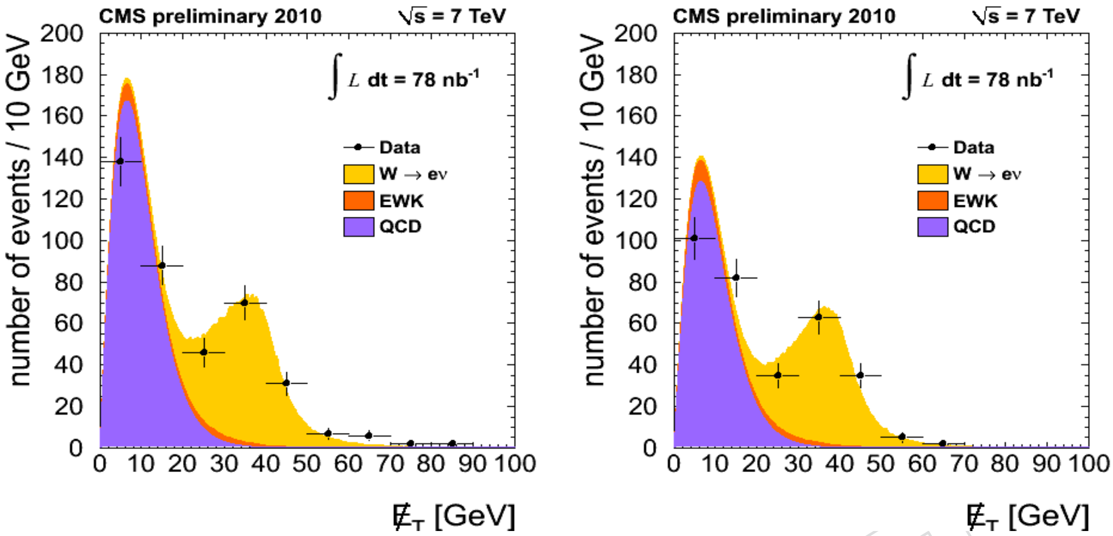

Figure 56: Hybrid $\not\!\!E_{\rm T}$ Fit for W^+/W^- in 78 nb^{-1}. We perform a simultaneous $\not\!\!E_{\rm T}$ fit for W^+ (left) and W^- (right) yields in 78 nb^{-1}. We find $N_{W^+}/N_{W^-} = 1.16 \pm 0.14$.

The ratio of W^+ to W^- events determined from the yields is 1.15 $\pm$ 0.14(stat) (TC: 1.14 $\pm$ 0.14(stat)), where we account for statistical correlations between the W^+ and W^- yields in the quoted uncertainties. We calculate these uncertainties using the error matrices returned from the fits. The full error matrix for the $\not\!\!E_{\rm T}^{PF}$ fit is :

$$\begin{pmatrix} \delta_{b-}^2 & \delta_{b+}\delta_{b-} & \delta_{s-}\delta_{b-} & \delta_{s+}\delta_{b-} & \delta_a\delta_{b-} \\ \delta_{b-}\delta_{b+} & \delta_{b+}^2 & \delta_{s-}\delta_{b+} & \delta_{s+}\delta_{b+} & \delta_a\delta_{b+} \\ \delta_{b-}\delta_{s-} & \delta_{b+}\delta_{s-} & \delta_{s-}^2 & \delta_{s+}\delta_{s-} & \delta_a\delta_{s-} \\ \delta_{b-}\delta_{s+} & \delta_{b+}\delta_{s+} & \delta_{s-}\delta_{s+} & \delta_{s+}^2 & \delta_a\delta_{s+} \\ \delta_{b-}\delta_a & \delta_{b+}\delta_a & \delta_{s-}\delta_a & \delta_{s+}\delta_a & \delta_a^2 \end{pmatrix} = \begin{pmatrix} 217.5 & 12.6 & -49.2 & -10.9 & 1.2 \\ 12.6 & 267.9 & -10.7 & -53.6 & 1.4 \\ -49.2 & -10.7 & 170.4 & 7.1 & -1.0 \\ -10.9 & -53.6 & 7.1 & 198 & -1.2 \\ 1.2 & 1.4 & -1.1 & -1.2 & 0.1 \end{pmatrix}$$

and the equivalent matrix for the $\not\!\!E_{\rm T}^{TC}$ fit is :

$$\begin{pmatrix} 206.8 & 6.1 & -38.7 & -5.2 & 0.7 \\ 6.1 & 258.9 & -5.0 & -41.9 & 0.9 \\ -38.7 & -5.0 & 160.3 & 2.1 & -0.6 \\ -5.2 & -41.9 & 2.1 & 184.2 & -0.8 \\ 0.7 & 0.9 & -0.6 & -0.8 & 0.1 \end{pmatrix}$$

We perform a second set of simultaneous fits to extract the W^+/W^- ratio and the overall W yield explicitly. We find a ratio of 1.16 ± 0.14(stat) (TC: 1.14 ± 0.14(stat)) and a yield of 289.6 ± 18.3(stat) (TC: 293.6 ± 19.2(stat)). These results agree with our previous measurements.

Figure 57 shows the results of simultaneous fits performed with M_T. Here the extracted W^+ (W^-) yield is 65.3 $\pm$ 8.9(stat) (46.8 $\pm$ 7.4(stat)).

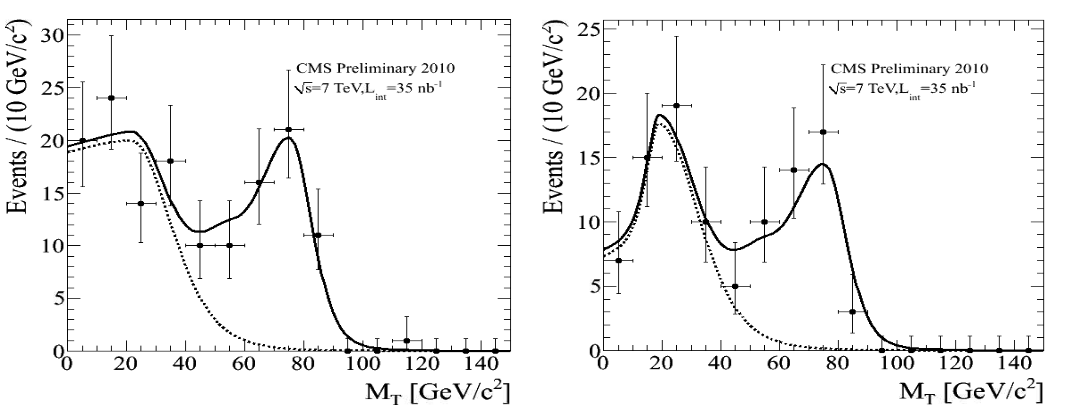

Figure 57: Hybrid M_T Fit for 37.7nb^{-1}. We perform a simultaneous $_T$ fit for W^+ (left) and W^- (right) yields in 37.7 nb^{-1}. We find $N_{W^+}/N_{W^-} = 1.33 \pm 0.24$.

Again, systematic uncertainty on our yield predictions follows from uncertainties on the shapes of the signal and background $\not\!\!E_{\rm T}$ and M_T distributions. We discuss methods for estimating these uncertainties in the following section.

12.3 Systematic Uncertainties

The precision and accuracy of our extracted W yields translate directly to those of the measured cross section. We estimate systematic uncertainties on yield predictions with data to the extent possible. In cases where 0.1 pb^{-1} datasets lack sufficient events for a completely "data-driven" approach to succeed, we bound our uncertainties using Monte Carlo estimates.

12.3.1 QCD $\not\!\!E_{\rm T}/M_T$ Shape

The flexibility provided by the hybrid $\not\!\!E_{\rm T}$ and M_T models should result in a small systematic uncertainty on the extracted signal yield due to background shape modeling. We assess this uncertainty using background control regions generated by cut inversion.

The simplest approach is to assume that our models are sufficient descriptions of the distributions of background after full selection and to test this assumption using an anti-selected $\not\!\!E_{\rm T}$ and M_T distribution. Monte Carlo studies suggest that the $\not\!\!E_{\rm T}$ and M_T distributions generated by reversing the WP80 $\Delta\eta$ and $\Delta\phi$ selections (maintaining the Iso$_{\rm ecal}$ cut) are close approximations of the background distributions obtained when the full set of $W \rightarrow e\nu$ selection criteria are applied. These anti-selections generate the distributions shown in Figure 58 for the 78 nb^{-1} dataset [**the MT plot is for 0.1 pb-1 MC**]. We perform fits of the hybrid models to these distribution and find best-fit values for the $\not\!\!E_{\rm T}$ background model parameters of $a = 7.32 \pm 0.58$ and $b = 0.16 \pm 0.03$. Best-fit values for the M_T fit are XXX. KS probabilities for the $\not\!\!E_{\rm T}$ (84%) and M_T (XXX) fits indicate good agreement. Our test is successful and, with this approach, we would assign zero uncertainty on signal yield due to background shape modeling.

We use anti-selected distributions with somewhat weaker assumptions in a second estimate of background modeling uncertainty. We identify two sets of anti-selections that generate $\not\!\!E_{\rm T}$ shapes that bound the distribution of background after all selection criteria are applied. Figure 59-left shows the $\not\!\!E_{\rm T}$ shapes obtained in Monte Carlo when inverting the $\Delta\eta$ selection (maintaining $\Delta\phi$) and when inverting both the $\Delta\eta + \Delta\phi$ selections (maintaining isolation and the other ID cuts). These shapes enclose the Monte Carlo distribution of QCD events following full event selection.

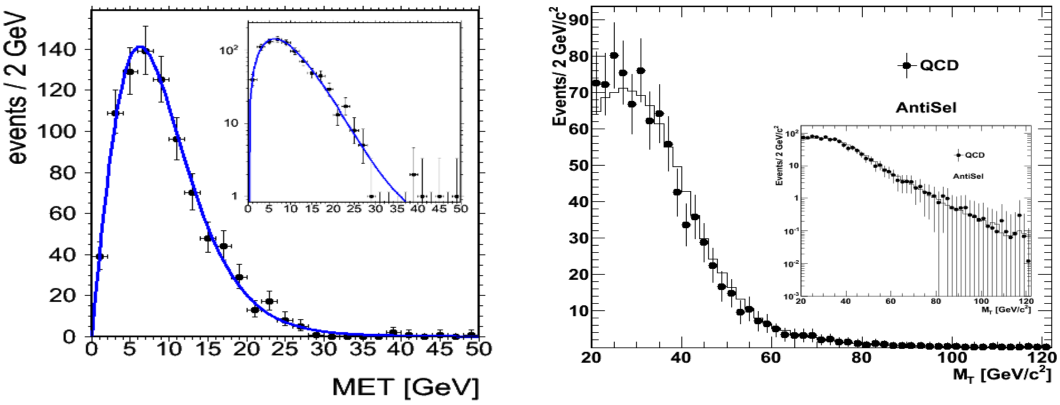

Figure 58: $\not\!\!E_T$ Fits to Anti-selected Distributions. We fit the hybrid $\not\!\!E_T$ and M_T models to background distributions obtained by reversing various WP80 selections. The high quality of the fits suggests that our models are an adequate description of background after full selection. [**the MT plot is for 0.1 pb-1 MC**].

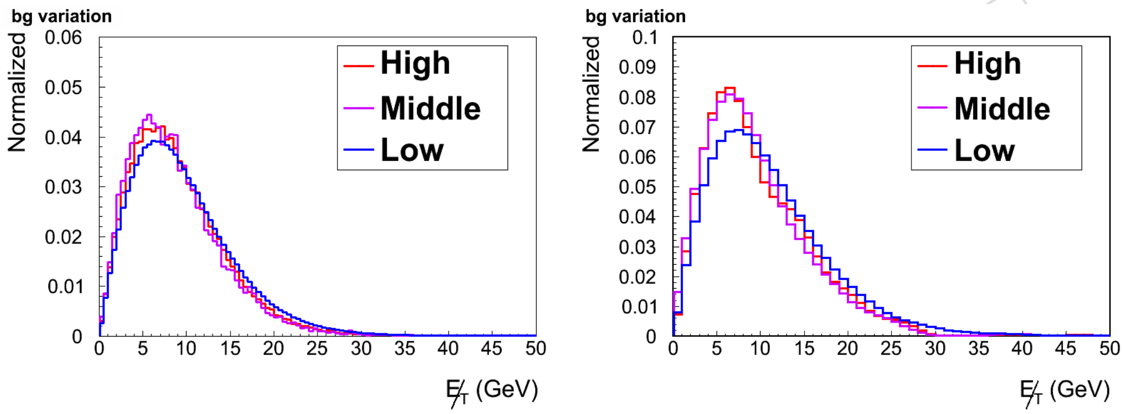

Figure 59: QCD $\not\!\!E_T$ Shapes from Cut Inversion. Left: We obtain a set of anti-selected background shapes in from MC that we expect to cover the true distribution of QCD background after event selection. Right: The same anti-selections in data generate similar shapes and are assumed to enclose the true distribution of background after full selection.

Figure 59-right shows that corresponding anti-selections in data generate shapes similar to those of Monte Carlo. We can therefore reasonably assume that the anti-selected shapes from data enclose the true background distribution after full selection, as they do in Monte Carlo. Bin-to-bin variations between the shapes are a bound on our background shape uncertainty.

Uncertainty in background shape must be propagated to our signal yield estimates. We achieve this by generating toy Monte Carlo in which the uncertainty bounds are taken as background shape PDFs. We perform pseudo-experiments with the anti-selected background shapes, the nominal signal template and signal/background normalizations from the original fit to data. We then fit the pseudo-data with the hybrid $\not\!\!E_T$ model to determine new yields. The largest difference between these yields and the original estimate from data is taken as the uncertainty associated with background shape modeling. Figure 60 shows the distribution of signal yields obtained from the procedure. We find a 1% (TC: 0.6%) relative difference in signal yield and quote this value as the uncertainty on our inclusive result due to background shape modeling. Equivalent uncertainties on the W^+ and W^- yields and their ratio are 0.4% (TC :0.3%), 0.9% (TC: 0.5%) and 0.4% (TC :0.2%), respectively.

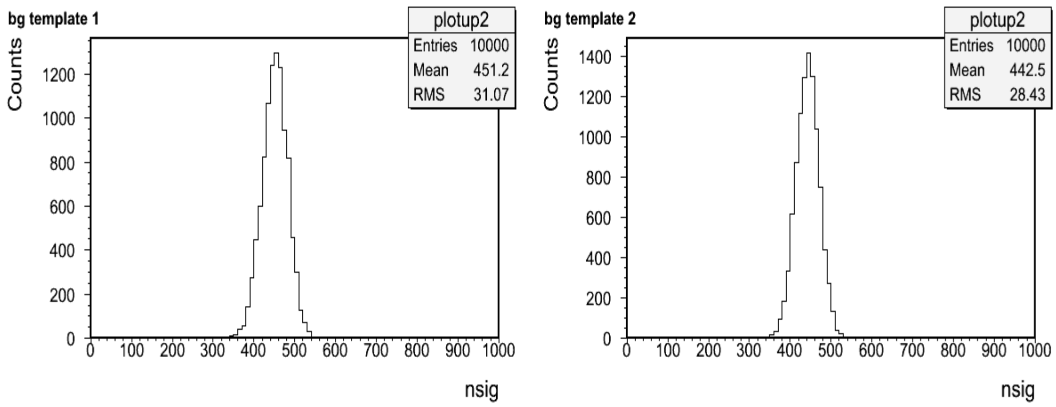

Figure 60: $\not\!\!E_{\mathrm{T}}$-Fit Signal Yields from Bounding QCD Shapes. We generate pseudo-experiments using the anti-selected background shapes of Figure 58 and fit with our nominal $\not\!\!E_{\mathrm{T}}$ model. We find a 1% difference in signal yield.

12.3.2 Signal $\not\!\!E_{\mathrm{T}}/M_T$ Shape

Our signal extraction techniques employ W $\not\!\!E_{\mathrm{T}}$ and M_T shapes derived from Monte Carlo simulation. Uncertainty in these shapes relates to how accurately our simulation represents both detector performance and the underlying physics of $W \rightarrow \ell\nu$ events. Simulated W $\not\!\!E_{\mathrm{T}}$ is usually improved by calibration with $Z \rightarrow \ell\ell$ data. This is typically performed using the so-called "recoil" technique, with uncertainties on calibrated $\not\!\!E_{\mathrm{T}}$ predictions determined as part of the procedure. The Z-driven recoil method is not feasible for the 0.1 pb^{-1} analysis. We alternatively consider two variations on the technique that allow signal shape uncertainties to be estimated from available data.

The first approach estimates recoil response and resolution uncertainties using $\gamma+$jet events [44]. The photon is subtracted from the $\not\!\!E_{\mathrm{T}}$ vector (the jet is not directly used) and the resulting recoil vector, $\vec{u}$, is projected on directions parallel and perpendicular to the photon. The mean (*i.e.:* response) and variance (*i.e.:* resolution) of the recoil components are compared in data and Monte Carlo as a function of photon p_T. Currently, recoil response (resolution) is found to be consistent in $\gamma+$jet data and Monte Carlo to within an uncertainty of 10% (20%).

We use these uncertainties in W Monte Carlo to assess uncertainty in signal $\not\!\!E_{\mathrm{T}}$ and M_T shape. We define the W recoil vector as $\vec{u} = \vec{\not\!\!E}_{\mathrm{T}} - \vec{E}^e_T$ and project components parallel ($u^W_{\parallel}$) and perpendicular ($u^W_{\perp}$) to the direction of the W boson. These components are modeled in Monte Carlo as Gaussian distributions, with means and widths that vary as functions of p^W_T. We fluctuate the Gaussian means and widths by the uncertainties quoted above and for each W Monte Carlo event, we sample these distributions as a function of p^W_T and recalculate a $\not\!\!E_{\mathrm{T}}$ vector. The extreme W $\not\!\!E_{\mathrm{T}}$ shapes that result from this procedure are shown in Figure 61.

Next, we propagate $\not\!\!E_{\mathrm{T}}$ shape uncertainty to the extracted signal yield following an approach analogous to that of Section 12.3.1. We use the W shape extrema in the generation of toy Monte Carlo, where background shape, background normalization and signal normalization are taken from the original fit to data. We fit the resulting pseudo-data using our nominal signal+background models and extract new yields. The relative difference in the resulting yields is the signal shape uncertainty on our result.

Figure 62 shows the distributions of signal yield obtained by this procedure. The two extreme $\not\!\!E_{\mathrm{T}}$ shapes shown in Figure 61 are used in the generation of separate toy Monte Carlos. The background shape, background normalization and signal normalization used for both sets of

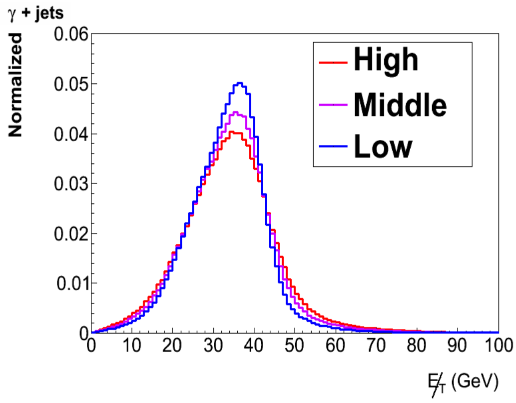

Figure 61: Signal Shape Uncertainty from $\gamma+$jet Recoil. Uncertainty on recoil response and resolution is determined using $\gamma+$jet events. This uncertainty translates to a range of possible signal $\not\!\!E_{\mathrm{T}}$ shapes.

pseudo-experiments are currently derived from 0.1 pb^{-1} pseudo-data. We find a difference in yield of 3.2% relative to the original 0.1 pb^{-1} yield estimate (Figure 51). The same procedure performed with $\not\!\!E_{\mathrm{T}}^{TC}$ leads to a relative uncertainty of 2.8%

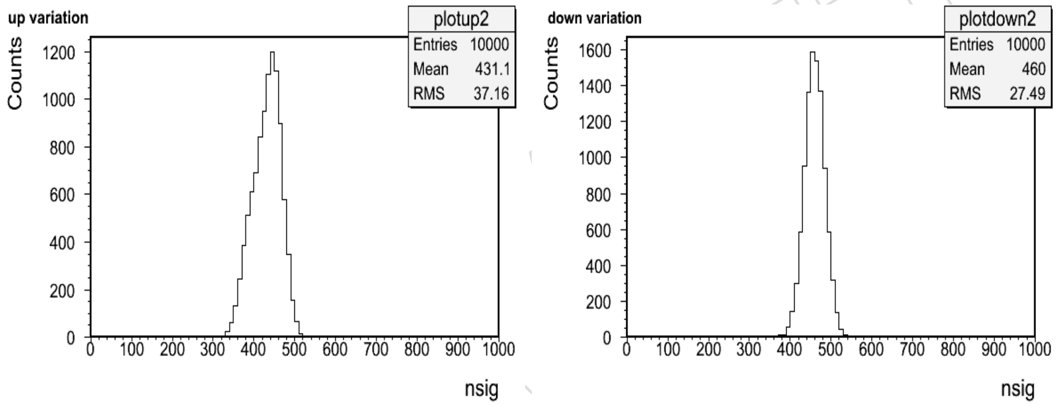

Figure 62: Signal Yields from $\gamma+$jet Recoil Uncertainties. We generate pseudo-experiments using the extreme signal shapes of Figure 61 and fit with our nominal $\not\!\!E_{\mathrm{T}}$ model. We find a 3.2% difference in yield relative to the original estimate.

We develop a second technique that extracts recoil resolution and response information directly from high $\not\!\!E_{\mathrm{T}}$ W data [29]. In this method, components of recoil parallel ($u_{\parallel}^{\ell}$) and perpendicular ($u_{\perp}^{\ell}$) to the direction of the leading lepton are again modeled as Gaussian distributions, with means and widths that vary as functions of p_T^W. Resolutions measured in Minimum Bias data constrain the functions that describe the evolution of the Gaussian widths with p_T^W. We assume that Monte Carlo models the p_T^W spectrum accurately and convolve it with the parametrized recoil functions to generate PDFs for the inclusive $u_{\parallel}^{\ell}$ and $u_{\perp}^{\ell}$ distributions :

$$f(u_i;p_T^W) = Gaus(\mu(p_T^W),\sigma(p_T^W)) \otimes f(p_T^W) \quad (23)$$
$$\mu(p_T^W) = K_i p_T^W + C_i \quad (24)$$
$$\sigma(p_T^W) = \sigma_{mb}(1+B_i p_T^W) \quad (25)$$

Best-fit parameters for the recoil model are determined by fitting the PDFs to the measured recoil distributions in a pure sample of W events, which is obtained with a $\not{E}_T > 30$ GeV selection in data. As in the $\gamma +$jet approach, we return to the W Monte Carlo and recalculate $\not{E}_T$ as a function of p_T^W with the recoil model parameters. Uncertainties on these parameters result in a spread of predictions that represent uncertainty in the W $\not{E}_T$ shape. Figure 63 shows the extreme $\not{E}_T$ shapes we find with recoil model parameters taken from fits to the 78 nb^{-1} dataset.

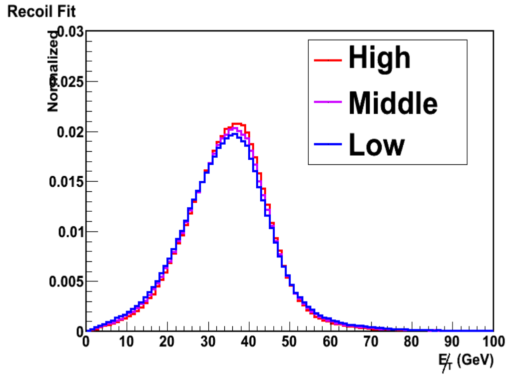

Figure 63: Signal Shape Uncertainty from W Recoil. We fit W recoil distributions in data to generate a range of $\not{E}_T$ shapes that represent uncertainty in the signal $\not{E}_T$ model.

We propagate these shape uncertainties to our signal yield estimate using toy Monte Carlo, as before. Figure 64 shows the signal yields determined from fits to pseudo-data generated with the extreme $\not{E}_T$ shapes of Figure 63. We find a difference in yield of 1.9% relative to the original estimate in 0.1 pb^{-1} pseudo-data. The same procedure performed with $\not{E}_T^{TC}$ leads to a relative uncertainty of 2.2%. Uncertainties on the W^+ and W^- yields and their ratio are 2.4%, 3.0% and 0.7% (TC: 1.3%, 1.4% and 0.2%), respectively.

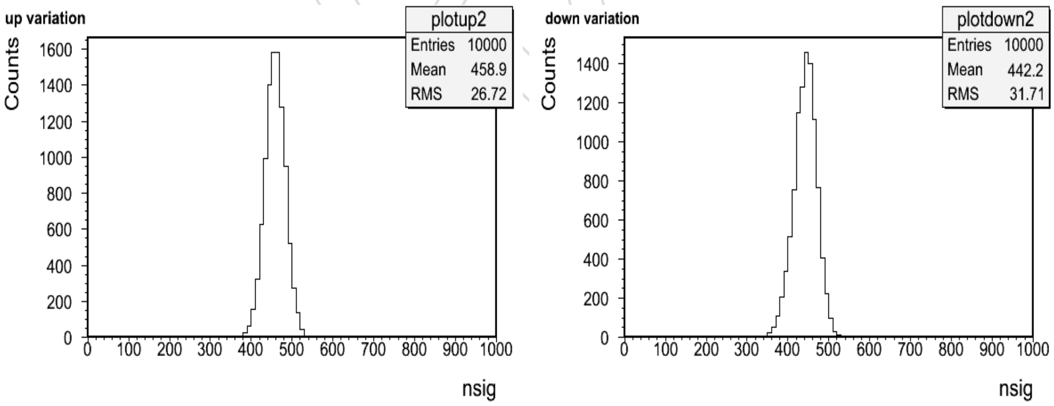

Figure 64: Signal Yields from W Recoil Uncertainties. We generate pseudo-experiments using the extreme signal shapes of Figure 63 and fit with our nominal $\not{E}_T$ model. We find a 1.9% difference in yield relative to the original estimate.

12.3.3 Electron Scale and Resolution

Electron energy scale is shown in a later section to be consistent in data and Monte Carlo within uncertainties of 1% (barrel) and 3% (endcap). We propagate these uncertainties to our signal yield estimates using a method similar to that of Section 12.3.2. For each Monte Carlo signal event, we increase/decrease the reconstructed electron E_T by the appropriate scale uncertainty and recalculate $\not{E}_T$ using the new electron E_T values. Figure 65 shows the shape extrema produced from this procedure. We observe a spread in $\not{E}_T$ shape comparable to that from the uncertainty on recoil response and resolution.

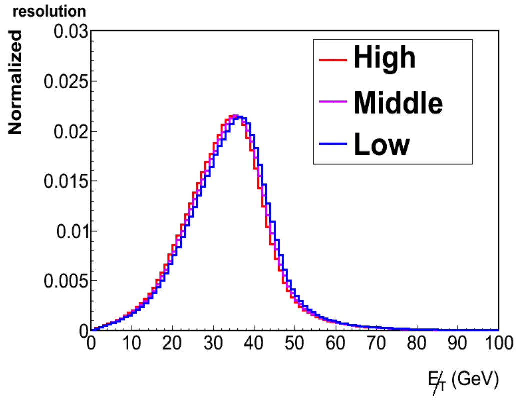

Figure 65: Signal Shape Uncertainty from Electron Scale/Resolution. We determine the variation in signal $\not{E}_T$ shape that results from shifting reconstructed electron E_T by its scale uncertainty.

Figure 66 shows the distribution of signal yields we obtain from toy Monte Carlo generated with the shape extrema of Figure 65. We find a 2.1% relative difference in the mean extracted signal yield (TC : 2.5%), which we take as the systematic uncertainty from electron scale/resolution effects. The corresponding uncertainties on W^+ and W^- yields and their ratio are, 2.0%, 2.4% and 0.5% (TC: 1.4%, 1.6% and 0.1%).

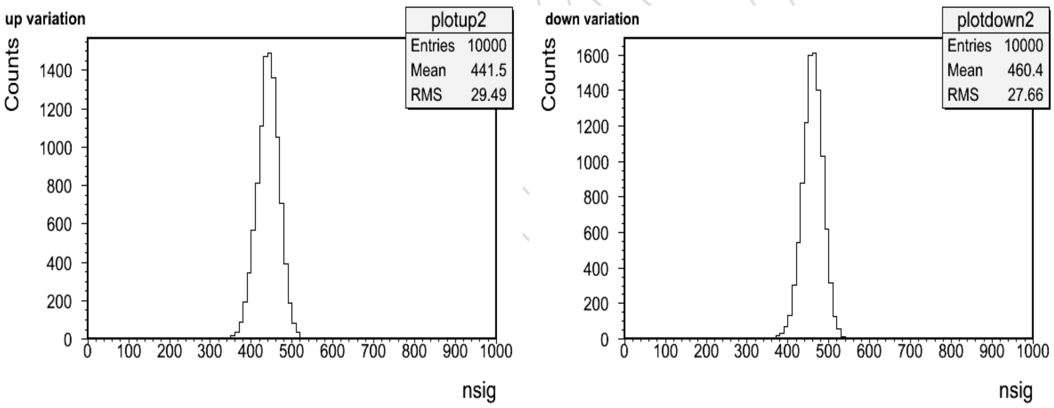

Figure 66: Signal Yields from Electron Scale/Resolution Uncertainties. We generate pseudo-experiments using the extreme signal shapes of Figure 65 and fit with our nominal $\not{E}_T$ model. We find a 2.1% relative difference in the mean inclusive W yield.

12.3.4 Efficiency Corrections

The uncertainties on barrel and endcap electron efficiency corrections differ. This difference leads to the spread in the inclusive W $\not{E}_T$ shape shown in Figure 67. We propagate these shape differences to signal yield using our usual toy Monte Carlo approach. We obtain the yield distributions shown in Figure 69 and find a relative difference in the mean of 0.3% (TC : 0.9%). The associated uncertainties on W^+ and W^- yields and their ratio are 0.2%, 0.2% and $< 0.0\%$ (TC: 0.8%, 1.2% and 0.4%).

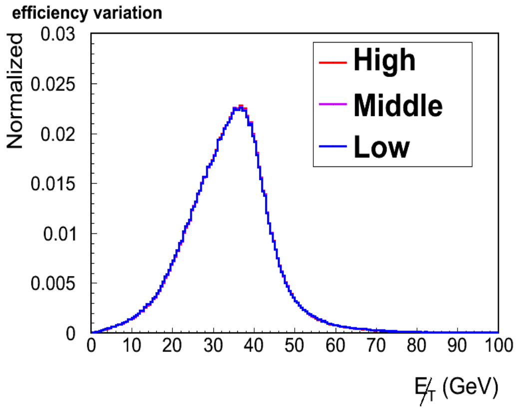

Figure 67: Signal Shape Uncertainty from Efficiency Corrections. We determine the maximal variation in signal $\not\!\!E_T$ shape that results from shifting barrel and endcap electron efficiency corrections by their uncertainties.

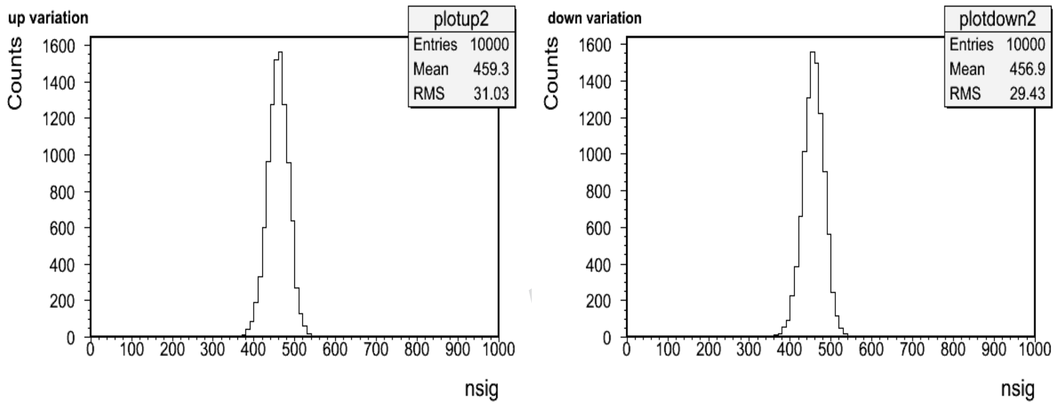

Figure 68: Signal Yields from Electron Scale/Resolution Uncertainties. We generate pseudo-experiments using the extreme signal shapes of Figure 67 and fit with our nominal $\not\!\!E_T$ model. We find a 0.3% relative difference in the mean inclusive W yield.

12.3.5 Electroweak Backgrounds

Each of our signal extraction techniques assume fixed, relative normalizations for EWK backgrounds. These normalizations are taken from the ratio of the respective NLO cross sections to that of the W. PDFs are the dominant source of uncertainty on the Z/W cross section ratio, leading to a 2.5% uncertainty on the normalization. We fluctuate the relative normalization of Z to W in the signal template by this amount and assess the impact on the signal yield using our usual toy Monte Carlo approach. The plots in Figure 69 show that this uncertainty has negligible impact on the extracted W yield. Uncertainties on W^+ and W^- yields and their uncertainties are also consistent with zero. Normalization uncertainties cancel for $W \to \tau\nu$ background and are ignored.

12.3.6 Systematics Summary

Table 20 summarizes the systematic uncertainties on extracted signal yield for the $\not\!\!E_T^{TC}$ and $\not\!\!E_T^{PF}$ fits.

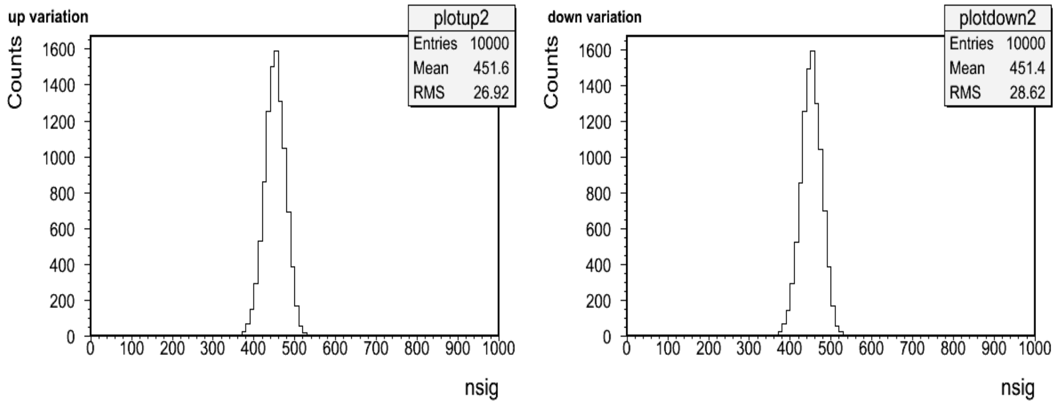

Figure 69: Signal Yields from Electroweak Background Uncertainties. We generate pseudo-experiments using signal templates in which we vary the Z/W normalization by the PDF uncertainty, 2.5%. We find no significant impact on the extracted W yield.

Uncertainty Source	W Yield (%)	W^+ Yield (%)	W^- Yield (%)	Ratio (%)
Using $\not{E}_T^{PF}$				
Background Shape	1.0	0.4	0.9	0.4
Recoil	3.2, 1.9	4.3, 2.4	5.9, 3.0	1.7, 0.7
Electron Energy Scale	2.1	2.0	2.4	0.5
Electron Efficiency	0.3	0.2	0.2	¡0.0
Electroweak Backgrounds	< 0.0	< 0.0	< 0.0	< 0.0
Using $\not{E}_T^{TC}$				
Background Shape	0.6	0.3	0.5	0.2
Recoil	2.8, 2.2	1.4, 1.3	1.7, 1.4	0.3, 0.2
Electron Energy Scale	2.5	1.4	1.6	0.1
Electron Efficiency	0.9	0.8	1.2	0.4
Electroweak Backgrounds	< 0.0	< 0.0	< 0.0	< 0.0

Table 20: Summary of Systematic Uncertainty on $W \to e\nu$ Yield Results.

12.4 Summary

The variety of signal extraction techniques available in the electron-channel provides useful leverage in the estimation of a 0.1 pb^{-1} $W \to e\nu$ yield. We apply each technique to the data currently available and obtain consistent results. The extracted yields translate to cross sections that agree with the NLO prediction, given the large statistical uncertainties on the yields.

Most of the extraction techniques have equivalent statistical performances in 0.1 pb^{-1}; we project 12.3%, 5.1%, 6.4% and 6.8% relative uncertainties on signal yield for the ABDCE, fixed-shape, hybrid $\not{E}_T$ and hybrid M_T methods, respectively. Studies of systematic uncertainty are in progress and it is difficult to judge the methods on that basis at present. In general, however, we expect that flexibility in the estimation of background will result in smaller bias, which simplifies the estimation of systematic uncertainties. The $\not{E}_T$ background shape is presently the simplest to understand, the easiest to model and is statistically competitive with other discriminating variables. We therefore choose the hybrid $\not{E}_T$ fit for the baseline cross section result. This choice is provisional and will be revisited with more data and with results from a realistic assessment of systematic uncertainty.

13 $\gamma^*/Z \longrightarrow e^+e^-$ signal extraction

In this section we describe the analysis to extract signal yield and production cross section for the $\gamma^*/Z \rightarrow e^+e^-$ events in pp collisions at $\sqrt{s} = 7\ TeV$ with early LHC data. For this iteration of the analysis, which is aimed for ICHEP 2010 approval using $\sim 100nb^{-1}$ integrated luminosity, we use a cut-and-count method to estimate the signal yield. Like in case of muon channel analysis, the $\gamma^*/Z \rightarrow e^+e^-$ candidates are selected with a robust and high purity signal selection. The amount of background under the signal peak and the event selection efficiency are estimated from MC simulation.

13.1 $\gamma^*/Z \longrightarrow e^+e^-$ event selection

The $\gamma^*/Z \rightarrow e^+e^-$ events are selected from events that pass the single isolated-electron High Level Trigger. We require two high-p_T electrons formed from the association of high E_T ECAL superclusters with high p_T GSF tracks in the Tracker. The electrons from the Z decay are isolated, so we demand very low track, ECAL, and HCAL activity around each electron candidate. This criterion rejects quite efficiently electrons from jets.

Also, the invariant mass of the two electrons should lie between 60 and 120 GeV.

The following signal selection has been used for the $Z \rightarrow e^+e^-$ cross section analysis:

- event passes an *EG5*-seeded trigger
- two *GsfElectrons* in ECAL fiducial ($|\eta|$ <2.5 with 1.4442< $|\eta|$ <1.560 excluded)
- two *GsfElectrons* with supercluster E_T >20.0 GeV
- both electrons are isolated
- both electrons pass identification and isolation criteria as defined in Tables **??**-**??** (see details in section 13.3)
- 60< $M_{e,e}$ <120 GeV

13.2 Acceptance for $\gamma^*/Z \longrightarrow e^+e^-$ events

Since the data itself is inherently biased with respect to geometric acceptance, this quantity must be estimated from Monte Carlo simulation. We use full NLO (POWHEG with CTEQ66 PDF) Monte Carlo simulation for this purpose.

We compute a combined geometric and kinematic acceptance for $\gamma^*/Z \rightarrow e^+e^-$ events which have both superclusters (matched to MC electrons by demanding DR<0.2) in the ECAL fiducial area ($|\eta|$ <2.5, 1.4442< $|\eta|$ <1.560 excluded) with E_T > 20 GeV and 60< $M_{SC,SC}$ <120 GeV, divided by all generated $\gamma^*/Z \rightarrow e^+e^-$ events with 60< $M_{e,e}$ <120 GeV. Since we use superclusters for the estimation of the acceptance, the clustering efficiency is included in the acceptance calculation.

We calculate separately the acceptances for the cases that both electrons are in the ECAL Barrel (EB,EB), both in the ECAL Endcaps (EE,EE) and one electron is in the Barrel and the other in the Endcaps (EB,EE).

The combined geometric and kinematic acceptance is (errors are due to MC statistics):

$$\mathcal{A}_{\mathcal{EB},\mathcal{EB}} = \frac{N_{ee}^{acc}}{N_{ee}^{tot}} = 0.2253 \pm 0.0007$$

$$\mathcal{A}_{\mathcal{EB},\mathcal{EE}} = \frac{N_{ee}^{acc}}{N_{ee}^{tot}} = 0.1625 \pm 0.0006$$

$$\mathcal{A}_{\mathcal{EE},\mathcal{EE}} = \frac{N_{ee}^{acc}}{N_{ee}^{tot}} = 0.0479 \pm 0.0003$$

So the total acceptance is:

$$\mathcal{A}_{\mathcal{TOT}} = \mathcal{A}_{\mathcal{EB},\mathcal{EB}} + \mathcal{A}_{\mathcal{EB},\mathcal{EE}} + \mathcal{A}_{\mathcal{EE},\mathcal{EE}} = 0.4357 \pm 0.0010$$

13.3 Electron identification and Isolation

In this analysis we use a very simple set of variables in order to perform the electron identification. The main idea is to keep the electron efficiency high using simple selection variables that will preserve their discrimination power at the initial data collection period. For the $Z \to e^+e^-$ selection, the optimized electron identification thresholds are defined in Table 13 and are refered to as WP95 (or *"VBTF-95"*) selection.

13.4 Distribution of kinematic variables

The reconstructed transverse momentum, pseudo-rapidity, and azimuthal angle distribution of electrons passing *VBTF-95* selection in current data and simulation are shown in Fig. 70. We show the transverse momentum, rapidity, and azimuth distribution of the γ^*/Z candidates passing our final selection criteria in Fig. 75. The Z boson $\cos\theta^*$ and forward-backward asymmetry are shown in Fig. 76.

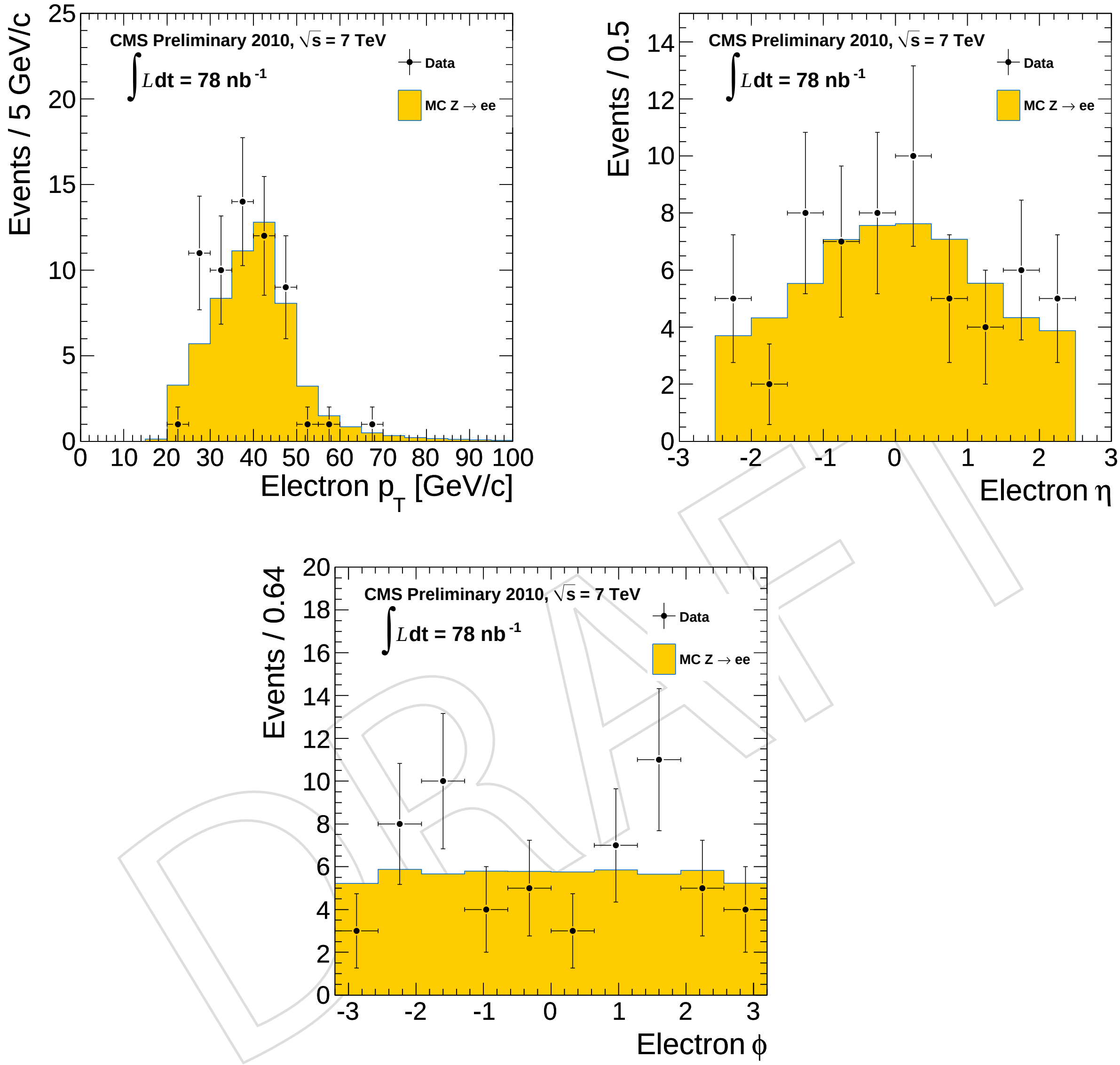

Figure 70: The reconstructed transverse momentum (top left), pseudo-rapidity (top right), and azimuthal angle (bottom) distribution of electron candidates passing our final selection criteria in $\gamma^*/Z \rightarrow e^+e^-$ events. The data points are shown as solid circles with error-bars. Predicted number of events from simulation (scaled to the given integrated luminosity) is overlaid as shaded regions.

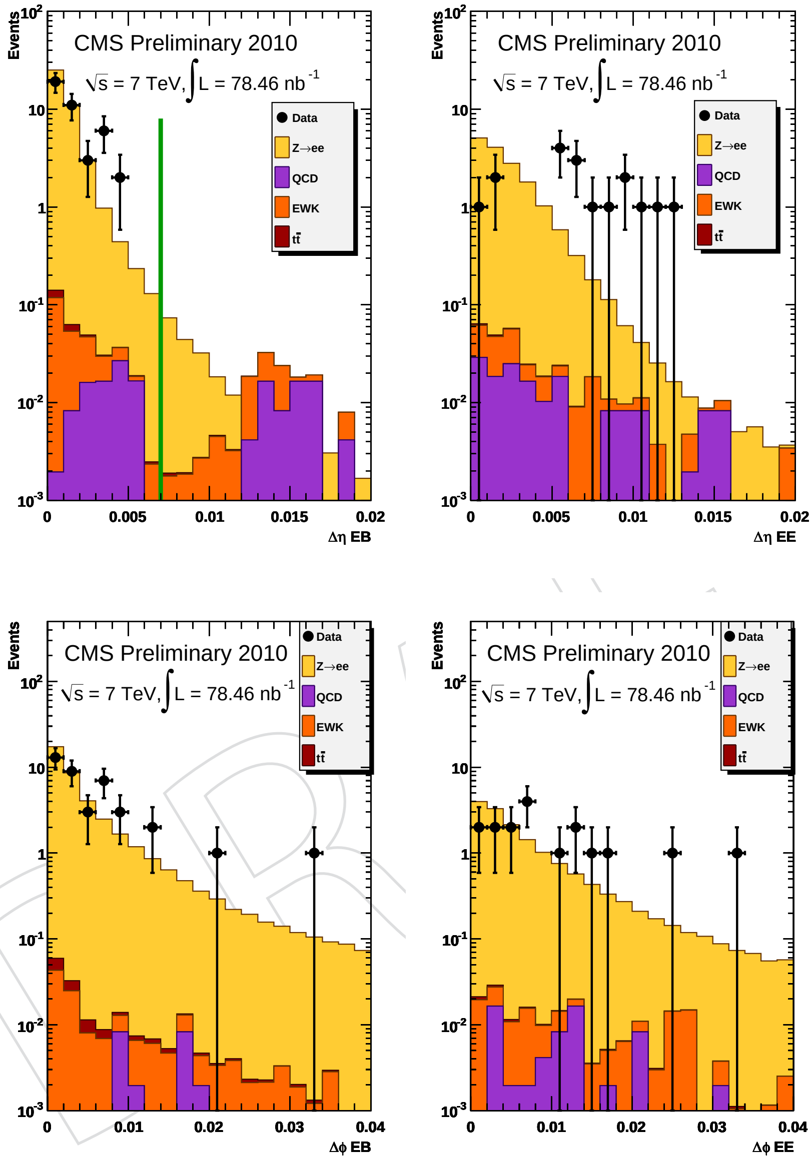

Figure 71: Distribution of electron identification variables: $\Delta\eta$, and $\Delta\phi$ in $\gamma^*/Z \rightarrow e^+e^-$ events considered for this analysis. The data points are shown as solid circles with error-bars. Predicted number of events from simulation (scaled to the given integrated luminosity) is overlaid as shaded regions. The cut applied to select a pure $\gamma^*/Z \rightarrow e^+e^-$ sample is denoted by vertical line.

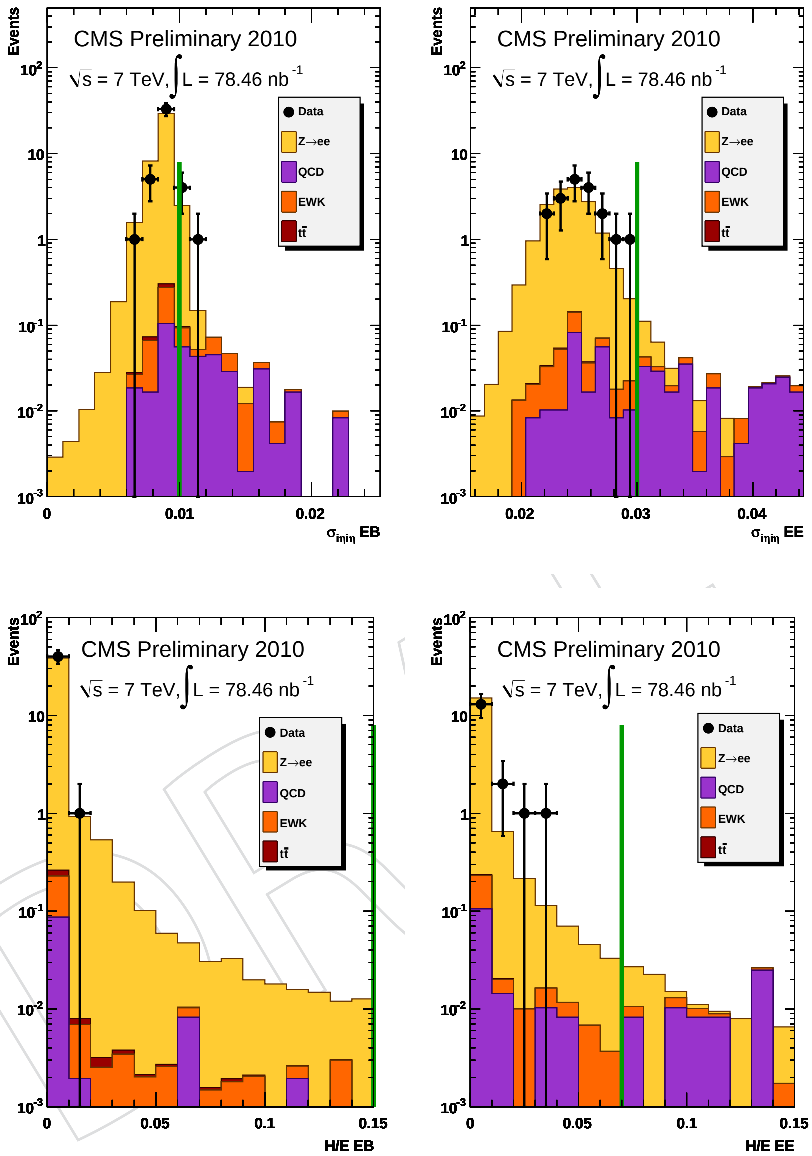

Figure 72: Distribution of electron identification variables: $\sigma_{i\eta i\eta}$ and H/E in $\gamma^*/Z \rightarrow e^+e^-$ events considered for this analysis. The data points are shown as solid circles with error-bars. Predicted number of events from simulation (scaled to the given integrated luminosity) is overlaid as shaded regions. The cut applied to select a pure $\gamma^*/Z \rightarrow e^+e^-$ sample is denoted by vertical line.

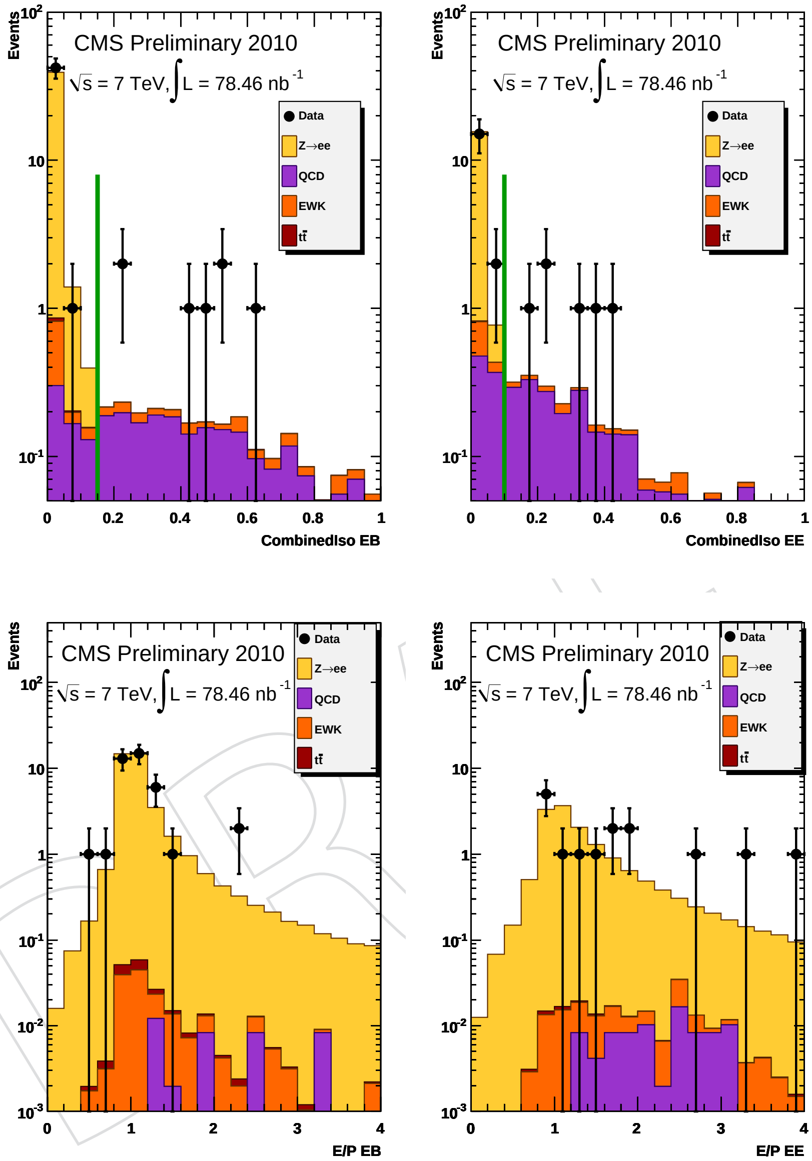

Figure 73: Distribution of combined isolation variable and E/p for electrons in $\gamma^*/Z \rightarrow e^+e^-$ events considered for this analysis. The data points are shown as solid circles with error-bars. Predicted number of events from simulation (scaled to the given integrated luminosity) is overlaid as shaded regions. The cut applied to select a pure $\gamma^*/Z \rightarrow e^+e^-$ sample is denoted by vertical line.

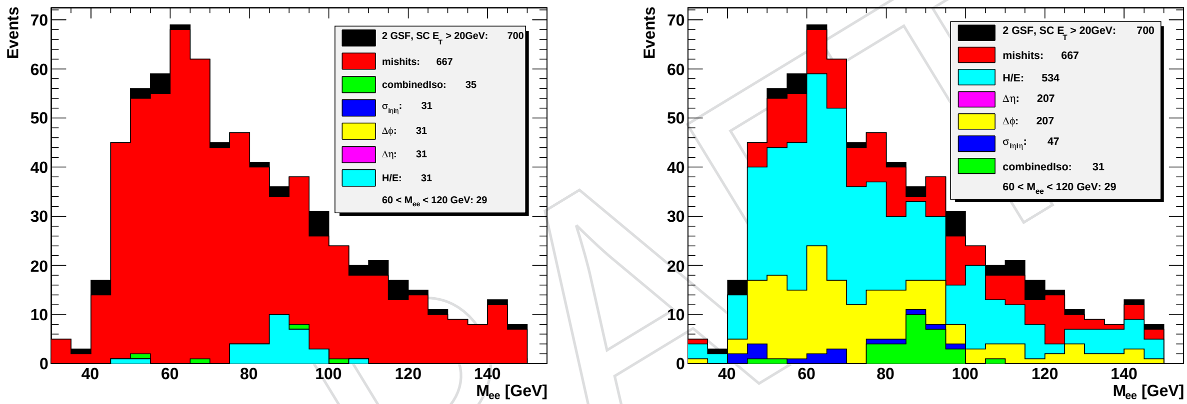

Figure 74: Flow of selection cuts in data. Number of $\gamma^*/Z \rightarrow e^+e^-$ events left after successive cuts.

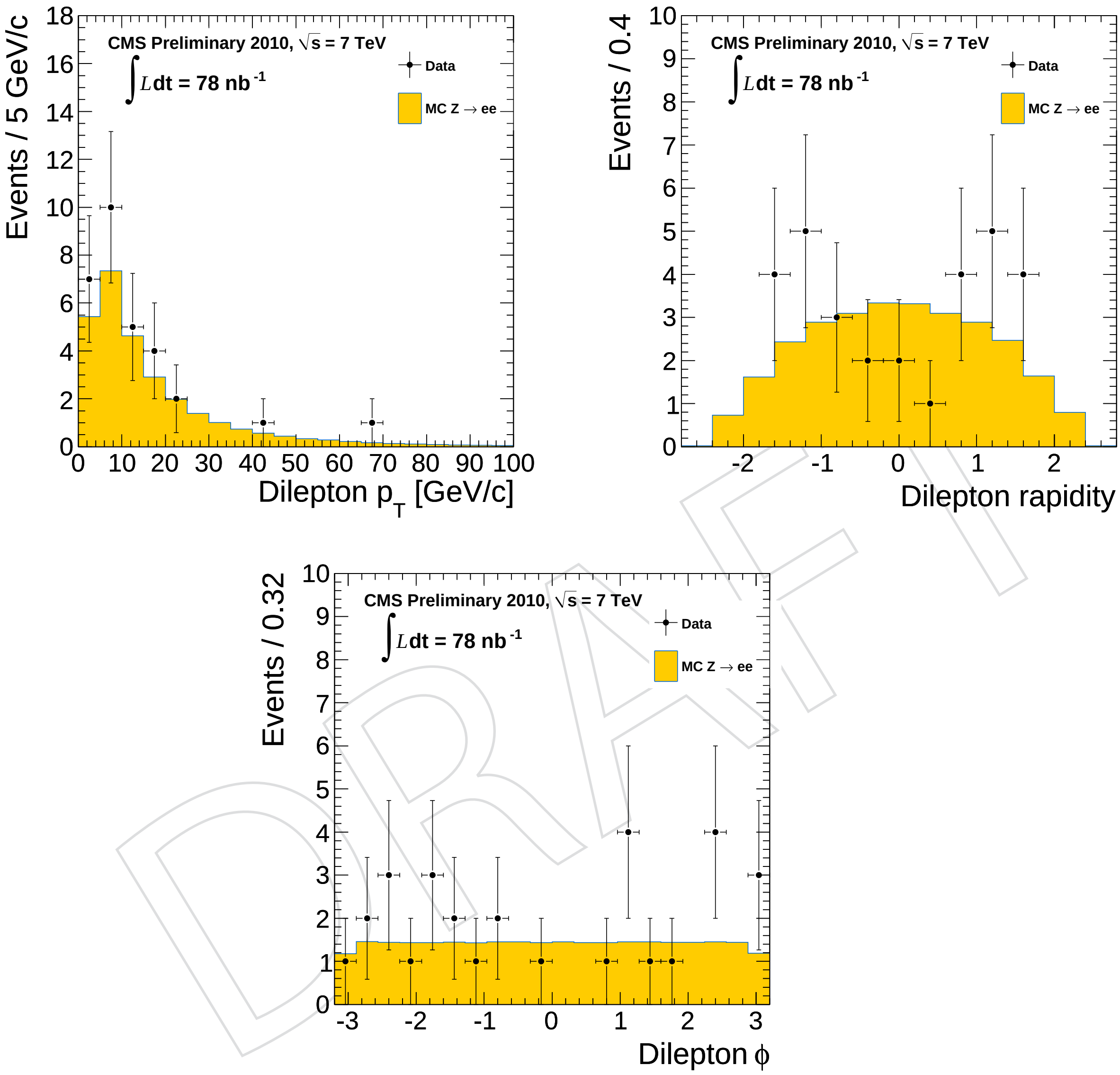

Figure 75: The reconstructed transverse momentum (top left), rapidity (top right), and azimuthal angle (bottom) distribution of the Z candidates passing our final selection criteria. The data points are shown as solid circles with error-bars. Predicted number of events from simulation (scaled to the given integrated luminosity) is overlaid as shaded regions.

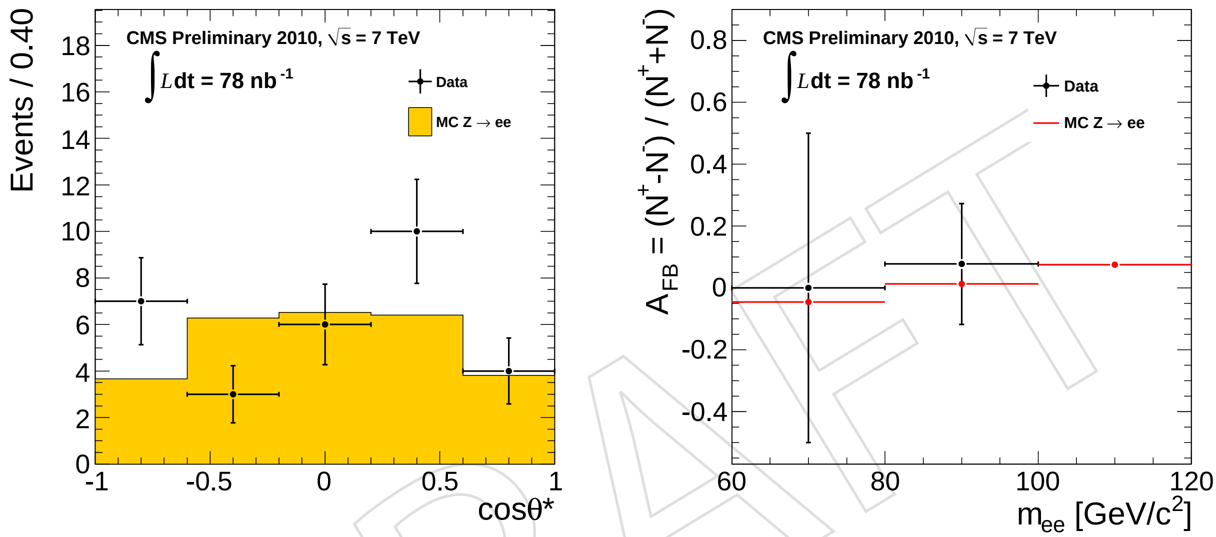

Figure 76: Z boson $\cos\theta^*$ (left) and forward-backward asymmetry (right). In Collins-Soper frame [45], $\cos\theta^*$ is the angle between the electron momenta and the Z' axis that bisects the angle between the quark and antiquark. For each Z mass bin, the forward-backward asymmetry is given by $A_{fb} = \frac{(N_f - N_b)}{(N_f + N_b)}$, where N_f is the number of events with $\cos\theta^* > 0$ and N_b is the number of events with $\cos\theta^* < 0$. The data points are shown as solid circles with error-bars. Predictions from simulation (scaled to the given integrated luminosity) are overlaid as shaded regions.

13.5 Efficiency for electron selection in $\gamma^*/Z \longrightarrow e^+e^-$ events

We compute efficiency for the electron selection (including all reconstruction, isolation, electron Id, and triggering steps) with respect to geometric and kinematic acceptance. Therefore, the numerator of the efficiency is the number of electrons passing selection criteria described in section 13.3 and also matched to single electron HLT triggerred object in the event. The denominator of the efficiency is the number of super clusters passing the geometric and kinematic acceptance described in section 13.2. In the current analysis we derive the efficiency separately for electrons in the barrel and in endcaps using simulation (NLO, POWHEG). When we get larger data sample ($\geq 1\ pb^{-1}$) we will derive the efficiency in bins of electron p_T and η directly from data.

The efficiency for our nominal electron selection is (errors are due to MC statistics):

$$\epsilon_{EB} = 0.9442 \pm 0.0036,$$

$$\epsilon_{EE} = 0.9193 \pm 0.0042,$$

and the overall average efficiency is:

$$\epsilon_{all} = 0.9310 \pm 0.0025.$$

So the average efficiency for $\gamma^*/Z \to e^+e^-$ reconstruction is:

$$\epsilon^{\gamma^*/Z}_{EBEB} = 0.8921 \pm 0.0033.$$

$$\epsilon^{\gamma^*/Z}_{EBEE} = 0.8452 \pm 0.0037.$$

$$\epsilon^{\gamma^*/Z}_{EEEE} = 0.8238 \pm 0.0068.$$

$$\epsilon^{\gamma^*/Z} = 0.8671 \pm 0.0023.$$

13.6 Estimation of small residual background under the Z peak

13.6.1 Monte Carlo based background subtraction

In this method we simply count the number of events passing our $\gamma^*/Z \to e^+e^-$ selection requirements in each background MC sample and scale this number by the corresponding cross section of the and the total integrated luminosity. We then subtract the predicted number of background events derived from MC from the number of $\gamma^*/Z \to e^+e^-$ candidate events observed in data. Table 21 lists the cross section values for the $\gamma^*/Z \to e^+e^-$ signal and various background processes. Table 22 shows the expected number of $\gamma^*/Z \to e^+e^-$ signal and background events per $^{-1}$ integrated luminosity from Monte Carlo prediction.

Table 21: Cross section values for the $\gamma^*/Z \rightarrow e^+e^-$ signal and various background processes.

Process	Cross section (in pb)
NLO $\gamma^*/Z \rightarrow e^+e^-$ ($m_Z > 20\ GeV$)	1606.6
QCD em-enriched: p_T $20-30\ GeV$	$0.235500 \times 0.00730 \times 10^9$
QCD em-enriched: p_T $30-80\ GeV$	$0.059300 \times 0.05900 \times 10^9$
QCD em-enriched: p_T $80-170\ GeV$	$0.000906 \times 0.14800 \times 10^9$
QCD $b,c \rightarrow e$: p_T $20-30\ GeV$	$0.235500 \times 0.00046 \times 10^9$
QCD $b,c \rightarrow e$: p_T $30-80\ GeV$	$0.059300 \times 0.00234 \times 10^9$
QCD $b,c \rightarrow e$: p_T $80-170\ GeV$	$0.000906 \times 0.01040 \times 10^9$
γ + jets ($p_T > 15\ GeV$)	1.922×10^5
$W \rightarrow e\nu$	9679.9×0.742
$W(\rightarrow e\nu) + \gamma$	23.2×1.8
$t\bar{t}$	165.0
$WW \rightarrow ee$	42.9
$WZ \rightarrow ee$	18.3
$ZZ \rightarrow ee$	5.9

Table 22: Expected number of $\gamma^*/Z \rightarrow e^+e^-$ signal and background events per nb^{-1} integrated luminosity.

Process	# events / nb^{-1}
$\gamma^*/Z \rightarrow e^+e^-$	0.3409 ± 0.0005
QCD dijets	0.00070 ± 0.00008
γ + jets	0.00011 ± 0.00017
$W \rightarrow e\nu$	0.00033 ± 0.000008
$W(\rightarrow e\nu) + \gamma$	0.00005 ± 0.000001
$t\bar{t}$	0.00048 ± 0.000016
$Z \rightarrow \tau^+\tau^-$	0.00042 ± 0.000016
Dibosons (WW,WZ,$ZZ \rightarrow ee$)	0.00039 ± 0.000008
$\gamma\gamma$	0.00003 ± 0.000002
Total Background from MC	0.0027 ± 0.0005

13.7 Results of γ^*/Z cross section measurement

Table 23 shows a summary of the results for the γ^*/Z cross section measurement from the current available data. As can be seen, the estimated γ^*/Z cross section agrees within the errors with the expected one. Systematic uncertainties in the γ^*/Z cross section measurement, reported in Tables 23, arise from experimental effects, uncertainty in the amount of integrated luminosity, and also from theoretical uncertainties in the acceptance calculation. We determine these separately and add them in quadrature (except for the luminosity uncertainty which we quote separately). The systematic uncertainty from the theoretical uncertainties on the acceptance calculation is estimated to be 3%. We assign a systematic uncertainty of 10% in the efficiency for $\gamma^*/Z \rightarrow e^+e^-$ signal reconstruction. A systematic uncertainty of 11% arises from the measurement of the integrated luminosity.

Table 23: Results for the $\gamma^*/Z \rightarrow e^+e^-$ cross section measurement.

$N_{selected}$	30.00 ± 5.48
N_{bkgd}	0.29 ± 0.05
ε	0.8671 ± 0.0023 (MC stat.) $\pm\ 0.0867$ (syst.) %
Acceptance	0.4357 ± 0.0010 (MC stat.) $\pm\ 0.0131$ (syst.) %
Integrated Luminosity	$0.0785 \pm 0.0086\ pb^{-1}$ (syst.)
$\sigma_{\gamma^*/Z} \times BR(\gamma^*/Z \rightarrow e^+e^-)$	1002.4 ± 184.8 pb (stat.) $\pm\ 100.2$ (syst.) $\pm\ 110.2$ (lumi.)
Theoretical prediction	LO: 740 pb, NLO: 911 pb ($60 < m_Z < 120\ GeV$) LO: 1300 pb ($m_Z > 20\ GeV$), NLO: 1607 pb ($m_Z > 20\ GeV$)

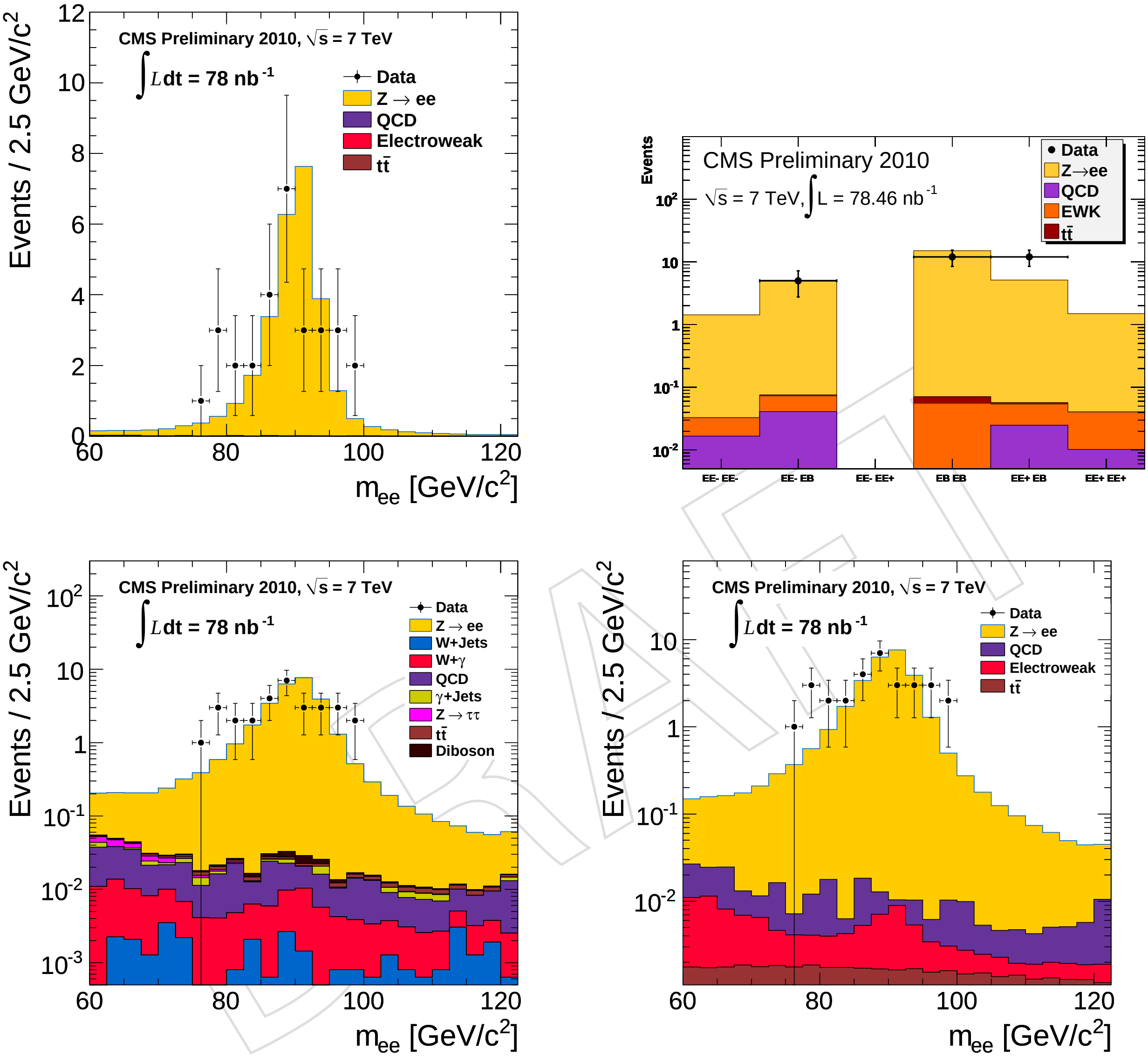

Figure 77: The reconstructed di-lepton invariant mass in $\gamma^*/Z \rightarrow e^+e^-$ events plotted with four different views. The data points are shown as solid circles with error-bars. The predicted number of signal events from NLO simulation and scaled to the given integrated luminosity is overlaid as solid curve. Estimation of various background events from simulation is shown by shaded regions.

13.8 New methodology: simultaneous fit for cross section and efficiency

In the traditional method for estimating the Z cross section, the efficiency $\overline{\varepsilon_Z}$ of a "final" high-purity selection is estimated from one or more "low purity" samples (*i.e.*, the denominator of the efficiency) using tag-and-probe method, the "final" N_Z selection candidates are counted, and the cross section is computed as

$$\sigma = N_Z/(\overline{\varepsilon_Z} A_Z \int L dt).$$

The statistical and systematic uncertainties for $\overline{\varepsilon_Z}$ and N_Z are computed separately and combined in quadrature, *i.e.*, any correlations are ignored. However, the effect of uncertainties for these two quantities are clearly anti-correlated so this overestimates the statistical uncertainties. Moreover, such a design artificially divides the cross section measurement into a multi-step process requiring strict coordination throughout to ensure consistency. In what follows, we describe an approach which can easily account for covarying factors in all of the cross section ingredients, and do so in a single step.

Signal yield in "high purity" sample (*i.e.*, both lepton passing the nominal selection)

$$N_{PP} = L\sigma A\bar{\varepsilon}_Z,$$

where the average efficiency can be written in terms of the single lepton efficiency and relative acceptance in each bin

$$\bar{\varepsilon}_Z = \Sigma_{i,j}\frac{A_{ij}}{A}\varepsilon_i\varepsilon_j.$$

Similarly, signal yield in high purity sample (*i.e.*, one lepton passing and the other lepton failing the nominal selection)

$$N_{P[i],F[j]} = \int L dt \cdot \Sigma_{i,j}\frac{A_{ij}}{A}\varepsilon_{[i]}(1-\varepsilon_{[j]}).$$

The results of the simultaneous fit performed on $\gamma^*/Z \to e^+e^-$ events is shown in reproduced below and shown in Fig. 78.

```
     Floating parameter                        Fit value
    -------------------------------------------------------
  1  Z signal Breit-Wigner mean           88.53   +-   1.18
  2  Gaussian resolution rms              5.44    +-   0.96
  3  Background shape: exponential       -0.0148  +-   0.0120
  4  Efficiency                           0.887   +-   0.111
  5  Number of Bkg in low purity sample   25.2    +-   6.4
  6  Z signal cross section               1114.3  +-   321.4

    Z width was fixed in the fit to its nominal value 2.5 GeV.
    The acceptance was fixed to the value derived from NLO MC.

      PARAMETER  CORRELATION COEFFICIENTS
      NO.  GLOBAL      1      2      3      4      5      6
       1  0.17559   1.000 -0.152 -0.053 -0.076 -0.053  0.068
       2  0.15263  -0.152  1.000  0.014 -0.001 -0.001  0.001
       3  0.15733  -0.053  0.014  1.000  0.148  0.103 -0.131
```

4	0.81607	-0.076	-0.001	0.148	1.000	0.548	-0.794
5	0.55538	-0.053	-0.001	0.103	0.548	1.000	-0.488
6	0.79670	0.068	0.001	-0.131	-0.794	-0.488	1.000

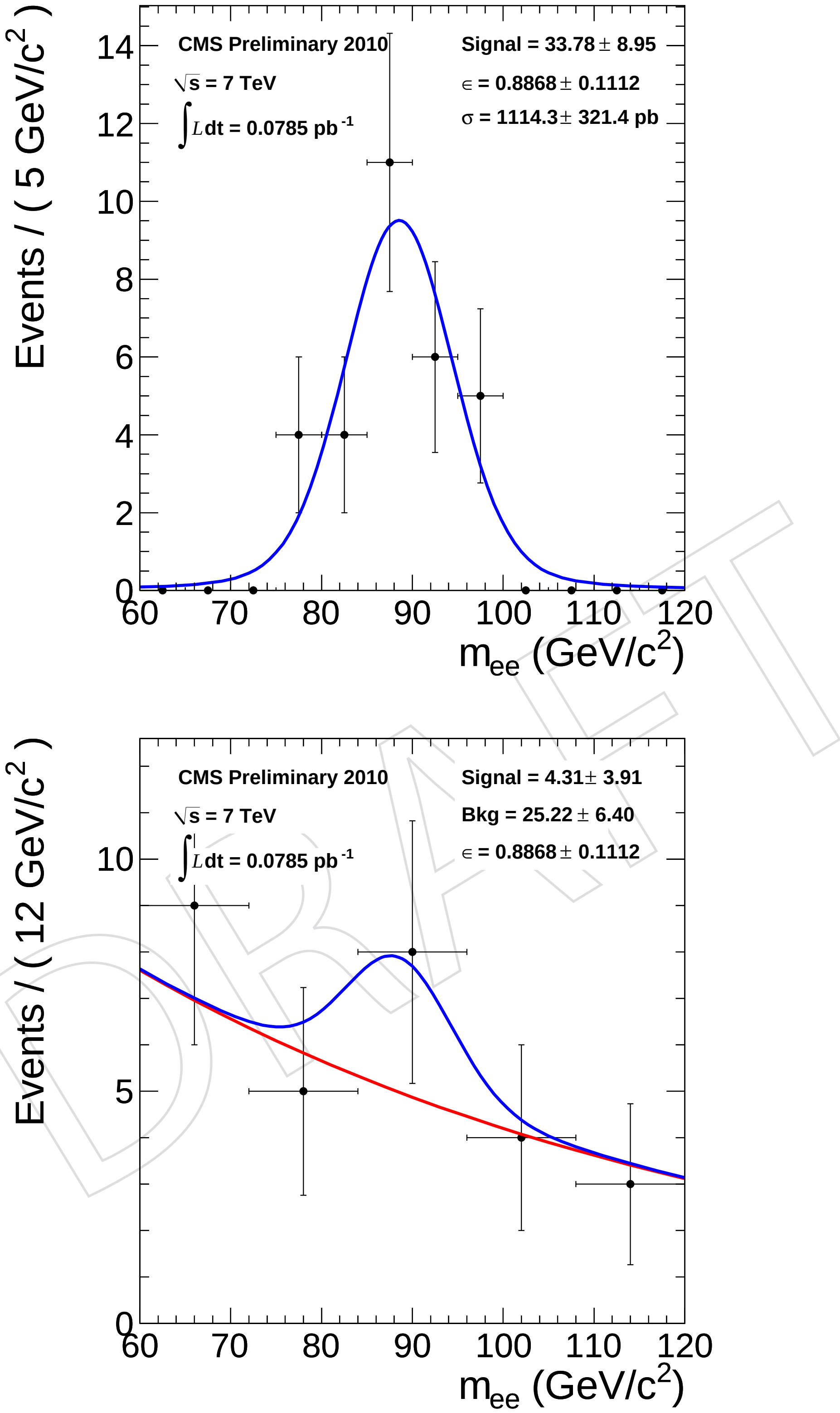

Figure 78: Simultaneous fit to extract the production cross section and electron reconstruction (and identification) efficiency from $\gamma^*/Z \to e^+e^-$ events in data: projection of the di-electron invariant mass in "high purity" sample (top) and in "low purity" sample (bottom).

14 Electron Energy Scale and Resolution

The estimated particle energy, obtained from the Electromagnetic Calorimeter, can be expressed as:

$$E = F \cdot \sum_{clusterRecHits} G(GeV/ADC) \cdot c_i \cdot A_i(ADC) \tag{26}$$

where the sum is over the crystals in a cluster. A_i are the reconstructed amplitudes in ADC counts (the uncalibrated RecHit). c_i is the inter-calibration constant while G is the ECAL energy scale. $(G \cdot c_i \cdot A_i)$ is the calibrated RecHit. F includes all the energy correction of the cluster such as containment corrections, Bremsstrahlung correction for electrons, dead channel corrections, crack corrections, etc.

The absolute scale of the Electromagnetic Calorimeter has been measured during the Test Beam campaign for EB and EE separately.

The main method to tune the ECAL energy scale in-situ is by using the di-electrons and di-photons invariant mass peaks. While the $Z \to e^+e^-$and samples collected so far are well below the amount of data needed to measure the energy scale, some preliminary indications come from π^0 and η.

Given the different calibration level of the detector, it is desirable to extract the energy scale independently for the barrel and the two endcaps by selecting events having both electrons or photons in the same sub-detector.

According to the formula 26, the accuracy of the scale can be derived looking at the ratio of the reconstructed invariant mass peak position between data and Monte-Carlo. Assuming a perfect simulation of the material in front of ECAL and the alignment of the detector, this ratio would provide the correction to be applied at the scale. More conservatively, we consider this number as an estimation of the scale accuracy.

The estimated precision on the Barrel scale determination is at the level of 1%, as confirmed by the dE/dx analysis with cosmics [46]. The estimated precision for the Endcaps is at the level of $\sim 3\%$.

After calibration of the energy scale from ECAL and of the momentum scale from the tracker, residual energy scale corrections for electrons will be extracted from the $Z \to e^+e^-$measurements, with the tag-and-probe method, after sufficient statistics is accumulated. In the momentum range relevant for the $Z \to e^+e^-$measurement, the energy resolution for electrons is dominated by the ECAL. In addition to the intrinsic resolution expected from test beam measurements, the bremsstrahlung in the tracker material induces large fluctuations. The electron resolution will be measured by fitting the width of the reconstructed Z mass and by comparing the reconstructed Z width with the Monte Carlo expectation.

15 Systematics

Even if the current cross section measurements are mainly statistically limited, systematic uncertainties play an important role in the measurement of the inclusive W and Z boson production cross section, in particular in perspective of more collision data collected. Future analyses will benefit from an enlarged data set allowing access to data-driven methods that will likely reduce the systematic uncertainties. In the following we describe the source for systematic effects and the estimated uncertainties.

15.1 Theoretical Uncertainties

The measurement of the W and Z cross section has been performed using a base-line MC generated with the NLO MC generator POWHEG and the parton distribution function CTEQ66. Uncertainties are quoted with respect to this baseline wherever applicable. It was verified that this base-line is in good agreement with the more complex integrator tool ResBos [47–52] which itself shows excellent agreement with results from Tevatron experiments. The following paragraphs discuss the individual contributions to the systematic uncertainties on the acceptance and the cross section measurement. PDF uncertainties are summarized in Table 24. Other uncertainties are summarized in Table 25 for W bosons, in Table 26 for Z bosons and in Table 27 for ratio measurements.

15.1.1 Parton Distribution Functions

PDFs are published by a number of collaborations. The studies presented here include results from sets CTEQ66 [53], MSTW2008NLO [11] and NNPDF2.0 [54]. In addition to the best fits, uncertainty sets are published which can be used to assign standard deviations on physical observables. In CMS, simulated events can be easily re-weighted at the hard scattering level using modified PDF sets using a set of utilities developed within the ElectroWeak group [55]. This way, the exact set of p_T and η cuts can be taken into account.

In this section we consider PDF systematics related with the experimental measurements, namely on the estimated acceptance for W, W^+, W^-, Z and the acceptance corrections for the W/Z and W^+/W^- ratios. The PDF uncertainties of the theory predictions are discussed separately in the section of final results. Correlations between experimental acceptance corrections and theory predictions due to PDFs (see Figure 79) are at the 10% level and therefore not a concern from the practical point of view.

In order to assign systematics we follow the strategy defined by the CMS Generator Group and described in [56], which is also consistent with the latest PDF4LHC recommendations [57]. In short, we consider the 68% CL positive and negative uncertainties obtained with CTEQ66, MSTW2008NLO and NNPDF2.0 sets, adopting the specific recommended recipes in each case. The final assigned systematics corresponds to half of the maximum difference observed between positive and negative variations for any combination of the three sets. Usually this maximum difference corresponds to a positive variation from one set minus a negative variation from a different set, since central values from different sets are typically of the size of the uncertainties within a set. Uncertainties due to α_S also considered, even if they are small (0.1% contribution to acceptance uncertainties and 0.02% to correction factor uncertainties).

We conclude that the PDF theoretical uncertainties on the estimated boson acceptances are below or of order 2% (2% is assigned conservatively for the moment). The uncertainty on the W^+/W^- acceptance correction factor is also $\sim$ 2%, while the one for the correction of the Z/W ratio is $\sim$ 1%.

15.1.2 Higher Order QCD Corrections and Initial State Radiation

The effect of soft non-perturbative effects, hard higher order effects and initial state radiation which are not accounted for in the baseline MC is studied by comparing ResBos at NNLO with the baseline MC.

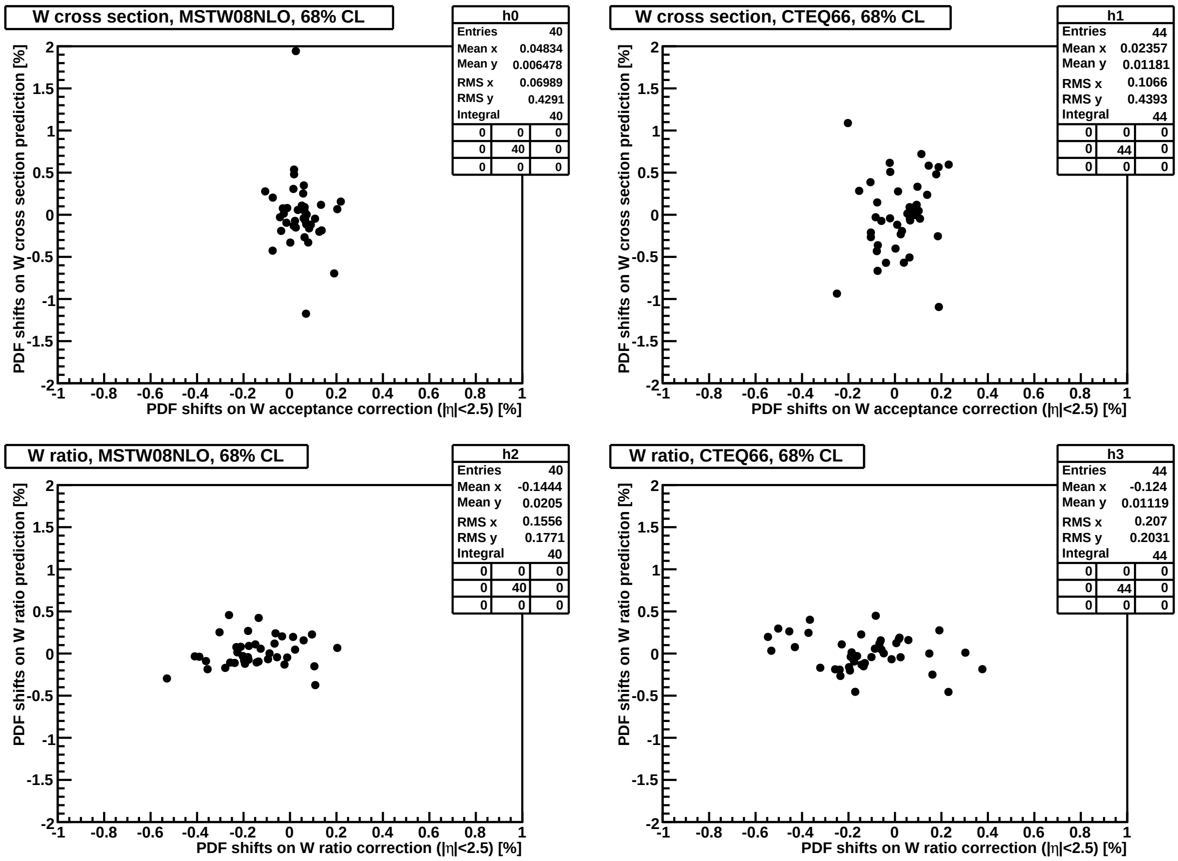

Figure 79: Correlations between experimental acceptance corrections and theory predictions. The Figure shows that both for the CTEQ66 and MSTW1008NLO cases and for total W cross section and W^+/W^- ratios, they are negligible ($\lesssim$ 10%).

15.1.3 Higher Order QCD Corrections

Higher order virtual processes influence the W (Z) boson momentum and rapidity distributions. The fixed-order calculations implemented both by generators and integrators lead to an unnatural dependence on the QCD factorization scale that must be quantified. The effect of scale dependence of NNLO calculations is estimated and quoted as a systematic uncertainty. FEWZ [8, 9] is used for those studies.

15.1.4 Electroweak Corrections and Final State Radiation

On top of higher order QCD corrections, we attempt to estimate the effect of Electroweak effects not fully implemented in our baseline MC. The HORACE generator [58–61] is used which implements both final state radiation and virtual and non-virtual corrections. Individual effects are separated and final state effect are then compared to PYTHIA results. PYTHIA is used for final state radiation in the POWHEG event generation.

15.2 Systematic error from muon momentum scale and resolution

The systematics due to the uncorrected bias in data is estimated by applying a bias in the MC according to

$$p'_T = f_{+(-)}(p_T, \eta) \times p_T \tag{27}$$

Quantity	Δ_{CTEQ} (%)	Δ_{MSTW} (%)	Δ_{NNPDF} (%)	Δ_{sets} (%)	Syst. (%)
W^+ acceptance (μ)	$\pm$0.7	$\pm$0.4	$\pm$0.5	0.6 (NNPDF-CTEQ)	1.3
W^- acceptance (μ)	$\pm$1.1	$\pm$0.7	$\pm$1.1	0.9 (NNPDF-MSTW)	1.9
W acceptance (μ)	$\pm$0.7	$\pm$0.4	$\pm$0.6	0.4 (MSTW-CTEQ)	1.1
Z acceptance (μ)	$\pm$0.9	$\pm$0.5	$\pm$0.8	0.4 (MSTW-CTEQ)	1.2
W^+/W^- correction (μ)	$\pm$1.1	$\pm$0.6	$\pm$0.9	1.3 (NNPDF-MSTW)	2.1
W/Z correction (μ)	$\pm$0.6	$\pm$0.4	$\pm$0.5	0.6 (NNPDF-MSTW)	1.1
W^+ acceptance (e)	$\pm$0.5	$\pm$0.2	$\pm$0.3	0.4 (NNPDF-CTEQ)	0.9
W^- acceptance (e)	$\pm$0.9	$\pm$0.5	$\pm$0.8	0.8 (NNPDF-MSTW)	1.5
W acceptance (e)	$\pm$0.5	$\pm$0.3	$\pm$0.4	0.3 (MSTW-CTEQ)	0.8
Z acceptance (e)	$\pm$0.8	$\pm$0.5	$\pm$0.7	0.4 (MSTW-CTEQ)	1.1
W^+/W^- correction (e)	$\pm$1.0	$\pm$0.5	$\pm$0.7	1.1 (NNPDF-MSTW)	1.7
W/Z correction (e)	$\pm$0.6	$\pm$0.3	$\pm$0.4	0.6 (NNPDF-MSTW)	0.9

Table 24: Systematic uncertainties from PDF assumptions on estimated acceptances and acceptance correction factors after analysis cuts. Acceptances are referred to full phase space in the W case and to 60 GeV $< M_{\ell^+\ell^-} <$ 120 GeV in the $Z/\gamma^* \rightarrow \ell^+\ell^-$ case. Δ_i denotes the uncertainty (68% CL) within a given set i (i = CTEQ66, MSTW08NLO, NNPDF20). Δ_{sets} corresponds to half of the maximum difference between the central values of any pair of sets. The final systematics (last column) considers half of the maximum difference between central values plus uncertainty, again for any pair of the three sets, plus remaining α_S uncertainties.

Source	$W^+ \rightarrow e\nu$	$W^- \rightarrow e\nu$	$W^+ \rightarrow \mu\nu$	$W^- \rightarrow \mu\nu$
QCD-HO and ISR	-1.30%$\pm$0.09	-0.78%$\pm$0.10	-1.39%$\pm$0.09	-1.17%$\pm$0.14
QCD-α_s scaling	0.23%$\pm$0.22	0.37%$\pm$0.32	0.23%$\pm$0.22	0.37%$\pm$0.32
FSR	0.08%$\pm$0.17	0.07%$\pm$0.19	0.11%$\pm$0.12	0.01%$\pm$0.17
EWK	0.07%$\pm$0.13	0.21%$\pm$0.19	-0.02%$\pm$0.12	0.26%$\pm$0.17
Total	1.33%	0.90%	1.42%	1.26%

Table 25: Systematic uncertainties from various sources for both W boson charges and lepton flavor.

where η is the pseudo-rapidity of the muon and $f_{+(-)}(p_T, \eta)$ are the functions describing the bias in data plus (minus) its error. The analysis on MC is repeated and the difference between the two cases and the unbiased MC is quoted as systematic error due to the muon momentum scale.

N.B. the MC is most probably biased itself. If the MC bias is not negligible with respect to the one in the data (and its error) it should be first corrected and then the same method can be applied. The idea is to apply a bias to the p_T in the MC so that it becomes the p_T in data plus/minus error.

The systematics due to the difference in the resolution in the MC (used to estimate the acceptance) and in data can be estimated by smearing the p_T of MC muons according to

$$p_{T,smear} = p_{T,MC} \times Gaus(1, \sigma_{add}) \tag{28}$$

with

$$\sigma_{add} = max\left(\sqrt{\sigma^2_{data,plus} - \sigma^2_{MC}}, \sqrt{\sigma^2_{data,minus} - \sigma^2_{MC}}\right) \tag{29}$$

where $\sigma_{data,plus(minus)}$ is the resolution measured from data plus (minus) the error and σ_{MC} is

Source	Z→ ee	Z→ $\mu\mu$
QCD-HO and ISR	±0.6%	±0.6%
QCD-α_s scaling	±1.1%	±1.1%
FSR	-0.11%±0.24	0.18%±0.21
EWK	-0.47%±0.22	-0.94%±0.20
Total	1.34%	1.58%

Table 26: Systematic uncertainties from various sources for Z bosons for both lepton flavor.

Source	W^+/W^- (e)	W^+/W^- (μ)	Z/W (e)	Z/W (μ)
QCD-HO and ISR	0.56%±0.13	0.22%±0.17	0.47%±0.17	0.70%±0.18
QCD-α_s scaling	1.13%±0.63	1.13%±0.63	0.57%±0.52	0.57%±0.52
FSR	0.15%±0.27	-0.08%±0.19	-0.10%±0.30	0.15%±0.27
EWK	0.00%±0.27	0.28%±0.19	-0.70%±0.29	-0.98%±0.24
Total	1.27%	1.19%	1.03%	1.35%

Table 27: Systematic uncertainties from various sources for W^+/W^- and Z/W ratio measurements for both lepton flavor.

the resolution in the MC. By repeating the analysis with the new smeared muon collection we can quote as systematic uncertainty the difference with respect to the original MC.

N.B. We are assuming here two things: 1) the resolution in data plus its error is worse than the resolution in MC; 2) the effect we get by smearing the MC is approximately the same than by un-smearing it.

The acceptance is estimated using generator level information for the muons. To estimate the error we use a MC where the muons were biased and smeared as explained in the previous paragraphs. We take a conservative approach and we apply a bias opposite to the corrections derived in appendix C. For the resolution we apply a smearing such that the resolution of the MC matches the one measured on data plus its error. The resulting variation in the number of Z bosons (N_Z) passing the selection cuts is

$$\frac{N_Z(\text{using generated muons}) - N_Z(\text{using smeared muons})}{N_Z(\text{using generated muons})} = 0.5\% \tag{30}$$

In the case of the $W \to \mu\nu$ the same prescriptions are used, with the addition of correcting the $\not{E}_{\mathrm{T}}$ for the change in the muons collection. The results show a slight increase in the acceptance for the distorted muons and $\not{E}_{\mathrm{T}}$ are shown in table 28.

Boson	systematic error on the acceptance
$Z \to \mu\mu$	0.5 %
$W^+ \to \mu\nu$ all cuts	$-0.80\% \pm 0.22\%$
$W^+ \to \mu\nu$ all cuts but M_T	$-0.72\% \pm 0.21\%$
$W^- \to \mu\nu$ all cuts	$-0.63\% \pm 0.22\%$
$W^- \to \mu\nu$ all cuts but M_T	$-0.51\% \pm 0.21\%$

Table 28: Systematic uncertainties on the acceptance from muon momentum scale and resolution for Z and W bosons.

15.2.1 Systematics error from alignment weak modes on Z and W

In this section we describe the steps that we have followed to estimate the systematic uncertainty in the measurement of the Z mass and W transverse mass due to the possible misalignments of the Tracker system.

The Tracker has been aligned using track based alignment procedure [62] [63] assuming as input collision and cosmics tracks. Alignment strategies were widely tested during CMS commissioning with cosmics ray tracks [64], which provided the basis for this alignment. In the reality there are several non-trivial transformations (weak modes) which can affect the geometry of the Tracker, and since they are χ^2-invariant, they can survive even after the alignment procedure, if not adequately constrained. If uncorrected, they would produce unacceptable systematic biases in physics measurements. For instance, an uncorrected systematic rotation of the layers of the Tracker would introduce an artificial charge-dependent momentum asymmetry to reconstructed tracks, given the use of magnetic bending to define the charge and transverse momentum of a track.

Following the analysis described in [65], nine systematic distortions, modeled for the cylindrical Tracker geometry, have been considered, in Δr, $\Delta\phi$, and Δz as a function of r, ϕ, and z. The introduction of these deformations on top of an aligned geometry and the consequent re-alignment allows to spot the presence of possible weak modes in the geometry which was not possible to solve with the current alignment procedure and track samples available.

These 3x3 independent modes of distorting the Tracker geometry are considered in this study. We remove one of them (the curl) which was already shown not to be a weak mode and instead consider a more complicated distortion which was studied in the charge ration analysis [66]. This so called *reduced*0.5 misalignment mode is built such that the resolution from muons reconstructed in the resulting geometry is consistent with the one obtained with the STARTUP geometry.

The data used in this analysis has been aligned with a set of alignment constants extracted from a collection of cosmic and minimum bias data. We select the 8 base distortions plus the *reduced*0.5 distortion as candidate weak modes and apply them on the Z and W Monte Carlo samples, on top of the design geometry, to see the worse case scenario that one can face - that of a distorted geometry even before trying to recover the distortion by following the alignment procedure. A full re-reco of the Monte Carlo samples was performed to take into account the effects of the different geometries on both muon and $\not{E}_T$ collections.

Once re-reconstructed the muon collection for the 9 different distortion modes, we apply the Z and W selection shown in this note and compare, for each of them, how the transverse invariant mass differs from the original one obtained in the design scenario. The results are shown in table 29

		twist		"reduced $\Delta\kappa$"	
resonance	N	μ (GeV)	RMS (GeV)	μ (GeV)	RMS (GeV)
W^+	900	0.1	1.2	0.0	1.0
Z *vs* μ^+	300	-0.1	0.7	-0.0	1.1
Z *vs* μ^-	300	0.1	0.9	0.2	1.1

Table 29: Number of selected candidates, mean and RMS for the deviation in the mass between the *twist* and "reduced $\Delta\kappa$" weak modes, and the design geometry.

For the W we find that in 7 out of 9 distortion modes the transverse mass barely changes. In the so-called "twist" mode there's a large RMS, as one can see in Figure 81. The *reduced*0.5

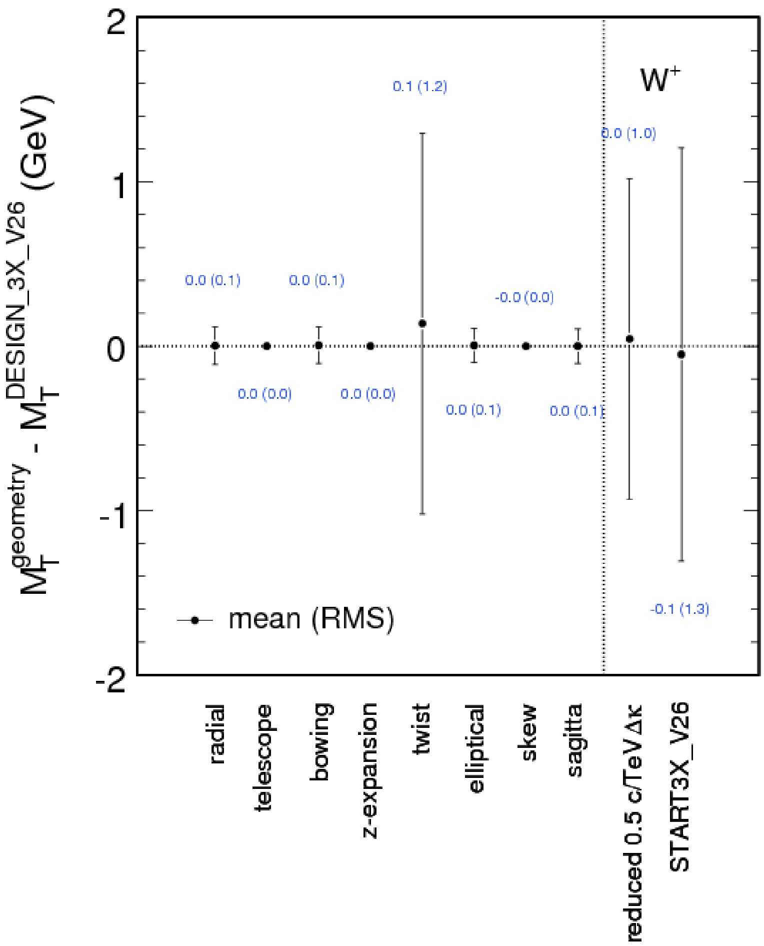

Figure 80: W mass difference for positive charge bosons. Note that the points on the left of the vertical dashed line must be compared with an ideal geometry scenario, while the *reduced*0.5 one must be compared with the startup scenario. Negative charged Ws give analogous results.

mode does not show a big difference with respect to the startup scenario. The biggest effect is coming from the "twist" mode which gives a deviation in the transverse mass of $\sim$ 100 MeV and a smearing of $\sim$ 1 GeV with respect to ideal geometry. We can use this mode to get a maximum estimation of the systematic uncertainty. For the Z we focus on the 4 modes that produce the biggest effect and the result is shown in figure **??**. Also in this case the mass is almost unaffected, while the biggest change is in the resolution.

Results for the Z go here.

Figure 81: Mean and RMS of the event-by-event difference in the $Z \rightarrow \mu\mu$ invariant mass, between several geometries and the design one. Note that "telescope" and "twist" modes must be compared with an ideal geometry scenario, while the *reduced*0.5 one must be compared with the startup scenario.

15.3 Luminosity

An error of 11% is assigned to the determination of LHC luminosity [67]. This systematic uncertainty is in common to all our cross section measurements, and will be quoted separately from other systematic errors.

15.4 Systematic uncertainty summary

The different sources of systematic uncertainties for muon channel and electron channel cross sections are summarized in Table 30 and 31 respectively.

Table 30: Table of systematic uncertainties for the muon channels. Dashed entries are either not applicable to the channel or negligible.

Source	W channel (%)	Z channel (%)
Muon reconstruction/identification	3	3.8
Trigger efficiency	2	0.8
Isolation efficiency	0.5	1.0
Muon momentum scale/resolution	1	0.5
$\not{E}_T$ scale/resolution	0.5	-
Background subtraction	2	-
PDF uncertainty in acceptance	2	2
Other theoretical uncertainties	0.5	0.5
TOTAL (without luminosity uncertainty)	4.8	4.6
Luminosity	11	11

Table 31: Table of systematic uncertainties for the electron channels. Dashed entries are either not applicable to the channel or negligible.

Source	W channel (%)	Z channel (%)
Electron reconstruction/identification	8.6	12.3
Trigger efficiency	0.7	< 0.01
Isolation efficiency	1.2	1.1
Electron momentum scale/resolution	2.1	-
$\not{E}_T$ scale/resolution	1.9	-
Background subtraction	1.0	-
PDF uncertainty in acceptance	2.0	2.0
Other theoretical uncertainties	0.5	0.5
TOTAL (without luminosity uncertainty)	10.2	14.2
Luminosity	11.0	11.0

16 Results

16.1 Cross Section Measurements

Wenu:37.7nb^{-1}; Zee:53.2nb^{-1}Wmunu:37.7nb^{-1}; Zmumu:198nb^{-1};

We report in this Section the cross section measurements including the systematic uncertainties evaluated in Section 15. Presented results are to be compared with theoretical predictions summarized in Tab. 32, that contains standard model predictions at NNLO accuracy. The theoretical undertainty on the standard model predictions includes the scale uncertainty, determined by varying independently the factorization and renormalization scale ($\Delta\sigma_{\mu}$ in the table), and the uncertainty due to the PDFs and to the value of α_S used in the PDF fits ($\Delta\sigma_{PDF+\alpha_S}$ in the table). The PDFs and α_S error has been determined conservatively at NLO for three PDF sets, MSTW2008, CTEQ66 and NNPDF2.0, according to the prescriptions in [12, 68, 69] Errors obtained in this way are then combined according to the PDF4LHC prescription [57]. PDF+α_S error and scale uncertainty are summed in quadrature to obtain the combined error ($\Delta\sigma_{NNLO}$ in the table)

process	σ_{NNLO} (nb)	$\Delta\sigma_{\mathrm{PDF}+\alpha_s}$ (nb)	$\Delta\sigma_{\mu}$ (nb)	$\Delta\sigma_{\mathrm{NNLO}}$ (nb)
$\mathrm{pp} \to \mathrm{W}^- \to \ell^- \bar{\nu}$	4.286	± 0.218	± 0.58	± 0.226
$\mathrm{pp} \to \mathrm{W}^+ \to \ell^+ \nu$	6.152	± 0.283	± 0.78	± 0.294
$\mathrm{pp} \to \mathrm{W} \to \ell\nu$	10.438	± 0.501	± 0.136	± 0.519
$\mathrm{pp} \to \mathrm{Z}/\gamma^* \to \ell^-\ell^+$ 60 GeV $< m_{\ell\ell} <$ 120 GeV	0.972	± 0.041	± 0.011	± 0.042

Table 32: Standard model expected W and Z cross sections with their theoretical uncertainty.

In Section 5 the $\mathrm{W} \to \mu\nu$ cross section was extracted. Adding systematic uncertainties, we obtain:

$$\boxed{\sigma(\mathrm{pp} \to \mathrm{W} + X \to \mu\nu + X) = (10.0 \pm 0.8(stat) \pm 0.5(syst) \pm 1.1(lumi))\,\mathrm{nb}\,.} \tag{31}$$

Adding systematics uncertainties to the $\mathrm{Z} \to \mu^+\mu^-$ cross section extraction from Section 6, limited to the $\mu^+\mu^-$ invariant mass interval $60 < m_{\mu^+\mu^-} < 120\,\mathrm{GeV}/c^2$, we obtain

$$\boxed{\sigma(\mathrm{pp} \to \mathrm{Z}(\gamma^*) + X \to \mu^+\mu^- + X) = (0.88 \pm 0.10(stat) \pm 0.04(syst) \pm 0.10(lumi))\,\mathrm{nb}\,.} \tag{32}$$

The inclusive $\mathrm{W} \to e\nu$ cross section from Section 12, including systematic uncertainties, is:

$$\boxed{\sigma(\mathrm{pp} \to \mathrm{W} + X \to e\nu + X) = (9.4 \pm 0.8(stat) \pm 1.1(syst) \pm 1.0(lumi))\,\mathrm{nb}\,,} \tag{33}$$

and the inclusive $\mathrm{Z} \to \mathrm{e}^+\mathrm{e}^-$ cross section from Section 13, limited to the $\mathrm{e}^+\mathrm{e}^-$ invariant mass interval $60 < m_{\mathrm{e}^+\mathrm{e}^-} < 120\,\mathrm{GeV}/c^2$, is:

$$\boxed{\sigma(\mathrm{pp} \to \mathrm{Z}(\gamma^*) + X \to \mathrm{e}^+\mathrm{e}^- + X) = (1.10 \pm 0.26(stat) \pm 0.17(syst) \pm 0.12(lumi))\,\mathrm{nb}\,.} \tag{34}$$

Within the still large statistical uncertainty, the results are in agreement with NNLO SM cross section predictions, and cross section measurements in the muon and electron channels are in agreement.

The results in the two lepton channels are combined in the following way. First, the statistical and systematic errors in the two channels are assumed to be uncorrelated (a good approximation, since the correlated pieces like PDFs and MET are small compared to lepton efficiency systematics), and the luminosity error is 100% correlated. Then the two results can be combined via a weighted least squares average. The central value is given by:

$$\sigma_W = (\sigma_{W,e}/\delta\sigma^2_{W,e} + \sigma_{W,\mu}/\delta\sigma^2_{W,\mu})/S\,, \tag{35}$$

$$S = (1/\delta\sigma^2_{W,e} + 1/\delta\sigma^2_{W,\mu}) \tag{36}$$

and the statistcial and systematic errors of the combined result by

$$\delta\sigma_W = 1/\sqrt{(1/\delta\sigma^2_{W,e} + 1/\delta\sigma^2_{W,\mu})}\,. \tag{37}$$

This results in the combined cross sections

$$\boxed{\sigma(\mathrm{pp} \rightarrow \mathrm{W} + X \rightarrow \ell\nu + X) = (9.8 \pm 0.6(stat) \pm 0.5(syst) \pm 1.1(lumi))\,\mathrm{nb}\,.} \tag{38}$$

[WARNING: to be updated with the new Zmm cross section]

$$\boxed{\sigma(\mathrm{pp} \rightarrow \mathrm{Z}(\gamma^*) + X \rightarrow \ell^+\ell^- + X) = (1.05 \pm 0.17(stat) \pm 0.05(syst) \pm 0.12(lumi))\,\mathrm{nb}\,.} \tag{39}$$

The corresponding results for $\mathrm{W}^+ \rightarrow \ell^+\nu$ and $\mathrm{W}^- \rightarrow \ell^-\overline{\nu}$ production are:

$$\begin{aligned}
\sigma(\mathrm{pp} \rightarrow \mathrm{W}^+ + X \rightarrow \mu^+\nu_\mu + X) &= 6.7 \pm 0.7(\mathrm{stat.}) \pm 0.3(\mathrm{syst.}) \pm 0.7(\mathrm{lumi.})\ \mathrm{nb},\\
\sigma(\mathrm{pp} \rightarrow \mathrm{W}^+ + X \rightarrow \mathrm{e}^+\nu_e + X) &= 5.2 \pm 0.6(\mathrm{stat.}) \pm 0.6(\mathrm{syst.}) \pm 0.6(\mathrm{lumi.})\ \mathrm{nb},\\
\sigma(\mathrm{pp} \rightarrow \mathrm{W}^+ + X \rightarrow \ell^+\nu + X) &= 6.0 \pm 0.5(\mathrm{stat.}) \pm 0.3(\mathrm{syst.}) \pm 0.7(\mathrm{lumi.})\ \mathrm{nb}.
\end{aligned}$$

$$\begin{aligned}
\sigma(\mathrm{pp} \rightarrow \mathrm{W}^- + X \rightarrow \mu^-\overline{\nu}_\mu + X) &= 3.6 \pm 0.5(\mathrm{stat.}) \pm 0.2(\mathrm{syst.}) \pm 0.4(\mathrm{lumi.})\ \mathrm{nb},\\
\sigma(\mathrm{pp} \rightarrow \mathrm{W}^- + X \rightarrow \mathrm{e}^-\overline{\nu}_e + X) &= 4.2 \pm 0.6(\mathrm{stat.}) \pm 0.4(\mathrm{syst.}) \pm 0.5(\mathrm{lumi.})\ \mathrm{nb},\\
\sigma(\mathrm{pp} \rightarrow \mathrm{W}^- + X \rightarrow \ell^-\overline{\nu} + X) &= 3.8 \pm 0.4(\mathrm{stat.}) \pm 0.2(\mathrm{syst.}) \pm 0.4(\mathrm{lumi.})\ \mathrm{nb}.
\end{aligned}$$

16.2 Cross Section Ratios

The cross section ratio of W and Z is given by:

$$\sigma(W)/\sigma(Z(\gamma^*)) = \frac{N_W}{N_Z}\frac{\varepsilon_Z}{\varepsilon_W}\frac{A_Z}{A_W}\,.$$

Standard model expectation computed at NNLO are given in Tab. 33. The theoretical uncertainty has been derived according to the same prescriptions described earlier for the cross section predictions, having the ratio in this case as the observable under study. The scale uncertainty was not calculated in this case.

The uncertainty from $\frac{N_W}{N_Z}$ is determined by combining the respective statistical errors of the individual cross sections. The uncertainty from $\frac{\varepsilon_Z}{\varepsilon_W}$ is determined by the relative error in the W signal efficiency. The uncertainty from $\frac{A_Z}{A_W}$ is determined from MC generator studies to be 2.6%. The two different decay channels are combined by assuming fully correlated uncertainty

	R_{NNLO}	$\Delta R_{\text{PDF}+\alpha_s}$
W^+/W^-	1.435	± 0.044
W/Z	10.739	± 0.043

Table 33: Standard model expected W+/W- and W/Z cross section ratios with their theoretical uncertainty.

for the acceptance factor, with other uncertainties assumed uncorrelated. This results in the measurements: **[WARNING: to be updated with the new Zmm cross section]**

$$\sigma(\text{pp} \to \text{W} + X \to \mu\nu + X)/\sigma(\text{pp} \to \text{Z}(\gamma^*) + X \to \mu^+\mu^- + X) = 9.7 \pm 2.3(\text{stat.}) \pm 0.5(\text{syst.})\,,$$
$$\sigma(\text{pp} \to \text{W} + X \to \text{e}\nu + X)/\sigma(\text{pp} \to \text{Z}(\gamma^*) + X \to \text{e}^+\text{e}^- + X) = 8.5 \pm 2.2(\text{stat.}) \pm 1.0(\text{syst.})\,,$$
$$\sigma(\text{pp} \to \text{W} + X \to \ell\nu + X)/\sigma(\text{pp} \to \text{Z}(\gamma^*) + X \to \ell^+\ell^- + X) = 9.2 \pm 1.6(\text{stat.}) \pm 0.5(\text{syst.})\,.$$

The cross section ratio of W^+ and W^- is given by

$$\sigma(W^+)/\sigma(W^-) = \frac{N_{W^+}}{N_{W^-}} \frac{\varepsilon_{W^-}}{\varepsilon_{W^+}} \frac{A_{W^-}}{A_{W^+}}$$

The uncertainty from $\frac{N_{W+}}{N_{W-}}$ is determined by combining the respective statistical errors of the individual cross sections (accounting also for correlations in the yield ratio in the combined fit performed for $\text{W} \to \text{e}\nu$). The uncertainty from $\frac{\varepsilon_{W-}}{\varepsilon_{W+}}$ is determined from propagating uncertainties in the regional efficiency correction factors into the efficiency ratio estimation; this results in a 1.2% uncertainty in $\text{W} \to \text{e}\nu$ and a negligible uncertainty in $\text{W} \to \mu\nu$. The uncertainty from $\frac{A_{W-}}{A_{W+}}$ is determined from MC generator studies to be 2.9%. The two different decay channels are combined by assuming fully correlated uncertainty for the acceptance factor, with other uncertainties assumed uncorrelated. This results in the measurements

$$\sigma(\text{W}^+ \to \mu^+\nu_\mu)/\sigma(\text{W}^- \to \mu^-\overline{\nu}_\mu) = 1.86 \pm 0.31(\text{stat.}) \pm 0.05(\text{syst.})$$
$$\sigma(\text{W}^+ \to \text{e}^+\nu_e)/\sigma(\text{W}^- \to \text{e}^-\overline{\nu}_e) = 1.24 \pm 0.21(\text{stat.}) \pm 0.04(\text{syst.})$$
$$\sigma(\text{W}^+ \to \ell^+\nu)/\sigma(\text{W}^- \to \ell^-\overline{\nu}) = 1.44 \pm 0.18(\text{stat.}) \pm 0.04(\text{syst.})$$

References

[1] M. Dittmar, F. Pauss, and D. Zurcher, "Towards a precise parton luminosity determination at the CERN LHC", *Phys. Rev.* **D56** (1997) 7284–7290, `arXiv:hep-ex/9705004`. `doi:10.1103/PhysRevD.56.7284`.

[2] V. A. Khoze, A. D. Martin, R. Orava et al., "Luminosity monitors at the LHC", *Eur. Phys. J.* **C19** (2001) 313–322, `arXiv:hep-ph/0010163`. `doi:10.1007/s100520100616`.

[3] W. T. Giele and S. A. Keller, "Hard scattering based luminosity measurement at hadron colliders", `arXiv:hep-ph/0104053`.

[4] M. W. Krasny, F. Fayette, W. Placzek et al., "Z-boson as 'the standard candle' for high precision W- boson physics at LHC", *Eur. Phys. J.* **C51** (2007) 607–617, `arXiv:hep-ph/0702251`. `doi:10.1140/epjc/s10052-007-0321-8`.

[5] R. Hamberg, W. L. van Neerven, and T. Matsuura, "A Complete calculation of the order α_s^2 correction to the Drell-Yan K factor", *Nucl. Phys.* **B359** (1991) 343–405. `doi:10.1016/0550-3213(91)90064-5`.

[6] C. Anastasiou, L. J. Dixon, K. Melnikov et al., "Dilepton rapidity distribution in the Drell-Yan process at NNLO in QCD", *Phys. Rev. Lett.* **91** (2003) 182002, `arXiv:hep-ph/0306192`. `doi:10.1103/PhysRevLett.91.182002`.

[7] C. Anastasiou, L. J. Dixon, K. Melnikov et al., "High precision QCD at hadron colliders: Electroweak gauge boson rapidity distributions at NNLO", *Phys. Rev.* **D69** (2004) 094008, `arXiv:hep-ph/0312266`. `doi:10.1103/PhysRevD.69.094008`.

[8] K. Melnikov and F. Petriello, "The W boson production cross section at the LHC through $O(\alpha_s^2)$", *Phys. Rev. Lett.* **96** (2006) 231803, `arXiv:hep-ph/0603182`. `doi:10.1103/PhysRevLett.96.231803`.

[9] K. Melnikov and F. Petriello, "Electroweak gauge boson production at hadron colliders through O(alpha(s)**2)", *Phys. Rev.* **D74** (2006) 114017, `arXiv:hep-ph/0609070`. `doi:10.1103/PhysRevD.74.114017`.

[10] S. Catani and M. Grazzini, "An NNLO subtraction formalism in hadron collisions and its application to Higgs boson production at the LHC", *Phys. Rev. Lett.* **98** (2007) 222002, `arXiv:hep-ph/0703012`. `doi:10.1103/PhysRevLett.98.222002`.

[11] A. D. Martin, W. J. Stirling, R. S. Thorne et al., "Parton distributions for the LHC", *Eur. Phys. J.* **C63** (2009) 189–285, `arXiv:0901.0002`. `doi:10.1140/epjc/s10052-009-1072-5`.

[12] A. D. Martin, W. J. Stirling, R. S. Thorne et al., "Uncertainties on $alpha_S$ in global PDF analyses and implications for predicted hadronic cross sections", *Eur. Phys. J.* **C64** (2009) 653–680, `arXiv:0905.3531`. `doi:10.1140/epjc/s10052-009-1164-2`.

[13] N.E. Adam, V. Halyo and S.A. Yost, *JHEP*, **05** (2008) 062.

[14] N.E. Adam, V. Halyo, S.A. Yost, and W.-H. Zhu, *JHEP*, **09** (2008) 133.

[15] CDF II Collaboration, "First measurements of inclusive W and Z cross sections from Run II of the Tevatron collider", *Phys. Rev. Lett.* **94** (2005) 091803, `arXiv:hep-ex/0406078`. `doi:10.1103/PhysRevLett.94.091803`.

[16] CDF Collaboration, "The transverse momentum and total cross section of e^+e^- pairs in the Z boson region from $p\bar{p}$ collisions at $\sqrt{s} = 1.8$ TeV", *Phys. Rev. Lett.* **84** (2000) 845–850, arXiv:hep-ex/0001021. doi:10.1103/PhysRevLett.84.845.

[17] D0 Collaboration, "Extraction of the width of the W boson from measurements of $\sigma(p\bar{p} \to W + X) \times B(W \to e\nu)$ and $\sigma(p\bar{p} \to Z + X) \times B(Z \to ee)$ and their ratio", *Phys. Rev.* **D61** (2000) 072001, arXiv:hep-ex/9906025. doi:10.1103/PhysRevD.61.072001.

[18] UA2 Collaboration, "Measurement of W and Z Production Cross-Sections at the CERN $\bar{p}p$ Collider", *Z. Phys.* **C47** (1990) 11–22. doi:10.1007/BF01551906.

[19] UA1 Collaboration, "Studies of Intermediate Vector Boson Production and Decay in UA1 at the CERN Proton - Antiproton Collider", *Z. Phys.* **C44** (1989) 15–61. doi:10.1007/BF01548582.

[20] S. Alioli, P. Nason, C. Oleari et al., "NLO vector-boson production matched with shower in POWHEG", *JHEP* **07** (2008) 060, arXiv:0805.4802. doi:10.1088/1126-6708/2008/07/060.

[21] P. Nason, "A new method for combining NLO QCD with shower Monte Carlo algorithms", *JHEP* **11** (2004) 040, arXiv:hep-ph/0409146. doi:10.1088/1126-6708/2004/11/040.

[22] S. Frixione, P. Nason, and C. Oleari, "Matching NLO QCD computations with Parton Shower simulations: the POWHEG method", *JHEP* **11** (2007) 070, arXiv:0709.2092. doi:10.1088/1126-6708/2007/11/070.

[23] T. Sjostrand, S. Mrenna, and P. Z. Skands, "PYTHIA 6.4 Physics and Manual", *JHEP* **05** (2006) 026, arXiv:hep-ph/0603175.

[24] GEANT4 Collaboration, "GEANT4: A simulation toolkit", *Nucl. Instrum. Meth.* **A506** (2003) 250–303. doi:10.1016/S0168-9002(03)01368-8.

[25] J. Allison et al., "Geant4 developments and applications", *IEEE Trans. Nucl. Sci.* **53** (2006) 270. doi:10.1109/TNS.2006.869826.

[26] VBTF TWiki, Reference MC samples: https://twiki.cern.ch/twiki/bin/viewauth/CMS/EWKVBTF#Reference_MC_samples_for_sqrt_s.

[27] G. Abbiendi, N. Adam, J. Alcaraz et al., "Muon Reconstruction in the CMS Detector", *CMS Note* **2008/097** (2008).

[28] M. Mulders, I. Bloch, E. James et al., "Muon Identification in CMS", *CMS Note* **2008/098** (2008).

[29] ref:phil-recoil.

[30] M. De Gruttola, A. De Cosa, S. Di Guida et al., "Determination of the $pp \to ZX \to \mu^+\mu^- X$ inclusive cross section with a simultaneous fit of Z yield, muon reconstruction efficiencies and High Level Trigger efficiency", *CMS Note* **2009/005** (2009).

[31] J. Campbell and R.K. Ellis, Monte Carlo for FeMtobarn processes, http://mcfm.fnal.gov/.

[32] S. Clopper, C. J.and Pearson, "The use of confidence or fiducial limits illustrated in the case of the binomial", *Biometrika* **26** (1934) 404–413.

[33] TagAndProbe.

[34] RndmCone.

[35] W. Adam et al., "Electron Reconstruction in CMS", *CMS Analysis Note* **2009/164** (2008).

[36] F. Beaudette et al., "Electron Reconstruction within the Particle Flow Algorithm", *CMS Analysis Note* **2010/034** (2010).

[37] C. Collaboration, "Electron reconstruction and identification at sqrt(s) = 7 TeV", *CMS PAS* **EGM-10-004** (2010).

[38] X. Claude et al., "For EGM-10-004", *CMS Analysis Note* **2010/XXX** (2010).

[39] S. Baffioni et al., "Electron Identification in CMS", *CMS Analysis Note* **2009/178** (2009).

[40] D. Barge et al., "Study of photon conversion rejection at CMS", *CMS Analysis Note* **2009/159** (2009).

[41] G. Daskalakis et al., "Data driven selection cut tuning for electrons", *CMS Analysis Note* **2009/108** (2009).

[42] Needs to be fixed... .

[43] M. Pivk and F. R. Le Diberder, "sPlot: a statistical tool to unfold data distributions", *Nucl. Instrum. Meth.* **A555** (2005) 356–369, `arXiv:physics/0402083`. `doi:10.1016/j.nima.2005.08.106`.

[44] recoil.

[45] D. E. Collins, J. C.and Soper, "Angular distribution of dileptons in high-energy hadron collisions", *Phys. Rev. D* **16** (1977) 2219.

[46] C. Collaboration, "Electromagnetic calorimeter calibration with 7 TeV data", *CMS PAS* **EGM-10-003** (2010).

[47] G. A. Ladinsky and C. P. Yuan, "The Nonperturbative regime in QCD resummation for gauge boson production at hadron colliders", *Phys. Rev.* **D50** (1994) 4239, `arXiv:hep-ph/9311341`. `doi:10.1103/PhysRevD.50.R4239`.

[48] C. Balazs, J.-w. Qiu, and C. P. Yuan, "Effects of QCD resummation on distributions of leptons from the decay of electroweak vector bosons", *Phys. Lett.* **B355** (1995) 548–554, `arXiv:hep-ph/9505203`. `doi:10.1016/0370-2693(95)00726-2`.

[49] C. Balazs and C. P. Yuan, "Testing multiple gluon dynamics at the Tevatron", *Phys. Rev. Lett.* **79** (1997) 2398–2401, `arXiv:hep-ph/9703405`. `doi:10.1103/PhysRevLett.79.2398`.

[50] C. Balazs and C. P. Yuan, "Soft gluon effects on lepton pairs at hadron colliders", *Phys. Rev.* **D56** (1997) 5558–5583, `arXiv:hep-ph/9704258`. `doi:10.1103/PhysRevD.56.5558`.

[51] F. Landry, R. Brock, P. M. Nadolsky et al., "Tevatron Run-1 Z boson data and Collins-Soper-Sterman resummation formalism", *Phys. Rev.* **D67** (2003) 073016, arXiv:hep-ph/0212159. doi:10.1103/PhysRevD.67.073016.

[52] A. V. Konychev and P. M. Nadolsky, "Universality of the Collins-Soper-Sterman nonperturbative function in gauge boson production", *Phys. Lett.* **B633** (2006) 710–714, arXiv:hep-ph/0506225. doi:10.1016/j.physletb.2005.12.063.

[53] P. M. Nadolsky et al., "Implications of CTEQ global analysis for collider observables", *Phys. Rev.* **D78** (2008) 013004, arXiv:0802.0007. doi:10.1103/PhysRevD.78.013004.

[54] R. D. Ball et al., "A first unbiased global NLO determination of parton distributions and their uncertainties", arXiv:1002.4407.

[55] J. Alcaraz, https://twiki.cern.ch/twiki/bin/view/CMS/SWGuideEWKUtilities#PDF_SYSTEMATICS_

[56] J. Alcaraz et al., "Accurate cross section estimates for key Standard Model processes in proton-proton collisions at $\sqrt{s} = 7$ TeV", CMS NOTE 2010/XXX.

[57] PDF4LHC web page, http://www.hep.ucl.ac.uk/pdf4lhc/.

[58] C. M. Carloni Calame, G. Montagna, O. Nicrosini et al., "Precision electroweak calculation of the production of a high transverse-momentum lepton pair at hadron colliders", *JHEP* **10** (2007) 109, arXiv:0710.1722. doi:10.1088/1126-6708/2007/10/109.

[59] C. M. Carloni Calame, G. Montagna, O. Nicrosini et al., "Precision electroweak calculation of the charged current Drell-Yan process", *JHEP* **12** (2006) 016, arXiv:hep-ph/0609170.

[60] C. M. Carloni Calame, G. Montagna, O. Nicrosini et al., "Multiple photon corrections to the neutral-current Drell- Yan process", *JHEP* **05** (2005) 019, arXiv:hep-ph/0502218.

[61] C. M. Carloni Calame, G. Montagna, O. Nicrosini et al., "Higher-order QED corrections to W-boson mass determination at hadron colliders", *Phys. Rev.* **D69** (2004) 037301, arXiv:hep-ph/0303102. doi:10.1103/PhysRevD.69.037301.

[62] V. Blobel and C. Kleinwort, "New Method for the High-Precision Alignment of Track Detectors", *Proceedings of the Conference on Advanced Statistical Techniques in Particle Physics, Durham (UK) e- print: hep-ex/0208021* (2002).

[63] V. Karimaki, T. Lampen, and F. P. Schilling, "The HIP Algorithm for Track Based Alignment and its Application to the CMS Pixel Detector", *CMS Note 2006/018* (2006).

[64] T. C. collaboration, "Alignment of the CMS Silicon Tracker during Commissioning with Cosmic Rays", *JINST 5:T03009* (2010).

[65] D. N. Brown, A. V. Gritsan, Z. J. Guo et al., "Local Alignment of the BABAR Silicon Vertex Tracker", *Nucl. Instr. Methods Phys. Res.* **A 603**, *467* (2009).

[66] charge-ratio.

[67] CMS PAS on Luminosiy.

[68] H.-L. Lai et al., "Uncertainty induced by QCD coupling in the CTEQ-TEA global analysis of parton distributions", arXiv:1004.4624.

[69] F. Demartin, S. Forte, E. Mariani et al., "The impact of PDF and alphas uncertainties on Higgs Production in gluon fusion at hadron colliders", *Phys. Rev.* **D82** (2010) 014002, arXiv:1004.0962. doi:10.1103/PhysRevD.82.014002.

[70] I. Shipsey and N. Leonardo, "Measurement of the Inclusive Upsilon production cross section in pp collisions at $\sqrt{s}$=7 TeV", *CMS Note* **2010/140** (2010).

[71] S. Bolognesi, M. A. Borgia, R. Castello et al., "Calibration of track momentum using dimuon resonances in CMS", *CMS Note AN-2010/059* **2010/059** (2010).

[72] CMS Collaboration, Onia PAS, 2010.

[73] tracker-pas.

[74] J. Santaolalla, M. Cepeda, C. Diez Pardos et al., "Understanding the muon transverse momentum resolution in CMS using pp-¿mumu + X events", *CMS AN-2010/105* (2010).

[75] C. Diez-Pardos, "Comparison between Pythia and ResBos for LHC Z production", *PH-Generators Tools,27-Nov-2008* **PythiaResBosComparison** (2008).

[76] C. Diez-Pardos, "Update on the comparison between Pythia and ResBos for LHC Z production", *EWK MuonMeeting, 26-Mar-2009* **PythiaResBosComparisonUpdate** (2009).

[77] M. Mulders, I. Bloch, E. James et al., "Study of Data-Driven Methods For Estimation of Fake Lepton Backgrounds", *CMS Note* **2009/120** (2009).

[78] Particle Data Group Collaboration, "The Review of Particle Physics", *Physics Letters* **B667** (2008 and partial update for the 2010 edition (http://pdg.lbl.gov)) 1.

[79] ref:abcd.

[80] W. Verkerke and D. Kirkby, "The RooFit toolkit for data modeling", *proceedings ofComputing in High Energy and Nuclear Physics, La Jolla, California* (2003) 24–28 March.

A Muon identification efficiency determination

Section 3 described the criteria adopted for muon identification. In particular, Eq. 1 described the parametrization of muon identification efficiency as:

$$\epsilon_{\mathrm{ID}} = \epsilon_{\mathrm{trk}} \times (\epsilon_{\mathrm{gbl+}} | \epsilon_{\mathrm{trk+}}) \times \prod_i \epsilon_i \,, \tag{40}$$

where ϵ_{trk} is the TRK muon efficiency, $\epsilon_{\mathrm{gbl+}} | \epsilon_{\mathrm{trk+}}$ is the GLB muon efficiency given a TRK muon with its selection cuts exists and ϵ_i is the efficiency of each of the remaining selection criteria (applied on TRK and GLB muons) of the muon identification.

To achieve an overall muon ID efficiency fully based on data the best suited algorithm is the so called Tag and Probe (T&P) method. It utilizes well known di-muon decays, for example $Z \to \mu\mu$, to provide a statistically pure sample of probe objects. It pairs well identified muons called Tags with the Probes (muon candidates).

With the integrated luminosity collected thus far the available Z statistics is not sufficiently large to allow via the T&P method a precise determination of the muon efficiencies. Therefore, for this time being, we are forced to use an extraction of the muon efficiencies based on MC in the momentum range of the EWK physics. However, in the lower tail of the muon p_T spectrum (10-30 GeV/c) there is an overlap with the momentum of the muons coming from the decay of the Y resonance. Profiting for the much larger Y production cross section we can define this low momentum range as a data-driven control region for the MC-based efficiency extraction. Inside the control region Z and Y probes have different kinematics; thus, a reweighting of the probe spectra is needed; this method has been already applied in data, as it is explained in [70].

At integrated luminosity of $\sim 100\,\text{nb}^{-1}$ we expect at best 5% statistical uncertainty of the cross-section measurements. Thus we need to provide an estimate of the cut efficiencies with accuracy at below the % level. More precisely, we need to make sure the relevant discrepancies between the data and the MC are at below the % level or we need to be able to account for them with this precision.

In the early analyzes we have to make use of a wider sample of muons than tentatively available in the signal samples. From them we are extracting the muon ID efficiencies and, comparing with MC, the correction factors which need to be applied to the analysis. The general procedure for each of the selection variables (cuts) is the following.

- The muon momentum criteria are relaxed with the initial idea that muon properties have no strong dependence on the transverse momentum. This is to be explicitly verified by estimating the efficiencies as a function of p_T and η. With the relaxed selection the increase of the muon statistics is significant - the main contribution being from QCD processes.
- All the muon ID selection criteria but the one under investigation are applied. This makes the muon as close to the ones desired for physics analysis as possible. Additional limited (and not correlated) selection could be applied serving the purpose above.
- The variable under investigation is compared with MC. The difference in the fraction of events under (above) the cut(s) applied in the selection is the first approximation to the efficiency correction to this cut.
- An estimate of correlations between variables are to be directly obtained by counting the accepted (rejected) events from each cut given that all the others passed and comparing the outcomes with each other (and with the full selection). In addition correlations are to be tentatively searched for. Taking these into account gives the second approximation to the efficiency corrections.

This general algorithm is applied with necessary case-by-case modifications in the way described below. What is important at the end are the relevant deviations from MC.

- **TRK muon efficiency**: A good quality standalone (STA) muon with a minimum transverse momentum requirement (it could not be too low) is selected. "Good quality" includes $\chi 2/NDF$, number of valid hits in the fit, no other STA muons, no unused segments and impact parameter requirements. The lower part of the detector is separately probed (as significantly less sensitive to cosmic muons). Then if no TRK muon is found this is counted as TRK muon inefficiency (there are no any requirements on the TRK muon). In addition, muons which are STA and GLB (with quality cuts) but not TRK are counted separately (normalized to muons which are STA and GLB). This latter definition should lead to consistently higher observed efficiency.
- **STA (GLB) muon efficiency**: A good quality TRK muon with a minimum trans-

verse momentum requirement is selected. It should pass all the TRK muon selection requirements for the muon ID described earlier. There should be only one such a muon in the event. Then if no STA (GLB) muon is found this is counted as STA (GLB) muon inefficiency (there are no any requirements on the STA/GLB muons). In addition, muons which are TRK and STA but not GLB are counted separately (normalized to muons which are TRK and STA). This latter definition should lead to consistently higher observed efficiency and gives the link to the full TRK*GLB efficiency.

- **Number of hits in the tracker track and number of pixel hits in the tracker track - cuts efficiency**: The general algorithm is directly applicable for each of the two. However these cuts are unique for their role in rejecting decays in flight but also low quality tracks. These have potentially strong Pt dependence which need to be closely monitored - lower momentum discrepancy between data and MC does not necessarily mean discrepancy for physics. In first approximation however we should take the discrepancy from the low momentum estimate and plug it in the systematic error expectations. On the other hand we do expect that the "physics" muons will not be so affected by these cuts This needs to be checked on tightly selected muons from W and Z decays.
- **Number of "matching" segments -cut efficiency**: It could also be affected by lower momentum discrepancies but in much lower degree. What is more probable is to encounter an alignment discrepancy between the tracker and the muon chambers or the muon chambers themselves. It could also point to magnetic field deviations or (less probable) muon hit uncertainty deviations. Inefficiency regions of the detector would also affect it. The efficiency procedure is directly applied.
- **Number of muon hits and $\chi 2/NDF$ in the GLB muon - cut efficiency**: These are other variables sensitive to the alignment of the detector and the rest of the cases just mentioned. The efficiency procedure is directly applied.
- **Impact parameter - cut efficiency**: For well reconstructed muons from W or Z decays the impact parameter with respect to the beam spot is expected to be well within the applied cut. This is also to be verified on tightly selected muons from W and Z decays.

Having collected enough data all efficiencies are to be parametrized as a function of η and p_T. Currently the only sensible separation possible is to provide estimations for the barrel, endcap and the overlap regions. The numbers extracted from data and appropriate MC samples are summarized in Tab. 34.

The correction factors to be applied to the muon reconstruction efficiency are obtained by assuming universal ratio of signal data and MC factors being valid for the current data and the QCD sample as well, i.e. $Corr = \epsilon(data)/\epsilon(ppMuX)$. The overall correction factor is obtained by multiplying all the single ones according to Eq. 1. The uncertainties of the single cut factors are summed in quadrature for the final result. However, as studies have shown, the matching segments selection criterion could be overestimated due to the nature of the QCD samples (data and MC). There is not negligible amount of punch-through particles reaching the second muon station (and the matching segments is one of the ways to suppress them). To account for this we investigated the effect of more stringent criteria like the presence of segment(s) beyond the second station. This does provide better agreement but could be also a way to mask out existing detector inefficiencies. For this reason we stay with the current estimate based on asking (as an additional requirement) for the existence of segment(s) beyond the first muon station

	matched chambers	tracker hits	pixel hits	muon hits	χ^2/NDF
data ($\|\eta\| < 0.9$)	$95.7^{+0.7}_{-0.8}$	$99.2^{+0.3}_{-0.4}$	$99.5^{+0.2}_{-0.3}$	$97.1^{+0.6}_{-0.7}$	$98.5^{+0.4}_{-0.5}$
$pp \to \mu + X$ ($\|\eta\| < 0.9$)	97.6 ± 0.2	99.7 ± 0.1	99.6 ± 0.1	99.3 ± 0.1	99.8 ± 0.1
$W \to \mu\nu$ ($\|\eta\| < 0.9$)	98.6	100.0	99.7	99.2	99.7
data ($0.9 < \|\eta\| < 1.2$)	$99.0^{+0.6}_{-0.9}$	$99.5^{+0.4}_{-0.8}$	$100.0^{+0}_{-0.6}$	$99.0^{+0.6}_{-0.9}$	$100.0^{+0}_{-0.6}$
$pp \to \mu + X$ ($0.9 < \|\eta\| < 1.2$)	98.3 ± 0.3	99.3 ± 0.2	99.7 ± 0.1	99.6 ± 0.1	99.9 ± 0.1
$W \to \mu\nu$ ($0.9 < \|\eta\| < 1.2$)	98.7	100.0	99.7	99.8	99.8
data ($\|\eta\| > 1.2$)	$97.2^{+0.6}_{-0.8}$	$99.8^{+0.1}_{-0.3}$	$99.8^{+0.1}_{-0.3}$	$99.0^{+0.4}_{-0.5}$	$98.3^{+0.5}_{-0.6}$
$pp \to \mu + X$ ($\|\eta\| > 1.2$)	98.8 ± 0.1	99.6 ± 0.1	98.8 ± 0.1	98.9 ± 0.1	99.7 ± 0.1
$W \to \mu\nu$ ($\|\eta\| > 1.2$)	99.5	99.9	99.8	98.5	99.7

Table 34: Eefficiency for each of the cuts, in %. The efficiency for each cut (column) is estimated with all the other cuts applied as explained. These are shown for different data and Monte Carlo samples and three $|\eta|$ regions (muon barrel, endcap and overlap). The selection here includes the following cuts: $p_T > 12$ GeV/c, $|\eta| < 2.1$. The statistical errors from the $W_{\mu\nu}$ sample are smaller that the last significant digit.

which should be always the case for higher P_T muons. We increase the upper bound of the uncertainty by 0.3% to take into account possible deviations allowed by the test with the stringent selection. For the final estimates we "symmetrize" the error bars, meaning we take the middle of the uncertainty interval when quoting the correction factors and their uncertainties.

According to the $W_{\mu\nu}$ sample the correlations between all the variables listed leads to an additional correction in the range $(0.998, 1)$. This is to be verified on real signal muons but we do not consider it here as it is well within the current uncertainty ranges.

The efficiencies to find a global or tracker muons have strong dependence on p_T . These efficiencies are generally well reproduced by MC for high p_T muons. The TRK and GLB muon efficiencies as estimated on the available samples are given in Table 2. These are not separated in different η regions and the tracker muon part is based on a compromise with the minimal momentum requirement (which is unavoidably too low for now). Nevertheless, these give an estimate for the consistency between the data and MC. As the results show there are no discrepancies but conservatively we take the largest possible difference, counting the error bars, to be representative for the possible deviation coming from this source. This additional error to the correction factor is estimated to be ± 1.0% and applied to all the three η ranges.

The impact parameter selection contribution is negligible.

The resulting correction coefficients, accounting for the data and MC divergence in signal muons are presented in Table 35.

	$\|\eta\| < 0.9$	$0.9 < \|\eta\| < 1.2$	$\|\eta\| > 1.2$
Correction factors	$0.980 \pm 0.023 \pm 0.010$	$1.00 \pm 0.020 \pm 0.010$	$0.975 \pm 0.014 \pm 0.010$

Table 35: Correction factors for the muon ID efficiency. These are to be applied on MC muons to obtain the "real" efficiencies. The first error is statistical, the second one is explained in the text.

Comparison plots for η and p_T distributions and data/MC ratio after the muon ID selection are shown on figure 82. Normalization is to the number of data entries in the plots.

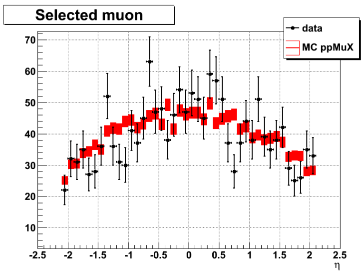

(a) η distribution

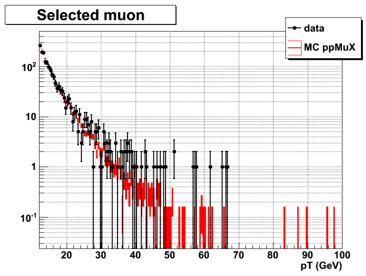

(b) p_T distribution

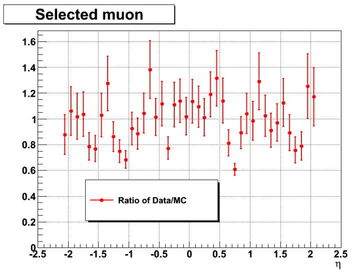

(c) Ratio of data/MC η distributions

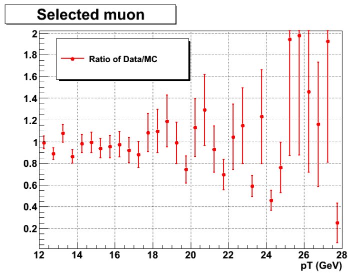

(d) Ratio of data/MC p_T distributions

Figure 82: Distributions after the muon ID selection (trigger is not applied). Uncertainties are Gaussian.

B Muon trigger efficiency determination

B.1 Dataset

We use two dataset with 7TeV collision data for trigger efficiency study:

- JetMET Tau triggered events (EWK group skim)
- Minimumbias triggered events.

B.2 L1 DT Efficiency

The basic detection unit in the Drift Tubes, which initiate the local DT L1 trigger sequence, is the DT cell. These cells are grouped in layers, having 12 of them per each DT station. The layers are arranged in three quartets (called super-layers), two of them measuring phi and one measuring the z (theta) coordinate. The local DT trigger collects the drift time information from 4 layers of DT and calculates track-segment position, angle and time in each superlayer. Results from the two phi-superlayers are combined, forming what is called as *correlated* trigger. This local information in each MB station is sent to the DT Track Finder (DTTF), which forms full tracks with defined p_T, η and ϕ and a trigger quality assigment. The Global Muon Trigger receives these candidates, after some ordering at the Muon DT Sorter.

The DT Trigger configuration used in the initial part of the 2010 collisions data taking is based on requiring the presence of a segment in a phi superlayer, with signals in all 4 layers, in at least two different MB stations, confirmed by a segment in a theta superlayer. This last requirement is not applied in the case of MB4 stations, which do not have a theta superlayer.

In order to perform correctly, the timing of all cells in all DT layers must be finely synchronized, in such a way that all hits belonging to a segment are properly assigned to it. A relatively good synchronization was already achieved during the different Cosmics data taking periods, but a finer one is needed now, given the different pattern of muons coming from collisions. According to the experts, the amount of muons needed for this task corresponds to a luminosity of 100 nb^{-1}.

Locally, at the level of a single station, the trigger efficiency is being studied extrapolating good quality reconstructed muons from the interaction point to a given chamber, looking for segments firing the trigger in the vicinity of it (in the same chamber). Results are still very preliminary as statistics are still very poor to obtain the efficiencies chamber by chamber in a reliable way.

In a more global way, the trigger efficiency is defined as the ratio of the number of offline reconstructed muons matched to a L1 Muon candidate to the whole set of offline reconstructed muons, in a given sample. Using this definition on two different data samples (Muon skim and JetMettau skim) and selecting good reconstructed muons according to the VBTF baseline selection, the trigger efficiency in the DT region ($|\eta| < 1.2$) is $\epsilon = 0.85 \pm xxx$

The L1 DT efficiency is shown in Figure 83 as a function of muon η. The result is compared to the MC prediction for the L1 DT Trigger efficiency, using the Trigger Emulator on pp$\rightarrow \mu$X and W Powheg samples.

Figure 83: L1 DT Efficiency as a function of muon eta.

A trigger candidate muon is matched to a reconstructed one if it lies in a cone of radius ΔR, where $\Delta R = \sqrt{(\Delta\phi)^2 + (\Delta\eta)^2} < xxx$. This distribution is shown in figure 84

Figure 84: $\Delta R = \sqrt{(\Delta\phi)^2 + (\Delta\eta)^2}$ distribution assigning DT trigger muon candidate to reconstructed muon.

B.3 L1 CSC Efficiency

B.3.1 Introduction

In this section we describe the performances of the L1 CSC Track Finder Trigger (CSCTF) [add reference to the TDR]. The CSCTF performances in terms of angular resolution, ϕ and η muon candidate assignment, and transverse momentum resolution, p_T assignment, as well as trigger efficiencies have been already part on extensive studies during the Cosmics data taking during winter 2008 and the results have been published in [reference to the Jinst Paper].

We will now review the operational status of the CSCTF in light of the 2010 collisions data recorded by CMS. In particular the studies reported are meant to investigate the CSCTF efficiencies to trigger given a reconstructed object. Due to the nature of the analysis for the $Z \to \mu\mu$ and $W \to \mu\nu$, we focused on the efficiency of triggering high quality reconstructed object, defined in CMS jargon as global muon [reference to offline reconstruted muons note].

B.3.2 CSCTF Trigger Definitions

The CSCTF in the current configuration setup for the 2010 collisions data taking is able to trigger on the coincidence of at least two stubs, called LCTs (Local Charge Tracks), whose difference in ϕ, $\Delta\phi$ is less than 15 degrees and whose difference in pseudorapidity, $\Delta\eta$ is less than 0.075. In the CSCTF jargon, these pattern are referred to as "coincidence" triggers. In all the track extrapolation, but in one special case, the CSCTF delivers trigger only if one of the LCTs is coming from the second station, ME2, or the third station, ME3. This is the concept of key station. The L1 CSCTF candidate track η and ϕ which are reported at the Global Muon Trigger will be coming from ME2 or ME3. In the case both ME2 and ME3 have LCTs belonging to the assembled track, the LCT in second station will be used to define the angular variable associated to the L1 muon candidate trigger. The aforementioned special case is designed for tracks with only 2 LCTs, one coming from ME1 and one from ME4: in this situation, the CSCTF logic will use the information from the LCT in the first station to assign the track η and ϕ.

On top of the LCTs track assembling, CSCTF is currently set to trigger also on single stubs if they are generated in the first (out of four) station, ME1. This latter configuration will allow to improve the number triggers for low P_T muons and it is of particular relevant for low P_T analyses.

Moreover the CSC is configured to send stubs up $\eta = 2.5$, above the fiducial cut at $\eta < 2.1$, defined as such because of the strips ganging in the high pseudorapidity chambers in ME1, the so labeled ME1/1a chambers [reference to CSC note].

B.3.3 Efficiency Definition

The CSCTF efficiency is defined as:

$$\epsilon_{CSCTF} = \frac{N_{Gbl\mu}^{CSCTF}}{N_{Gbl\mu}}, \tag{41}$$

where $N_{Gbl\mu}$ is the total number of global muons in the sample and $N_{Gbl\mu}^{CSCTF}$ is the number of global muons which are triggerd by the CSCTF.

All the terms convoluted in this simple definition can be disantangled using the following definitions:

- $\epsilon_{CSCTF}(coincidence)(\eta = 0.9 \rightarrow 1.2) = \epsilon_{LCT} \times \epsilon_{DT} \times \epsilon_{TM} \times \epsilon_{CSCTF}$
- $\epsilon_{CSCTF}(coincidence)(\eta = 1.2 \rightarrow 2.5) = \epsilon_{LCT} \times \epsilon_{LCT} \times \epsilon_{TM} \times \epsilon_{CSCTF}$

Thus the efficiency is naturally broken in two main blocks: one in the overlap region with Drift Tubes (DT) muon system, $\epsilon_{CSCTF}(\eta = 0.9 \rightarrow 1.2)$ where DTTF and CSCTF can exchange stubs and one for the CSC only system, $\epsilon_{CSCTF}(\eta = 1.2 \rightarrow 2.5)$.

While the terms ϵ_{LCT} and ϵ_{DT} will be studied by the relative subsystems, what we are going to discuss in this section is the efficiency to match the CSCTF triggers and the reconstructed object ϵ_{TM} and the efficiency to have fired one of the CSCTF pattern, ϵ_{CSCTF}.

B.3.4 Matching Algorithm

One of the most crucial tool in the trigger efficiency calculation is the development of an offline matching algorithm able to match the L1 trigger information as closely as possible.

The simplest matching tool one could imagine consists in finding the closest trigger to the reconstruted offline muon in ΔR cone, where $\Delta R = \sqrt{(\Delta\phi)^2 + (\Delta\eta)^2}$.

We have already seen that the L1 η and ϕ assignment varies with the number and location of LCTs in the track extrapolation. Therefore, at the beginning we developed an algorithm in order to select the best reconstructed hit (rechit) candidate from the standalone component of the global muon fit. The algorithm was designed to scan all the available reconstructed hits in the CSC chambers and rank them. The highest rank will be given, in order, to rechits coming from ME2, ME3, ME1 and ME4. We know that one single LCT in a CSC chamber can have up to 6 hits associated to it, each coming from one of the 6 layers of the chamber. To cope with the multiple choices in a single chamber, the rank is assigned from the highest to the lowest to layer 3,4,2,5,1,6. This should guarantee a close match between the offline muon reconstruction in the endcap and the L1 CSC Track Finder assignment.

The ΔR distribution for such algorithm is shown in figure 85.

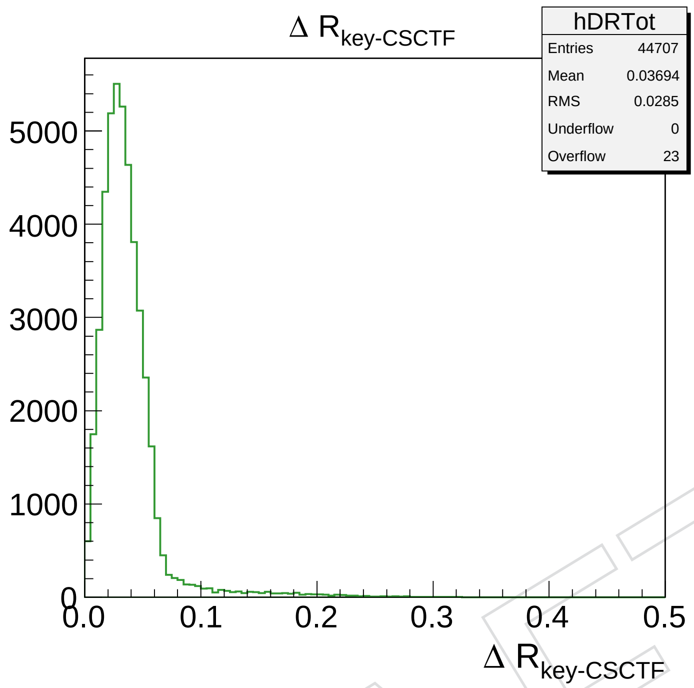

Figure 85: $\Delta R = \sqrt{(\Delta\phi)^2 + (\Delta\eta)^2}$ between the offline reconstructed muon and the L1 CSCTF trigger.

The efficiency of a cut on ΔR are reported in Table 36

Table 36: Efficiency as a function of a cut on the maximum ΔR:

$\Delta R < X$	% global μ rejected
0.05	17.16
0.10	3.34
0.20	0.74
0.30	0.09
0.40	0.06
0.50	0.05

The analysis of the ΔR suggests a cut at 0.2 as best tradeoff between introducing artificial inefficiency by tightening the cut and efficiency by relaxing it.

The investigation of the ΔR distribution for different η regions, shows some of imbedded features of the CSCTF logic. Some of these distribution are shown in Fig. 86. In particular, one could notice the ΔR distribution to get wider in the region around η 1.6. This is a known CSCTF feature, as there is a nonlinear effect put in the logic by design. If a muon hits ME1/1, the CSCTF always considers η to be larger than a value η 1.58. If it hits ME1/2, the CSCTF always consider η less than this value. The chambers actually overlap in η, but this feature saves some space in the P_T LookUp Tables address memory.

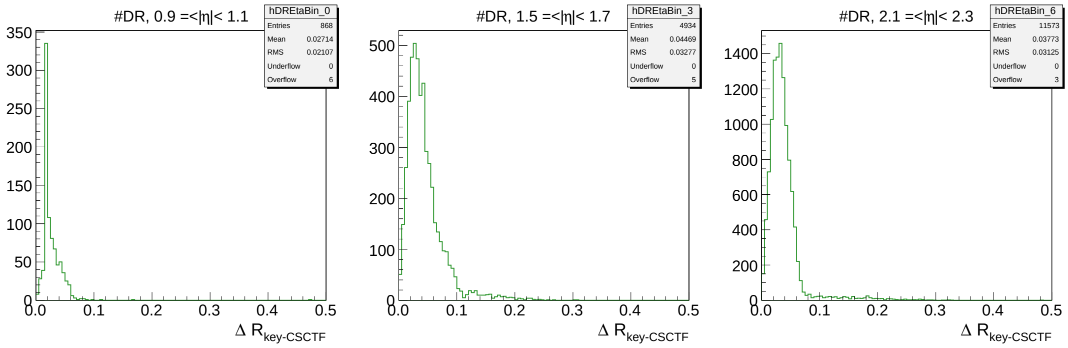

Figure 86: ΔR distribution for different η ranges. From left to right: $\Delta R(0.9 < |\eta| < 1.1$, $\Delta R(1.5 < |\eta| < 1.7$ and $\Delta R(2.1 < |\eta| < 2.3$,

All the CSCTF logic nuances are difficult to be comprehensively encode in a simple ΔR matching. In fact the current proposed cut of 0.2 is asking for a trigger matching in a very wide window. Let us make some calculation to show how wide. From the Techincal Design Report (TDR) [reference], we know that ME2 covers a region radially from 1.2 m to 7.0 m, and is 8.5 m away from the interaction point. At $R = 1.2m$, $\Delta\phi = \pm 0.2$ is a 48 cm wide window, while $\Delta\eta = \pm 0.2$ is a 53 cm wide window. At $R = 7.0m$, $\Delta\phi = \pm 0.2$ is a 2.8 m wide window and $\Delta\eta = \pm 0.2$ corresponds to a 2 m wide window. All these windows are extremely wide, while the muon trajectory can be known to better than a centimeter and the readout is the same for the trigger and the reconstructed muon candidate.

It is evident that the matching algorithm cannot give satisfactory level of identification and could result in an artificial higher efficiency. Therefore a new technique has been developed to calculate the CSCTF matching to offline reconstructed muons.

B.3.5 Matching LCTs To Segments

Instead of looking at the higher level triggered object, namely CSCTF track candidates, the idea is to associate to the segment composing the global muon its LCT, if any. This is made possible by looking at the digital information present both in the trigger and in the CSC readout. With such technique one can exploit the high correlation between readout channels used in hit construction and readout channel reported in LCT.

In Figure 87, the difference along the ϕ direction between a segment and an LCT in the same chamber in term of half strip is shown. From the left to the right we show the difference for all the segments, regardless if they belong to a global muon or not, for all the segments when only one LCT present in the CSC chamber and the same distribution zoomed in the region $\pm 15\ halfstrips$. The cut which will be used for the analysis is $\pm 10\ halfstrips$. Since the strip size varies with the CSC chambers type, this cut corresponds to look for a match in ϕ in $\pm 4 - 15\ cm$.

In Figure 88, the difference along the η direction between the segment and the LCT is shown in term of wire groups. As before, from the left to the right we show the difference for all the segments, then for all the segments with only one LCT present in the CSC chamber and the same distribution zoomed in the region $\pm 15\ wiregroups$. The cut which will be used for the analysis is $\pm 5\ wiregroups$. The wire group size varies with the CSC chambers type, so this cut corresponds to look for a match in η in $\pm 8 - 15\ cm$, depending on the CSC chamber.

By using this identification tool, we are capable to associate a segment to the global muon at the cm level. Exploiting this powerful handle, we can now define a global muon as "triggerable"

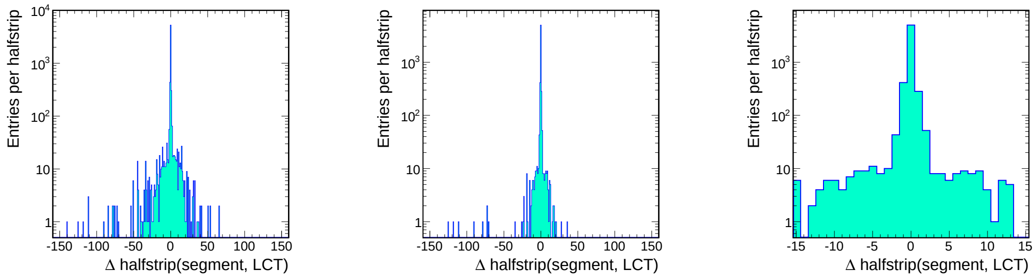

Figure 87:

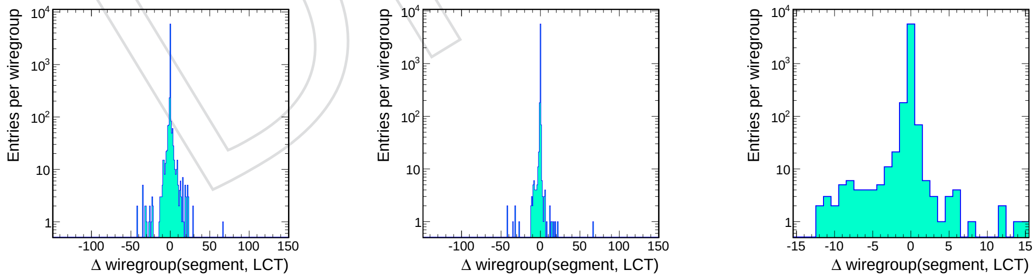

Figure 88:

if two or more segments belonging to it are matched to an LCT. With such definition the term $\epsilon_{TM} \times \epsilon_{CSCTF}$ can be re-written as:

- $\epsilon_{TM} \times \epsilon_{CSCTF} = \epsilon_{Match} \times \epsilon_{Match} \times \epsilon_{CSCTF}$

where ϵ_{TM} is the probability that given a segment this will be matched by an LCT.

B.3.6 Offline Reconstructed Muon Selection

All the results shown in this section are obtained with the dataset $/MinimumBias/Commissioning10-May6thPDSkim_GOODCOLL-v1/RAW-RECO$ and using the official good run list from runs 132440 to 134987, for a total integrated luminosity of 0.99 nb^{-1}.

The offline selection criteria for the global muons are:

- Have a standalone component
- Have a tracker component
- To be flagged as "GlobalMuonPromptTight"
- $\chi^2/NDF < 10$
- $|d_0| < 2\ cm$
- At least one hit in the CSC subsystem
- At least two segments matched to an LCT, "triggerable" muon

These selection criteria provide with 34902 global muons to be used in the study. It is important to notice that the two segments requirement is only applicable to CSC subdetector as this matching tool works only for the CSC. Thus, the efficiency in the overlap region will results in a CSC only efficiency measurement and may result in an underestimation of the trigger efficiency in the overlap region with DT.

B.3.7 Efficiency Calculation

Finally the CSCTF efficiencies as a function of P_T, η and ϕ are shown in Figure 89. The total cumulative efficiency is 99.7%. The possible sources of inefficiency could be due to:

- LCTs do not actually pass the CSCTF extrapolation cuts
- LCTs pass the extrapolation of cuts but they are as away as 3 BXs, i.e. CSC-CSCTF not synchronized
- Firmware features

The analysis of the data, showed that currently 0.01% of inefficiency comes from LCTs which do not pass the extrapolation requirements. The remaining 0.02% is due to firmware logic implementation. For instance, all tracks which have low P_T quality assignment and are in the edge of the sectors are removed. No LCTs passing the cuts and being out-of-time are found. This is an additional proof of the fact that the CSC-CSCTF is an extremely well synchronized system.

B.3.8 Conclusions

The presented study manifest a deep understanding of the CSCTF trigger mechanism as well as it provides evidences for the need of matching tool which supersedes the more classical ΔR matching algorithm. We recommend the physics analyses to require at least two segments present in their global muon in the endcap. This will guarantee trigger stability in the efficiency calculation over the luminosity increases, which is approximately 99.7%.

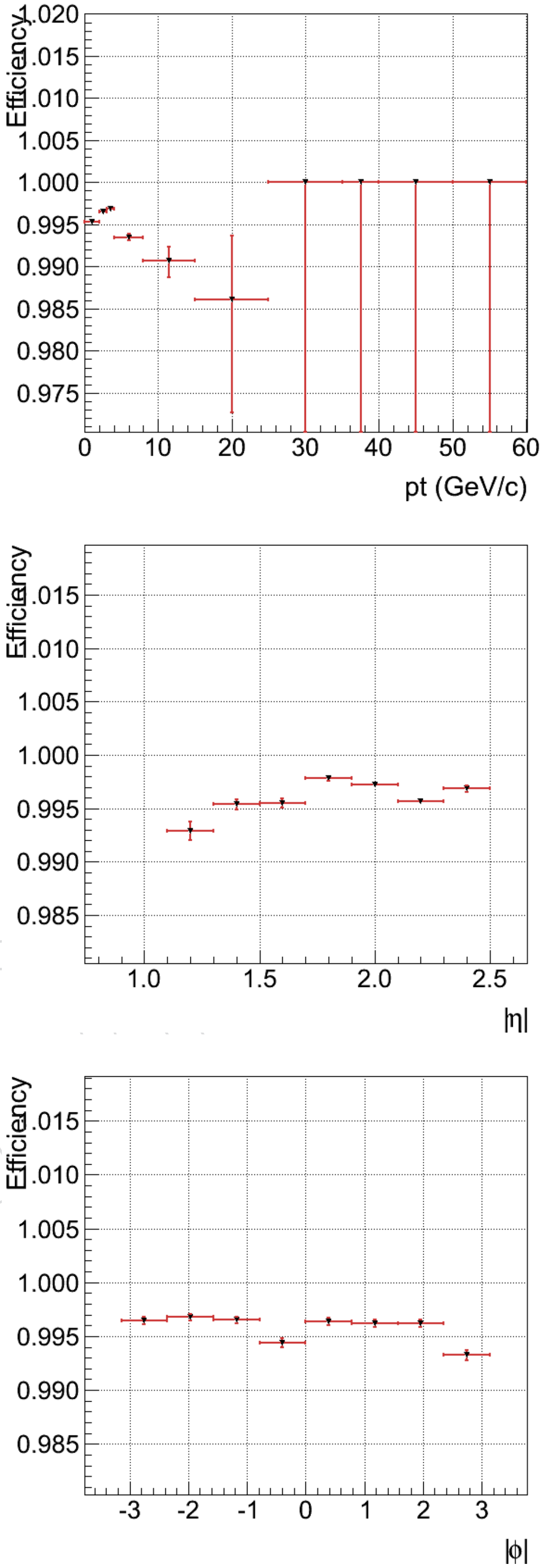
Efficiency
1.020
1.015
1.010
1.005
1.000
0.995
0.990
0.985
0.980
0.975
0
10
20
30
40
50
60
pt (GeV/c)
Efficiency
1.015
1.010
1.005
1.000
0.995
0.990
0.985
1.0
1.5
2.0
2.5
|η|
Efficiency
1.015
1.010
1.005
1.000
0.995
0.990
0.985
-3
-2
-1
0
1
2
3
|ϕ|

Figure 89:

B.4 L1 RPC Efficiency

B.5 L1SingleMu7 Efficiency

Final L1 trigger efficiency in this study should be estimated on L1SingleMu7 bit, because this L1 trigger is a seed for HLT_Mu9 trigger path. This trigger bit requires pt threshold at 7 GeV and L1 quality greater than 3.

The matching method which is desccribed in Section B.6.2 is used to calculate the L1 trigger efficiency. Offline global muon for the matcing is selected by the quality requirements which are described in Section 4. As summarized in the section, the L1 efficiency is measured by two different selections: with isolation and without isolation respectively. $\Delta R(L1, offline\ global\ muon) <$ 0.3 is applied for the matching

$$\varepsilon_{L1} = \frac{N_{GLB}^{matching\ by\ L1}(L1SingleMu7)}{N_{GLB}} \tag{42}$$

$$\tag{43}$$

Figure 90 shows the L1 trigger efficiency without isolation cut (left) and with isolation cut (right) as a fucntion of offline muon p_T. On the left plot, the red circle denotes the L1 trigger efficiency on the data, and blue square indicates the L1 trigger efficiency on InclusiveMu15 MC sample. The efficiency is determined by fitting the plateau of the efficiency distribution. The right plot shows the red circle (data), the blue square (W^+ MC), and the black triangle (W^-), respectively. In this figure, the L1 trigger efficiency is for overall η region. The fit results for three split η regions are summarized in Table 4. We observe 93.1% without isolation cut and 86.7% with isolation cut for the scale factor between data and MC.

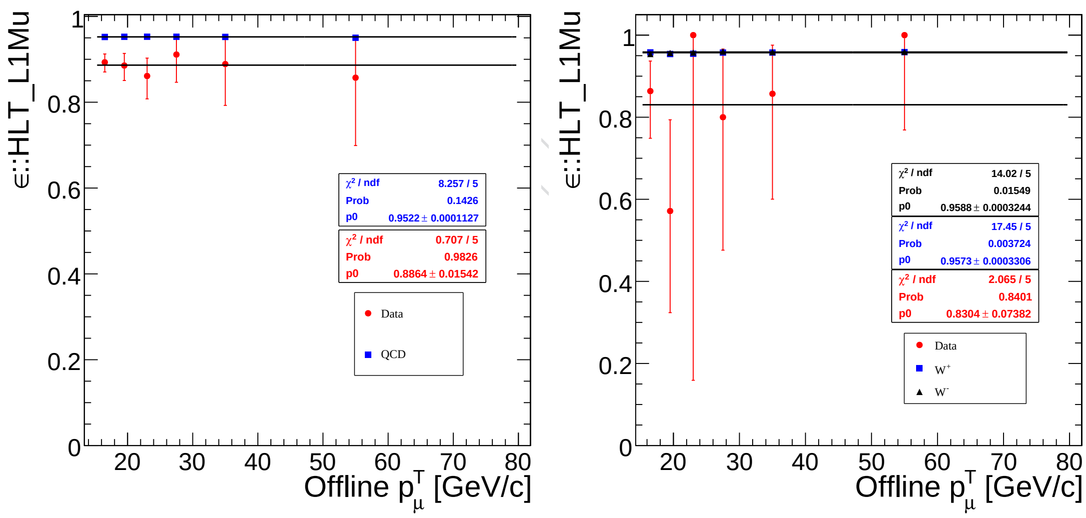

Figure 90: Left plot shows the L1 trigger efficiency without isolation cut and right plot shows the result with isolation cut. The trigger efficiency is for overall η region.

In addition, the L1 trigger efficiency is estimated on minbias triggered events with same method and same quality cuts on the offline global muon. Only "without isolation" selection is applied on the minbias sample. $87.7 \pm 9.0\%$ (data) and $85.1 \pm 4.0\%$ (MC) are observed. Figure 91 shows the determined L1 trigger efficiency as a function of the offline global muon p_T. On the figure, the red denotes the efficiency on data and the black denotes the efficiency on MC.

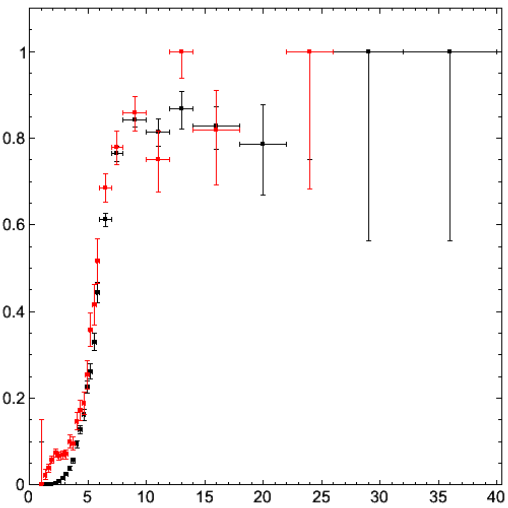

Figure 91: The plot shows the L1 trigger efficiency without isolation cut on minbias sample as a function of the offline global muon. On the plot, the red denotes the efficiency on data and the black denotes the efficiency on MC. The trigger efficiency is for overall η region.

B.6 HLT Efficiency

B.6.1 Introduction

In this section, we discuss the trigger efficiency measurement for `HLT_L2Mu9` and `HLT_Mu9` trigger paths.

B.6.2 Trigger Efficiency Measurement Using Offline Muon Matching

To estimate the HLT trigger efficiency, the sample should be unbiased with muon trigger. The jet triggered events or minimum bias triggered events are assumed orthogonal with the muon trigger. Therefore the samples are used in this study. To find the sample with muons, we require at least one global muon with muon id, which is described in Section 4 as quality cuts. Then the trigger efficiency is determined by matching between muon trigger object and the offline global muon using ΔR cut.

Matching criteria is that $\Delta R(L1, offline\ global\ muon) < 0.3$, where $\Delta R = \sqrt{(\Delta\phi^2 + \Delta\eta^2)}$. To calculate the ΔR, the offline global muon is propagated to the station 2, which L1 muon is reconstructed in general. The propagation can be done by two different ways: the first one is to propagate from the outermost position of inner track of the global muon (tracker track), and the other choice is to propagate from the outermost postion of outer track (muon track). More details are described in **??**, and in this section, we use the former. Figure 92 shows the ΔR distribution between L1 and offline global muon.

Same matching is applied for L2 and L3 muons to calculate the HLT trigger efficiency. The criteria is dependent on the ΔR distribution, and $\Delta R < 1.2$ for L2 and $\Delta R < 0.5$ for L3 are used respectively.

The trigger efficiency in this method is defined as follows:

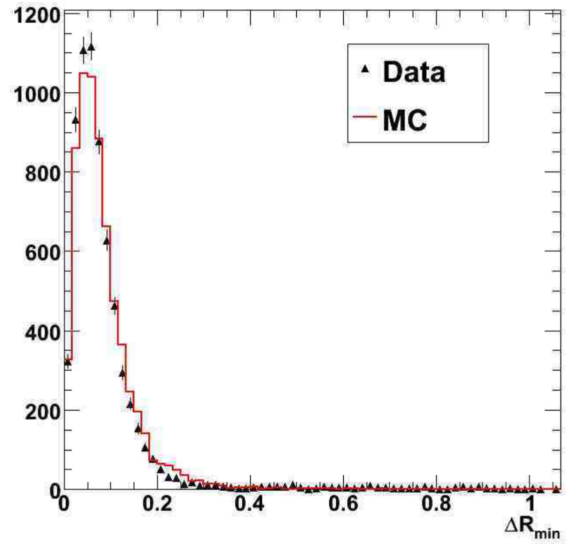

Figure 92: This plot shows the ΔR distribution. The red line indicates MC distribution, and black triangle denotes data distribution. The comparison is in good agreement, and 0.3 cut is applied.

$$\varepsilon_{HLT\_L2Mu9} = \frac{N_{GLB}^{matching\ L2}(HLT\_L2Mu9)}{N_{GLB}^{matching\ L1}} \quad (44)$$

$$\varepsilon_{HLT\_Mu9} = \frac{N_{GLB}^{matching\ L3}(HLT\_Mu9)}{N_{GLB}^{matching\ L1}} \quad (45)$$

where the $N_{GLB}^{matching\ L1}$ is the number of offline global muons matched by L1 muons (passing $\Delta R < 0.3$ cut). The HLT_Mu9 trigger efficiency w.r.t. L1 is measured by two different quality cuts: without isolation and with isolation. Figure 93 shows the result of the HLT_Mu9 trigger efficiency on jet-triggered events. The format of the plot is same as Figure 90. In this figure, the HLT_Mu9 trigger efficiency is for overall η region. The fit results for three split η regions are summarized in Table 4. We observe 97.2% without isolation cut and 96.2% with isolation cut for the scale factor between data and MC.

(HLT_L2Mu9 result will be added soon)

The HLT_Mu9 trigger efficiency is also estimated on minbias triggered events with same method and same quality cuts on the offline global muon. Only "without isolation" selection is applied on the minbias sample. $90.1 \pm 2.1\%$ (data) and $95.7 \pm 2.7\%$ (MC) are observed. Figure 94 shows the determined L1 trigger efficiency as a function of the offline global muon p_T. On the figure, the red denotes the efficiency on data and the black denotes the efficiency on MC. The result is consistent with the observation on the jet-triggered sample.

In addition, same method is applied on $Z \rightarrow \mu\mu$ MC sample. $93.2 \pm 0.1\%$ trigger efficiency (L1+HLT) is observed on this sample, and the result is consistent with the trigger efficiency determined by using the $W \rightarrow \mu\nu$ MC sample, described in Table 4. Figure 95 shows the result of trigger efficiency on the sample as a function of p_T (left) and η (right).

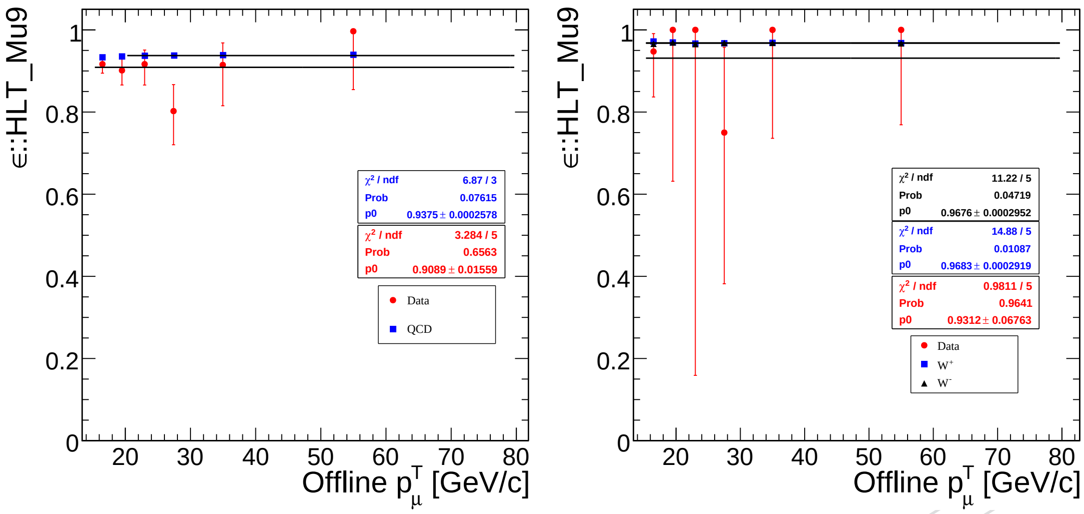

Figure 93: Left plot shows the HLT_Mu9 trigger efficiency (w.r.t. L1) without isolation cut and right plot shows the result with isolation cut. The trigger efficiency is for overall η region.

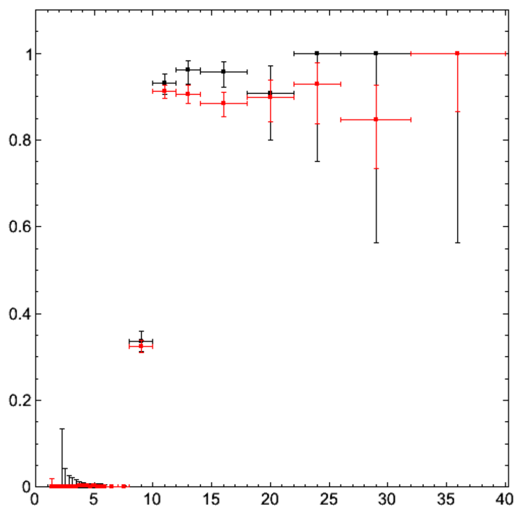

Figure 94: The plot shows the L1 trigger efficiency without isolation cut on minbias sample as a function of the offline global muon. On the plot, the red denotes the efficiency on data and the black denotes the efficiency on MC. The trigger efficiency is for overall η region.

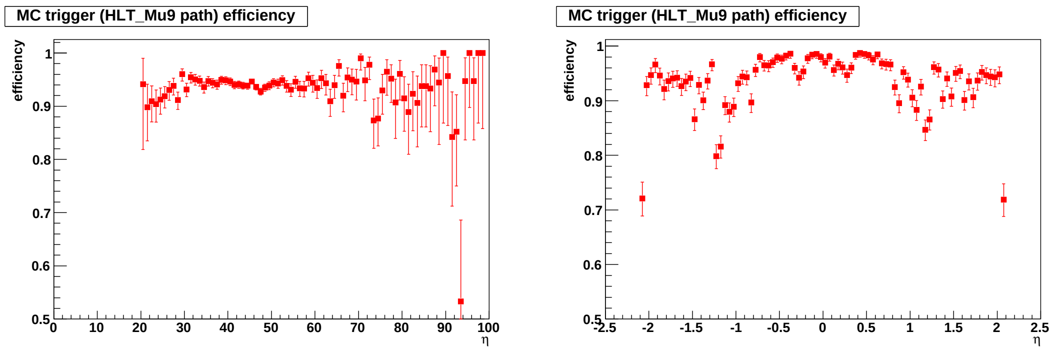

Figure 95: The plot shows the trigger efficiency (L1+HLT) on $Z \to \mu\mu$ MC sample.

B.6.3 Trigger Efficiency Measurement Using Tag and Probe Method

In this section, the trigger efficiency is estimated by using the tag and probe, which is a generic data-driven method. More details are described at (cite).

The method will exploit Z to dimuons, but currently the channel has too small statistics. Instead, we use J/Psi peak to run the tag and probe, and try to estimate the HLT_Mu3 trigger efficiency on the peak. We are trying to switch by Upsilon peak.

The following result is done by using J/Psi skimmed sample with good runs from 132440 to 134987. The requirements for tag and probe muons are as follows:

- common requirement on tracker track for both: number of valid hits > 11, number of pixel hits > 1, chi2/ndof < 5, $|d0| < 2$, $|dz| < 20$
- tag muon only: global muon, chi2/ndof < 20, matched to HLT_L1MuOpen
- probe muon only:

and the figure 96 shows the estimated trigger efficiency by tag-and-probe on J/Psi resonance.

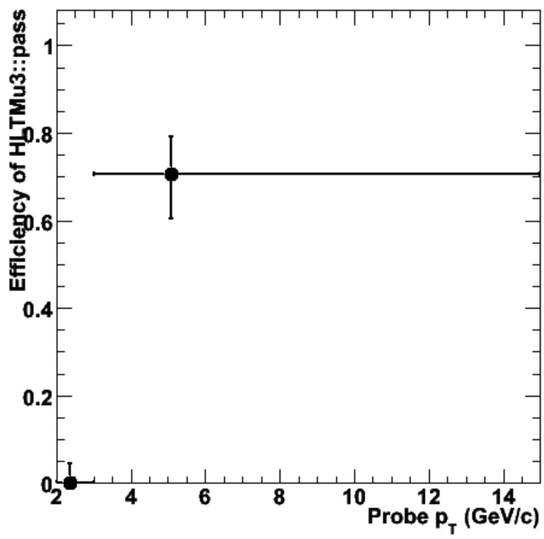

Figure 96:

There is another tag and probe tool in $Z \to \mu^+\mu^-$ cross section package, and the estimation can be done in parallel to the above generic tag and probe tool. As described in Section 6, currently we find 5 Z candidates in dimuon channel, and the estimated trigger efficiency from the candiates is $89^{+10}_{-24}\%$.

(more descriptions will be added)

B.6.4 Trigger Efficiency Measurement Using MC-based Method

The trigger efficiency based on $W \rightarrow \mu\nu$ MC sample will be discussed in this section. The efficiency definition of this method is as follows:

$$\varepsilon_{HLT\_Mu9} = \frac{N_{presel}(HLT\_Mu9)}{N_{presel}}, \quad (46)$$

where N_{presel} denotes the number of total events passing standard preseletion, described in Section 5 on $W \rightarrow \mu\nu$ MC sample, and $N_{presel}(HLT\_Mu9)$ denotes the number of events passing both the preselection and HLT_Mu9 trigger path. Trigger object in HLT_Mu9 is matched to the offline muon in the event and trigger efficiency is estimated as a function of offline muon p_T and η.

Figure 97 shows the results for the method. Top two plots show the results on Wplus MC sample and bottom two plots show the results on Wminus MC sample.

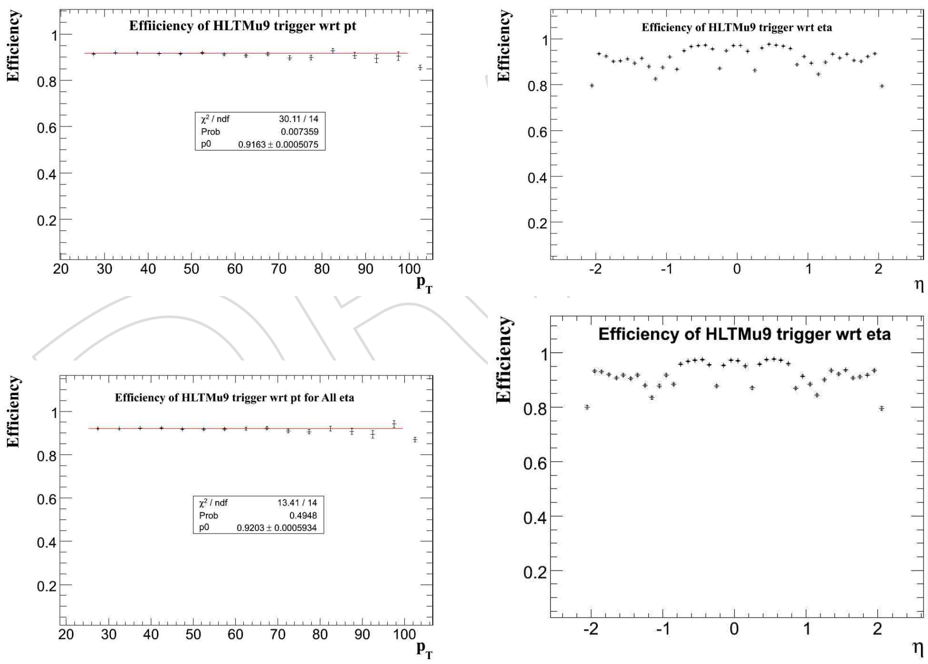

Figure 97:

C Determination of muon momentum scale and resolution

C.1 Calibration of muon momentum using di-muon resonances

The first method relies on di-muon resonances and is based on an unbinned multivariate likelihood fit. The fit determines the correction to the muon p_T such that the corrected mass

parameter	value±error
a_0	1.0019 ± 0.0008
a_1	$(-4 \pm 2) \times 10^{-4}\ c/\mathrm{GeV}$

Table 37: Results of the scale fit on $15nb^{-1}$ of integrated luminosity using J/ψ resonances.

distribution better matches the reference model. The reference model takes into account the background and the effects of detector resolution on an event by event basis using the full information from both muons. The method is described in full detail in [71]. In 0.1 pb^{-1} we do not have enough $Z \to \mu\mu$ events to directly perform a measurement, therefore we use lower mass resonances (J/ψ, Υ) and extrapolate to the higher p_T range of muons from Z and Ws. The few $\mathcal{O}(100)$ $Z \to \mu\mu$ events we expect are used to further constrain the measurement in the higher p_T range.

Performing a calibration of the muon momentum scale using J/ψ resonances with $15nb^{-1}$ of integrated luminosity a scale bias is found and it is corrected at first order using the function:

$$p'_T = (a_0 + a_1 p_T) \cdot p_T\,, \qquad (47)$$

with the parameters reported in Table 37. The effects of the correction on the J/ψ mass peak are shown in Figure 98.

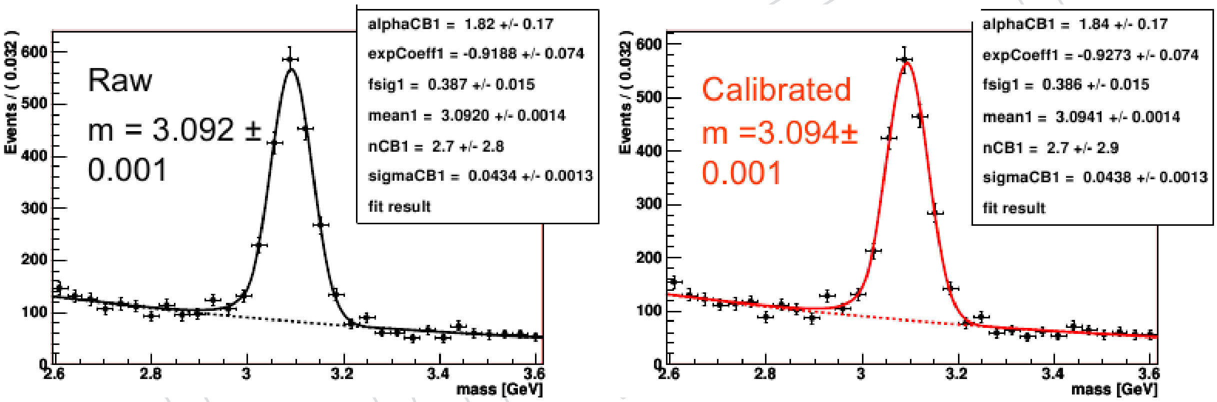

Figure 98: (Left) J/ψ mass distribution as measured with $15\mathrm{nb}^{-1}$ of integrated luminosity using the selection discussed here [72]. (Right) Same distribution after the correction of the momentum scale using the functions and parameters discussed in the text.

The function describing the measured muon momentum resolution is:

$$\frac{\sigma(p_T)}{p_T} = \begin{cases} c + b_1\eta^2 & \text{for } |\eta| \le b_0 \\ b_2 + b_3(|\eta| - b_4)^2 & \text{for } |\eta| > b_0 \end{cases},$$

where c is such that the function is continous and the other parameter values are shown in Table 38. The results for the transverse momentum resolution are shown in Figure 99 where they are compared with the muon resolution in the MC used to compute the acceptance. We will use the difference to compute the systematics due to the muon momentum resolution on the cross section measurements. The method and the resulting systematic error are detailed in section 15.2.

parameter	value±error
b_0	1.66 ± 0.09
b_1	$(5.8 \pm 0.9) \times 10^{-3}$
b_2	$(2.1 \pm 0.2) \times 10^{-2}$
b_3	$(3 \pm 3) \times 10^{-2}$
b_4	1.8 ± 0.3

Table 38: Results of the resolution fit on $15nb^{-1}$ of integrated luminosity using J/ψ resonances.

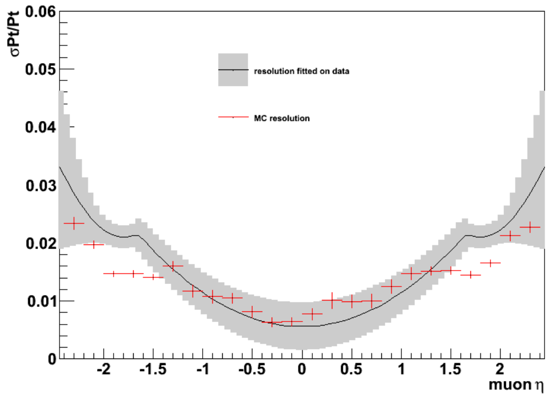

Figure 99: Resolution on transverse momentum as measured with 15nb^{-1} of integrated luminosity (black line) compared to the MC resolution (red points). The grey bands represent the error on the fitted function computed from the errors on the parameters.

C.2 Analysis of tracker tracks vs standalone muons residuals

The second method is based on the residuals between tracker tracks and standalone muon segments. Tracker tracks are propagated to the barrel muon chambers and residuals are computed as the difference between the measured segment and the intersection of the track with the chamber surface. The mean of the Gaussian fits to the distribution of residuals in bins of $\kappa_T = q/p_T$ depends on the momentum scale of tracker tracks. In case of no bias the mean values are expected to be compatible with zero. Any deviation depends on the bias in the muon transverse momentum. This method can be used both with cosmic and collision muons and it covers the mid-high p_T spectrum ($\gtrsim$ 40-50 GeV/c, limited by the actual statistics, study ongoing).

The data show a linear trend of the mean of residual gaussian fits vs q/p_T which can be interpreted as due to a bias of the form $p'_T = (1+k) \cdot p_T$. An example of the residual distribution is shown in figure 100. This kind of bias is applied to tracks in CMSSW by changing the TrajectoryStateOnSurface of the Tracker and propagating them with the full reconstruction algorithm to the muon chambers to compute the effect such a distortion has on the residuals as a function of k. The relation found is $slope = (0.0016 \pm 0.0010) + k \cdot (589.4 \pm 1.4)$(cm·GeV), where $slope$ is the slope of a line fitted to the distribution of residuals vs q/p_T. When performing the same fits on data the slope varies depending on the muon chamber considered. We take the one showing the biggest effect and set an upper limit to the momentum bias. The biggest slope found is 2 cm·GeV and the corresponding value of k is found to be:

$$k = 0.0031 \pm 0.0005 \text{ (stat)} \tag{48}$$

(need to estimate the systematic error from the toy MC approximation).

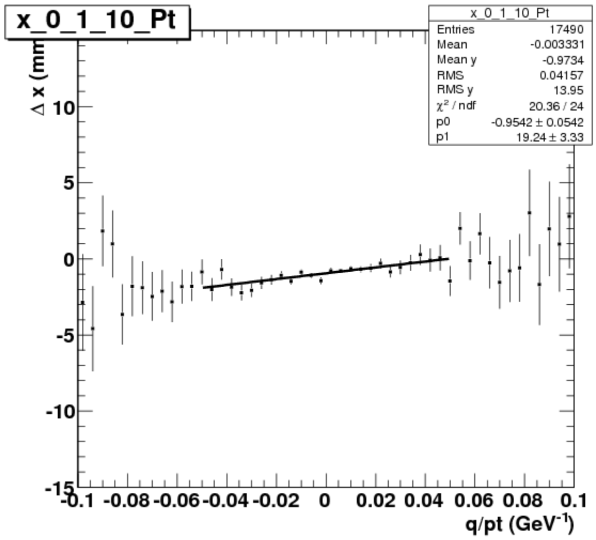

Figure 100: Residuals distribution vs q/p_T for chamber 0 1 10 with results from a linear fit.

C.3 Cosmics end-point method

The third method relies on the cosmic muon flux spectrum. The spectra of positive and negative muons as a function of the transverse curvature κ_T die off as the momentum approaches infinity. The shape of this distribution (studied for $p_T > 200$ GeV/c) will be significantly distorted by a (constant) curvature bias. Therefore, we can use the distinct shape of this distribution to fit for the curvature bias in high momentum tracks. The details of the method are documented in [73]. The sample used for the study consistes in the CRAFT 10 muons reconstructed with ICHEP geometry for the Tracker and hardware geometry for the muon chambers. The bias extracted is $\delta_{\kappa_T} = 0.045 \pm 0.022$ c/TeV. This result can be used as the best estimate of the curvature bias at high momentum.

C.4 Measurement of momentum scale using muons from W bosons

The fourth method measures muon momentum scale and resolution as described in the Analysis Note [74]. It relies on the good precision and robustness of the MC generation of electroweak bosons, W and Z. In this case the W boson is used. Given the muon transverse momentum distribution from Ws from collisions, we fit to it the MC modifying the muon p_T depending on some parameters, in order to find the values of the parameters describing the data. This is done changing the muon transverse momentum with a resolution term (σ_{κ_T}) and a scale factor (δ_{κ_T}) applied on the variable $1/p_T$. The fit is implemented via a binned log-likelihood method. The algorithm is tested using MC events acting as collision data. The sensitivity after this test for a 100 nb^{-1} data sample (around 400 W bosons) is 0.75 (c/TeV) for the resolution term and 0.22 (c/TeV) for the scale factor. In Fig. 101 (left) the p_T distribution for the muons selected with the W-baseline selection for the first Y nb^{-1} of data is shown, compared with a reference W MC (POWHEG). In Fig. 101 (right) we can see the muon p_T distribution once the method is applied and the fit performed (comments on the figure). In Fig. 102 the log-likelihood for the resolution and scale terms is shown. (**comments on the figure. This figure could be removed**).

Studies about the theoretical uncertainties affecting the distributions of muons from W bosons have also been carried out. The most important one at this level is the ISR effect. Using a

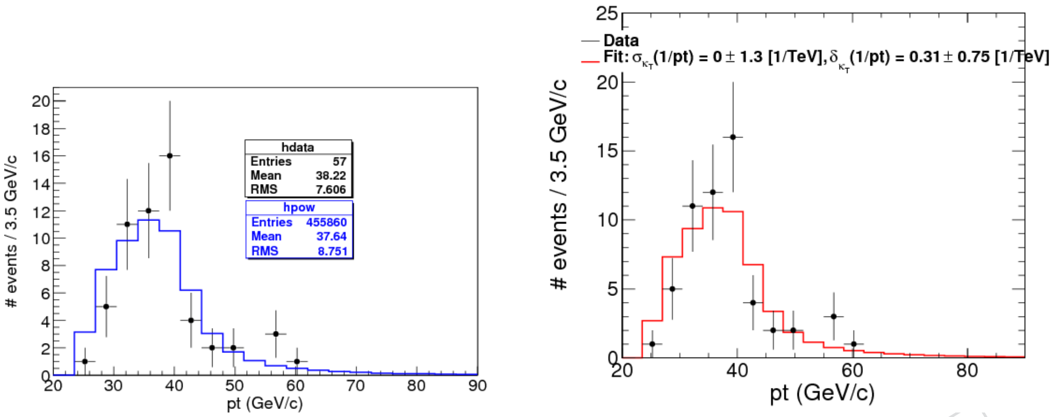

Figure 101: Muon pt distribution for data (black) and non-distorted MC (blue) (left). Muon pt distribution for data (black) and best fit to data (red) (right).

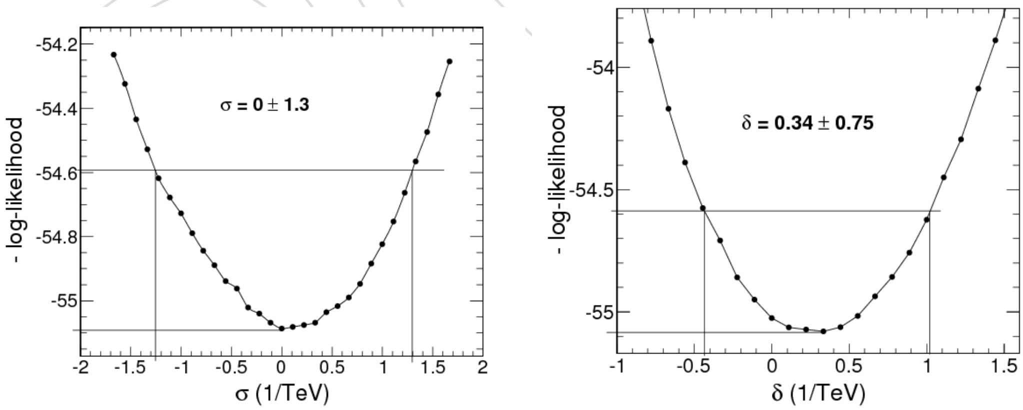

Figure 102: Log-likelihood curve for the resolution term (left) and the scale factor (right).

reweighted sample from PYTHIA, changing the parameter PARP(64) from 0.2 to 0.1 [75, 76], we have observed a distortion in the p_T distribution such that the resolution term is 0.66 c/TeV and scale factor 0.18 c/TeV when applying this method. Consequently, for effects lower than this values we would not be able to distinguish a possible scale/resolution effect from ISR effects.

D Distributions of the selection variables for $Z \to \mu^+\mu^-$

In Figures 104, 105, and 106, we show the distributions of the muon legs of the Z candidates for the kinematical, quality, and isolation variable used in the signal selection. Distribution in data is superimposed to expectation from MC, normalized to the nominal luminosity of the data sample.

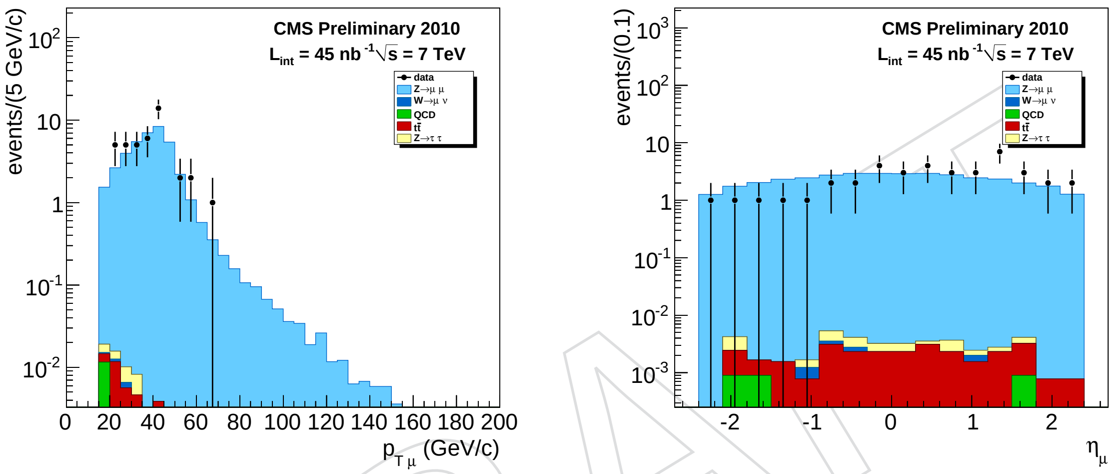

(a) p_T (b) η

Figure 103: Distributions of kinematic variables for the muon legs of the $Z \to \mu^+\mu^-$ candidates. All cuts, except on the plotted variable, for the $Z \to \mu^+\mu^-$ selection have been applied. Black points: data; histograms: MC samples normalized to the nominal luminosity of data.

E Cross-checks of background estimates for $Z \to \mu^+\mu^-$

The fake rate method is described in detail in [77]. The method involves extracting from a background enriched sample the efficiency ϵ_{fake}, parametrised in p_T and η, for loosely defined "fakeable objects" to satisfy selection requirements. This efficiency or fake rate is then applied to the set of fakeable objects found in the sample for the cross section measurement in order to construct a background prediction. We use this technique to perform a data-driven cross-check of the Monte Carlo estimates for QCD background. To obtain a background enriched sample, we consider events triggered by `HLT_Jet15U`. We define the fakeable object as a tracker track with $p_T > 10\,\mathrm{GeV}/c$, and the estimated fake rate is on the order of 10^{-3}. In the fake rate application, we consider pairings of a well identified muon with a fakeable object in events triggered by `HLT_Mu9` and give these events a weight of $\epsilon_{fake}/(1-\epsilon_{fake})$. To reduce contamination from signal events, we require that the fakeable object fails muon selection requirements. The selection of a muon plus a fakeable object inherently double counts events where a pair of jets fake leptons. However, this is predominantly the way which the QCD background contributes,

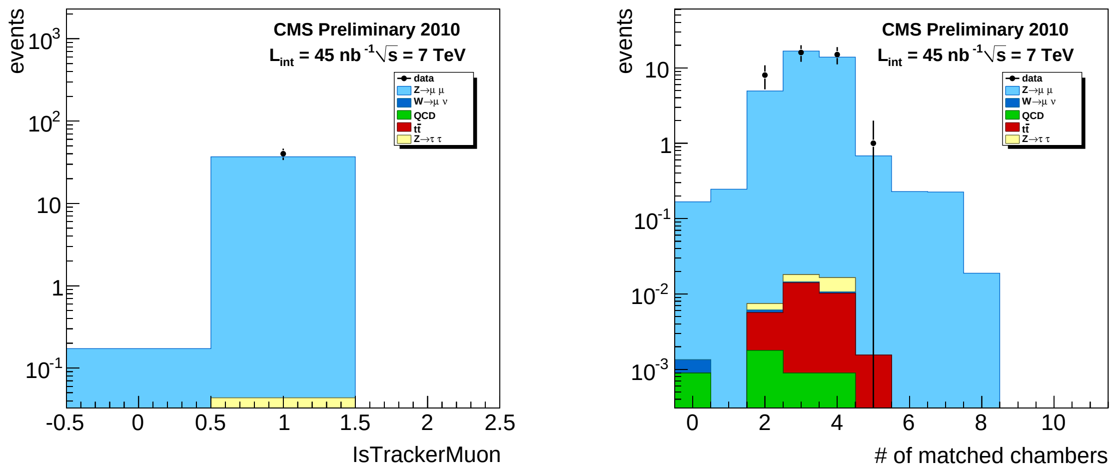

(a) *IsTrackerMuon* flag

(b) Number of chambers with matched muon segments

Figure 104: Distributions of quality variables for the muon legs of the $Z \to \mu^+\mu^-$ candidates. Only kinematical and isolation cuts have been applied. Black points: data; histograms: MC samples normalized to the nominal luminosity of data.

hence we scale our predictions by 1/2. The value of predicted background from this cross-check is work in progress.

Low-purity categories of di-muon candidates allow us to obtain an estimate of background from several sources (see [30]). The di-muon candidates that pass all requirements described above, but with one or both muons failing the isolation criterion, provide a sample that has roughly a signal-to-background ratio around 1. The background in this sample is almost purely QCD. In the data sample, which has an integrated luminosity of 17.8 nb^{-1}, no events are observed in this category. From simulation we expect 0.40 background events and 0.30 signal events. We can make a conservative estimate of the QCD background by assuming that no signal is expected and set a 95% C.L. upper limit of 3.0 events [78]. Simulation predicts that the probability for a QCD event to pass the full $Z \to \mu^+\mu^-$ selection, including the isolation cuts, is $\sim$1/100 of the probability to enter this low-purity sample that allows non-isolated muons. Thus we set an upper limit on the QCD background in the high-purity sample for the cross section measurement at 0.03 events. This value is close to the expectation from MC for the QCD background listed in Table 11. With a larger data sample, we will be able to extract a better estimate of QCD background from the low-purity category by a maximum likelihood fit to the mass distribution.

We also consider another low-purity sample where di-muon candidates are composed out of a muon passing full selection requirements, and an isolated track. From simulation we expect 0.18 background events and 0.02 signal events in the analyzed data sample of 17.8 nb^{-1}. The primary contributors to the background are QCD events (30% of the sample) and $W \to \mu\nu$ (40% of the sample). In the data, we observe zero events. Similarly to what was done for the non-isolated low-purity sample, we can place the upper limits on each of these two backgrounds, the QCD and $W \to \mu\nu$, at 3 events at 95% C.L. To propagate the limit for the QCD background to the sample with the full selection, we apply the factor $\sim$1/30, derived from MC, and obtain the upper limit of 0.1 events. This is a weaker bound than the one derived from the non-isolated sample.

For the $W \to \mu\nu$ case, the scale factor for extrapolation to the high-purity sample is $\sim$1/100.

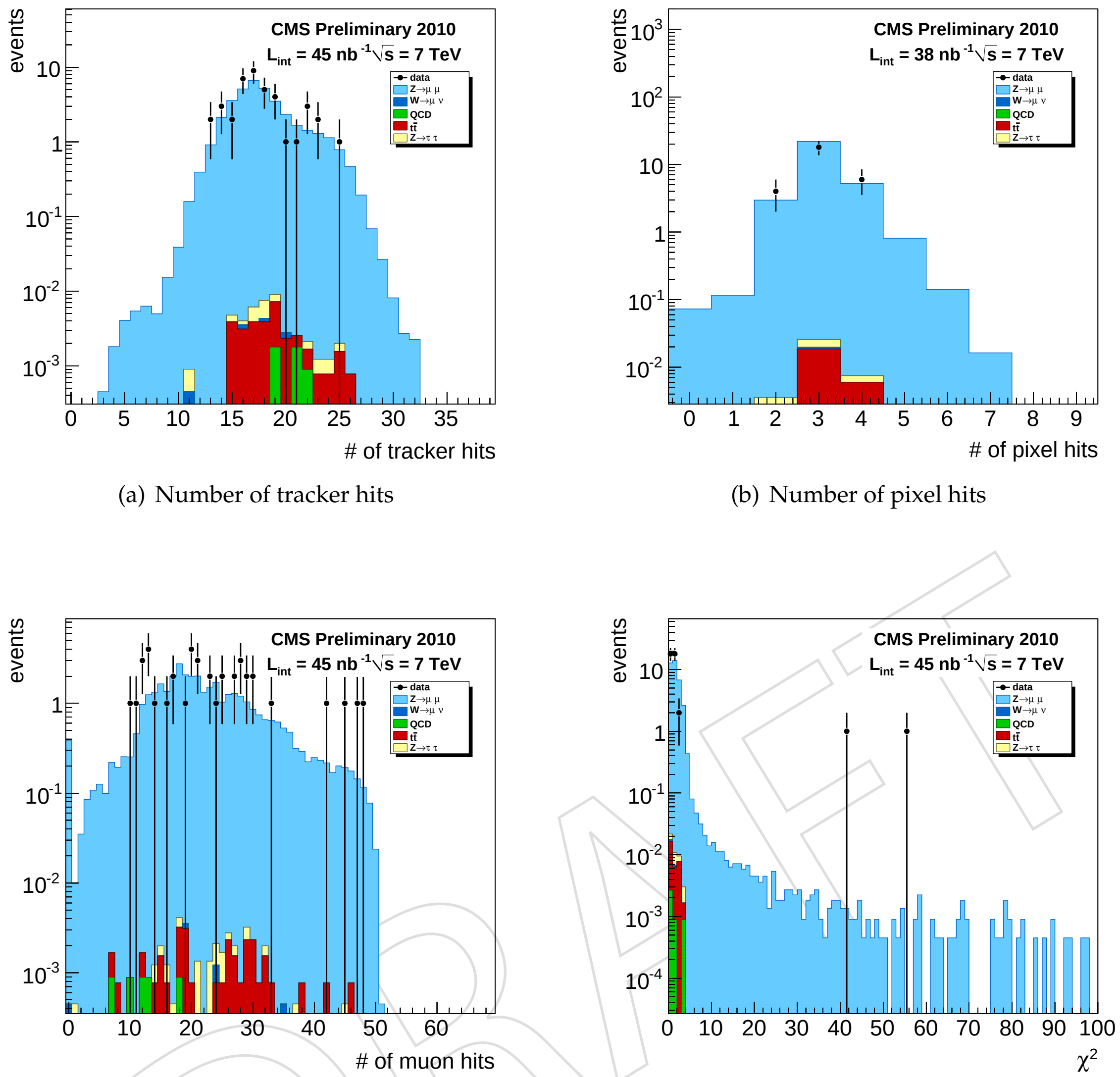

(a) Number of tracker hits

(b) Number of pixel hits

(c) Number of valid muon hits

(d) χ^2/NDF of the global fit

Figure 105: Distributions of quality variables for the muon legs of the $Z \to \mu^+\mu^-$ candidates. Only kinematical and isolation cuts have been applied. Black points: data; histograms: MC samples normalized to the nominal luminosity of data.

This leads to the 95% C.L upper limit on the $W \to \mu\nu$ background of 0.03 events. The prediction from the simulation is about 0.005 ($W \to \mu\nu$ entry in Table 11 scaled by luminosity).

F Additional studies to subtract QCD bck. and extract W signal

Performance studies of the template fitting on M_T

The performance of the method presented in section 5 is established by fitting 100 pseudo-data samples of 100 nb^{-1}, simulated by MC in conditions close to the experimental ones. These tests were done using for the QCD template the MC prediction and not any data-driven templating and it was finally the case with the real data. The cross section is determined with a statistical relative uncertainty of $\sim$ 5%. The systematic uncertainty due to the method in this case, is bound to be smaller than 1%. For illustrative purposes, Figure 107 (left) shows the expected

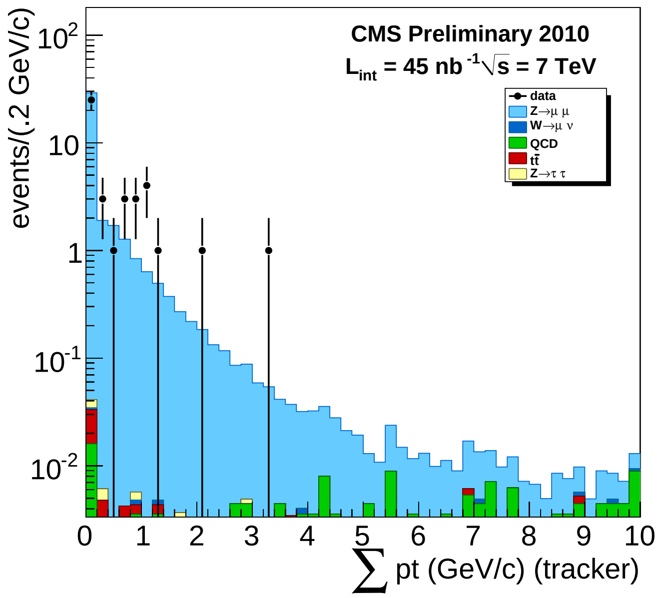

Figure 106: Distribution of the tracker isolation for the muon legs of the $Z \to \mu^+\mu^-$ candidates. All cuts, except on the plotted variable, for the $Z \to \mu^+\mu^-$ selection have been applied. Black points: data; histograms: MC samples normalized to the nominal luminosity of data.

M_T distribution from one 100 nb^{-1} pseudo-data sample. The relative contributions from the different processes and their respective M_T templates derived from high statistics MC are also shown. The right plot of the Figure presents the result of the fit and the ratio with respect to the fake-data sample.

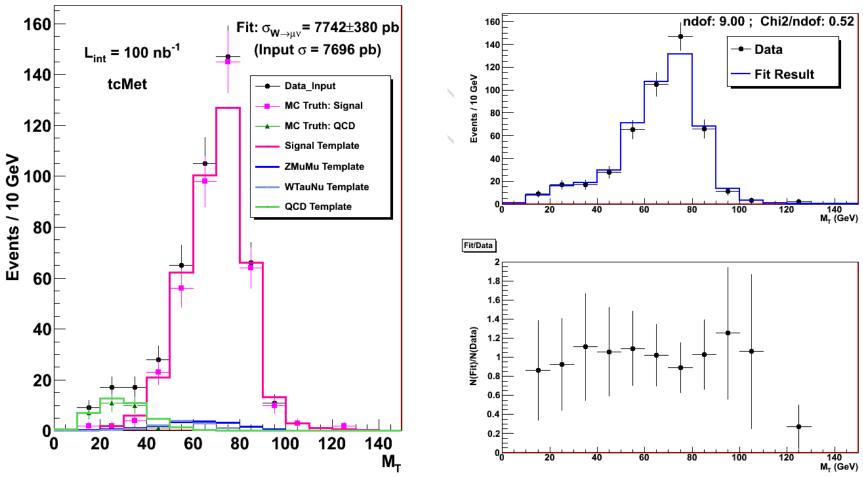

Figure 107: An example of fake-data sample distributions, the simulated luminosity is $\mathcal{L}_{int} \simeq$ 100 nb^{-1}. Left: reconstructed mass in the transverse plane of events passing the $W \to \mu\nu$ selection (including the isolation cut) (black dots). Individual contributions from W signal (pink squares) and QCD background (green triangles) are also shown together with the templates derived from high statistics MC. Right: result of the fit to a sum of the three contributions. Black dots are data and the solid histogram is the result of the fit. The $\not{E}_T$ reconstruction algorithm applied is TcMET.

ABCD method on (M_T vs Isolation)

An alternative way to estimate QCD background starts from the assumption that for all events, the M_T and muon isolation variables are uncorrelated. The number of background events in the signal region is estimated by counting events in control regions, with either low M_T or high isolation, once events from W decays are accounted for. In practice it resembles very much a template method, with a reduced number of bins in M_T, and making use of the non-isolated part of the data to model the isolated part (Uff). The boundaries defining the signal region are set to $M_T > 50$ GeV and $I^{\rm rel}_{\rm comb} < 0.15$.

Figure 108 shows the experimental distribution of reconstructed transverse mass versus relative combined isolation for the events passing the $W \to \mu\nu$ selection criteria except the Isolation one. The limits of the signal and background regions are also shown in the plot. Tests done with pseudo-data samples of 100 nb^{-1} luminosity, generated according to theoretical cross sections and in the same conditions as expected with data prove the good performance of the method. The expected statistical uncertainty is of the order of 4.5% for 100 nb^{-1} sample. Possible systematic uncertainties arise from weak correlation existing between the working variables. Checks performed with the pseudo-data samples show that bias smaller than 1%.

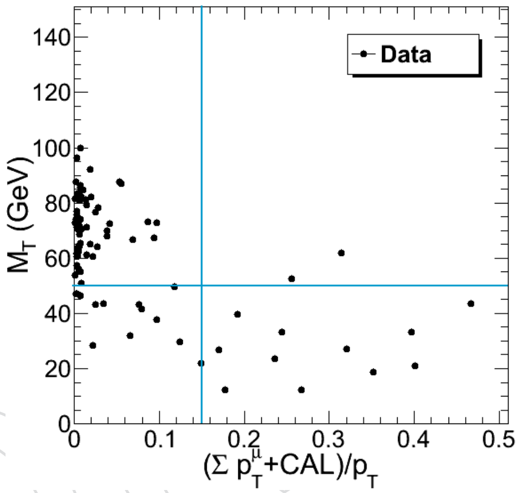

Figure 108: Reconstructed transverse mass versus combined isolation distribution for events with a high p_T ($p_T > 25$ GeV/c) muon ($\mathcal{L}_{\rm int} = 16{\rm nb}^{-1}$). The limits of the A, B, C and D regions are represented in the plot with the solid lines: $M_T = 50$ GeV, $I^{\rm rel}_{\rm comb} = 0.15$.

Simple counting of events

Due to the limited collected luminosity, statistical uncertainty will be the dominant source of error in the W cross section determination, and therefore the possibility to evaluate remaining background from MC, after extensive validation with experimental data is also considered. Contribution from EWK processes ($Z \to \mu^+\mu^-$, $W \to \tau\nu$, $Z \to \tau^+\tau^-$) are taken from MC expectation. They are determined to be YY $\pm$ delta-YY events in the signal region, where the error includes the uncertainty due to the theoretical assumptions in the predictions etc.

To set the level of QCD background, a control sample is defined selecting events with only one good muon and muon $p_T > 20$ GeV/c (could be lowered down to 15 GeV/c) in the fiducial region $|\eta| < 2.1$. The contribution from the non-isolated region (combined isolation ¿ 0.1) in data would be compared with the MC expectation and the background shape in the signal region is normalized according to this ratio.

1D Template fitting on Isolation distribution

A similar procedure can also be followed by fitting the distribution of the other most discriminant variable, isolation. A combined Isolation variable (sum of the pt of the tracks plus sum of the energy in the calorimeters in a cone of radius 0.3 around the muon) is used. W signal template is derived from MC simulation and the same template is used for the rest of EWK processes as the isolation distribution is expected to be very similar to the signal one. The ratio of the yields of EWK processes with respect to the signal one are kept fixed to their theoretical value. The template used for the QCD background is also taken from MC. The statistical error in the determination of the W cross section is of the order of 5%. The systematic uncertainty due to the fitting procedure is of the order of 1% and takes into account effects due to the modeling of the templates, the EWK subtraction, isolation $|\eta|$ dependence and the fit range.

1D parametrized fit on Isolation distribution

A 1D parametrized fit was also explored. The variable used in this method is the total transverse energy in a 0.3 cone around the muon direction ($\Sigma(E_T)$). It is the sum of the combined isolation variable (tracker+calorimeter) and the transverse calorimeter energy in the veto cone which is used in the CMS standard reconstruction isolation calculation. The calorimeter energy in the veto cone is mainly dominated by muon energy deposit, which has roughly $1/\sin\theta$ dependence in barrel, and $1/\cos\theta$ dependence in the forward region. We corrected the calorimeter energy in the veto cone for this geometric dependence so that the $\Sigma(E_T)$ variable has uniform distribution over muon pseudorapidity.

The signal contribution is mainly driven by the muon energy deposition in the calorimeter and it is modeled with a Landau function convoluted with a Gaussian resolution function. Background contribution does not exhibit any particular behavior and it is parametrized with a general function, $x^\alpha \exp(\beta\sqrt{x})$. The shapes of both signal and background were determined with high statistics MC except that the mean of signal Landau peak was allowed to be floating.

The $\Sigma(E_T)$ distribution in the region close to zero exhibits a non smooth behavior mainly due to the Zero Suppressed readout of calorimeters thus the functional definition starts above 0.5 GeV but the events in [0, 0.5] are included in estimating total yields. The expression we have used to determine the W yield is as follows:

$$N_0(< 0.5\ \text{GeV}) + N_{\text{fit}}(> 0.5\ \text{GeV}) = (1 + r(N_{\tau\nu}/N_{\mu\nu})) * N_{W\text{sig}} + N_{\text{Drell Yan}} + N_{\text{t}\bar{\text{t}}} \tag{49}$$

The contribution due to Z $\rightarrow \mu^+\mu^-$ and $t\bar{t}$ are estimated with MC and the contributions due to Z to tau tau and W to tau nu are normalized to that of the processes Z to mumu and the signal one W mu nu. We perform an extended unbinned maximum-likelihood fit over the positively charged muon sample and negatively charged muon sample to determine both the total signal yield and the charge ratio between W^+ and W^- simultaneously. The result of the fit for a Lint=14.2 nb-1 collected data is shown in Figure 109. The fitted W yield is $N_W = 41.5 \pm 6.6 \pm 0.6$. The fitted background yield is zero. Systematic error is mainly due to the uncertainty in ttbar and DrellYan subtraction. A conservative 20% variation in MC predicted yields due to luminosity, efficiency, cross sections (NLO used), is taken.

In addition to the standard selection described in a previous section, tests with relaxed M_T and angular cuts are also done. n this case the remaining QCD background level in a signal-dominated region (0< $\Sigma(E_T) < 6$ GeV) is higher ($\sim$ 9%) but nonetheless, the background level can be better adjusted as the fit is less affected by lack of statistics in the background region (high $\Sigma(E_T)$ values). Figure 110 shows the result of the fit in this case. The fitted signal yield is $N_W = 46.1 \pm 7.4 \pm 2.4$. In this latter case, additional sources of systematic were studied:

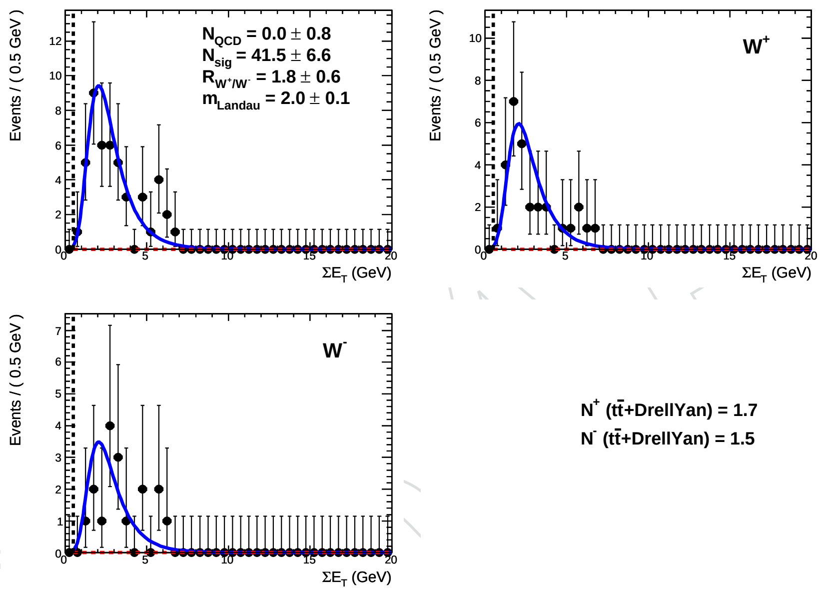

Figure 109: Result of the fit of the isolation distribution to a sum of three components (W signal, EWK background and QCD background).

- We extended the counting region from 0.5 GeV to 0.8 GeV, refitted the data and took the difference in fitted results as systematic errors.
- We extended fitting region from 20 GeV to 25 GeV, refitted the data, and took the shift in fitted results as systematic errors.
- Modeling of signal shape. In the fit the mean of the Landau signal shape was allowed to be floating. We selected good muons with selections $|\eta| <2.1$ and $15\ \mathrm{GeV}/c < p_T < 20\ \mathrm{GeV}/c$ from both data and QCD MC. We fitted the calibrated transverse muon energy in both data and MC with the signal function. The width of the Gaussian resolution function in data was fixed to the MC expectation. We found that in data the Landau mean was about 170 MeV lower and the Landau width was 45 MeV wider than in MC. We increased the width of the signal Landau function by 45 MeV and refit the data. The difference in the fitted results were taken as systematic errors due to modeling of signal shape.

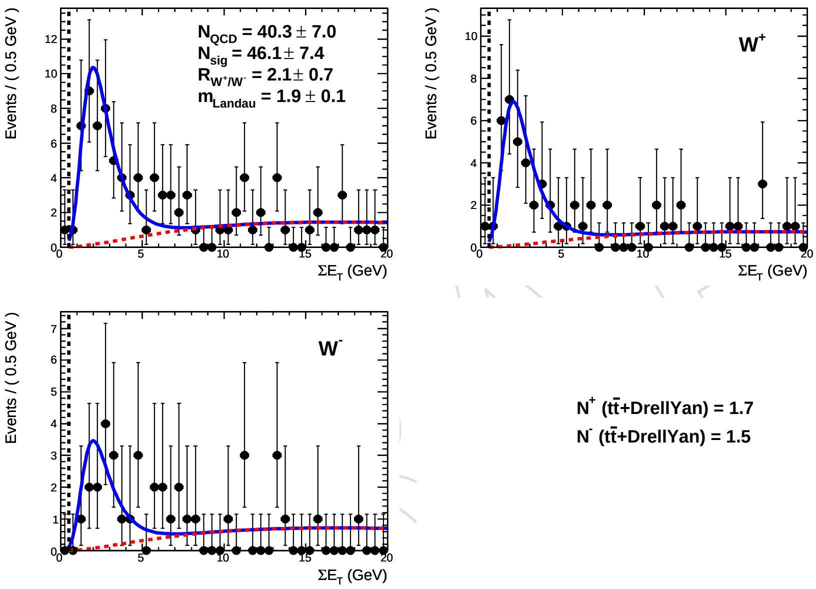

Figure 110: Result of the fit of the isolation distribution to a sum of three components (W signal, EWK background and QCD background). M_T and acoplanarity cuts are relaxed, so the background level is higher.

- Background shape modeling. We defined a control region by selecting events with only one good muon and muon $p_T > 15$ GeV/c and $|\eta| < 2.1$ and $M_T < 30$ GeV/c^2. In this region, QCD events dominate. We compared the $\Sigma(E_T)$ distributions between data and MC. The difference was used to scale the background function and refit the data. We took the difference in the fitted results as the systematic errors due to modeling of background shape.

G Alternative Methods for the extraction of the Wev signal

In this section we describe additional electron-channel W extraction techniques. These methods provide valuable cross-checks on our primary signal yield estimates. The techniques share several sources of systematic uncertainty, which we review in Section 12.3.

G.1 ABCDE

The ABCD method used in the electron channel builds upon the nominal technique [79]. We separate a signal-rich region from background control regions using $\not{E}_T$ and Iso_{trk}, which provide good signal/background discrimination and are only loosely correlated. Additional discriminating variables have been explored (*e.g.*: Iso_{ecal} and $\sigma_{i\eta i\eta}$) and while these perform nearly as well as Iso_{trk}, the latter exhibits the least correlation with $\not{E}_T$ in Monte Carlo studies. We will finalize our choice of discriminating variable with results from an equivalent study performed in data.

We extend the baseline ABCD method to include a fifth region, E, that contains events with Iso_{trk} larger than the WP80 selection. Figure 111 sketches the regions used in the extended "ABCDE" technique. Region E limits the contribution of poorly reconstructed tracks to the regions used for signal extraction.

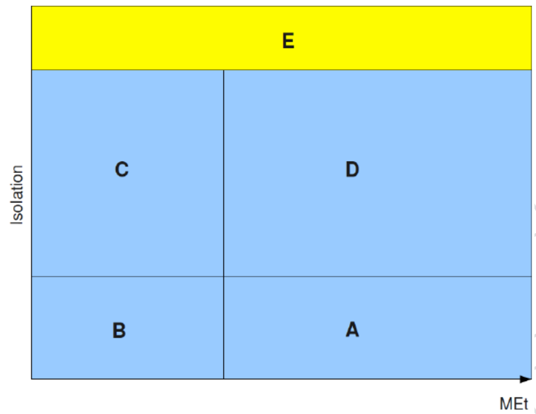

Figure 111: Illustration of ABCDE boundaries.

We define signal efficiencies for the high $\not{E}_T$ and low isolation regions :

$$N_i = S_i + B_i \tag{50}$$

$$\epsilon_A^{sig} = \frac{S_A}{S_A + S_B} \tag{51}$$

$$\epsilon_D^{sig} = \frac{S_D}{S_D + S_C} \tag{52}$$

$$\epsilon_{A+B}^{sig} = \frac{S_A + S_B}{S_A + S_B + S_D + S_C} \tag{53}$$

and assume that Iso_{trk} and $\not{E}_T$ are uncorrelated for QCD background. This results in equal QCD efficiencies :

$$\epsilon_A^{qcd} = \frac{QCD_A}{QCD_A + QCD_B} \tag{54}$$

$$\epsilon_D^{qcd} = \frac{QCD_D}{QCD_D + QCD_C} \tag{55}$$

$$\epsilon_A^{qcd} = \epsilon_D^{qcd} \tag{56}$$

Using the above equations, we solve for the total number of signal events (S) in regions A+B+C+D :

$$
\begin{aligned}
aS^2 + bS + c &= 0\,\text{, where} && (57)\\
a &= \epsilon_{A+B}(\epsilon_{A+B} - 1)(\epsilon_A - \epsilon_D) && (58)\\
b &= N_A(1 - \epsilon_{A+B}(1 - \epsilon_D) && (59)\\
&\quad + N_C \epsilon_A \epsilon_{A+B} && (60)\\
&\quad - N_B \epsilon_C (1 - \epsilon_{A+B}) && (61)\\
&\quad - N_D \epsilon_{A+B} (1 - \epsilon_A) && (62)\\
c &= N_D N_B - N_A N_C && (63)
\end{aligned}
$$

Optimal values for the $\not\!\!E_T$ and Iso_{trk} boundaries are determined by simultaneously minimizing the bias and relative statistical uncertainty of Monte Carlo signal estimates. A choice of Iso_{trk} boundary of 0.027 for electrons in the barrel and 0.02 for electrons in the endcaps was found to minimise the bias (less than 1% whilst keeping the statistical uncertainty to around 6%. This procedure uses a "pseudo-data" sample comprised of QCD and W signal Monte Carlo normalized to 0.198 pb^{-1}. Figure 112 shows estimated signal yields versus truth for a range of $\not\!\!E_T$. These plots suggest an optimal value for the $\not\!\!E_T$ boundary separating regions A from B and D from C of 24 GeV, which is consistent with results from our minimization procedure.

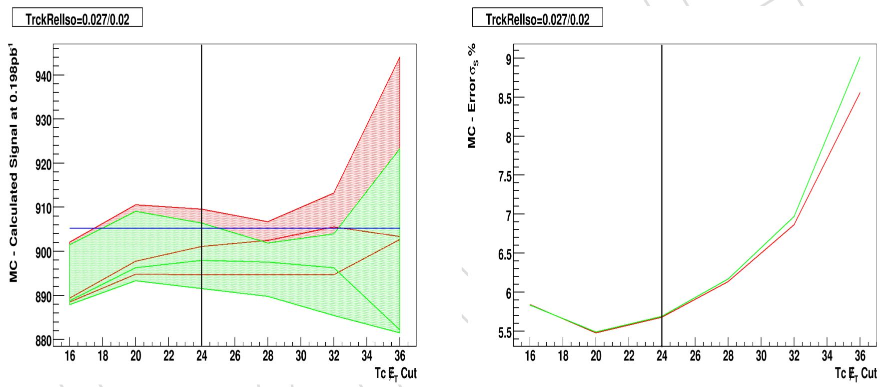

Figure 112: ABCD Boundary Optimization. We optimize $\not\!\!E_T$ boundary definitions by minimizing the bias (left) and relative statistical uncertainty (right) of signal yield estimates in 0.198 pb^{-1} Monte Carlo. Vertical lines indicate our boundary choices.

The biases in Figure 112 are on the order of a few events for most of the $\not\!\!E_T$ ranges shown, confirming that these variables are largely uncorrelated. Table 39 lists the true number of signal/background events and corresponding ABCDE estimates for each optimally defined region in our pseudo-data sample. Predicted signal yields agree with Monte Carlo truth.

We apply the ABCDE method to 198 nb^{-1} and estimate a signal yield of 741.3 $\pm$ 58.6 events. Using PYTHIA acceptance and efficiency estimates, we determine $\sigma(W) \times BR(e\nu) = 8.5 \pm 0.7$ (stat) from events in the full acceptance region.

Systematic uncertainty on ABCDE-predicted yields arises from correlation between the discriminating variables in background, from signal contamination of the background control regions and from uncertainty in our signal efficiencies. We discuss how these impact the ABCDE measurement in Section 12.3.

Region	True QCD	True Signal	Estimated Signal
A	10.3	694.9	689.3
B	541.7	161.9	160.6
C	196.7	8.4	8.4
D	4.7	39.9	39.8
Total QCD MC			743.4
Total Signal MC			905.2
Total Estimated Signal			901.1 $\pm$ 51.2 (stat)

Table 39: True and ABCDE estimated yields in pseudo data.

G.2 Fixed-Shape Template Fits

While $\not\!\!E_T$ shapes are implicit in the two-dimensional ABCD method, template fitting techniques exploit this additional information explicitly. The simplest template method uses fixed $\not\!\!E_T$ or M_T shapes in an extended maximum likelihood (EML) fit for the signal and background yields. The template shapes are static and the technique relies on an accurate modeling of signal and background $\not\!\!E_T$ or M_T distributions. The fixed-shape fit involves just two free parameters however, and can provide for robust fitting even with the small yields in 0.2 pb^{-1}.

We take W Monte Carlo $\not\!\!E_T$ predictions as the signal template in the electron channel. The shapes of EWK backgrounds are predicted from Monte Carlo and included in the signal template with fixed, relative normalizations given by the NLO cross sections. We obtain a fixed-shape $\not\!\!E_T$ template for QCD background by selecting events with $\Delta\eta > 0.007$ (barrel), 0.009 (endcap) and $\Delta\phi > 0.06$ (barrel), 0.04 (endcap), *i.e.:* inverting the WP90 selections on these variables. Monte Carlo studies show that these "anti-selections" generate a sample of relatively pure background with a $\not\!\!E_T$ distribution similar to that of QCD events passing the full set of WP80 ID criteria (see Figure 113). We maintain the WP80 selection on $\mathrm{Iso}_{\mathrm{ecal}}$ when generating the template. $\mathrm{Iso}_{\mathrm{ecal}}$ is strongly correlated with MET and the application of this cut significantly improves agreement in the shapes. No additional cuts are applied.

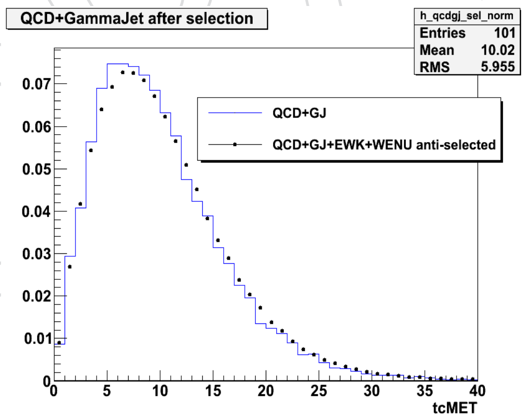

Figure 113: Fixed-Shape QCD Template. We generate a QCD template by imposing $\Delta\eta$ and $\Delta\phi$ anti-selections and the WP80 $\mathrm{Iso}_{\mathrm{ecal}}$ cut. Monte Carlo shows that this shape is a close match to the background distribution found after the full WP80 selection.

We study the performance of the template method by running 5K pseudo-experiments in RooFit [80]. The input templates are normalized to 198 nb^{-1} expectations and we generate data points for each pseudo-experiment by Poisson fluctuating the combined signal+background $\not\!\!E_T$ distribution. We then perform binned EML fits for the total signal and background yields. Fit results for a particular pseudo-experiment are shown in Figure 114. Figure 115 shows the distribution of fit signal yield and the value input to the pseudo-experiments. The RMS of this distribution indicates a relative statistical uncertainty on the 198 nb^{-1} signal yield of $\sim$ 3.5%. This is also reflected in the mean of the error distribution in Figure 116.

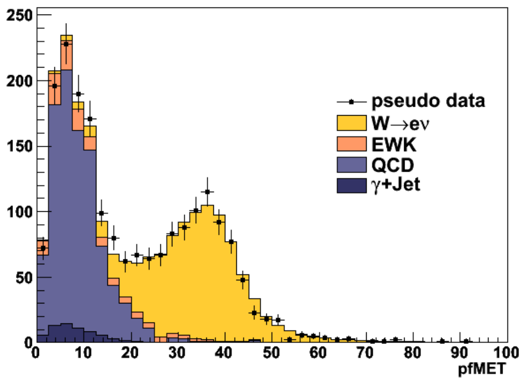

Figure 114: A Fixed-Shape Template Fit. We perform an EML fit of signal and background templates to 198 nb^{-1} pseudo-data.

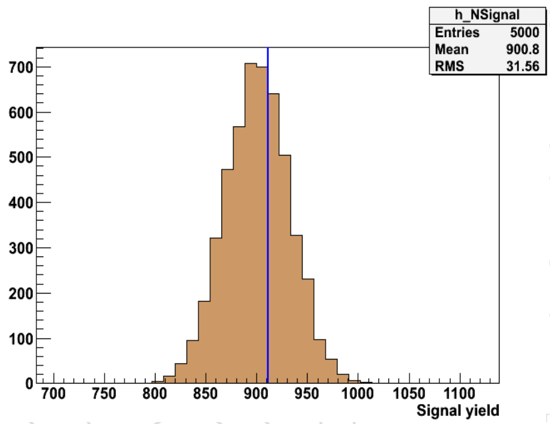

Figure 115: Fixed-Shape Signal Yields. The distribution of fitted signal in 5K pseudo-experiments has an RMS of $\sim$ 3.5%, close to what would be obtained from Poisson statistics alone.

Fit performance is more clearly demonstrated by pull distributions of signal yields. Figure 116 shows that the fit is slightly biased as a result of shape discrepancies between true background and the template, but provides a proper account of the statistical uncertainties on the yields.

Figure 117 shows results of the fixed-shape fit performed in 197.9 nb^{-1}. We extract a W yield of 795 ± 30 (stat) events in the full acceptance region. We use the fit yields and LO Monte Carlo acceptance and efficiencies to estimate $\sigma(W) \times BR(e\nu) = 9.29$ nb $\pm$ 0.35 nb (stat). This result is in agreement with the NLO prediction, 10.3 nb.

Uncertainty in the true shape of the signal and background $\not{E}_{\mathrm{T}}$ distributions leads to corresponding systematic uncertainties on fixed-shape fit predictions. We describe how these uncertainties are estimated in Sections 12.3.1 and 12.3.2

H TC $\not{E}_{\mathrm{T}}$ plots for $W \longrightarrow e\nu$ Signal Extraction

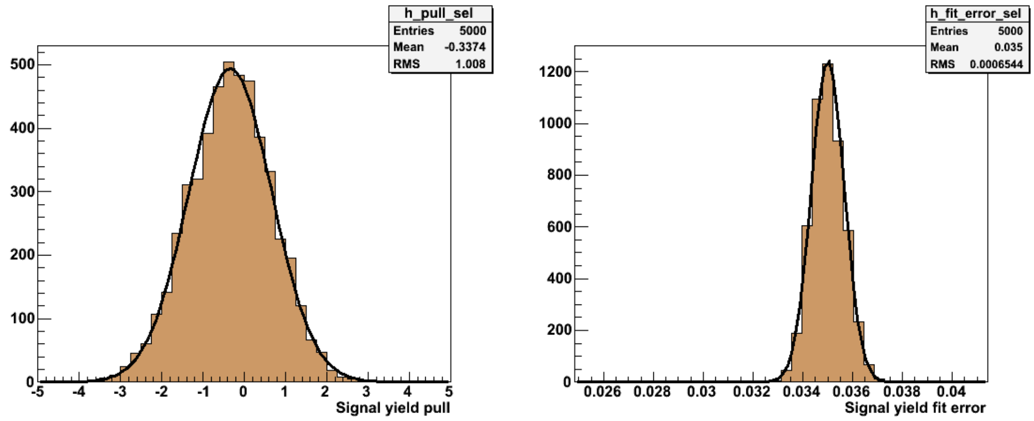

Figure 116: Fixed-Shape Pulls and Uncertainty. The shape of the QCD template differs from the true background distribution, causing a small bias in the pull. The width of the pull distribution indicates that fit uncertainties are well modeled.

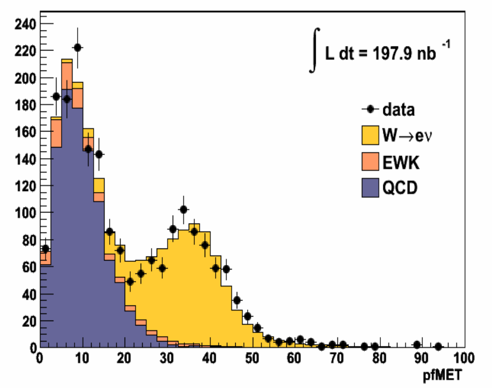

Figure 117: Fixed Shape Fit Results for 197.9nb^{-1}. We find that the fixed-shape models provide a good fit to available data.

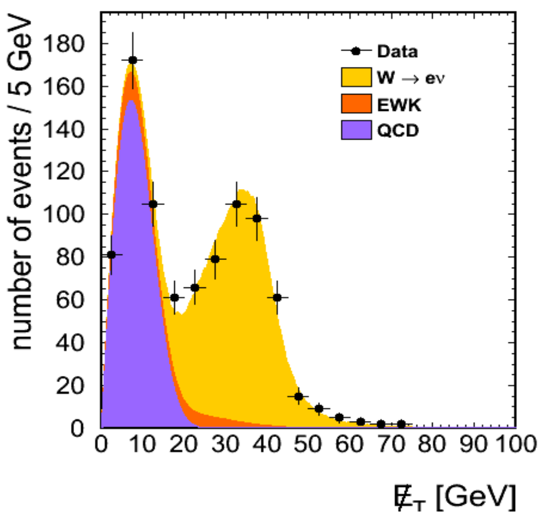

Figure 118: Example Hybrid $\not\!\!E_T$ Model Fits ($\not\!\!E_T^{TC}$). We perform unbinned EML fits of the hybrid $\not\!\!E_T$ model to 0.1 pb^{-1} pseudo-data.

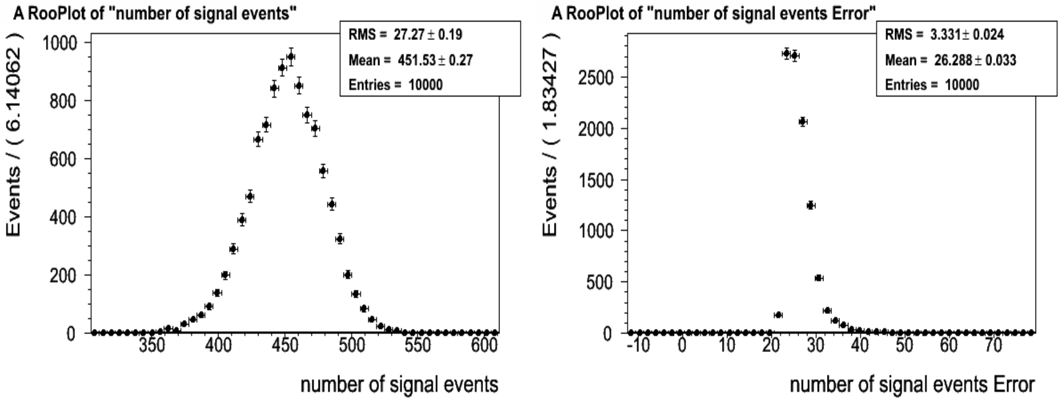

Figure 119: Yields (left) and Uncertainties (right) for the Hybrid $\not{E}_{\mathrm{T}}$ Model ($\not{E}_{\mathrm{T}}^{TC}$). The statistical uncertainty on signal yield from the hybrid $\not{E}_{\mathrm{T}}$ model is 6.0%, which is slightly larger than $1/\sqrt{N}$.

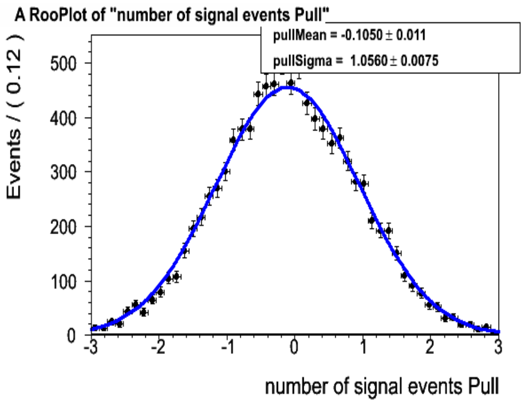

Figure 120: Hybrid $\not{E}_{\mathrm{T}}$ Model Signal Pulls ($\not{E}_{\mathrm{T}}^{TC}$). The hybrid model shows low bias in 0.1 pb^{-1} pseudo-experiments. The widths of the pull distributions indicate that statistical uncertainty on the yield is properly modeled.

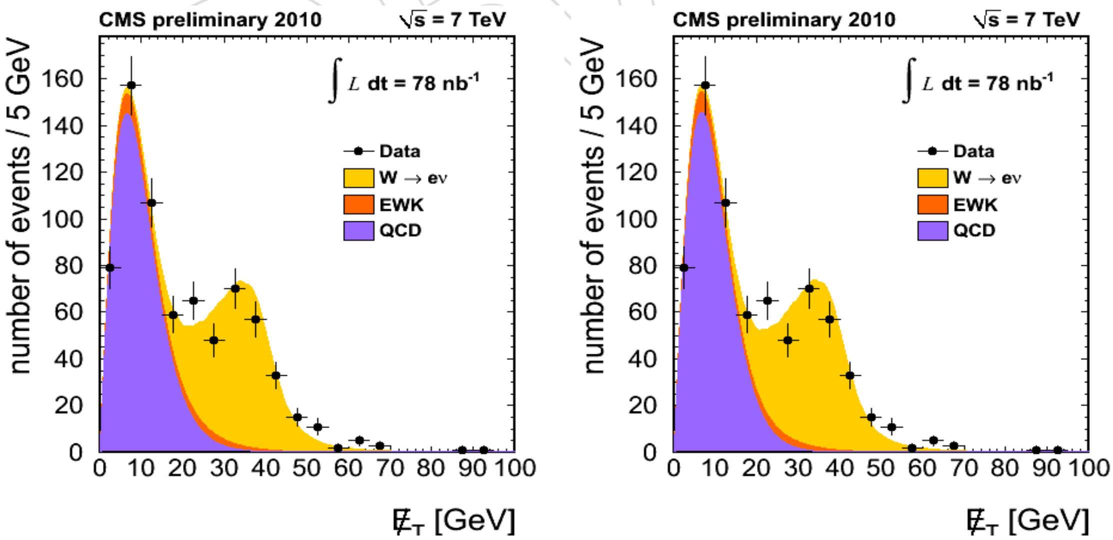

Figure 121: Hybrid $\not{E}_{\mathrm{T}}$ Fit for 78 nb^{-1} ($\not{E}_{\mathrm{T}}^{TC}$). We fit the hybrid $\not{E}_{\mathrm{T}}$ model to 78 nb^{-1} with parameter b fixed to its expected value (left) and with parameters a and b floating (right). The yield results are consistent to within 1.7%.

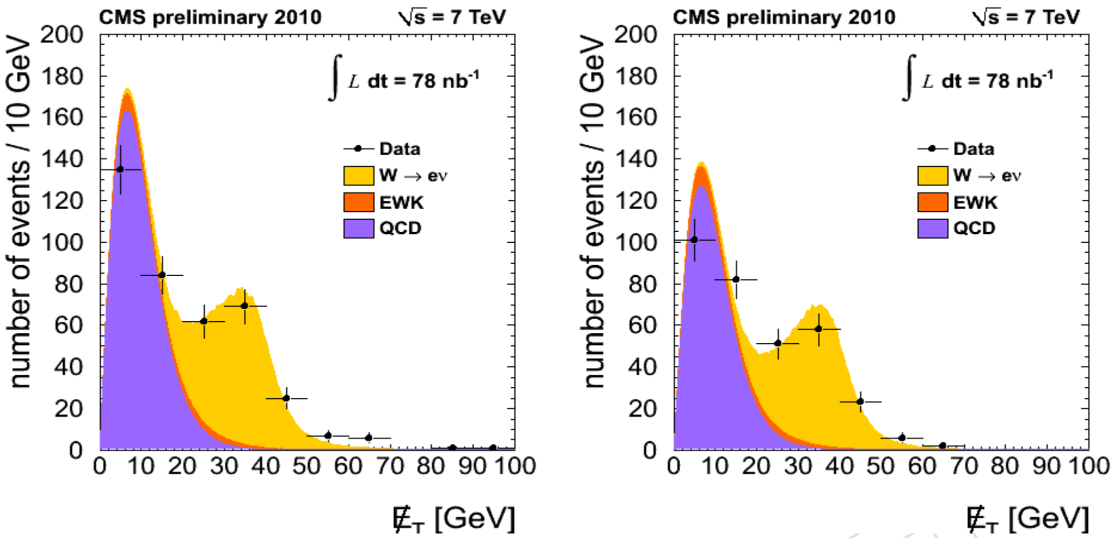

Figure 122: Hybrid $\not\!\!E_{\mathrm{T}}$ Fit for W^+/W^- in 78 nb^{-1} ($\not\!\!E_{\mathrm{T}}^{TC}$). We perform a simultaneous fit for W^+ (left) and W^- (right) yields in 78 nb^{-1}. We find $N_{W^+}/N_{W^-} = 1.14 \pm 0.14$.

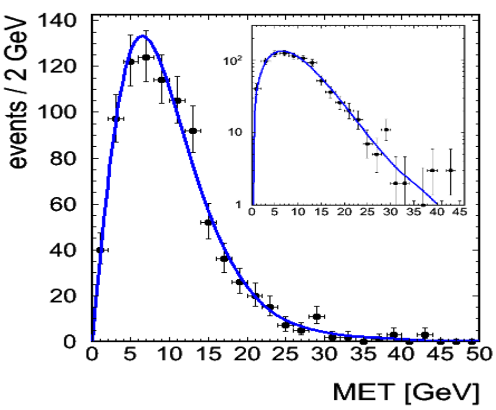

Figure 123: $\not\!\!E_{\mathrm{T}}$ Fits to Anti-selected Distributions in Data ($\not\!\!E_{\mathrm{T}}^{TC}$). We fit the hybrid $\not\!\!E_{\mathrm{T}}$ model to background distributions obtained by reversing various WP80 selections. The high quality of the fit suggest that our model is an adequate description of background after full selection.